HIGH-RESOLUTION SEISMIC AND CORE-BASED STRATIGRAPHY OF THE SOUTHWESTERN BLACK SEA SHELF DURING THE HOLOCENE

Olga Ankindinova, B.Sc., M.Sc

A Dissertation submitted to the
School of Graduate Studies in
partial fulfilment of the requirements
for the degree of

Doctor of Philosophy

Department of Earth Sciences
Memorial University of Newfoundland

February 2020

St. John's Newfoundland and Labrador

ABSTRACT

The paleo-environmental evolution of the Black Sea during the last 12,000 years is studied using high-resolution seismic-stratigraphic and geochemical results for two long composite cores from the southwestern shelf, constrained by 56 radiocarbon dates on mollusc shells. A grid of Huntec deep-tow seismic-reflection profiles (~9150 line-km), complemented by 72 gravity cores and 25 piston cores reveals a prominent shelf-crossing transgressive unconformity α which is overlain in most areas by, in succession, allounit 1b (~12.5–7.4 cal ka BP) between α and the α1 submarine unconformity/correlative conformity, allounit 1c (~7.4–5.3 cal ka BP) between the α1 and α2 submarine unconformities/correlative conformities, and allounit 1d (deposited since ~5.3 cal ka BP).

The $^{87}Sr/^{86}Sr$ isotopic signature in molluscs shows four stages of increase corresponding to salination associated with the reconnection of the Black Sea to the global ocean: 12,145–9580 cal yr BP (stage A; stable, brackish lacustrine conditions); 9580–9490 cal yr BP (stage B: freshish waters); 9465–9380 cal yr BP (stage C; sharp $^{87}Sr/^{86}Sr$ increase to a plateau spanning 350–400 years); ~8985 cal yr BP to the present day (stage D; step-wise salination). The existence of the first plateau provides strong evidence against catastrophic flooding of a lowstand Black Sea as proposed by other workers. $\delta^{18}O$ and $\delta^{13}C$ values in ostracod species *Palmoconcha agilis* and *Loxoconcha lepida* define three isotopic substages corresponding to a transition from the Neoeuxine Lake to modern conditions. These are mirrored in trace-element/Ca data, which reveal a Neoeuxine Lake stage (12.1–9.4 cal ka BP), the transition from lacustrine to marine conditions (9.4–6.3 cal ka BP) and the establishment of marine conditions (6.3–0 cal ka BP). At ~6.3 cal ka BP, isotopic data

and trace-element/Ca ratios exhibit a major shift contemporaneous with a sharp increase in water temperature from 12–14°C to 17–19°C. This shift coincides with the weakening of Black Sea outflow and the proliferation of marine organisms.

This study proves that the level of the Neoeuxine Lake must have been significantly higher than −70 m at the time of the reconnection at 9.4 cal ka BP with the gradual step-like transition to present-day conditions.

ACKNOWLEDGEMENTS

Many people have supported me during this study. Without this support I could not have come so far. First and foremost, I would like to express my deepest appreciation and gratitude to my supervisors Dr. Ali E. Aksu and Dr. Richard Hiscott for the opportunity to take part in this exiting research project, for their trust, continuous patience, guidance, constructive feedback and even occasional babysitting of my kids. I am truly grateful for the precious gift of time you gave me that's the greatest gift because you only have a set amount of it. When you give someone your time, you are giving them a portion of your life that you'll never get back. It is a pleasure and privilege to work with you and to know you in person.

I would like to send a special thanks for the guidance and expertise to Alison Pye during the acquisition of the oxygen and carbon isotopic analyses in the Stable Isotope Lab, Markus Walle during the acquisition of the trace-element data using the LA-ICP-MS, Wanda Aylward during the acquisition of the CaO data using EPMA, Alison Harris during Sr extraction, Rebecca Lam during strontium isotopic analysis using Neptune Multi-Collector ICPMS, Sherri Furey for the assistance in laboratory data acquisition, Peter Bruce for his assistance in seismic data reduction. We are grateful for the assistance and advice received from Drs. Raina Hristova and Dimitar Dimitrov of the Bulgarian Academy of Sciences, Dr. Vladimir Kostylev of the Geological Survey of Canada for his assistance with mollusc identifications and ecology and Professor Patrick De Dekker of the Australian National University for his advice on application of the LAICP-MS technique to ostracods.

My dissertation committee members Dr. Jeremy Hall, Dr. John Hanchar, Dr. Vaughan Grimes for their help, support, interest and valuable suggestions.

A journey is easier when you go together. I am grateful to my husband and my best friend Antonio Ramirez for being near all these years providing, emotional and financial support, for all the encouragement and for being there for me unfailingly. I am thankful to my kids Elizabeth and Vivienne Ramirez for been my biggest motivation and a biggest ever source of joy.

Last but certainly not least I want to thank my mom Natalia Ankindinova who couldn't make it until the end of my study but was supporting me till the last days of her life and my father Vladimir Ankindinov for made me who I am today. To my sister Veronika Ankindinova and my wonderful mother-in-law Martha Elena Pichardo Guzman who never hesitated to come a long way from their countries to help me take care of my children.

Without all these people this thesis won't be possible.

Table of Contents

List of Tables

List of Figures

List of Equations

List of Abbreviations

^{14}C yr BP Abbreviation for uncalibrated radiocarbon years before present.

Cal yr BP Abbreviation for calendar years before present.

Chapter 1. Introduction

This thesis is part of a continuing research program started ca. 1995 by thesis supervisors Drs. Aksu and Hiscott (with a rotating list of other collaborators) in the lands and waterways around the Aegean, Marmara and Black seas. The overarching theme has been the tectonic history, and watermass, sea-level and climatic changes which occurred during the Quaternary, both in the immediate area and elsewhere in central and northern Europe as they influenced the study region. This thesis contributes an integrated paleoceanographic reconstruction of the southwestern Black Sea shelf during the latest Quaternary based on seismic stratigraphic analysis, lithostratigraphy and geochemistry of sediments. The results of this study have generated three peer reviewed manuscripts which have been accepted and published in the highly visible journals Marine Geology and Palaeogeography, Palaeoclimatology, Palaeoecology (Ankindinova et al., 2019a,b; 2020).

1.1. Geographical Location

The Black Sea is situated between 40°55' N and 46°32' N latitudes and 27°27' E and 41°42' E longitudes in the east–west-oriented depression between two alpine fold belts, the Pontic Mountains of Turkey to the south and the Caucasus and Crimea mountains of Russia and Ukraine to the north and northeast. The large Danube delta and the relatively smaller Dniester, Dnieper and Bug deltas and their coastal plains lie to the northwest. The Black Sea is one of the largest marginal seas, locally as deep as 2206 m and over 420,000 km^2 in area. Its coastline borders on six countries: Bulgaria, Georgia, Romania, Russia, Turkey, and Ukraine (Fig 1.1).

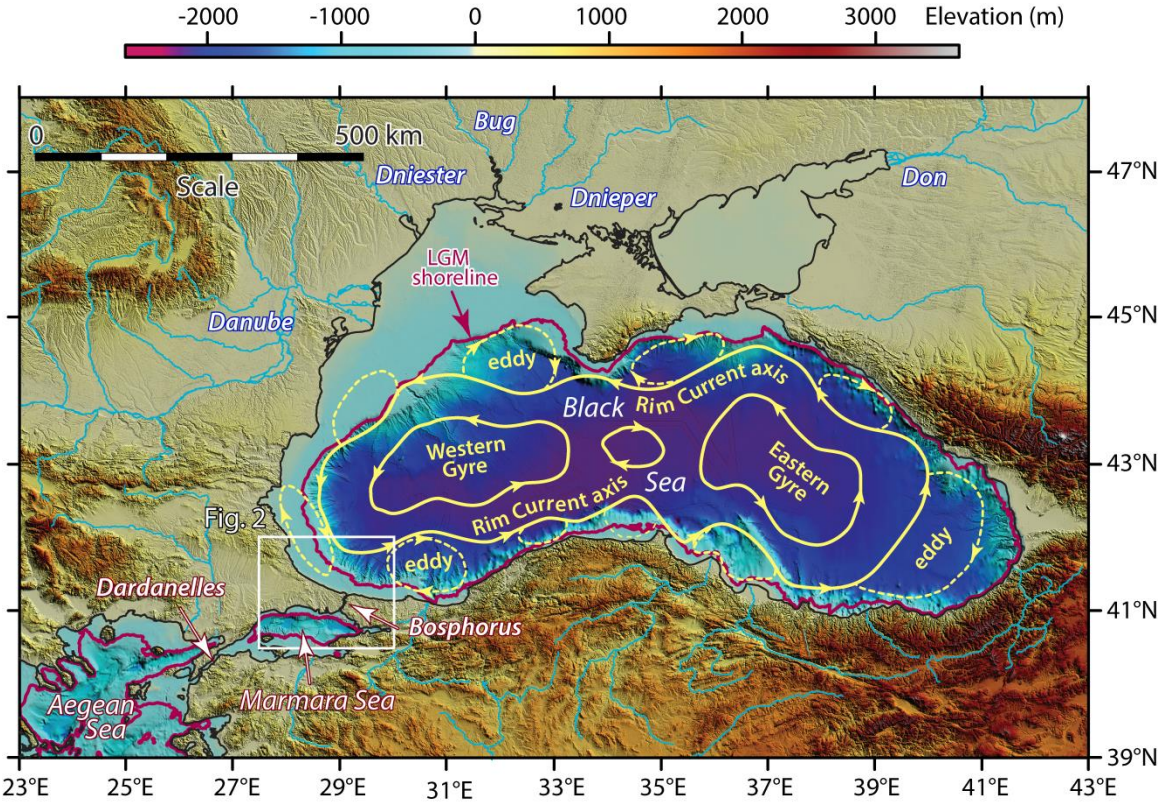

Figure. 1.1. Location map showing the Black Sea and its connection to the Aegean Sea via the Marmara Sea Gateway. The last glacial maximum (LGM) shoreline is drawn at the ~ –125 m isobath (IOC, 1981); at that time the water body labeled as the Black Sea was instead the Neoeuxine Lake. The outlined area is shown in detail in Figure1.2. Surface currents are from Oğuz et al. (1993). Topography and bathymetry compiled using GeoMapApp (Ryan et al., 2009) in Global Mapper. Coastline and rivers are from NOAA National Geophysical Data Center (http://www.ngdc.noaa.gov/mgg/shorelines/ shorelines. html).

1.2. Bathymetry and Morphology of the Black Sea

The Black Sea is the world's largest permanently anoxic and euxinic basin. Its only connection to the global ocean is through the shallow and narrow straits of Bosphorus and Dardanelles and the intervening land-locked Marmara Sea, collectively referred to in this thesis as the Marmara Sea Gateway (Fig. 1.2). The Black Sea has a surface area of 4.2 x $l0^5$ km^2 and a volume of 5.3 x $l0^5$ km^3. There are four main physiographic provinces in the

Black Sea Basin: The continental shelf, the slope, the basin apron and the abyssal plain (Mamaev & Musin, 1997; Fig. 1.3).

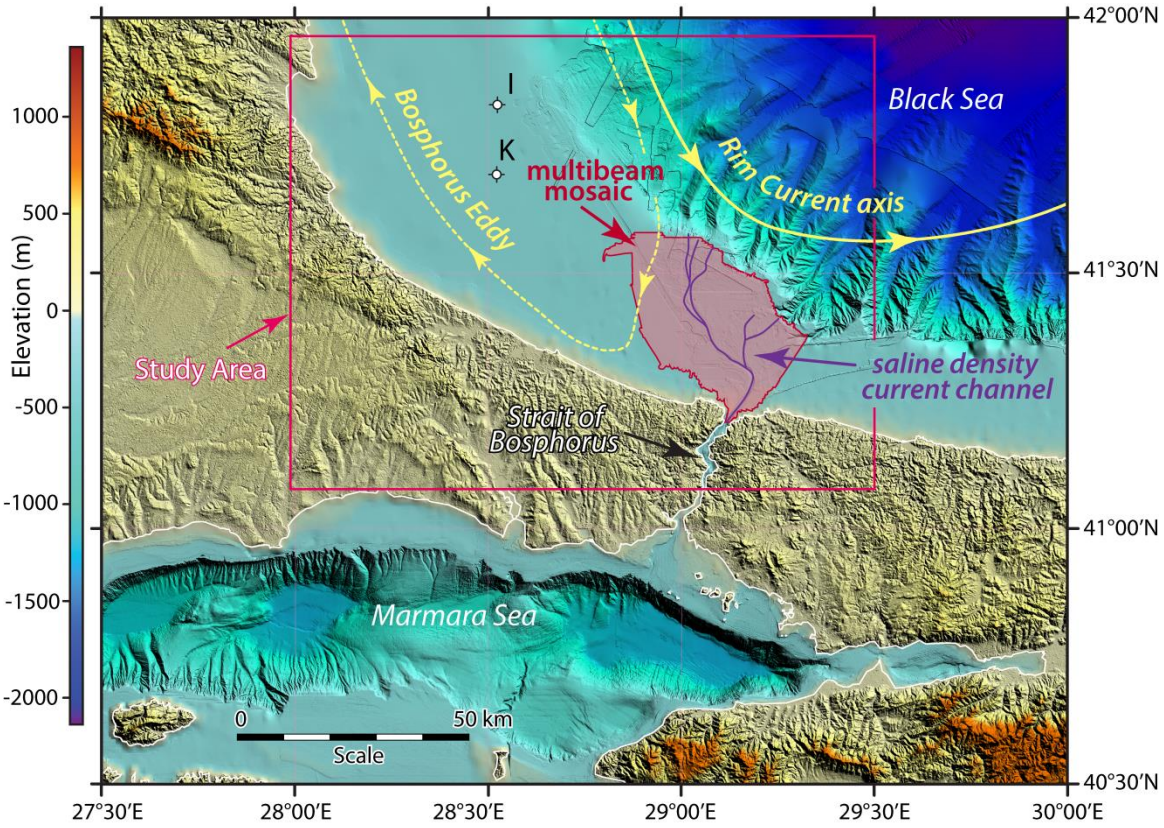

Figure 1.2. Location map showing the southwestern Black Sea and its connection to the Marmara Sea via the Strait of Bosphorus. The cyclonic Rim Current and the anticyclonic Bosphorus Eddy are from Oğuz et al. (1993). Bathymetry of the Black Sea and the regional topography (extracted from GeoMapApp, Ryan et al., 2009) and gridded bathymetry data for the Marmara Sea (from Rangin et al., 2001) are compiled using Global Mapper v14. Coastline and rivers are from NOAA National Geophysical Data Center (http://www.ngdc.noaa.gov/mgg/shorelines/shorelines.html). White circles are exploration wells: I = İğneada–1 and K = Karadeniz–1. Light red fill is the area of a detailed multibeam mosaic, where dark purple lines highlight the main channels of a saline density-current network created by the saline underflow of Mediterranean seawater (explained in text). The box outlines the study area, illustrated in various text figures.

The continental shelf is narrow (35–50 km) along the southern and northeastern Black Sea, but widens considerably (~100–220 km) in the northwest and west off the

mouths of major rivers; reaching ~140 km off the Danube mouth and ~190 km off western Crimea (Fig. 1.1). Near the Kerch Strait, the shelf is about 40 km wide. The southern and eastern shelves are much narrower, from 20 km to almost 0 km in the southeastern corner of the Black Sea.

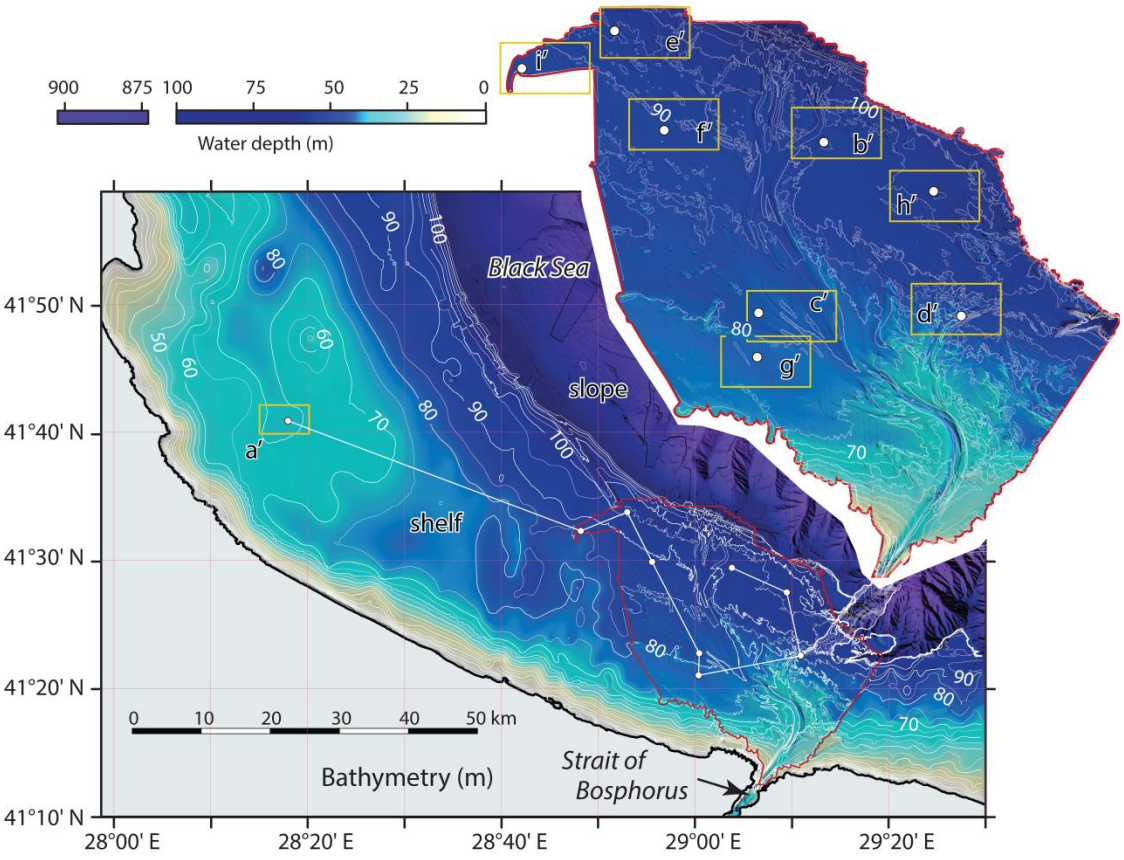

Figure 1.3. Bathymetric map of the southwestern Black Sea margin extracted using GeoMapApp (Ryan et al., 2009). The detailed bathymetry of the saline channel area is from Flood et al (2009) and Hiscott et al. (2013). Small white circles are composite key and reference cores discussed in the text. Location is shown in Figure 1.2

A large portion of the modern continental shelf was exposed as a subaerial coastal plain during the Last Glacial Maximum (LGM). The modern shelf-to-slope break occurs between the –100 and –200 m isobaths, beyond which slopes of 2–15º (e.g., Aksu et al.,

2002a; Çifçi et al., 2002; Constantinescu et al., 2015) lead to abyssal depths of 2210–2258 m (Ivanov and Belokopytov, 2011). In front of the mouths of the Danube, Dniester, Dnieper and Bug rivers the shelf edge lies at a depth of 120 m; whereas on the northern shelf offshore of the Crimea Peninsula and at the outlet of the Sea of Azov, it occurs at ~130 m deep.

The continental slope is usually steep (average slope ranging between 5° and 8°; Ross et al., 1974) and highly dissected by canyons, especially across the areas with narrow shelves in the eastern and southern Black Sea. Where canyons extend landward onto the shelf, they are interpreted as the drowned valleys of paleo-rivers (e.g., Lericolais et al., 2002; Constantinescu et al., 2015). The slopes of the northwestern and northern Black Sea are less steep and high fluvial sediment input in those areas leads instead to the deposition of deep-sea fans. The Danube fan and the Dnieper/Dniester fan systems are situated on the northwestern slope, while the Don/Kuban fan system lies off the Kerch Strait that connects the Black Sea and the Sea of Azov.

Terrestrial sediments are deposited on the basin apron, which is morphologically equivalent to what is called the continental rise in major ocean basins. The basin apron is less steep than the slope. The average bottom slope of the continental rise does not exceed 2°, where its width is largely a function of sediment input via major rivers, ranging from 9–12 km across the eastern Black Sea, to 45–55 km in the north and northwest.

The central Black Sea Basin is characterized by the flat abyssal plain with seabed angles from 0° to 1°. The deepest point of the Black Sea lies in the western part of the abyssal plain; it has a water depth of 2258 m.

1.3. Physical Oceanography of Black Sea

The Black Sea is the world's largest semi-enclosed marginal sea, and its physical and chemical structures are determined by its hydrological balance (Table 1.1). The Black Sea is connected to the World Ocean through two shallow and narrow straits. The Bosphorus Strait (0.76–3.60 km wide; <93 m depth; 31 km length) connects the southwestern Black Sea to the Marmara Sea. The depth of the sills in the strait has significant impact on both the volume of incoming waters, and their salinity. The southern sill at the entrance of the Sea of Marmara near Golden Horn Bay is 40 m deep; the northern sill, which is 3.5 km long, is located 3 km from the exit to the Black Sea and is 60 m deep (Aksu et al., 2016; Latif et al, 1991).

Table 1.1. Physical characteristics of the Black Sea (Murray et al., 2007).

Total area	423,000 km^2
Total volume	534,000 km^3
Deep water volume (>50 m)	520,000 km^3
Depth of permanent halocline	50 to 200 m
Maximum depth	2258 m

The Marmara Sea in turn is connected to the Aegean Sea by the Dardanelles Strait with sill depth of ~63 m (Aksu et al., 2016). The Black Sea is also connected to the Sea of Azov by the Strait of Kerch in the north.

The level of the Black Sea oscillates seasonally by ~10–15 cm in response to changes in freshwater input from large rivers such as the Danube, Don, Dneiper, Dneister and Bug (Stanev et al., 2000). Tides are generally less than 10 cm.

In the southwestern Black Sea, waves generated by 100-year storms influence the seafloor to depths of up to 80–95 m (Aksu et al., 2002a). On shorter time scales, significant wave base is at a depth of ~35–50 m, with the result that Holocene muds remain suspended and are rarely able to accumulate in water depths less than ~65 m (Hiscott and Aksu, 2002).

The range of seasonal fluctuations in air temperature decreases from 22–23°C on the northern coast to 15°C in the south. The average air temperature for the whole coast is 12.8°C, which is 2°C lower than the average sea surface temperature. In contrast to summer months, the warming influence of the Black Sea on the air temperature is most noticeable from December until January, when the temperature difference between air and water in the coastal zone reaches 3–4°C. This leads to the development of thermal stratification in the water column, known as a seasonal thermocline. Seasonal variations of salinity are characterized by two maxima: one at the sea surface and the second in the upper part of the permanent halocline. The existence of the second peak is explained as a result of seasonal variation of the general circulation of the sea, causing vertical motions of the main halocline (Filippov, 1968). Variability of meteorological characteristics, along with the seasonal heat balance variations, is largely determined by atmospheric circulation. The Black Sea is influenced by a permanent large anticyclone – the Azores High – and a few seasonal pressure systems: the Siberian high and the Mediterranean depression in winter, and Arabian depression in summer. Seasonal variations in atmospheric pressure are characterized by a maximum during the cold season, and a minimum in the warm season. A local extreme of high atmospheric pressure is observed in April–May, when low-gradient pressure fields prevail. On the synoptic scale, the weather over the sea is determined by

movement of cyclones and anticyclones. According to Drozdov et al. (1989), frequency of moving cyclones over the Black Sea increases from 5% in July to 10–15% in January, while the number of moving anticyclones over the Black Sea does not change much through an average year (about 4%). According to Polonsky et al. (2007), frequency of cyclones in the Black Sea through 1952–2000 increased from 7% in summer to 17% in January and, conversely, frequency of anticyclones decreased from 21% in summer to 13% in winter with considerable interannual variability and with differently directed trends. For regional oceanography, characteristics of the wind regime are crucially important, as wind directly affects circulation and mixing of water, heat and water balance.

According to the character of the wind activity over the sea, heavy waves develop mostly in the autumn and winter in the northwestern, northeastern, and central parts of the sea. In open sea regions, the maximum wave heights may reach 7 m; during strong storms the surge along the coastline may be even higher. The southwestern and southeastern parts of the sea are the calmest; here, strong winds are rare and usually wave heights do not exceed 3 m even during storms (Kosarev et al., 2008), although rare events in the southwest generate significant waves of 5–8 m (Valchev et al., 2012, their figure 7). In addition to different types of wave motions, other physical processes contribute to oceanographic variability on mesoscale and synoptic time scales. In the coastal zone, a significant role is played by wind-induced motions and upwelling. In the surface layer of the sea, atmospheric forcing is important: the heat and water balance, the magnitude of which increases from winter to summer; the moving synoptic pressure systems, storms, sea-breeze circulation (Ivanov, Belokopitov, 2011).

1.3.1. Water Masses

Salinity in this thesis is expressed as the so-called "practical salinity", S. The UNESCO Practical Salinity Scale of 1978 (PSS78) defines salinity in terms of an electrical conductivity ratio which is a dimensionless quantity. A standard seawater of practical salinity 35 has, by definition, a conductivity ratio of unity at 15°C when compared to a KCl solution containing a mass of 32.4356 g KCl in a mass of 1 kg of solution. For salinity values reported as permil chlorinity in cited publications, the numerical values are taken to be identical to the corresponding practical salinity whenever the accuracy is expressed at no better than integer values.

The two-way flow across the Bosphorus Strait contributes to water-column stratification in the Black Sea and makes it the world's largest meromictic water body. The seawater flowing northward out of the Bosphorus Strait, at depth, is the only source of saline water for the Pontic basin. The saline inflow maintains a deep-water salinity of 22.33 in the Black Sea. Freshwater inflow from several European rivers (especially the Danube, Dniester, Dnieper, Don and Kuban) is the other major contributor to stratification, maintaining low salinity in the surface layer (S = 18.0 to 18.5 in the central region).

As a result of the limiting effect of the salinity stratification on convention, the halocline and pynocline coincide at a typical depth of 50–200 m, lying at the lower boundary of the Cold Intermediate Watermass, characterized by the 8°C limiting isotherm. The oxycline and the chemocline also occur in the same depth range as the halocline, because similar mechanisms determine the vertical exchange of these scalar properties. Because of the surface circulation patterns, density surfaces are deeper around the margins

and dome in the central regions. The chemical stratification has finer details such as the existence of a suboxic zone (transition zone between the oxic and anoxic domains) and particulate layers, governed by redox reactions (e.g. Murray et al., 1991; Murray and Dijulio, 2007).

Thus there are five distinct watermasses in the Black Sea: the Black Sea Coastal Water and the Black Sea Surface Water are upper watermasses, whereas the Cold Intermediate Water, the Black Sea Intermediate Water and the Black Sea Deep Water are subsurface watermasses (Ivanov and Belokopytov, 2011).

These watermasses are created by the mixing of two types of water: the Marmara Sea Water which enters the Black Sea as an undercurrent, often referred to as the Lower Bosphorus Current (T = 12–15°C, S = 38–35 , σ = 26–28), and fresh water (T = 0–28°C, S = 0) which originates either from precipitation over the Black Sea itself or from the discharges of the Danube, Dnieper, Dniester, Southern Bug and Don rivers draining east-central Europe.

The Black Sea Coastal Water is a product of river runoff and precipitation in the coastal zone and is characterized by very low salinity ($S \approx 14$; Murray et al., 1991). It is best developed near the mouths of major rivers and shows very large seasonal variations in temperature and salinity. The Black Sea Surface Water occurs over the deep-water regions of the central Black Sea. It is characterized by small salinity variations (i.e., 18–18.4), by strong vertical gradients of temperature and salinity and by significant annual variations of temperature.

The Cold Intermediate Water coincides with a temperature minimum between the level of the seasonal pycnocline and the permanent pycnocline; it is a subsurface watermass which forms as the result of winter convective mixing in the central regions of cyclonic gyres and in shelf areas (Fig. 1.4). The 8ºC isotherm is a good marker for the position of this watermass. The Black Sea Intermediate Water occupies the level of the permanent pycnocline. Between the top and base of this watermass, practical salinity increases by ≈ 3 steps and density by 2.4–2.6 kg m^{-3}. Below is the Black Sea Deep Water, a homogeneous and stable watermass (T = 8.98–9.11ºC, S = 22.32).

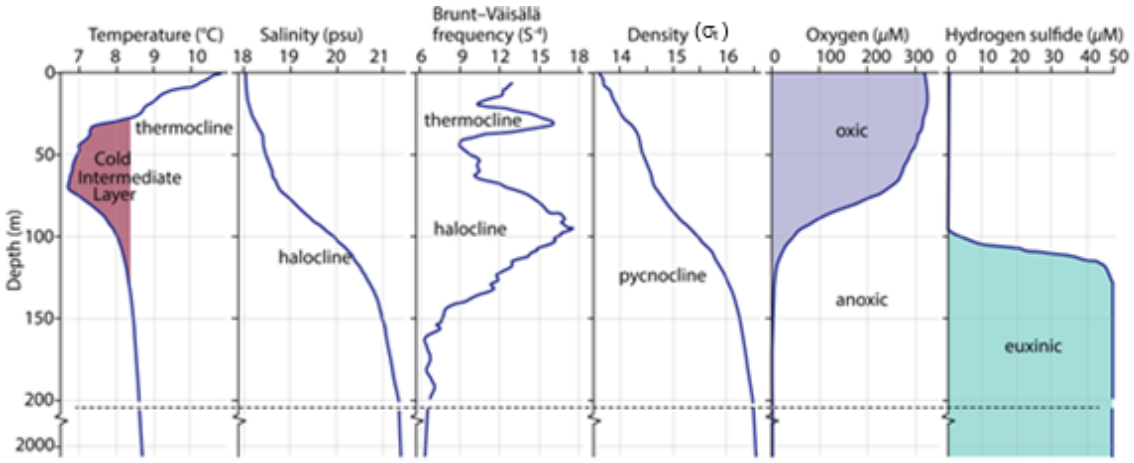

Figure 1.4. Typical profiles of temperature, salinity, Brunt–Väisälä frequency, potential density anomaly, oxygen and hydrogen sulfide concentrations in the central Black Sea for the month of May (modified from Capet et al., 2016). The hydrogen sulfide concentrations are adopted from Oğuz, 2008).

The deep watermasses of the Black Sea are nearly completely isolated from the world ocean and the atmosphere, with only a very restricted exchange with the Mediterranean Sea through the Marmara Sea Gateway. As a result, the deep basin is completely anoxic and euxinic, containing no oxygen but instead hydrogen sulphide at

depths below 100–150 m (Özsoy and Ünlüata, 1997). The sharp permanent halocline separates the oxic and anoxic waters.

1.3.2. Hydrology of the Black Sea

1.3.2.1. River Input

Large rivers discharge into the Black Sea from the northwest, the Caucasus, and the coasts of Turkey, Bulgaria and Romania. They play an important role in the water balance. The total fresh-water discharge into the Black Sea ranges between 294 km^3 $year^{-1}$ and 474 km^3 $year^{-1}$ (Table 1.2; Murray et al., 2007). The largest discharges of freshwater into the Black Sea occur in April and May.

The biggest rivers entering the Black Sea basin are the Danube Dniester, Dnieper, Don and Kuban (Table 1.2). They feed the Black Sea with a total volume of 350 km^3 $year^{-1}$. These rivers constitute ~72% of the fresh water discharge into Black Sea; the remaining small rivers do not play an important role in the water balance (Özsoy et al., 1997).

1.3.2.2. Evaporation and Precipitation

The Black Sea is a semi-enclosed basin, thus the rates of precipitation and evaporation over the water surface are essential factors in the Black Sea water balance. Highest precipitation rates occur during the winter time. The east and the southeast regions receive larger amount of precipitation compared with the north and northwest. Many authors (Efimov et al., 2011 their Table 2) indicate that the amount of precipitation is slightly overcompensated for by the amount of evaporation (Table 1.2).

Table 1.2. Present day water fluxes of the Black Sea (Murray et al., 2007)

River Input	350 km^3 yr^{-1}
Danube	250 km^3 yr^{-1}
Dniester	8 km^3 yr^{-1}
Dnieper	51 km^3 yr^{-1}
Don	28 km^3 yr^{-1}
Kuban	12 km^3 yr^{-1}
Precipitation	300 km^3 yr^{-1}
Evaporation	353 km^3 yr^{-1}
Bosphorus outflow to Black Sea	313 km^3 yr^{-1}
Average Salinity	34.9 psu
Temperature – summer	14.5–15 ℃
Temperature – winter	12.5–13.5 ℃
Bosphorus outflow to Marmara Sea	610 km^3 yr^{-1}
N–S elevation difference of water surface along Bosphorus	35 cm
Current velocities along Bosphorus (surface)	2 m s^{-1}
Current velocities along Bosphorus (deep)	0.5 m s^{-1}
Current velocities over the Bosphorus sill	1.5 m s^{-1}

1.3.3. Water circulation

Similar to the open oceans, the Black Sea has predominantly wind-driven circulation with gyres, eddies, deep-water thermohaline circulation and shallower ventilation into the thermocline. The surface circulation of the Black Sea consists of two large cyclonic (counter-clockwise) central gyres that define the eastern and western basins (Fig. 1.1; Özsoy and Ünlüata, 1997; Ivanov and Belokopytov, 2011). The cyclonic basinal gyres and anticyclonic coastal eddies are separated by the Rim Current which is < 75 km wide and transports water counter clockwise around the periphery of the Black Sea basin at a velocity of ~20 cm s^{-1} (Oğuz et al., 1993). This is a geostrophic current driven in part by prevailing winds and in part by river discharge steered by the Coriolis Effect. The Rim Current

exhibits large meanders and filaments that protrude into the regions of the central gyres. Shoreward of the path of the Rim Current, several quasi-stationary anticyclonic eddies occur along the coastal zone, such as the Batumi, Sevastopol, Caucasian, Sakarya, Sinop and Bosphorus eddies. Some of these eddies are permanently controlled by topography (e.g. the Sakarya eddy located over the Sakarya submarine canyon) while others are more temporally and spatially variable (e.g. the Sevastopol eddy). There are conflicting views on the circulation of the deeper layers (i.e., Cold Intermediate Water, Black Sea Intermediate Water and Black Sea Deep Water). Although most researchers believe that there is a cyclonic rotation through the entire water column down to the basin floor (e.g., Özsoy and Ünlüata, 1997), others advocate an anticyclonic circulation in the deep layers of the Black Sea (Ivanov and Belokopytov, 2011).

1.3.4. Water balance

Many authors have estimated the water balance in the Black Sea (for reviews see Ivanov and Belotopykov, 1991; Oğuz et al., 2004). According to one set of estimates (Murrey et al., 2007), the Black Sea receives ~300 km^3 of precipitation (P) annually. The annual river runoff (R) is ~350 km^3 which is slightly greater than the annual loss of water through evaporation (E) of ~353 km^3. Thus, the annual average freshwater balance [(R+P) – E] is ~297 km^3. The strait of Bosphorus provides an annual inflow of ~313 km^3. The annual outflow of water through the strait is estimated at 610 km^3:

1.3.5. Communication of Black Sea with global oceans; residence times of water masses

The Black Sea is connected to the Mediterranean Sea via the Marmara Sea and two straits: the Bosphorus and Dardanelles. The Black Sea level lies on average 30 cm (±10 cm) above the level of the Marmara Sea (Beşiktepe et al., 1994) and the level of the Marmara Sea is approximately 5–27 cm above the level of the northern Aegean Sea (Bogdanova, 1969). Because of the narrow outlet through the Bosphorus Strait, the level of the Black Sea tracks inter-annual variations of the freshwater input so that its height reaches a maximum of ~50 cm above the level of the Marmara Sea (Özsoy et al., 1995, 1996). Smaller-scale base-level oscillations occur in response to variations in barometric pressure (Özsoy et al., 1996).

In the Bosphorus Strait, the bottom layer of high salinity water flowing northward from the Marmara Sea thins as it enters the Black Sea. Salinity gradients are sharp at its upper boundary indicating limited mixing with overlying water. Most of the mixing between the Bosphorus outflow and the Cold Intermediate Layer occurs on the continental shelf just north of the Bosphorus (Tolmazin, 1985b). This mixture of Bosphorus outflow and Cold Intermedıate Layer forms the Bosphorus Plume which ventilates the deep layers of the Black Sea (Özsoy et al., 1993; Stanev et al., 2014). The most common mixing conditions result in ventilation of the upper 500 m but there must be occasional rare ventilation events that reach abyssal depths, because the only source for relatively warm and saline water is the Bosphorus Plume, and salinity and temperature increase continuously all the way to the bottom of the sea. From the salinity balance of the deep

Black Sea (50–2200 m) it has been determined that the ventilating water is composed of an average Cold Intermediate Layer to Bosphorus entrainment ratio of ~ 4:1 (Murray et al., 1991). Thus, the average composition of the Bosphorus Plume consists of a mixture of 4 parts Cold Intermediate Layer with 1 part high salinity Bosphorus inflow from the Mediterranean basin. In detail, this ratio must vary with depth and is higher in the upper few hundreds of meters and lower in the deeper water.

An early estimate of the residence time of deep water based on ^{14}C was 2000 yr (Ostlund and Dyrssen, 1986), while a budget of heat and salt suggested a residence time of 387 years (Murray et al., 1991). Lee et al (2002) used chlorofluorocarbon (CFC) data to model the decrease in ventilation and increase in residence time with depth over the upper 500 m. The model-calculated residence times are ~5 yr in the suboxic zone (80–120 m), increasing to ~625 yr at 500 m. The residence time of water in the Cold Intermediate Layer (~50–100 m depth) is estimated to be < 5 yr.

1.4. Pleistocene-Holocene paleoclimate and paleoceanography

Quaternary cooling and warming events are recorded by base level fluctuations and changes in seabed geomorphology of the Black Sea (e.g., Ostrovsky et al., 1977; Panin and Strechie, 2006). During glacial periods, the Black Sea became periodically isolated from the World Ocean as its base level fell below the sill depth of the Bosphorus Strait (see also Badertscher et al., 2011). Geomorphological, geochemical and paleontological evidence records these events and the effects on the environment.

During the Riss-Würm (or Eemian) interglacial (126–119 cal ka BP) the Black Sea level was higher than it is today. At that time, the Black Sea was connected to the Caspian

Sea through the Manych Strait and had a surface salinity of 30–37 (Nevesskaya, 1970, in Panin and Strechie, 2006). After this highstand there was a 100–110 m drop in base level in the Black Sea basin (then occupied by a lake) coincident with marine isotopic stage 4 (Chepalyga, 1984). During this time the water in the basin became brackish to fresh (S= 5–10) and the fauna living there were low-salinity Caspian types. During the following interstadial sometime around ~40–26.5 cal ka BP (i.e., marine isotopic stage 3; Imbrie et al., 1984) the water level in the lake rose to breach the Bosphorus Strait.

At around 26.5 cal ka BP, the Würm glaciation (i.e., marine isotopic stage 2) led to a dramatic regression and extreme drop in base level. There is some debate regarding the actual amount of this drawdown: Ryan et al. (1997) estimated a level of –140 m, whereas Aksu et al. (2002) and Hiscott et al. (2002) estimated a level of –110 m. The last glacial maximum occurred at ~26.5 to 19–20 cal ka BP. At this time the water body in the Black Sea basin once again became an isolated brackish lake (the 'Neoeuxine Lake'). Between 17.2–15.7 cal ka BP, post-glacial melting associated with the transition from the Würm glacial to the Holocene interglacial began in northern Eurasia and Alpine mountain belts and by ~7 cal ka BP the Black Sea had attained approximately its present level. There is debate regarding the effect of the post-glacial ice-cap melting on the level of the Black Sea/Neoeuxine Lake and the ensuing reconnection with the Mediterranean Sea, as explained in Section 1.6.6.

1.5. Tectonic setting of southwestern Black Sea

The Black Sea is part of the Ponto-Caspian basins which also include the Sea of Azov, the Caspian Sea and the Aral Sea (Boomer et al., 2010). These basins are the

remnants of the Paratethys Sea, which existed from the Late Jurassic (~150 Ma) to Early Pliocene (~5 Ma). The Tethys Ocean, to which the Paratethys Sea was connected, closed during the Paleogene with the subduction of the Tethyan plate (Robinson, 1997) and the western part of this ocean became the Mediterranean Sea (Rögl, 1999). The Paratethys Sea to the north became progressively shallower during the Pliocene and was partitioned into the Ponto-Caspian basins.

In terms of crustal structure, the Black Sea basin is composed of two deep depressions: (a) the western Black Sea basin, which is underlain by oceanic crust overlain by >14 km-thick, flat-lying, undisturbed probably Cretaceous to Holocene sediment, as inferred from the age of initial rifting of the Black Sea in the Aptian to Cenomanian (Görür, 1988) and (b) the eastern Black Sea basin, which has oceanic crust with >12 km of sediment cover. These basins are separated by the Mid-Black Sea Ridge (Finetti et al., 1988) and originated as two back arc basins in the Early Cretaceous as the Neo-Tethys Ocean floor was subducted beneath the Balcanides-Pontides volcanic arc (Letouzey et al., 1977; Robinson, 1997). A previous study of the southwestern Black Sea shelf by Aksu et al. (2002) revealed the presence of five seismic units with the youngest Unit 1 accumulating in the late Pleistocene and Holocene. As revealed in that study, this unit does not show any evidence of tectonic deformation, except that gentle shingling of uppermost Pleistocene prograded deltas at the shelf edge implies mild seaward warping.

There are numerous small historical earthquakes across the southwestern shelf of the Black Sea ranging in magnitudes from 2–3 to 3–4, with only two at magnitudes 4–5 (Fig. 1.5). The earthquake activity notably increases toward the south, where swarms of

moderate- to high-magnitude events clearly trace the prominent North Anatolian Transform Fault and its splays across the northern Marmara Sea (e.g., Yamamoto et al., 2017). There have been a number of historical larger earthquakes around the Black Sea which generated tsunami waves locally as high as 4–5 m along the coast (Yalçiner et al., 2003). For example, the 1901 7.2 magnitude Balchik earthquake (Matova 2000) with epicenter 30 km east of Cape Kaliakra and hypocenter at 15 km depth, off the northeast coast of Bulgaria, generated a 4–5 meter-high tsunami (Altınok, 1999). The 1927 6.7 magnitude earthquake with epicenter southeast of Crimea (hypocenter at 35 km depth), the 1957 5.5 magnitude earthquake with epicenter west of Crimea (hypocenter at 15 km depth) and the four 5.5–5.7 magnitude quakes east of Kerch Strait (https://earthquaketrack.com/r/black-sea/biggest) are also reported to have created tsunamis (Altınok, 1999). The author believes that these infrequent earthquakes and the solitary waves that they created must have had only local impact and are not expected to have left a regional sedimentological and seismic stratigraphic imprint on the seabed across the southwestern Black Sea shelf.

Konerding (2008) provided a comprehensive evaluation of subsidence across the western Black Sea shelves off Bulgaria, Turkey, Romania and Ukraine for the Quaternary (their tables 6.4, 6.5, 6.6), which shows that total tectonic and sedimentary subsidence rates increase toward the southwest caused mainly by sedimentary compaction. The available data suggest insignificant Holocene neotectonic effects on sedimentation.

Previous seismic stratigraphic studies suggested little regional tectonic activity (e.g., Aksu et al., 2002a). These authors show occasional reactivation of basement faults extending into the Holocene Unit 1.

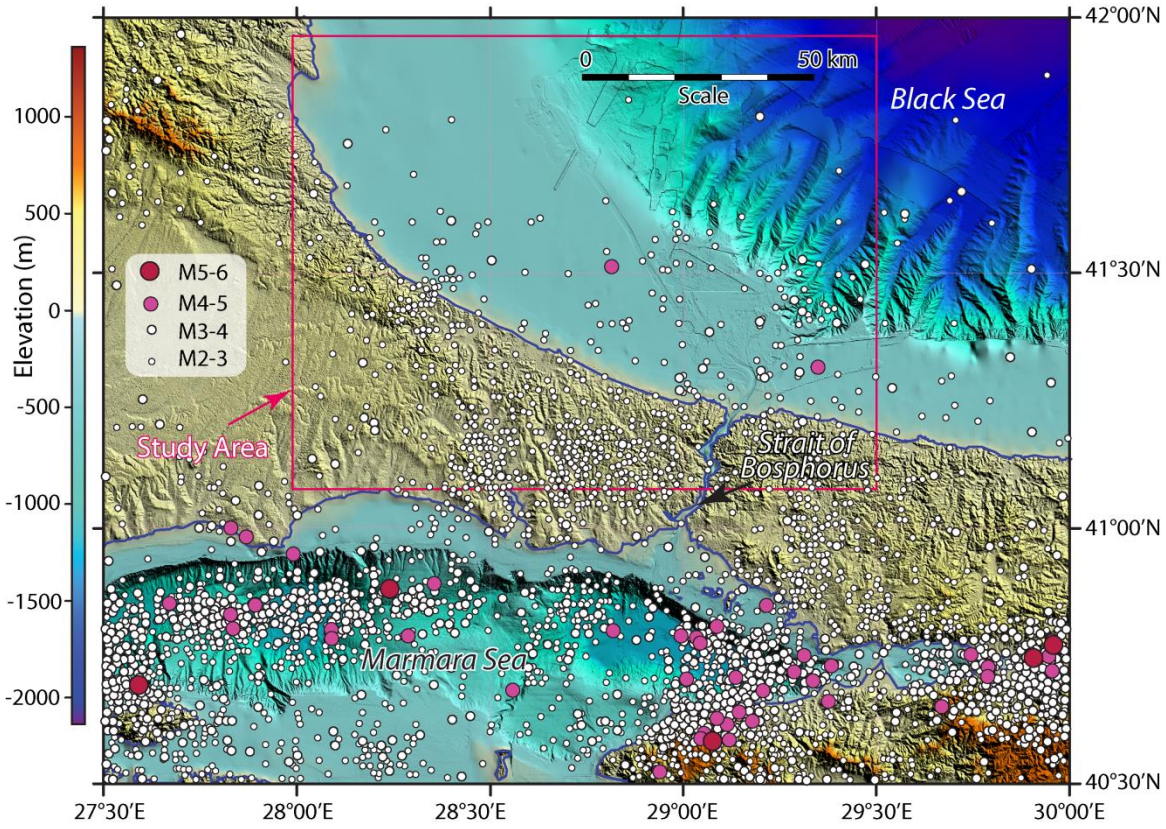

Figure 1.5. Earthquake epicenters in the northern Marmara Sea and southwestern Black Sea (data plotted using the Kandilli Observatory (Istanbul) digital archive between 1971 and 2000).

Other studies show organized linear arrangments of inferred mud volcanoes associated with fluid seepages along orthogonal patterns in the saline channel area (Flood et al., 2009). These authors suggested that the fluid seepage rises along basement faults. Finally, the presence of shelf-edge deltas exhibiting oblique clinoform progradation and bypass of sediments across the northwestern sector of the study area (Aksu et al., 2002a) and the general absence of structures related to regional subsidence strongly argue for a tectonically stable shelf during at least the Holocene.

1.6. Previous studies

1.6.1. Previous studies on Pleistocene-Holocene base level

There is general agreement that the Black Sea became reconnected with the Mediterranean Sea between 7 and 9 ^{14}C ka BP. There was an evaporative base-level drawdown leading up to the LGM, causing a decoupling from the Mediterranean Sea as the level of the then Neoeuxine Lake fell to –90 m to –110 m (Chepalyga, 1984), or –100 m to –110 m (Görür et al., 2001; Demirbağ et al., 1999), or –110 m (Aksu et al., 2002a), or –140 m (Ryan et al., 1997) or as much as –150 m (Winguth et al., 2000).

Until the beginning of the 1990's, the rate of rise in the level of the Neoeuxine Lake after the glacial low stand was considered to be slow with some short-term oscillations, with the reconnection to the global ocean between 9 and 7.5 ^{14}C ka BP (e.g. Ross et al., 1970; Degens and Ross, 1972; Deuser, 1972). New data collected from 1993 onward led to what is now referred to as the 'Flood Hypothesis' which advocates a very rapid ('catastrophic') flooding of the Neoeuxine Lake with Mediterranean waters (Ryan et al., 1997). William Ryan and co-workers proposed that meltwater input to the lake was high enough in early post-glacial times to drive outflow via the Sea of Marmara into the Aegean Sea. Subsequently, around 12 ^{14}C ka BP, the retreat of the Scandinavian ice sheets led to a redirection of meltwaters into the North Sea. Without meltwater input and due to a cold and dry climate in the region during the Younger Dryas (12.8-11.7 cal ka BP), these researchers proposed that the Neoeuxine Lake fell again to a lowstand. The Mediterranean level, however, was rising at the same time, cresting a sediment dam at the southern-most

Bosphorus sill around 7.5 cal ka BP according to Ryan et al. (1997). This event was hypothesized to have led to a catastrophic reconnection when Mediterranean waters invaded the Black Sea in less than 2–3 years. The timing of the hypothetical flood was later revised by Ryan et al. (2003) to 8360 ^{14}C yr BP (~9140 cal yr BP) based on strontium isotopic data. The sill depth was assumed to be –35 m. Ryan et al. (2003) revised other details of the Flood Hypothesis. They advocated two lowstands and two flood events instead of one. First, there was a lowstand of –120 m at ~15200–12400 cal yr BP, possibly followed by a short period of outflow (see also Major et al., 2002). They then postulated that outflow had ceased between ~12500 and 10100 cal yr BP and the lake had fallen to a new lowstand of –95 m. Finally, at ~9140 cal yr BP a second and more significant flooding event took place as revealed by the imposition of a marine strontium isotopic signal on contemporary biogenic carbonate (Major et al., 2006).

According to Lericolais et al. (2011), there was a latest Pleistocene transgression to an elevation of –40 m caused by an increased influx of meltwater carried into the Black Sea by large rivers such as the Danube, Dnieper and Dniester, followed by a Bølling-Allerød to Younger Dryas evaporative drawdown to ~ –100 m elevation, and then a 'catastrophic' early Holocene filling of the basin by Mediterranean seawater when the sill in the Strait of Bosphorus was breached. Yanchilina et al. (2017) proposed that this transgression was completed in ~100 years based on interpretations of abrupt shifts in stable isotopic records (δ^{18}O, δ^{13}C, ^{87}Sr/^{86}Sr), and the occurrence of 1–2 unconformities veneered by coquinas and imaged in seismic reflection profiles from the outermost shelf and upper slope of the western and northwestern Black Sea.

Several workers from eastern European countries have disputed that an early Holocene base-level drawdown and catastrophic flood occurred (Fedorov, 1988; Chepalyga, 1984; Filipova-Marinova, 2006; Yanko-Hombach, 2006). Based on benthic foraminiferal assemblages, Yanko-Hombach et al. (2007) concluded that the Holocene reconnection of the Black Sea to the Mediterranean Sea occurred in an oscillating manner, permitting periodic immigration of Mediterranean organisms into the Pontic basin. After the LGM when the climate warmed, these authors advocate a large water input from high river discharge, melting permafrost and Caspian Sea spillover, raising the isolated Neoeuxine Lake from –100 to –20 m before it temporarily dropped again to –50 m during the Younger Dryas cold period from ~12800 cal yr BP to~11700 cal yr BP. At ~10800 cal yr BP, the Neoeuxine Lake then began to spill over the Bosphorus sill into the Marmara Sea; Mediterranean waters which reached the height of the sill 1500–2000 years later raised the level gradually to –20 m. According to these authors, the Black Sea level never again dropped below –50 m, never experienced fluctuations greater than about ±20 m and occasionally rose a few meters higher than present base level during the Holocene (Yanko-Hombach et al., 2007). Martin et al. (2007) concurred that Holocene water levels rose and fell periodically due to changes in freshwater discharge and repeated marine incursions and proposed that these oscillations decreased in magnitude through the Holocene. Filipova-Marinova (2007) and Ivanova et al. (2007) presented paleontological evidence for Holocene base-level oscillations which became increasingly attenuated and closer to the modern level in the last ~5000 years. Giosan et al. (2006) stated that immediately before the reconnection to the Mediterranean Sea the level of the Neoeuxine Lake was around –30 m based on cores from the Danube Delta and once reconnection occurred the level

gradually climbed with the global ocean level and did not fluctuate more than ±1–2 m in the last 5000 years. Constantinescu et al., 2015 studied Danube deep-sea fan also dismissed the > –100 m lowstand for any time after 11 cal ka BP, proposing instead ≤ −70 and ≥ −30 m between 11,700 and 9000 cal yr BP

Core M02-45 was cored 9.5 m into the post-transgressive succession on the SW Black Sea middle shelf at a water depth of –69 m. It established that the level of the lake was shallower than –70 m by ~9.3 cal ka BP and remained so until the present. Sedimentary facies from this core suggested to Hiscott et al. (2007) that the water depth was actually shallower than ~ –48 m. These constraints are consistent with the 11.1–10.2 cal ka BP age of an outflow delta at the southern end of the Bosphorus Strait (Aksu et al., 2016) and the mineralogy of the sand in this delta and its overlying mud drape (Hiscott et al., 2017), both pointing to a high Neoeuxine Lake (at ~ –40 m) for at least 2000 years before saline water finally reached the elevation of the sill in the strait and penetrated into the Black Sea basin.

1.6.2. Previous sedimentological and seismic stratigraphic studies

In the western Black Sea, systematic hydrological and geological studies were carried out between 1924 and 1933 (e.g., Arkhangel'skiy and Strahov, 1938). During the 1970's, the Ukrainian shelf was extensively surveyed by Prichernomorskoe State Regional Geological Enterprise (e.g., Podoplelov et al., 1975; Karpov et al., 1978; Sibirchenko et al., 1983; Gozhik et al., 1987; Avrametz et al., 2007) and by the Department of Physical and Marine Geology of Odessa I.I. Mechnikov National University (Tkachenko, 1971). Thousands of cores recovered during these surveys provided lithological details and underpinned reconstructions of the Pleistocene lowstand and the subsequent Holocene

transgression across the northwestern Black Sea shelf. Beginning in the 1990's, a large number of seismic reflection profiles were collected from the Ukrainian, Romanian, Bulgarian and some parts of the Turkish shelf using the *RV Akvanavt* in 1993 (Ryan et al., 1996; Ryan et al., 1997), the *RV Le Suroît* in 1998 (BLASON1) and 2002 (BLASON2; Lericolais et al., 2007 a,b; Konerding, 2008), and the Bulgarian navy ship *RV Hydrograph* in 1998 (Genov, 2004). These profiles revealed a widespread and prominent shelf-crossing unconformity, the presence of a Holocene mostly muddy drape above the unconformity, and the presence of numerous buried meandering river channels immediately below the unconformity off the mouths of present-day major rivers. A systematic survey carried out by GeoEcoMar Institute across the Romanian shelf also documented the presence of ancient river valleys crossing the shelf area (Popescu et al., 2004; Lericolais et al., 2007a).

Various previous studies have suggested that the post-LGM lowstand shorelines are characterized by wave-cut terraces around the Black Sea, varying in water depth (relative to modern base level) from –110 m off Ukraine (Ryan et al., 1997), to −100 m on the Romanian shelf (Lericolais et al., 2007a, b), to −122 m on the Bulgarian shelf (Dimitrov, 1982), and to −155 m off the very narrow Sinop shelf (Ballard et al., 2000). Multibeam echo-sounder data and seismic reflection profiles across the Romanian and Bulgarian shelves have identified wave-cut terraces at about –100 m water depth and well preserved drowned beaches, sand dunes, and soils across the shallower shelves (Lericolais et al., 2007a, b). The presence of submerged shorelines with wave-cut terraces and coastal dunes, or delta mouth bars at depths between –80 m to –100 m indicates that the Black Sea was completely isolated from the global ocean during, and for millennia after, the LGM (e.g.,

Ryan et al., 1997; Lericolais et al., 2011). However, later study of the Danube deep-sea fan provided an improved chronostratigraphic framework since the LGM (Constantinescu et al., 2015).

Aksu et al. (1999, 2002), Kaminski et al. (2002), Mudie et al. (2007) and Hiscott et al.(2007) presented evidence that there could not have been a catastrophic flood of the Neoeuxine Lake (later Black Sea) anytime after ~12 cal ka BP. These authors believed that the shores of the lake were fully transgressed and water was beginning to flow out through the Strait of Bosphorus by ~11.9 cal ka BP (Aksu et al., 2002a; Hiscott et al., 2002) and that the base level in the basin had not changed significantly since that time. Hiscott et al. (2002) and Aksu et al. (2016) used high resolution seismic profiles to show the presence of two south-prograded delta lobes at the southern exit of the Bosphorus Strait. They argued that these deltas are the result of persistent Black Sea outflow because there are no rivers in the area that could account for the observed volume or sand-grain mineralogy of the sediments (Hiscott et al., 2002, 2017). The younger delta was constructed between ~11.1–10.2 cal ka BP based on radiocarbon dates presented by Aksu et al. (2016) and seismic correlation to an equally well dated giant Calypso core (Eriş et al., 2007). After 10.2 cal ka BP, it was hypothesized that bedload supply to the delta was interrupted because a salt wedge of Mediterranean water had penetrated into the strait but had not yet reached the open Neoeuxine Lake. These results strongly suggest that lake water was already vigorously flowing out into the world ocean at a time when the Flood Hypothesis would have the Neoeuxine Lake at a maximum lowstand.

Additional support for prolonged Holocene outflow from the Neoeuxine Lake/Black Sea comes from radiocarbon dating of a sapropel layer (mud with >~2 % organic carbon deposited under reduced-oxygen conditions) in Marmara Sea cores. The sapropel, called M1, was deposited between ~11,850 and ~6750 cal yr BP when the outflow from the Neoeuxine Lake – Black Sea would have maintained a low salinity lid over the Marmara Sea deep water, inducing persistent stratification (Aksu et al., 2002a). Flora and fauna found within the sapropel are of Black Sea affinity, suggesting they were introduced by Black Sea outflow (Mudie et al., 2002; Aksu et al., 2002a). Sperling et al. (2003) and Vidal et al. (2010) disagreed with the notion that sapropel M1 is evidence for Black Sea outflow. For example, Vidal et al. (2010) indicated that the oxygen isotopic evidence from carbonate shells shows rising Marmara Sea surface salinity until ~9.9 cal ka BP and suggested that the implication of this is that Neoeuxine Lake outflow was not significant enough to contribute to sapropel deposition and that outflow only began in earnest after this date as indicated by decreasing salinity. Aksu et al. (2016) have countered that strongly brackish surface waters might have been toxic to the types of organisms studied by Vidal et al. (2010), so that they would have been unable to discern the existence of such a surface layer, instead studying organisms that lived deeper in the water column.

1.6.3. Studies on paleosalinity variations and paleotemperature variations

Studies of paleosalinity in the Black Sea basin have led to a disagreement as to whether the Neoeuxine Lake water was fresh or brackish. Ryan et al. (1997) proposed that the isolated Black Sea became a giant freshwater lake and continued to regress to a lowstand of –150 m. A test is available using dinoflagelyate cyst assemblages, which

provide a reliable tracer for changes in surface water salinity in epicontinental seas (Wall and Dale, 1973; Aksu et al., 1995a; Mudie et al., 2001). Mudie et al. (2001) documented the presence of *Spiniferites cruciformis* and *Pyxidinopsis psilate* dynoflagelyate cysts prior to reconnection. These species can be interpreted as indicators of a cold and freshwater environment (e.g. Kouli et al., 2001; Yanchilina et al., 2017). However, the presence of *cruciformis* morphotypes with reduced or no processes can be interpreted to indicate stress caused by brackish surface water conditions (Mudie et al., 2001, 2002a). The calibration of these assemblages against $\delta^{18}O$ data and salinity estimates derived from planktonic foraminifera indeed point to brackish conditions (salinity from 4 to 12) (Mudie et al., 2004). Besides, the presence of other species not known from modern freshwater environments (*P. ponticum, S. inaequalis, S. ramosus, S. mirabilis, Lingulodinium machaerophorum, Operculodinium centrocarpum* and *Brigantedinium* spp.*)* add an additional argument against freshwater lake conditions during early Holocene. Further work on dinoflagellate cyst process length shows a very gradual change from salinities of about 14 psu after the first reconnection at 9.14 cal ka BP, to minimum salinities of about 12.3 psu at 8.5 cal ka BP, reaching current conditions of about 17.1 psu at around 4.1 cal ka BP (Mertens et al., 2012). The latter salinity estimates fall within the qualitative ranges of 7–18 (Wall and Dale, 1973) and 14–18 (Mudie et al., 2001).

Based on ostracods from core MAR02-45, Evans (2004) suggested a brackish salinity (~5) before a faunal turnover beginning at ~7500 cal yr BP indicating rising salinity because of inflow from the Mediterranean Sea. The work of Hiscott et al. (2007) and Marret et al. (2009) initially suggested the presence of marine shells at approximately 78

m depth on the southwestern shelf before ~8.0 cal ka when the majority of evidence indicated a far lower salinity than these molluscs could tolerate. Subsequently, several shell identifications were corrected to species of *Dreissena*, *Didacna* and *Theodoxus* (Hiscott et al., 2010; Marret et al., 2009) which are indicative of non-marine, fresh to low-salinity brackish water (Orlova et al., 2005). Lericolais et al. (2010) documented the presence of *Pisidium*, the pea clam, as an indicator of freshwater conditions. Major et al. (2006) reported the bivalve molluscs *Monodacna caspia* and *Dreissena* (*D. rostiformis*, maximum normal salinity tolerance from 0–6, Orlova et al., 2005) in the Black Sea between 8600 and 7130 ^{14}C yr BP (the age of youngest *Monodacna* on the shelf at 49 m water depth), suggesting a period of ~1300 ^{14}C years after the initial entry of Mediterranean waters (at ~8400 ^{14}C yr BP) before conditions became suitable for Mediterranean-type faunas to replace the Ponto-Caspian communities and thrive. Bradley et al. (2012) used ostracod assemblages to conclude that the salinity of the Black Sea prior to reconnection was brackish. Williams et al. (2011, 2018) studied ostracod assemblages from two long piston cores collected from the southwestern shelf area and documented a brackish stage followed by a transitional period when brackish and marine species co-existed prior to complete salination. A study of bacteria discovered genera that are only known from the marine environment in sediments older than 9 cal ka BP, consistent with non-fresh water conditions before marine reconnection (More et al., 2018).

Early pore-water chemistry studies (Brujevich, 1952; Kvasov, 1968; Manheim and Chan, 1974) observed downward trends in salinity and chlorinity. Soulet et al. (2010) converted the chlorinity of pore water into salinity of the ambient water during

accumulation, with the minimum measured value of dissolved chloride corresponding to a practical salinity of 1. However those authors could not explain the complete difference between their conclusions and various paleontological results.

Oxygen isotopic studies of ostracods and bivalves (Bahr et al., 2006; Major et al., 2006) revealed that temperature changes were restricted to the uppermost water column. Later, Bahr et al. (2008) presented Mg/Ca and Sr/Ca measurements on ostracod valves from the western Black Sea which, in combination with previously published $\delta^{18}O$ and $^{87}Sr/^{86}Sr$ data on biogenic calcite, indicated abrupt changes in the water chemistry of the Black Sea in response to climatic and hydrologic changes between the Last Glacial Maximum and the early Holocene. They concluded that there had been a temperature drop of 1–2 ℃ in the deep water of the Neoeuxine Lake during the Younger Dryas and that the reconnection of the lake with the Mediterranean Sea via the Sea of Marmara started at 9.3 cal ka BP coincident with a marked increase in the Mg/Ca, Sr/Ca and $^{87}Sr/^{86}Sr$ ratios. Their modeling of the $\delta^{18}O$ record indicated that it took nearly 100 years for the Neoeuxine Lake to achieve a full reconnection with the global ocean and become the Black Sea.

High-resolution studies (decadal to millennial scale) of pollen-spore assemblages in cores from the Marmara and Black seas indicates warm and humid conditions with year-round precipitation by 10,500 cal yr BP (Mudie et al., 2002, 2007). This conflicts with the cold, dry conditions necessary for a –100 m drawdown in the Black Sea.

1.6.4. Studies on the development of the anoxia and euxinia in Black Sea

The modern Black Sea has an oxygenated surface layer overlying a sulfidic (anoxic and euxinic) deep layer. Because of the strong vertical stratification, the deep water is not

replenished fast enough to replace the oxygen consumed by respiration and decay of organic matter. Over the deep central basinal areas, the first appearance of free sulfide species occurs at about 90 m depth, or $\sigma = 16.15$ (= density of 1016.15 kg m^{-3}), and then sulfide increases continuously to maximum values of about 380 µM by 2200 m depth. Sulfide decreases to zero before the first appearance of oxygen thus sulfide is apparently not oxidized by the downward flux of oxygen (Murray et al., 2005). The suboxic zone is defined as the region between the depth where oxygen decreases to near zero ($O_2 < 10$ µM) and where sulfide first appears ($H_2S > 10$ µM) (Murray et al., 1989; 1995). This zone varies in thickness from year to year due to climatic variability and mixing by waves and surface currents (Konovalov and Murray, 2001).

Despite the considerable interest in the geochemical history of the Black Sea, controversy remains about the evolution of anoxia in the Black Sea water column. Deuser (1974) proposed that oxygen depletion was initiated when Mediterranean waters began spilling into the basin through Bosphorus Strait 9 cal ka BP. The influx of saline waters led to a density stratification in the basin, progressive depletion of deep-water oxygen through respiration and decay of organic matter, and the rise of the O_2–H_2S interface by ca. 7.3 cal ka BP, followed by a continued rise of the redox transition to the present depth of about 100 m below the surface in the open deep basin. It also is possible that the position of the oxic–anoxic boundary has been largely stationary over the past 7.3 cal ka BP with the exceptions of possible short-term advances and retreats (e.g., Arthur and Dean, 1998; Glenn and Arthur, 1984; Lyons et al., 1991).

1.6.5. Studies on western Black Sea shelf (emphasis on Romania and Bulgaria)

Several oceanographic surveys were carried in the western Black Sea during the last two decades. A French–Romanian joint project and the European ASSEMBLAGE project (EVK3-CT-2002-00090) have collected a large amount of data (multibeam echosounder data, Chirp seismic, Kullenberg and Calypso cores). Bathymetry and acoustic imagery were acquired using multibeam echosounders (SIMRAD EM1000 and EM300) .

The research vessel *Le Suroît* was used during the 1998 BlaSON and the 2000 BlaSON 2 cruises. Additional multibeam data (Thomson SEAFALCON 11) were collected by the *R/V Marion Dufresne* during the 2004 ASSEMBLAGE1 cruise. Seismic lines were also collected during the BlaSON 1 and 2 cruises. The BlaSON cruises focused on the Romanian, Bulgarian and Turkish shelves and the distal part of the Danube deep-sea fan. The deep-sea fans were supplied by the Danube, Dniestr, Bug and Dnieper rivers and are the largest Quaternary geological features of the western Black Sea. According to Paluska and Degens (1979) these rivers started to drain into the Black Sea during the Chaudian (Günz glaciation), thus providing an upper limit for the age of the fan systems. There are two morphological fans: (a) the Danube fan, and (b) a fan system fed by the Dniestr, Bug and Dniepr rivers (named the Dniepr Fan hereafter). These two fans slightly interfinger with one another (Winguth et al., 2000); approximate boundaries have been mapped by Wong et al. (1994) and Popescu et al. (2001).

The study of the Romanian shelf resulted in a number of publications by Lericolais et al. (2009, 2010, 2011) in which those authors documented preservation of sand dunes

and the occurrence of small, buried incised valleys interpreted as evidence of a rapid transgression. The buried, anastomosed fluvial channels that suddenly disappear below 90 m water depth and a wave-cut terrace between 95–100 water depths indicate a major lowstand at around −100 m between 11.0 and 8.5 ^{14}C ka BP (~13.0–9.3 cal ka BP). Later, Constantinescu et al. (2015) used seismic and core data from the Danube Fan to conclude that: lowstand conditions (≤ −110 m) prevailed during the Last Glacial Maximum, and possibly between 15,700 ± 300 cal yr BP and 14,700 cal yr BP; water level ranged between −110 and −70 m between 14,700 and 11,700 cal yr BP; water level ranged between −70 and −30 m from 11,700 cal yr BP until the reconnection of the Neoeuxine Lake with the global ocean.

The study of the oceanography of the Black Sea offshore Bulgaria started in earnest in the 1960's. There were multiple surveys on the Bulgarian shelf since 1973 performed by oceanographic and geological institutions. Russian-Bulgarian joint surveys resulted in monographs “Geology and Hydrogeology of the Western part of Black Sea” (1979), “Geological and Geophysical study of the Bulgarian part of Black Sea” (1980), “Oil and gas research of the Bulgarian part of Black Sea” (1984), “Geochemistry of the lithogenesis in the hydrogen sulfide dominated environment” (1988) and “Geological evolution of the western part of the Black Sea during Neogene-Quaternary” (1990).

The expeditions aboard the *R/V Akademik* were performed on the Bulgarian shelf in 2001, 2002, 2006, 2009 and 2011 and focused on studies of the ancient Black Sea shorelines (Dimitrov, 1982; Ryan et al., 1997; Major et al., 2002; Ryan et al., 2003; Dimitrov and Dimitrov, 2004; Ryan, 2007; Dimitrov, 2010) and deep-water sediments

(Coolen et al., 2009; Dimitrov, 2010). Based on lithostratigraphy from the shelf area, the pre-transgression base-level in the Neoeuxine Lake was assessed at –120 m.

Climatic and base-level fluctuations were studied in the Bulgarian sector by correlating the terrace complexes along the coastline and shelf using cores from a number of bore holes (Hristova 2003, 2006, 2007, 2015, 2018). According to this reconstruction, the Late Pleistocene-Neoeuxinian epoch was marked by a deep regressive phase with base level 90–100 m below modern sea level. The subsequent Neoeuxine transgressive phase was dominated by a Caspian-type molluscan fauna implying fresh-water influx from the Caspian Sea. Polinological data and dinoflagellate cysts suggested respectively a cold and dry climate and low water salinity down to S = 7.

1.6.6. Conflicting hypotheses on the reconnection of the Black Sea with the global ocean

Despite extensive research on the paleoclimatic and paleoceanographic evolution of the Black Sea region, the history of the Holocene reconnection of the Neoeuxine Lake/Black Sea with the eastern Mediterranean via the Marmara Sea Gateway is still controversial. During the last two decades, two main hypotheses have been proposed to explain the post-glacial reconnection: (a) a catastrophic reconnection preceded by a profound lowstand (Ryan et al., 1996, 1997, 2003, 2013; Lericolais et al., 2006, 2007a,b, 2009, 2010, 2011; Major et al., 2002, 2006; Ryan, 2007; Yanchilina et al., 2017), and (b) a gradual reconnection preceded by the existence of a high and outflowing lake (Aksu et al., 1999, 2002a,b, 2016; Hiscott et al., 2002, 2007a,b, 2017; Leonov, 2005; Mudie et al., 2010; Mertens et al., 2012; Bradley et al., 2012; Lister et al., 2015). A variant of the latter,

involving oscillating and increasing water levels (Yanko-Hombach et al., 2006, 2007), is problematic and not considered here because several significant oscillations are proposed to have occurred well after reconnection of the Black Sea to the global ocean, at odds with the fact that these oscillations are not recognized elsewhere in the major ocean basins of the world (Giosan, 2007).

The catastrophic reconnection hypothesis advocates a geologically rapid rise of the base level from ~ –120 m at 9300–9400 cal yr BP to ~ –30 m in approximately a century, or less (e.g., Ryan, 2007; Yanchilina et al., 2017). The arguments to support this hypothesis are based on interpretations of abrupt shifts in stable isotopic records ($\delta^{18}O$, $\delta^{13}C$, $^{87}Sr/^{86}Sr$), and the occurrence of 1–2 unconformities veneered by coquinas and imaged in seismic reflection profiles from the outermost shelf and upper slope of the western and northwestern Black Sea, and descriptions of now-transgressed windblown dunes and subaerial vegetated surfaces in cores (Yanchilina et al., 2017).

The gradual reconnection hypothesis is based on ~3500 line-km of high-resolution seismic reflection profiles and multiproxy data from several well-dated cores on the southwestern shelf. It suggests that the Neoeuxine Lake rose to the level of the Bosphorus sill (~ –40 m) shortly before ~11.1 cal ka and began to export brackish water south through the Strait of Bosphorus and into the Marmara Sea (Aksu et al., 2002a,b; 2016; Hiscott et al., 2002; 2007a,b; 2017). The development of a Holocene climbing delta in the northeastern Marmara Sea, immediately south of the exit of the Strait of Bosphorus, provides critical underpinning for the gradual reconnection hypothesis (e.g., Hiscott et al., 2002, 2017; Aksu et al., 2016). Radiocarbon dates in several cores constrain the age of this

delta to ~11.1–10.2 cal ka BP (Aksu et al., 2016), superseding a much younger estimate that was based on faulty correlation of seismic data to a giant Calypso piston core (Eriş et al., 2007). Lobe geometry, the required sediment supply and the detrital mineralogy collectively point to a Strait of Bosphorus (Black Sea) source. Furthermore, several well-dated cores from the southwestern Black Sea shelf have recovered lacustrine sediments at modern elevations well above the lowstand shoreline yet older than the time proposed by other workers for a catastrophic entry of Mediterranean water (Williams et al., 2018). Hiscott et al. (2017) and Aksu et al. (2016) infer an increase of river discharge and/or outburst floods generated by ice-dam collapses in the Altay and Sayan mountains of central Asia to explain the base-level rise in the Neoeuxine Lake.

1.7. Scientific objectives

This thesis aims to develop a paleoceanographic reconstruction of the southwest Black Sea shelf area based on seismic stratigraphic analysis, lithostratigraphy and geochemistry of sediments.

Methods and materials are described in the next chapter (Chapter 2), after which the results of the research are presented in the next three chapters.

Chapter 3 is dedicated to the:

- Establishment of a seismic stratigraphic framework for the southwestern Black Sea shelf using a large database of high-resolution seismic reflection profiles;

- Determination of the lithological composition of the various seismic units and environment interpretation of their development by correlation of the seismic data with available core data;
- Mapping of two post-reconnection unconformities and interpretation of their origins;
- Clarification of the regional extent of the regression associated with the Last Glacial Maximum and regional distribution of the post-glacial sediments across the southwestern Black Sea shelf;
- Establishment of solid stratigraphic framework for the study area.

Chapter 4 is dedicated to:

- Assessment of the Sr isotopic evolution of waters in the Neoeuxine Lake/Black Sea water during the last 12 cal ka using high-resolution continuously cored successions on the modern shelf;
- Decadal to centennial interpretation of the local paleoceanography and water chemistry through the Late Quaternary transgression and subsequent salination.

Chapter 5 is dedicated to:

- Presentation and interpretation of new oxygen and carbon isotope ratios and trace-element data for ostracod valves from two high-resolution piston cores raised from the modern Black Sea shelf;
- Interpretation of environmental changes through the last 12 cal ka which took place within the Ponto-Caspian region over time steps as short as ~50 years;

- Documentation of various aspects of the chemical evolution of surface waters of the Neoeuxine Lake/Black Sea associated with its Holocene reconnection to the global ocean.

Chapter 6 presents a holistic discussion of the paleoceanographic evolution of the southwest Black Sea, and Chapter 7 lists the salient conclusions arising from this thesis.

Chapter 2. Material and Methods

2.1. Acquisition of seismic reflection and multibeam profiles and cores

2.1.1. Navigation

Knowing accurately where the survey vessel is at sea is extremely important, because one can only study objects of interest by plotting them on maps with spatial coordinates X, Y and Z (i.e., latitude, longitude, depth). The degree of navigational accuracy needed in marine research must be better that the dimensions of the geological feature of interest.

During cruises in 1998, 2000 and 2002, navigation was achieved using a satellite navigation system (or Global Navigation Satellite System), which is estimated to have several tens of meters X and Y accuracy depending on the number of satellites visible, precise orbital information for those satellites, overall system integrity, and the integrity of the ship's GPS receiver. During the 2005, 2008 and 2011 cruises, a DGPS system was used for navigation, which provided sub-meter accuracy, often as good as ~10 cm on X, Y and Z. In 1998, 2000 and 2002, the navigational information was hand recorded in cruise log books, whereas during the 2005, 2008 and 2011 cruises the navigation data were digitally recorded as time stamps in the Huntec DTS and EM3000/EM3002D data.

2.1.2. Acquisition of the seismic reflection profiles

The following data were collected from the southwestern Black Sea using the RV *Koca Piri Reis* of the Institute of Marine Sciences and Technology, Dokuz Eylül University: (a) ~9150 line-km of high-resolution seismic reflection profiles collected

during cruises in 1998, 2000, 2005, 2008 and 2011, (b) 935 km^2 of multibeam bathymetry collected during cruises in 2005, 2008 and 2011, and (c) 72 gravity cores and 25 piston cores collected during cruises in 1998, 2000, 2002, 2005, 2008 and 2011 (Fig. 2.1). The author of this thesis did not participate in these cruises and instead was provided with primary materials and data for the project by thesis supervisors Aksu and Hiscott.

Approximately 9150 line-km of Huntec DTS profiles were acquired during cruises in 1998, 2000, 2005, 2008 and 2011 using a 500–1000 J boomer source, with echoes recorded using a single very high-resolution internal hydrophone as well as a single-channel 21-element 6 m-long external hydrophone array. The data were band-pass filtered at 600–6000 Hz, and displayed using time-varying gain to compensate for decay of reflection strength with depth below the seabed. The Huntec fish was towed at 20–50 m water depth. In addition to the Huntec DTS profiles, during the 1998 cruise, ~550 km of single-channel seismic profiles were acquired using a 1580 J sparker source and a 50-element, 9-m long Benthos hydrophone streamer. Similarly during the 2000 cruise, ~ 2250 km of single-channel airgun profiles were collected using a 40 in^3 (655 cm^3) sleeve-gun source and two separate streamers: a 6 m-long, 21-element Nova Scotia Research Foundation Corporation streamer, and a 9 m-long, 50-element Benthos streamer. The incoming single-channel data were band-pass filtered at 150–1500 Hz. All data were analogue recorded using a reel-to-reel tape recorder in 1998 and a multi-sensor digital Data Acquisition system CODA DA200™ digital recording system in 2000, 2005, 2008 and 2011. The data were also analogue recorded to paper rolls during all cruises using several EPC (Electric Printing Company) recorders.

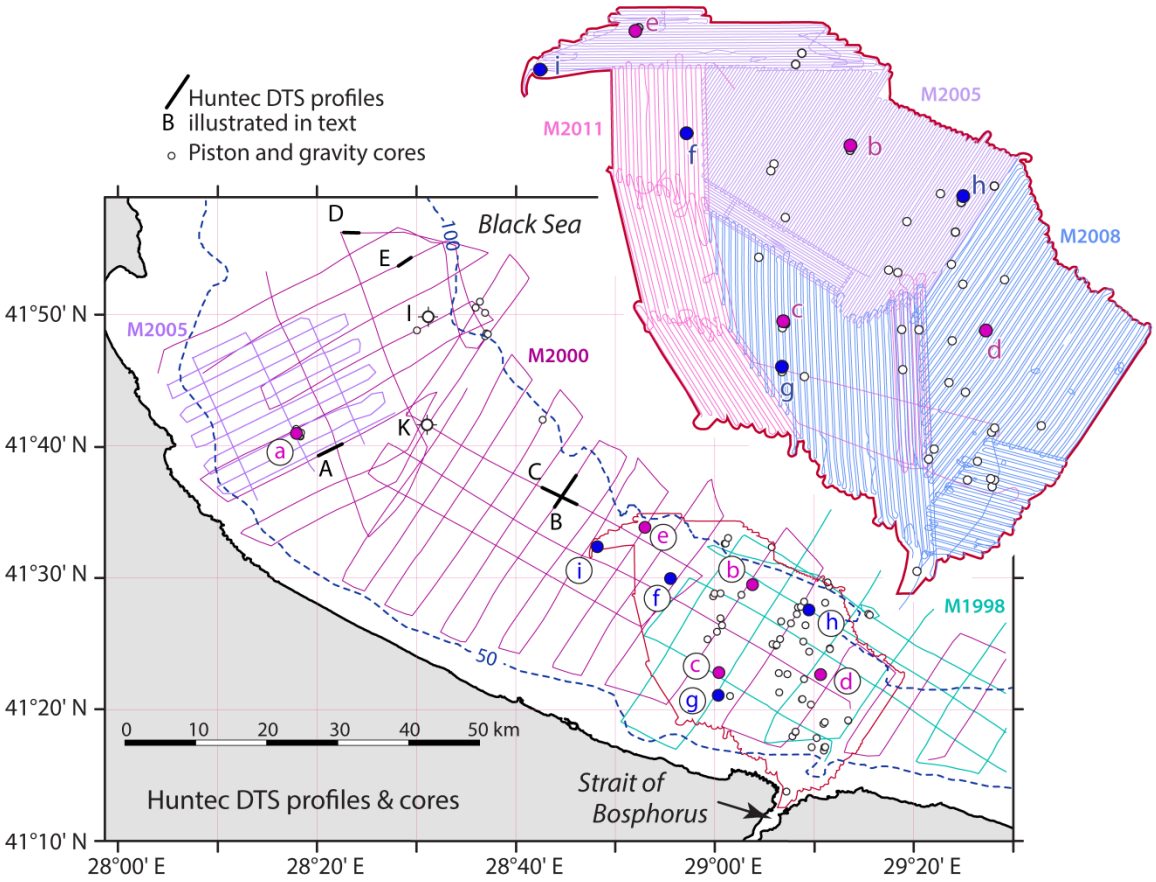

Figure 2.1. Map of the study area showing the data base used in this study. The Huntec DTS seismic reflection profiles are color coded according to their respective acquisition cruises (i.e., M1998–M2011). Note the very dense grid of Huntec DTS profiles across the saline channel area. White circles with black outline are piston and gravity cores collected during various cruises (explained in the text). Larger purple- and blue-filled circles with a–i lettering are composite key cores and composite reference cores, respectively (explained in the text). Thick black lines with A–E lettering are Huntec DTS profiles illustrated in figures in Chapter 3. The 50 m and 100 m isobaths are from IOC (1981).

2.1.3. Acquisition of the multibeam echosounder profiles

The multibeam bathymetry data (inset in Fig. 2.1) were collected along a series of parallel tracks to form an uninterrupted seafloor mosaic at the northern exit of the Strait of Bosphorus using a Kongsberg EM3000™ multibeam echo sounder (single transducer) in 2005 (~200 m swath) and a Kongsberg EM3002D™ system (dual transducers) in 2008 and

2011 (~300 m swath). The transducer was mounted on the port side of the vessel near mid-ship with a steel pole extending ~1 m below the keel of the vessel in 2005 and ~2 m below the keel in 2008 and 2011. The transducer(s) broadcasted a 300 kHz fan (130° for the EM3000 and 200° for the 3002D) consisting of 254 soundings (EM3000) to 508 soundings (EM3002D) per ping with a maximum ping rate of 40 Hz. Under ideal conditions, the resulting data have a depth resolution of 1 cm, and a range resolution of 5 cm. Tracklines were spaced to provide ~30% overlap between adjacent swaths. These data were collected in conjunction with Huntec DTS seismic reflection profiles.

The multibeam data were processed by supervisors Aksu and Hiscott using Caris Hips & Sips 6.0–9.0™. Multibeam mosaic and contour maps were created by Aksu using Caris Base Editor 4.2™. Horizontal resolution was set to 2×2 m, and for detail to 0.5×0.5 m. Given variable sea states during 2005, 2008 and 2011 surveys, the vertical resolution of the EM3002D system is best quantified as being better than 10 cm.

2.1.4. Collection of gravity and piston cores

Piston cores were acquired using a 9–12 m-long Mooring Systems Inc™ Kullenburg-type piston corer (original Benthos™ design) with split piston option, 1000 kg head, and ~4.5 m free-fall. During cruises in 2002 and 2011, a gravity corer was used as trigger-weight, whereas in 2005 a dead weight was used to trigger the piston corer and a separate gravity core was acquired no more than a few tens of meters away to capture the uppermost sedimentary section. All gravity cores were collected using a 3 m-long Benthos-type corer and 300 kg head weight. Core locations were recorded using a GPS (Global Positioning System) receiver in 1992 and 2002 and a DGPS (Differential GPS) receiver in

2005, 2008 and 2011. Water depths at the core sites were determined using a 12 kHz echo-sounder during cruises in 1998, 2000 and 2002, a Kongsberg EM3000 multibeam echosounder in 2005, and a Kongsberg EM3002D echosounder in 2008 and 2011 (Table 2.1).

Table 2.1. Locations and water depths of core sites. G= gravity core, P= piston core, T= trigger weight core. M = Marmara Sea Gateway Project, 02= 2002, 05= 2005, and 11=2011 cruises, respectively. Water depths are rounded to the nearest meter.

Core identifier	Latitude (N)	Longitude (E)	Core Length (cm)	Water depth (m)
M02-045T	41º 41.170'	28º 19.080'	183	69
M02-045P	41º 41.170'	28º 19.080'	851	69
M05-3P	41º 40.878'	28º 19.024'	588	68
M05-19G	41º 33.961'	28º 53.719'	168	94
M05-19P	41º 33.948'	28º 53.670'	960	94
M05-22T	41º 32.416'	28º 48.854'	210	86
M05-22P	41º 32.416'	28º 48.854'	666	86
M05-44T	41º 27.529'	29º 10.004'	208	82
M05-44P	41º 27.529'	29º 10.004'	925	82
M05-50P	41º 29.634'	29º 04.445'	760	91
M05-51G	41º 29.471'	29º 04.393'	159	93
M11-8T	41º 22.787'	29º 01.047'	272	77
M11-9T	41º 21.123'	29º 01.018'	190	76
M11-15G	41º 22.657'	29º 11.122'	251	71
M11-16P	41º 22.663'	29º 11.116'	735	70
M11-22P	41º 21.118'	29º 00.983'	299	75
M11-23P	41º 22.784'	29º 01.060'	517	77
M11-29G	41º 30.007'	28º 56.160'	216	83
M11-30P	41º 29.978'	28º 56.188'	673	83

Cores were shipped to Memorial University of Newfoundland where they were split and described by supervisors Hiscott and Aksu. Sediment color was determined using the Rock Color Chart published by the Geological Society of America in 1984. Two long composite cores (M02-45 and M05-50) have been extensively studied and provide a detailed latest Pleistocene–Holocene paleoclimatic and paleoceanographic evolutionary

history of the southwestern Black Sea (Hiscott et al., 2007b; Marret et al., 2009; Hiscott et al., 2010; Bradley et al., 2012; Mertens et al., 2012; Lister et al., 2015; Williams et al., 2018, Ankindinova et al., 2019a,b).

2.2 Radiocarbon dating and Reservoir Effect

Radiocarbon dating uses the steady decay of radioactive ^{14}C to date materials that are of late Pleistocene to Holocene age (younger than ~50,000 yr). The production of the radioactive isotope ^{14}C occurs naturally as a secondary effect of the cosmic-ray bombardment of the upper atmosphere. The radiogenic isotope of carbon quickly oxidizes (on the order of hours to days) to form $^{14}CO_2$. Stratospheric winds then distribute these molecules throughout the atmosphere, resulting in a relatively well-mixed distribution of $^{14}CO_2$ at the Earth's surface. The world's oceans absorb approximately 85% of these molecules, while only 1% is absorbed by terrestrial material, primarily through photosynthetic processes. As a result, the $^{14}C/^{12}C$ ratio of living organisms is the same as the ratio in the atmosphere at the time of absorption. This content is maintained in equilibrium with the atmosphere through metabolic processes until the living organism dies. Given that ^{14}C decays at a steady rate (half-life = 5730 ± 40 years), the age of biomineralization by the dead organism can be calculated (Taylor and Aitken, 1997).

Radiocarbon dates are reported in years before present (yr BP), where "present" is 1950 by international convention. During the 1955–1963 Common Era, the detonation of nuclear and thermonuclear bombs created an artificial and dramatic increase in ^{14}C in the atmosphere. As a result, dates after 1950 generally are not available using the radiocarbon dating technique. Dates taken directly from geological and archeological samples are

considered raw or uncalibrated, as they do not account for the variation of the levels of atmospheric ^{14}C over the course of geologic time, nor the offset between the age of carbon isolated from the atmosphere in water bodies (lakes and seas) before its incorporation into biological materials.

The dates presented in this thesis were acquired by supervisors Aksu and Hiscott from three laboratories: (a) the IsoTrace Radiocarbon Laboratory, Accelerator Mass Spectrometry Facility at the University of Toronto in Ontario, Canada, (b) the Radiocarbon Dating Laboratory, Université Laval, via either KECK Carbon Cycle AMS Facility, University of California, Irvine, or Centre for Applied Isotope Studies, the University of Georgia and (c) Beta Analytic Inc., Miami Florida, USA. Samples of mostly biogenic carbonate were processed in an accelerator mass spectrometer using a conventional analytical ^{14}C half-life of 5,568 years, and the errors reported in the thesis represent 68.3% confidence limits.

Radiocarbon dates obtained from fossil material cannot be considered as calendar ages because of changes in atmospheric ^{14}C production through time and reservoir effects whereby "old" carbon is recycled and partitioned into marine shells resulting in a date that is too old by hundreds of years. In this thesis, most dates are given in calendar years before present (cal yr BP) or 1000 calendar years (cal ka). The conversion of the raw radiocarbon dates (reported in the thesis with units of ^{14}C yr BP) to the astronomical timescale was done with the Marine13 calibration curve (Reimer et al., 2013) and estimates of the age of the contemporary inorganic carbon reservoir from which biogenic carbonate was precipitated. The Marine13 curve incorporates a modelled, time-varying reservoir age (R) of ~400 yr,

but adjustments (ΔR) are required based on the composition and history of the local watermass (controlled in part by residence times of carbonate and bicarbonate ions in deeper waters, and any hard-water effect through supply of old carbon by rivers). Reservoir age is defined (Stuiver and Braziunas, 1993) as the difference in radiocarbon age between (a) marine precipitates (e.g., shells) or organic matter and (b) contemporaneous terrestrial organic material (e.g., wood) or precipitates (e.g., speleothems) that formed in contact with the atmosphere.

The reservoir age of the modern Black Sea is ~415 yr (Siani et al., 2000), but appropriate reservoir ages prior to reconnection with the global ocean are controversial. Kwiecien et al. (2008) and Soulet et al. (2011) advocated applying a time-varying reservoir age in the range 0–300 ^{14}C yr to pre-reconnection radiocarbon dates of Black Sea shells back to ~12.0 ^{14}C ka. Mudie et al. (2014) warned that the pre-reconnection reservoir age might have been, at times, >1120 ^{14}C yr, but could not be firm on this assessment because of the possibility that a *D. polymorpha* shell in their study was reworked. Yanchilina et al. (2017) proposed an approach based on the expectation that carbon and oxygen incorporated into the Sofular Cave dripstones (i.e., stalactites and stalagmites; Badertscher et al., 2011) would inherit their isotopic signatures from regional vegetation patterns (i.e., the distribution of C3 versus C4 plants) and from water vapour in equilibrium with the surface waters of the adjacent sea. They hypothesized that the Black Sea reservoir age could be determined by tuning (a) the δ^{13}C and δ^{18}O stable isotopic records for radiocarbon-dated shells secreted in the Black Sea to (b) the U/Th-dated stable isotopic records from stalagmites of the Sofular Cave, located immediately inland of the southern Black Sea

coast. The key advantage of U/Th dates is that they are considered calendar ages. Williams et al. (2018) replotted the Yanchilina et al. (2017) data for carbon and oxygen isotopes. The U/Th age for each Sofular Cave data point was converted to an equivalent atmospheric radiocarbon date using the definition table for the IntCal13 calibration curve (Reimer et al., 2013). The isotopic values for the Sofular Cave stalagmites were plotted against these atmospheric ^{14}C ages. Isotopic values for Black Sea molluscs were then superimposed, first as plots against uncorrected ^{14}C dates for each shell, second after subtracting Yanchilina et al. (2017) *R* values and third after subtracting *R* values similar to those used by co-authors AEA and RNH in earlier work (e.g., Bradley et al., 2012; Mertens et al., 2012; Williams et al., 2018; their Fig 8 a,b,c,d). Williams et al. (2018) accepted the good correspondence between mollusc and dripstone records in the Bølling/Allerød warm interval if *R* was very low (~50–100 ^{14}C years), but found no justification for matching peaks and troughs of the two data sets in Holocene samples. Instead, they used reservoir corrections midway between the suggested trends of Kwiecien et al. (2008) and Soulet et al. (2011) until the time of reconnection with the global ocean (Williams et al., 2018 their Fig.7) , and then the modern reservoir age of 415 ^{14}C years determined by Siani et al. (2000). A full explanation of this procedure is available in Williams et al. (2018).

In this thesis, the procedure proposed in Williams et al. (2018) is used to estimate reservoir effect. Calibration of radiocarbon dates was done using a gradual increase in *R* from its pre-reconnection minimum of ~50 ^{14}C yr at ~10200 ^{14}C yr BP to reach 19th–20th century values (Siani et al., 2000) by the time euryhaline molluscs populated the Black Sea shelves (~7100 ^{14}C yr BP according to Ryan et al., 2003; Hiscott et al., 2007b). After 7100

^{14}C yr BP, the default Marine13 calibration curve was used with a fixed ΔR value of +10 years. Online conversions were employed using either Oxcal 4.3 (Bronk Ramsey, 2019) or Calib 7.1 (Stuiver et al., 2019) utilities.

2.3. Construction of shaded contour maps

There are seven shaded contour maps that were drawn by supervisor Aksu using point values supplied by the author for the 2000 survey; Aksu acquired the point values for the 2005, 2008 and 2011 surveys. These shaded contour maps are displayed in Figures 3.3, 3.4; 3.7, 3.8, 3.20, 3.21, 3.23. The raw data for the construction of these maps are mainly hand-picked values from Huntec DTS seismic reflection profiles. In the northwestern portion of the study area, gas-charged sediments often mask reflections in the Huntec DTS profiles, so in that area the acoustic parameters were hand-picked from 40 in^3 airgun profiles collected in 2000. Outside the saline channel area (Fig. 1.2.), acoustic parameters were measured at each fix (spaced ~1.75 km apart) in 2000 and 2005 vintage data. In the saline channel area where multibeam data were acquired along closely spaced survey lines (2005, 2008 and 2011 cruises), acoustic parameters were measured every 1/5 of a fix distance (spaced ~350 m apart). The parameters recorded at each position are explained in the following bullet points.

- Water depth was measured in meters, generally from single-beam or multibeam echosounder readings, but occasionally from airgun data using a sound velocity of 1500 m s^{-1} in water. Thicknesses of seismic units and subunits (Chapter 3) were measured in milliseconds of two-way travel time, later converted to meters using a sound velocity of 1500 m s^{-1} in water and in the water-saturated Holocene muds. The seismic

units and subunits are bounded by laterally persistent key reflectors (from the base of the Holocene upward, α, α1 and α2 as defined by Aksu et al., 2002a). Over wide areas, these key reflectors exhibit the characteristics of unconformities. The geometrical relationships below the α1 and α2 reflectors were classified according to four possibilities: (i) there is an unconformity marked by variable amounts of erosion expressed as angular truncation of deeper reflectors; (ii) there is a concordant geometry (an assumed conformable surface) with reflectors α1 and α2 parallel to reflectors immediately below, with no evidence of erosion; (iii) there is a composite unconformity truncating the next deeper unconformity (so truncation of the α unconformity by α1, or truncation of the α1 unconformity by α2); or (iv) the geometry is largely masked by gas-charged sediments. The geometrical relationships of the reflectors above the α1 and α2 surfaces were classified as one of three alternatives: (i) reflectors immediately above α1 and/or α2 show onlap and/or downlap terminations on the α1 and/or the α2 reflector; (ii) the α1 and/or α2 reflectors are parallel to those immediately above, with no evidence of missing strata; or (iii) the geometry is largely masked by gas-charged sediments. Several derivative parameters were calculated and/or determined using the hand- picked data, and are explained below.

- Total thickness of the Holocene sediments was determined by summing the thicknesses of seismic units above the α transgressive unconformity.
- Paleo-water depths during α1 and α2 times were calculated at each location using:

$$PW\alpha1 = W - (T1d + T1c + SL\alpha1) \qquad (2.1)$$

$$PW\alpha2 = W - (T1d + SL\alpha2) \qquad (2.2)$$

where *PWα1* and *PWα2* are paleo-water depths (in meters; expressed as negative values) for α1 and α2, respectively; *W* is the present-day water depth (in meters; negative values); *T1d* and *T1c* are the thicknesses in meters of seismic subunits between the seabed and the particular surface (where subunit 1d lies above α2 and 1c lies between α2 and α1); *SLα1* and *SLα2* are the sea level deficits relative to today during development of α1 and α2 (in meters; negative values), taken as –15 m below and –5 m below present-day sea level, respectively, based upon the sea level curve of Lambeck et al. (2007) for the sill in the Strait of Bosphorus and the ages determined for the α1 and α2 correlative conformities in Section 3.2.

- If not obscured by gas, the geometrical relationship of each key reflector (α1 and α2) to underlying and overlying strata was used to classify the reflector at that locality as a local conformity, an unconformity, or a composite unconformity (each numerically coded to allow plotting).

The resulting XYZ data matrix consists of 14,952 coordinates and 12 acoustic parameters. The raw data were opened in Global Mapper™ by supervisor Aksu and shaded contour maps were constructed. Once the various key surfaces and subunit thickness were contoured, the volume of each seismic subunit was calculated using Global Mapper™, from which volumes and masses of solid detritus were estimated based on an assumed mud porosity in the range of 60–70%, consistent with typical porosities of Holocene terrigenous muds elsewhere (Kukal, Z., 1971).

2.4. Strontium isotopic work

2.4.1. Details of mollusc samples and sampling

Intact bivalve shells were picked manually from cores M02-45P, M02-45T and M05-03 (Table 2.1) at mostly 10 or 20 cm intervals for strontium isotopic analyses. In those intervals penetrated by more than one core, only one core was sampled, generally M02-45P, to ensure the best possible stratigraphic continuity. The shells were cleaned by surface leaching in 0.1N HCl for one minute, washed with distilled water, then agitated for one hour in an ultrasonic bath of 0.02 N HCl, following the procedure of Major (2002). Each sample was digitally imaged and weighed; ~10 mg of shell was used for strontium extraction.

2.4.2. Isolation of strontium from interfering elements

The shell samples were prepared for strontium extraction, purification and analysis of $^{87}Sr/^{86}Sr$ using a modified version of the method described in Copeland et al. (2008) and Madgwick et al. (2017). The pre-cleaned shells were transferred into clean 3 mL Savillex™ vials (Minnetonka, MN, USA) and dissolved in 1.5 mL of distilled 8M HNO_3, remaining on a hot plate for one hour to ensure complete digestion. Solutions were removed from the hot plate and allowed to cool to room temperature, when 1.0 mL of each solution was transferred into an Axygen™ 2.0 mL MaxyClear Snaplock microcentrifuge polypropylene tube (Union City, California, USA) for Sr determination using a multi-collector system integrated with an inductively coupled plasma mass spectrometer (MC-ICPMS).

All analytical reagent-grade acids were thoroughly purified by sub-boiling distillation using an in-house distillation unit in the clean laboratory of the Earth Sciences Department at Memorial University of Newfoundland, to remove possible contaminants and to reduce blank contributions of strontium. VWR™ 1000 µL pipet tips, each with a SCIENCEWARE™ Fritware™ porous polyethylene sheet (Bel-Art products, NJ, USA) at the bottom, were used as microcolumns. These were rinsed twice at the beginning of each separation run with high-purity deionised (17.8 MΩ) water, followed by rinsing with 1 mL of 6M HCl and 8M HNO_3. Sr-Spec resin (EiChrom Technologies Inc., Darien, IL, USA; cleaned following the procedure in Charlier et al., 2006) was added to the columns and subsequently rinsed twice with 6M HCl and three times each with H_2O and 8M HNO_3. Then the 1.0 mL sample solutions were loaded directly onto the clean resin in the columns and washed three times with 8M HNO_3 to remove Ca, Rb and other minor matrix elements (De Muynck et al., 2009). A column test verified the efficacity of the removal of these potentially interfering elements. Finally, the purified strontium fractions were eluted with 2 mL H_2O into clean Axygen™ 2.0 mL MaxyClear Snaplock microcentrifuge polypropylene tubes (Union City, California, USA). New Sr-Spec resin and newly prepared columns and frits were used in each sample to avoid memory effects.

2.4.3. Mass-spectroscopic procedures

Strontium isotope analyses were performed at the MicroAnalysis Facility (CREAIT Network, Memorial University of Newfoundland) using a Thermo Fisher Neptune Multi-Collector ICPMS with the operating parameters given in Table 2.2.

Table 2.2: Instrument operating parameters.

RF Power	1200 W
Cool gas flow (Ar)	16 L/min
Auxiliary gas flow (Ar)	0.90 L/min
Sample gas flow (Ar)	0.98-0.99 L/min
Interface cones	Nickel, standard sample cone with H skimmer cone
Mass resolution	Low (400)
Nebulizer	100 µL/min
Integration time	2.097 seconds
Number of cycles	50 cycles per block for samples, 25 cycles for calibration solutions
Number of blocks	1 block
Detectors	Faraday cups

The gas flows were optimized daily for maximum ^{88}Sr sensitivity, typically achieving about 70V/ppm for ^{88}Sr. Sample solutions and standards were diluted in 0.3N HNO_3 and introduced into the MC-ICPMS using a Microflow PFA-100 self-aspirating nebulizer connected to a ESI SC-2 autosampler (Elemental Scientific, NE, USA). The signal intensities for sample solutions ranged from 4–34V on ^{88}Sr. The measurements of $^{87}Sr/^{86}Sr$ were made in static mode using the cup configuration shown in Table 2.3. At the start of each analysis, baselines were measured for 30 seconds at half mass on ^{86}Sr followed by 50 cycles of 2.097-second integrations (i.e., ~105 seconds in total). Corrections for interferences from Kr in the argon gas were determined by monitoring ^{82}Kr and ^{83}Kr, and were applied to ^{84}Sr and ^{86}Sr, while corrections for interferences from Rb in the argon gas and samples were applied to ^{87}Sr through monitoring ^{85}Rb and using an $^{85}Rb/^{87}Rb$ ratio of 2.463. The $^{87}Sr/^{86}Sr$ ratio was corrected for mass bias by normalizing to $^{86}Sr/^{88}Sr = 0.1194$ with an exponential law.

Table 2.3. Neptune cup collector configuration for Sr isotope analysis.

Cup	L4	L3	L2	L1	C	H1	H2
Isotopes	^{82}Kr	^{83}Kr	^{84}Sr (+ ^{84}Kr)	^{85}Rb	^{86}Sr (+^{86}Kr)	^{87}Sr (+ ^{87}Rb)	^{88}Sr

Calibration solutions of 200, 400 and 600 ppb Sr were run at the start and end of each session to determine the concentrations of Sr in each sample. These solutions were measured for 25 cycles instead of 50 cycles. A regression equation was created for these data points (^{88}Sr signal, V, as a function of Sr concentration in ppb). The ^{88}Sr signal (V) of the samples was then used to calculate the Sr concentration (ppb) in the sample solutions. Using the dilution factor and starting mass of each sample, the solution concentrations in ppb are converted to Sr concentration of the original sample in ppm.

A 200 ppb solution of strontium isotope standard SRM987 (strontium carbonate) dissolved in 0.3N HNO_3 was analyzed between every five samples for quality control purposes. Sixteen determinations of $^{87}Sr/^{86}Sr$ in SRM987 averaged 0.710272 ± 0.000026 (2σ). This compares well with the long-term (2014–2016) average at the Memorial University MicroAnalysis Facility of 0.710268 ± 0.000028 (2σ, n = 338). These averages are higher than a commonly accepted SRM987 ratio of 0.710240 reported in publications using more traditional methods of thermal ionization mass spectrometry (TIMS) (Terakado et al., 1988; Johnson et al., 1990). To facilitate comparison of our MC-ICPMS isotopic ratios with Major (2002), Yanchilina et al. (2017) and others who normalized their results to SRM987 = 0.710240, the difference between 0.710240 and the average SRM987 ratio obtained during each analytical session was subtracted from all ratios for the session, thus

shifting the SRM987 average for the session to 0.710240 and sample values accordingly. Wherever $^{87}Sr/^{86}Sr$ values from literature sources are used in the thesis, they are adjusted (if required) to be compatible with the same SRM987 value.

Replicates were run to answer two questions: (a) what is the isotopic variation between different shells at a given depth, and (b) what is the isotopic variation in a single shell? If greater than the precision obtained on laboratory standards, then some additional uncertainty would have to be attached to data from the M02-45 site because only single shells were analysed at all but a few depths. The isotopic variation between separate shells was determined by analyzing five separate shells at 140 cm sub-seafloor (composite) depth (392 cal yr BP) and four separate shells at 920 cm depth (10,335 cal yr BP). The strontium isotopic variation within an individual shell was determined in one of the shells at each of these same depths by dividing that shell into 4–5 fragments, which were processed separately. All acquired data were plotted using Microsoft Excel™ Software against composite core depth for MAR02-45 and MAR03-05.

2.5. Stable isotopic and Trace element work

2.5.1. Details of ostracod samples and sampling

The adult shells of two ostracod species (*Palmoconcha agilis* and *Loxoconcha lepida*) were chosen for stable isotopic and trace-element studies. Complete ostracod shells are called carapaces, and each carapace consists of two valves. *P. agilis* is abundant today on clay substrates around the shorelines of the Black Sea at depths of 10–100 m (Schornikov, 1967), and forms part of a Mediterranean-type assemblage which has become established in the post-reconnection period (Zenina et al., 2017; Williams et al., 2018). *P.*

agilis is the dominant species in the upper ~500 cm and ~530 cm of composite cores M02-45 and MAR05-50, respectively (Williams et al., 2018). *L. lepida* lives in the brackish-water environments (practical salinity 5–12) of the present-day Black Sea and Caspian Sea (Schornikov, 1964, 1967), and together with *Loxoconcha sublepida* dominates the fauna at core depths of ~490–1010 cm (M02-45 composite) and ~530–780 cm (M05-50 composite; Williams et al., 2018). Between 430 cm and 520 cm in core M02-45 and 540 cm and 620 cm in core MAR05-50 there is an interval where brackish and marine ostracod species co-occur.

Composite cores M05-50 and M02-45 were sampled at approximately 10 cm intervals, with ~20–25 cm^3 of sediment extracted from each interval. The samples were placed in 250 mL beakers: 150 mL of distilled water and 25 mL of 1% sodium hexametaphosphate (Calgon) were added. In most cases, disaggregation was achieved by gentle shaking. However, for the more dry samples from core M02-45 and a few replicate samples from core M05-50, ~5–10 min of gentle boiling on a hot plate was added to the procedure. In the upper 430 cm of composite core M02-45, 20 of 32 samples were boiled. Local surface water used in the Memorial University of Newfoundland laboratory has a $\delta^{18}O$ value of ~ –11‰ (Finkenbinder et al., 2016), so boiled samples were checked for any systematic shift toward negative $\delta^{18}O$ values relative to un-boiled samples. Adjacent boiled and un-boiled samples have fully overlapping $\delta^{18}O$ values in the range –1‰ to +1‰, confirming no adverse effect. The disaggregated samples were then wet-sieved using a stack of three sieves with openings of 180, 125 and 63 μm. Ostracod valves were handpicked from the 180–125 μm size fraction under a stereoscopic microscope; the 125

μm sieve retains adult valves of most species (Boomer et al., 2003). Valves were rinsed with Nanopure™ water, dried overnight in a 25°C Fisher Scientific Isotemp™ oven and placed into acid-cleaned 4.5 mL vials. Approximately four mono-specific adult valves were picked from each sample to make up the ~0.1 mg of calcium carbonate necessary for oxygen and carbon stable isotopic analyses.

2.5.2. Chemical preparation and analytical procedures

The isotopic ratio measurements of $\delta^{18}O$ and $\delta^{13}C$ for all samples and standards were made using a high-precision (i.e., standard deviation of 4–6 significant digits) continuous-flow isotope-ratio mass spectrometer in the Stable Isotope Laboratory at Memorial University of Newfoundland. Approximately 0.1 mg of carbonate was inserted into 4.5 mL round-bottomed vials. The vials were covered with Exetainer screw caps with pierceable septa and were placed in a heated sample holder held at 50°C. Using a GC Pal Autosampler™, the vials were flushed with ultra-high purity-grade helium for 5 minutes using a double-holed needle connected by tubing to a helium gas source. Samples were then manually injected with approximately 0.05 mL of 100% phosphoric acid using a syringe and needle. A minimum of 1 hour was allowed for samples to react and fully dissolve.

The samples were analysed using a Thermo Electron DeltaVPlus™ isotope-ratio mass spectrometer. The GC Pal was used to sample the headspace in each vial using a double-holed needle flushed with ultra-high purity-grade helium. The helium/sample gas mixture from each vial was carried through fused glass capillary tubing into a Thermo Electron GasBench II™, where the gas mixture passed through a Nafion™ drier. The dried

gas then passed through an 8-port switching valve with a 50 µL sampling loop. Using the sampling loop, portions of the sample gas were injected onto a 30 m × 0.32 mm GS-Q fused silica capillary GC column in the GasBench II™ to separate CO_2 from other gases. After the GC column, the gases passed through an additional Nafion™ drier. The gas stream, containing the CO_2 gas, was carried by the He carrier gas into the DeltaVPlus™ mass spectrometer via an open split interface. The GasBench II™ acts as an interface between the samples in the vials and the mass spectrometer. An open split tube allows a portion of the sample gas mixture to enter into the source of the mass spectrometer via a fused glass capillary. Multiple aliquots of sample gas (usually eight) were injected for each sample analysis. Another open split tube in the GasBench II™ allows the injection of a reference CO_2 gas. An isotope ratio is assigned to the reference gas in the processing software, and this value is used with the reference peak(s) in each analysis for comparison with the sample peaks. Three different standards of known isotopic composition were included throughout each run and treated to the same processes as the unknown samples. The "raw" isotope ratios determined by IsodatNT 3.0™ software were calibrated offline using an Excel™ spreadsheet. Two of the reference values were used to calibrate (or normalize) the data, while the third was used as a check standard. Table 2.4 provides the analytical precision and accuracy of the laboratory standards. The calibrated data were then imported into a LIMS (Light Stable Isotopes) database. The oxygen and carbon isotopic compositions are expressed using the δ notation where $\delta^{18}O$ and $\delta^{13}C$ can be written as:

$$\delta^{18}O = \left(\frac{\left(^{18}O/^{16}O\right)_{sample}}{\left(^{18}O/^{16}O\right)_{standard}} - 1\right) \times 1000 \qquad (2.3)$$

$$\delta^{13}C = \left(\frac{(^{13}C/^{12}C)_{sample}}{(^{13}C/^{12}C)_{standard}} - 1 \right) \times 1000 \qquad (2.4)$$

The $\delta^{18}O$ and $\delta^{13}C$ values are reported with respect to the Pee Dee Belemnite (PDB) standard.

Table 2.4. Precision and accuracy of the CMB, NBS19 and MUNCO1 standards. SD = standard deviation. Number of analyses = 24.

Standard	**isotope**	**laboratory measurements**		**SD**
CMB	$\delta^{13}C$	0.75	0.72	0.09
	$\delta^{18}O$	-8.58	-8.60	0.16
NBS-19	$\delta^{13}C$	1.95	1.95	0.05
	$\delta^{18}O$	-2.20	-2.20	0.04
MUN-CO-1	$\delta^{13}C$	-21.02	-21.02	0.07
	$\delta^{18}O$	-13.40	-13.40	0.11

2.5.3. Loxoconcha lepida – Palmoconcha agilis vital effect determination

Ostracods occur widely in almost all aquatic environments. Carapaces are built with low magnesium calcite, ensuring good preservation. This makes ostracod carapaces an excellent material for paleoenvironmental studies using stable isotopes of carbon and oxygen, and trace elements (e.g. Decrouy , 2009, Heaton et al., 1995). However, in some cases ostracods do not precipitate their biogenic carbonate in isotopic equilibrium with the surrounding water, and there is a "vital effect" that must be taken into account (Decrouy, 2009; Decrouy et al., 2012).

The adult shells of two ostracod species (*Palmoconcha agilis* and *Loxoconcha lepida*) were chosen for stable isotopic and trace-element studies. Valves are exquisitely preserved (Williams et al., 2018), suggesting minimal to no diagenetic alteration. As noted

in Section 2.4.1, between 430 cm and 520 cm in core M02-45 and 540 cm and 620 cm in core MAR05-50 there is an interval where brackish and marine ostracod species co-occur. Both *P. agilis* and *L. lepida* were collected in 15 samples across these transitional intervals to quantify any stable isotopic offsets between these two species that might be attributed to vital effects.

2.5.4. Ca measurements using electron microprobe

The Ca reference concentration in the ostracod valves was determined as the average of 38 CaO determinations using a JEOL JXA 8230™ electron probe micro-analyzer (EPMA) with a tungsten filament and five wavelength-dispersive spectrometers. The EPMA was operated at 15 kV, 5 nA with a beam defocused to 15 μm. A calcite standard was used for Ca, while the secondary standard was dolomite. Mean CaO wt% in the ostracod valves was 53.3440 (SD = 1.594) with a corresponding Ca concentration of 381250 ppm. This average Ca value from EPMA was used as the internal standard in the LA-ICP-MS calculations. Table 2.5 shows the reproducibility for the internal standard.

Table 2.5. Precision and accuracy of the MUN dolomite standard. SD = standard deviation. N = number of analyses.

	CaO	**SD**	**N**
Laboratory measurements	29.50	0.26	11
Standard values	30.01	0.42	100

2.5.5. Analytical procedures using laser-ablation ICP-MS

For trace element measurements on ostracods, 4–6 valves of *P. agilis* or *L. lepida* were hand-picked from each core depth in composite cores M02-45 and M05-50 following

the sampling procedure described in Section 2.4.1. Recommendations of de Deckker (2017) regarding sample preparation were used in this study. Shells were mounted on glass slides using double-sided sticky tape. For measurements involving laser ablation inductively coupled plasma mass spectrometry (LA-ICP-MS), a 193 nm ArF Excimer GeoLas™ laser system (Coherent, Germany) was coupled to an Element XR™ (Thermo Fisher, Germany). The LA-system at Memorial University of Newfoundland is equipped with a cylindrical ablation cell with a volume of ~10 cm^3 capable of holding one microscope slide at a time. NIST SRM 610 was used as the primary standard, MACS-1 as a secondary standard and for quality control during the measurement sessions, and BCR-2G was analyzed each day for quality control with the same parameters except a broader element menu. An internal standard is needed for the LA-ICP-MS procedure because the system measures the relative amounts of the various elements and isotopes and not absolute concentrations. However, with an accurately known concentration of one element, (i.e., with an internal standard) concentrations of the other elements can be calculated by the ICP-MS software. Ca was used as the internal standard, and was set to 380000 ppm as an initial 'working' value for determinations based on the isotope ^{43}Ca.

The laser was operated with a repetition rate of 4 Hz, an energy density of 4 J/cm^2. Five pre-ablation shots were performed on the samples. Pre-ablation shots were designed to remove the uppermost layer of the ostracod valves which are generally enriched in various elements adsorbed onto those surfaces. The carrier gas flow was 1L/min He and the ICP-MS was optimized for high sensitivity and a low oxide formation ratio (i.e., a

ThO+/Th + ratio of <0.2%). A crater size of 40 μm was used during the ablations. In each sample, 4–5 valves were ablated at each core depth, with one ablation per valve.

2.5.6. Data extraction

During The Laser Ablation procedure, the abundances of Al, B, Ba, Cd, Ce, Cu, Fe, Li, La, Mg, Mn, Mo, P, Pb, Rb, Sc, Si, Sr, Ti, U, V, Zn and Zr were determined. As a check, calcium was determined redundantly based on its isotope ^{44}Ca to compare with the internal standard value of 380000 ppm which was based on ^{43}Ca. All results were initially expressed as concentrations in ppm after multiplication of each raw value by 381250/380000 to adjust the results to a Ca average concentration of 381250 ppm (from independent electron probe micro-analyzer measurements). Concentrations were then converted to mmol $1000g^{-1}$, except for Ca which was expressed as mol $1000g^{-1}$ using the same concentration of 381250 ppm for each analysis (so Ca throughout = 24.951 mol $1000g^{-1}$). The element/Ca ratios were obtained by division and have units of mmol/mol. Except for Mg/Ca and Sr/Ca in selected plots, all element/Ca ratios are abbreviated in Section 5 by the symbol for the trace or minor element, followed by an asterisk; for example, Ba*= Ba/Ca, La*= La/Ca, Zr*= Zr/Ca, etc. The detection limits of the elements are listed in Table 2.6, the analytical precision and accuracy of the analyses of the NBS610 standard are given in Table 2.7.

Table 2.6. Detection limits (DL) of the elements used in the high-resolution double-focussing magnetic-sector inductively coupled plasma mass spectrometry during the 26 analyses of the NIST610 standard.

Elements	DL (ppm)	SD	Elements	DL (ppm)	SD
Al	4.650	1.964	P	69.846	13.593
B	9.431	1.676	Pb	0.141	0.111
Ba	0.609	0.168	Rb	0.289	0.118
Cd	0.405	0.123	^{86}Sr	11.273	1.843
Ce	0.136	0.110	^{88}Sr	0.712	0.211
Cu	0.534	0.108	Ti	1.334	0.382
Fe	34.154	6.038	U	0.166	0.105
La	0.147	0.107	V	0.274	0.093
Mg	3.350	0.945	Zn	1.236	0.243
Mn	2.688	0.365	Zr	0.217	0.121
Mo	0.290	0.168			

Table 2.7. Precision and accuracy of the NIST610 standard. Elemental concentrations are "preferred averages" as indicated in Pearce et al., 1997 (their Table 8). SD = standard deviation. Number of analyses of NIST610 = 26.

	NIST610 (ppm)	SD (ppm)	Laboratory (ppm)	SD (ppm)	SD as % of reported
B	356.4	7.3	356.885	10.690	3.00
Ba	424.1	29.3	435.873	7.555	1.73
Cd	259.4	4.7	259.185	3.196	1.23
Ce	447.8	16.8	448.427	6.284	1.40
Cu	430.3	23.6	430.550	9.435	2.19
Fe	457.1	22.2	459.962	21.568	4.69
La	457.4	72.4	457.642	4.894	1.07
Mg	465.3	26.6	465.265	5.579	1.20
Mn	433.3	31.8	485.308	5.984	1.23
Mo	376.8	45.0	410.085	7.558	1.84
P	342.5	53.1	344.308	32.551	9.45
Pb	413.3	15.4	426.115	8.069	1.89
Rb	431.1	11.4	425.988	6.009	1.41
Sr	497.4	18.3	516.319	6.464	1.25
Ti	434.0	14.7	434.308	5.945	1.37
U	457.1	13.6	461.665	9.536	2.07
V	441.7	42.7	442.442	5.262	1.19
Zn	456.3	19.2	457.000	8.338	1.82
Zr	349.9	7.8	440.435	6.322	1.44

Chapter 3. Seismic stratigraphy, allostratigraphy, chronology and facies from cores

Shelves do not aggregate gradually and continuously. Instead, they experience repeated regressive-transgressive cycles, which are controlled by eustasy, local tectonics and rate of sedimentation. These cycles can contribute to the stratal architecture, with deposition punctuated by erosional surfaces bounding sedimentary (and therefore seismic) units on the shelf. Subaerial erosional truncation, formed during a base level fall, is considered as a sequence-bounding unconformity (Van Wagoner et. al., 1988). The subaerially exposed shelf is considered to be an area of sediment bypass which subsequently experiences backfilling during the next base level rise. Identification of these and other widely traceable unconformities permits the defining of seismic units and sedimentary allostratigraphic units which directly reflect sequential changes in the depositional environment.

Seismic stratigraphy provides a conceptual framework for developing deterministic numerical models of stratigraphic architecture, sedimentary facies distributions, and basin evolution. Cross and Lessenger (1988) identified four major approaches within the practice of seismic stratigraphy. Each approach has a different set of objectives, questions, scales of observation, and methodologies:

1. *seismic sequence analysis* aims to define the regional stratigraphic architecture and establish the time-stratigraphic framework of a sedimentary basin through recognition of unconformity-bounded depositional sequences;

2. *seismic facies analysis* aims to interpret the depositional environments, lithologies, and geological history represented by strata in different positions within a sequence;

3. *seismic lithology analysis* involves the detailed analysis and modeling of an individual seismic reflection or a small number of adjacent reflections;

4. *integrated seismic stratigraphic analysis* aims to integrate geological and geophysical observations and analytical techniques at all scales.

This chapter is focused on the Holocene sedimentary evolution of the southwestern Black Sea shelf. The primary objectives are to elucidate the timing and products of the most recent Holocene transgression and to set a number of long piston cores that are considered in later chapters into a coherent chronological and stratigraphic context. The results of this chapter underpin the 2020 paper by Ankindinova, Aksu and Hiscott ("Holocene sedimentation in the southwestern Black Sea: interplay between riverine supply, coastal eddies of the Rim Current, surface and internal waves, and saline underflow through the Strait of Bosphorus") published in the high-impact journal *Marine Geology*.

3.1. Stratigraphic framework of the southwestern Black Sea

The stratigraphic framework of the southwestern Black Sea is presented under three subheadings: (a) seismic stratigraphic architecture, (b) allostratigraphy and lithologic attributes of the cores, and (c) chronology based on ^{14}C dates and age models for a number of key cores.

In a previous study using a more limited set of data, Aksu et al. (2002a) described five seismic stratigraphic units: Unit 1 (uppermost Pleistocene and Holocene), Unit 2

(Upper Pliocene to Quaternary), Unit 3 (Middle Miocene to Lower Pliocene), Unit 4 (Middle Eocene to Lower Miocene) and Unit 5 (Mesozoic successions). This general seismic stratigraphic framework is maintained here, but is refined based on the interpretation of a dense grid of recently acquired Huntec DTS profiles and piston cores. Aksu et al. (2002a) recognized four unconformities such that their Units 1, 2, 3 and 4 are underlain, respectively, by the unconformities α0 (α in the 2002 publication), β, γ, and δ (Fig. 3.1).

Aksu et al. (2002a) did not recognize a separate α0 unconformity and designated this youngest discontinuity as α, not α0. The difference between α and α0, as defined here, is that α occurs within Unit 1 and formed in part by transgressive erosion preceding the present highstand, whereas the older α0 is overlain by pre-last-transgression Pleistocene deposits which might be remnants of falling-stage, post-LGM (Last Glacial Maximum) lowstand, and perhaps pre-LGM successions that escaped later erosion on what is now the southwestern shelf. The deposits between the α0 and α unconformities occur in scattered lenses across the shelf. More commonly, the α0 unconformity is itself truncated by α (Figs. 3.1, 3.2). Units 5 through 2 offlap toward the shelf edge, so that Unit 5 occurs landward of Unit 4, Unit 4 occurs landward of Unit 3, and so on to Unit 2, which is largely restricted to the shelf edge.

Units 5–2 dip basinward and are all truncated by the shelf-crossing α unconformity. In so doing, α also truncates the α0, β, γ and δ unconformities (Fig. 3.1). Several of these unconformities are recognized across the western Black Sea shelf off Bulgaria and Romania (Konerding, 2009). The ages of Unit 1 and the uppermost portion of Unit 2 are

established by ties to a number of well-dated piston and gravity cores from the southwestern Black Sea shelf (see Fig. 2.1 for grid; details are presented in the Chronology section 3.3). The ages of the older Units 3–5 come from two exploration wells (Aksu et al., 2002a), Iğneada–1 and Karadeniz–1 (Figs. 2.1). This chapter solely focuses on the seismic stratigraphy of Unit 1 and its component subunits.

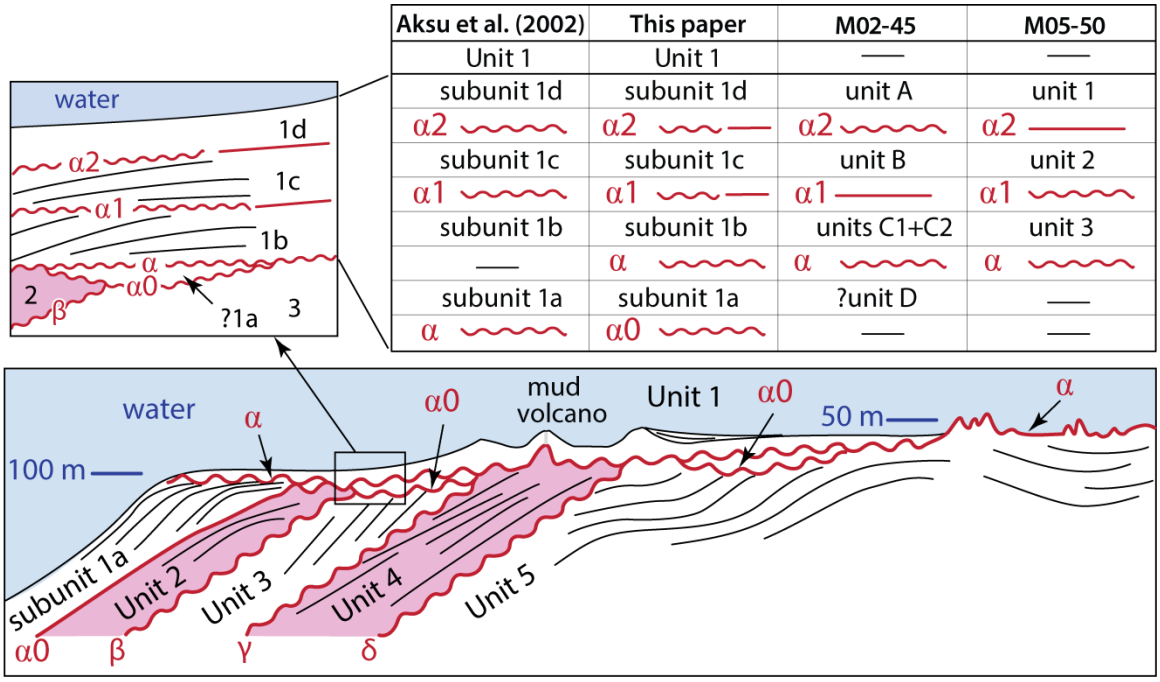

Figure 3.1. Schematic dip cross section across the southwestern Black Sea shelf showing the relationships between seismic-stratigraphic units 1–5 and unconformities α, α0 , β, γ and δ (modified from Aksu et al., 2002a). Note that the uppermost Unit 1 is also divided into three subunits bounded at their base by the α unconformity and two additional mild unconformities (and their correlative disconformities/conformities), α1 and α2. The table to the upper right compares the nomenclature used in this thesis to that used in Aksu et al., (2002), and publications that used the stratigraphies of composite cores M02-45 and M05-50, including Hiscott et al. (2007a), Flood et al. (2009), Bradley et al. (2012), Williams et al. (2018) and Ankindinova et al. (2019a,b; 2020).

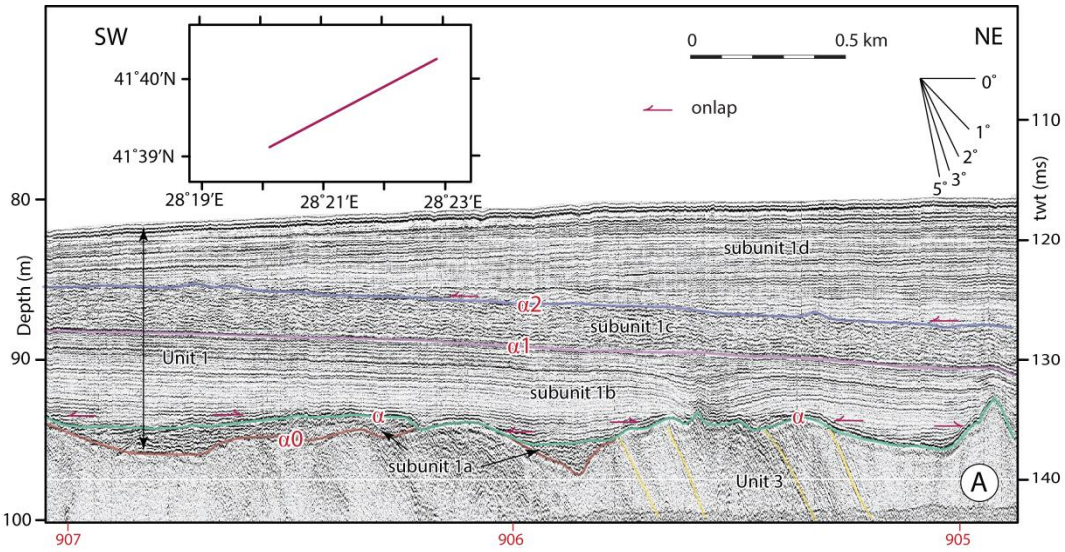

Figure 3.2. Representative Huntec DTS seismic reflection profile A showing the seismic stratigraphic architecture of the southwestern Black Sea shelf. The folded and faulted strata of Unit 3 are truncated by the prominent unconformities α0 and α. Note that α0 unconformity itself is truncated by α, indicating that the latter is a composite unconformity. Also note that two prominent reflectors, α1 and α2, divide the upper portion of Unit 1 into three subunits. Prominent reflectors α0, α, α1, and α2, are explained in the text. Water depth and sediment thicknesses are calculated using an acoustic velocity of 1500 m s^{-1}. Red numbers with vertical ticks are navigational fix positions. Location is shown in Figure 2.1.

3.1.1. Seismic stratigraphic Unit 1

Seismic stratigraphic Unit 1 is characterized by acoustically strong and continuous reflections that can be traced long distances across the southwestern Black Sea shelf (Fig. 3.2). It is generally bounded at its base by the α unconformity and locally by the α0 unconformity. The α unconformity and two younger, regionally mappable but less prominent reflectors called α1 and α2 divide seismic stratigraphic Unit 1 into four subunits (from oldest to youngest, 1a, 1b, 1c and 1d; Figs. 3.1, 3.2). Subunit 1a is underlain by α0, 1b by α, 1c by α1 and 1d by α2. The α1 and α2 reflectors are local unconformities based on reflection terminations, but laterally transition into disconformities/paraconformities

and/or their correlative conformities. Unit 1 is inferred to have accumulated during lowstand progradation at the shelf edge, and during and after the subsequent MIS1 (Marine Isotopic Stage 1) transgression; hence, it was deposited during and after the last glacial lowstand. Aksu et al. (2002a) included some inconsistent statements which suggested a base-level fall and second Holocene transgression during development of α1 and α2, but those statements were subsequently retracted and corrected (Hiscott et al., 2007b; Flood et al., 2009) and are not supported by more recent work.

Conformable and unconformable relationships were determined by studying reflection terminations at the α0, α, α1 and α2 levels. Procedures are consistent with Mitchum and Vail (1977). Angular truncation of reflections indicates erosion and a depositional break. Depositional onlap (or downlap) on a pre-existing surface, whether that surface shows evidence for erosion or not, requires a hiatus (hence unconformity). Where reflections are parallel and continuous across a key surface, the most that can be said is that the transition from one seismic unit to the next is concordant, because a disconformity or paraconformity can only be discovered by examining fauna/floral trends in cores, or with absolute dating (e.g., radiocarbon dating).

Seismic markers α1 and α2 have the same definitions found in Aksu et al. (2002a), so seismic profiles in that 2002 publication can be consulted as an additional resource pertinent to this thesis, in particular to provide additional examples of geometry and attributes of subunits 1d and 1c. Seismic reflection α in the 2002 paper is generally α0 of this thesis, but there is not a one-for-one correspondence, so readers of this thesis must be careful regarding picks of the base of subunit 1b in Aksu et al. (2002a), as those picks might

be deeper than examples in this thesis. [Most captions in Aksu et al. (2002a) incorrectly refer to the subunits as 5a–5d, rather than 1a–1d, but the graphics themselves are correct.]

Yanchilina et al. (2017) employed the names α and α1 for two erosional surfaces in their seismic profiles and cores offshore Romania and Bulgaria, and explicitly correlated these with the unconformities defined for the first time by Aksu et al. (2002a). This appropriation of previously defined terms creates confusion, because the water depths where α1, in particular, is found and its age as reported by Yanchilina et al. (2017) are inconsistent with Aksu et al. (2002a). Specifically, Yanchilina et al. (2017) state that α1 only occurs beyond the lowstand paleoshoreline (i.e., below ~–95 m), that it is underlain by Younger Dryas strata (~12.7–11.6 cal ka) and overlain by Bugaz strata (~8.4–6.5 cal ka). As defined by Aksu et al. (2002a) and as used in this thesis, α1 is only recognized on the shelf (so in modern water depths of –50 m to –120 m), it is underlain by lower Holocene deposits (~11.0–7.3 cal ka) and overlain by lower to middle Holocene deposits (~8.2–7.3 cal ka). Hence, there is no reason to seek a common origin or significance to the α1 of Yanchilina et al. (2017) and the α1 of this thesis, and they certainly are not correlative surfaces. Likewise, the Yanchilina et al. (2017) α unconformity is proposed by those authors to separate Bølling/Allerød strata (~14.7–12.7 cal ka) from Younger Dryas strata, so is significantly older than the α unconformity described in this thesis.

3.1.2. Seismic stratigraphic subunit 1a

Along the present-day shelf edge, subunit 1a is characterized by several overlapping seaward-prograded wedges interpreted by Aksu et al. (2002a) to have been deposited during the latest Pleistocene lowstand. Landward of the shelf-edge, subunit 1a consists of

erosional remnants, mostly not sampled in cores, which pre-date the last transgression. These consist of overlapping lenticular deposits, often separated by prominent reflections (e.g., Fig. 3.3). Internally, these lenticular deposits may show low-angle (1–3º) clinoforms or prominent onlap and basin-fill architecture (Fig. 3.3). The base of the subunit is marked by the locally very prominent α0 reflector, which separates the subunit from the folded and faulted successions of Unit 3. The top of the subunit is delineated by the equally prominent α reflection.

In map view, Subunit 1a occurs as a series of northwest–southeast-trending, 3–5 km-wide zones with central thicknesses ranging between 2–10 ms of two-way travel time (twt, Fig. 3.3). These zones, or bands, are best developed across the southeastern sector of the study area between 28º30'E and 29º30'E longitudes in mid-shelf water depths of 60 m to 90 m. In this region, the α unconformity is notably flat, whereas the α0 unconformity shows prominent erosional notches into the underlying Unit 3 (Fig. 3.2), thus indicating that subunit 1a fills pre-existing paleotopography. Across the northwestern portion of the study area, subunit 1a is largely absent (Fig. 3.3). Here the α unconformity frequently cuts much deeper into the section, often truncating the α0 unconformity (Fig. 3.2). Very thin and locally restricted occurrences of Subunit 1a are present where small pockets of sediment are preserved between the α0 and α unconformities (Figs. 3.2, 3.3).

Subunit 1a is a lowstand systems tract deposit. Landward of the lowstand shoreline, the scattered erosional remnants are interpreted to have escaped erosion during the LGM lowstand when the shelf was subaerially exposed, as well as erosion by ravinement during the subsequent base level rise.

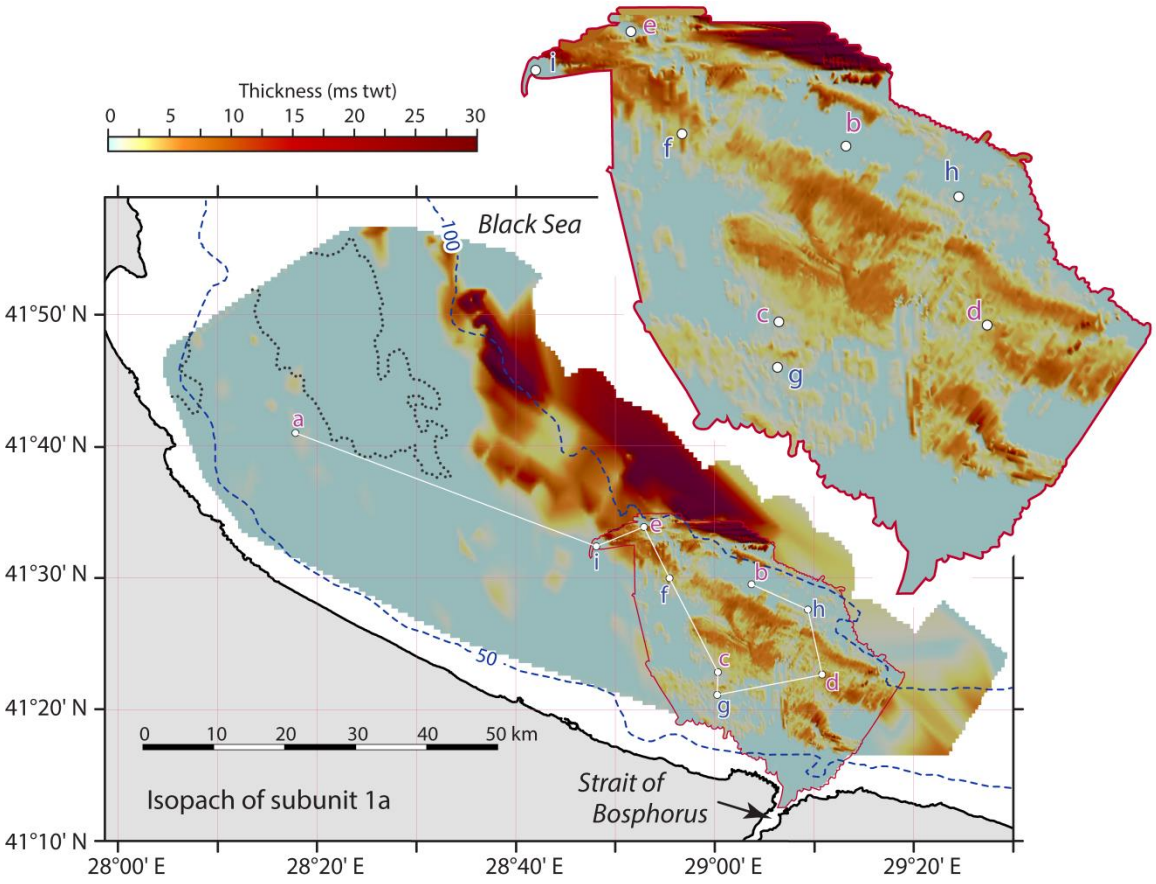

Figure 3.3. Isopach map of the Pleistocene subunit 1a (in ms twt) across the southwestern Black Sea. Coastline and rivers are from NOAA National Geophysical Data Center (http://www.ngdc.noaa.gov/mgg/shorelines/shorelines.html). The data are contoured using Global Mapper v14. The –50 m and –100 m isobaths are from IOC (1981). Small white circles are composite key and reference cores discussed in the text.

3.1.3. Seismic stratigraphic subunit 1b

Subunit 1b is characterized by a strongly reflective, laterally continuous package of high-frequency reflections between the α unconformity and the α1 unconformity or its correlative discontinuity/conformity (Fig. 3.2). The base of the subunit shows a protracted onlap over the α unconformity, filling depressions which existed along the unconformity

surface prior to the early Holocene transgression. As accumulation continued, the onlapping basin fill overstepped the highs and created a shelf-wide blanket of sediments.

Subunit 1b is thickest across the northwestern sector of the study area where it defines a broadly elliptical northwest–southeast-aligned accumulation with a central thickness exceeding 7 ms twt (or ~5.25 m @ 1500 m s^{-1}; Fig. 3.4). Farther toward the southeast across the saline channel area, subunit 1b exhibits a very patchy distribution as WNW–ESE-trending relatively thin accumulations (Fig. 3.4).

3.1.4. Seismic stratigraphic subunit 1c

Subunit 1c is characterized by a 'crinkly' acoustic appearance with laterally discontinuous high-frequency reflections displaying a quasi-corrugated look (Figs. 3.2, 3.5). In rare cases, convex-upward corrugations (2D mound-like features regardless of track orientation) appear to climb upward through the subunit (Fig. 3.6). Subunit 1c extends from the α1 unconformity (or its correlative conformity) at its base to the α2 disconfomity/paraconformity (or its correlative conformity) at its top. In map view, Subunit 1c shows several distinct accumulation patterns (Fig. 3.7).

There is a prominent northwest–southeast-trending arcuate tongue of thick sediments in the northwestern sector of the study area which exhibits central thicknesses of 10–12 ms twt (or 7.5–9 m @ 1500 m s^{-1}; Fig. 3.7). The subunit quickly narrows toward the southeast, becoming largely confined to the mid-shelf and thinning to <5 ms around the western fringes of the saline underflow channel.

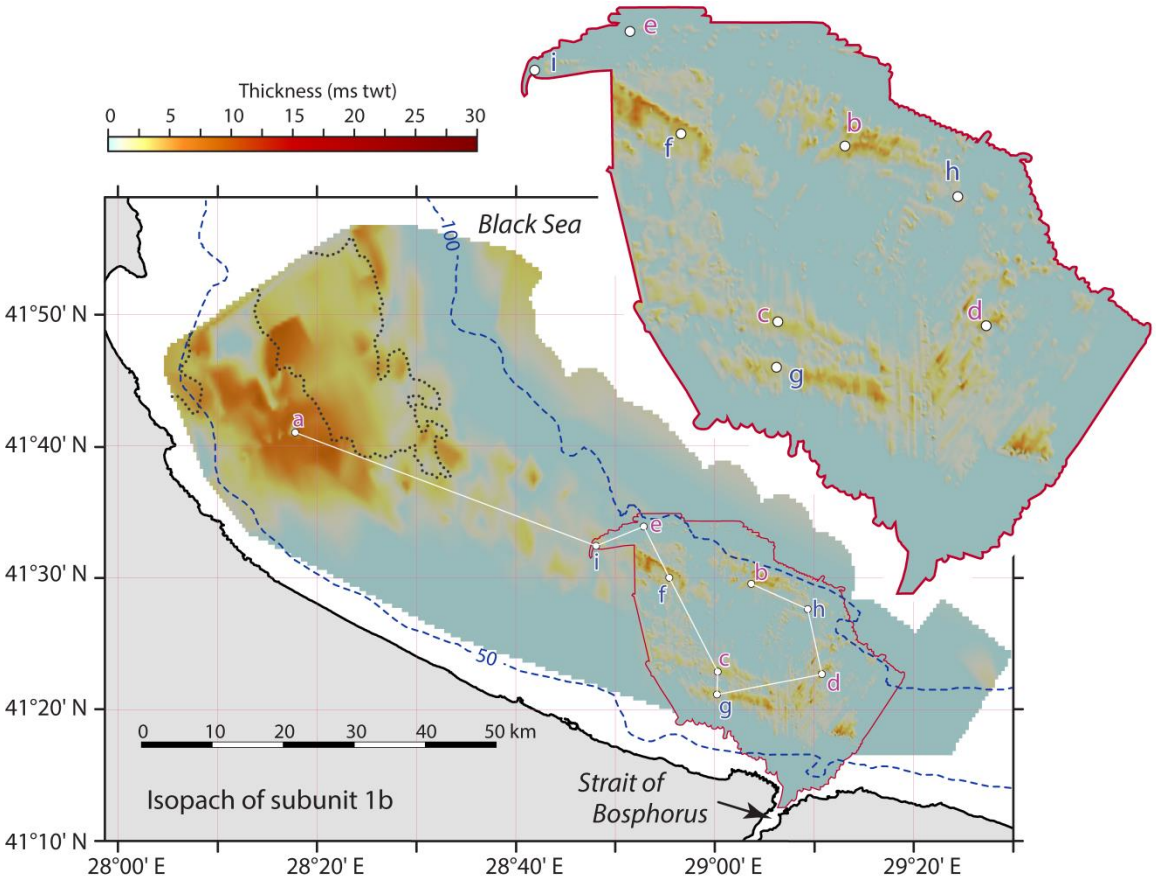

Figure 3.4 Isopach map of the lower Holocene subunit 1b (in ms twt) across the southwestern Black Sea. Coastline and rivers are from NOAA National Geophysical Data Center (http://www.ngdc.noaa.gov/mgg/shorelines/shorelines.html). The data are contoured using Global Mapper v14. The –50 m and –100 m isobaths are from IOC (1981). Small white circles are composite key and reference cores discussed in the text.

There is also an equally thick, but very local accumulation of subunit 1c immediately north of the Strait of Bosphorus beneath the levées of the underflow channel (Fig. 3.7). The channel floor itself is nearly barren of subunit 1c (and 1d). Elsewhere, subunit 1c is very thin both toward the present-day coastline and along the present-day shelf-edge, but shows slightly increased thicknesses immediately seaward of the shelf-edge on the upper slope (Fig. 3.7).

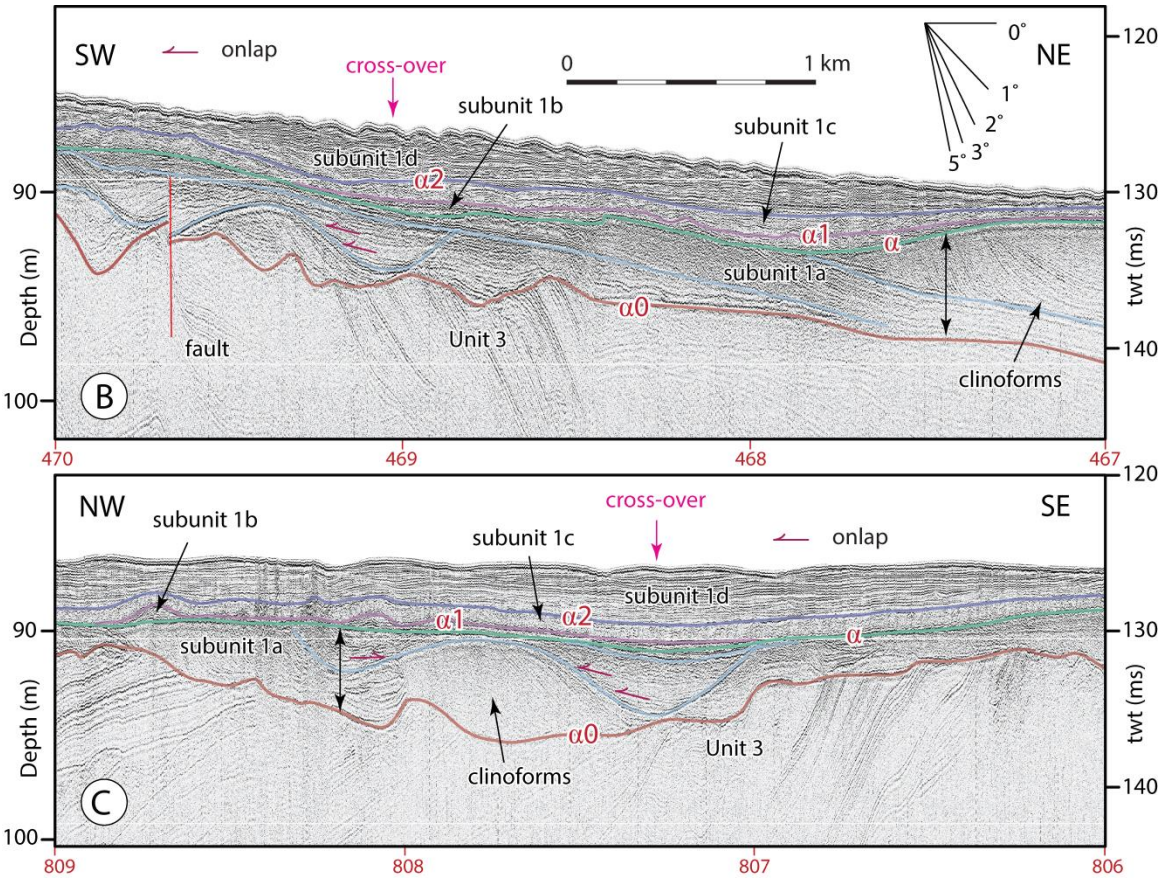

Figure 3.5. Huntec DTS seismic reflection profiles B and C showing the seismic stratigraphic architecture of subunit 1a across the southwestern Black Sea shelf. In this region the folded and faulted strata of Unit 3 are truncated at their top by the prominent α0 unconformity. Note that there are 2–3 prominent reflectors within subunit 1a, separating seismically distinctive packages from one another. Also note that the NE–SW-running profile B crosses the NW–SE-running profile C at nearly a 90º angle at the point labeled "cross-over". Prominent reflectors α0, α, α1 and α2, are explained in the text. Water depth and sediment thicknesses are calculated using an acoustic velocity of 1500 m s^{-1}. Red numbers with vertical ticks are navigation fix positions. Location is given in Figure 2.1.

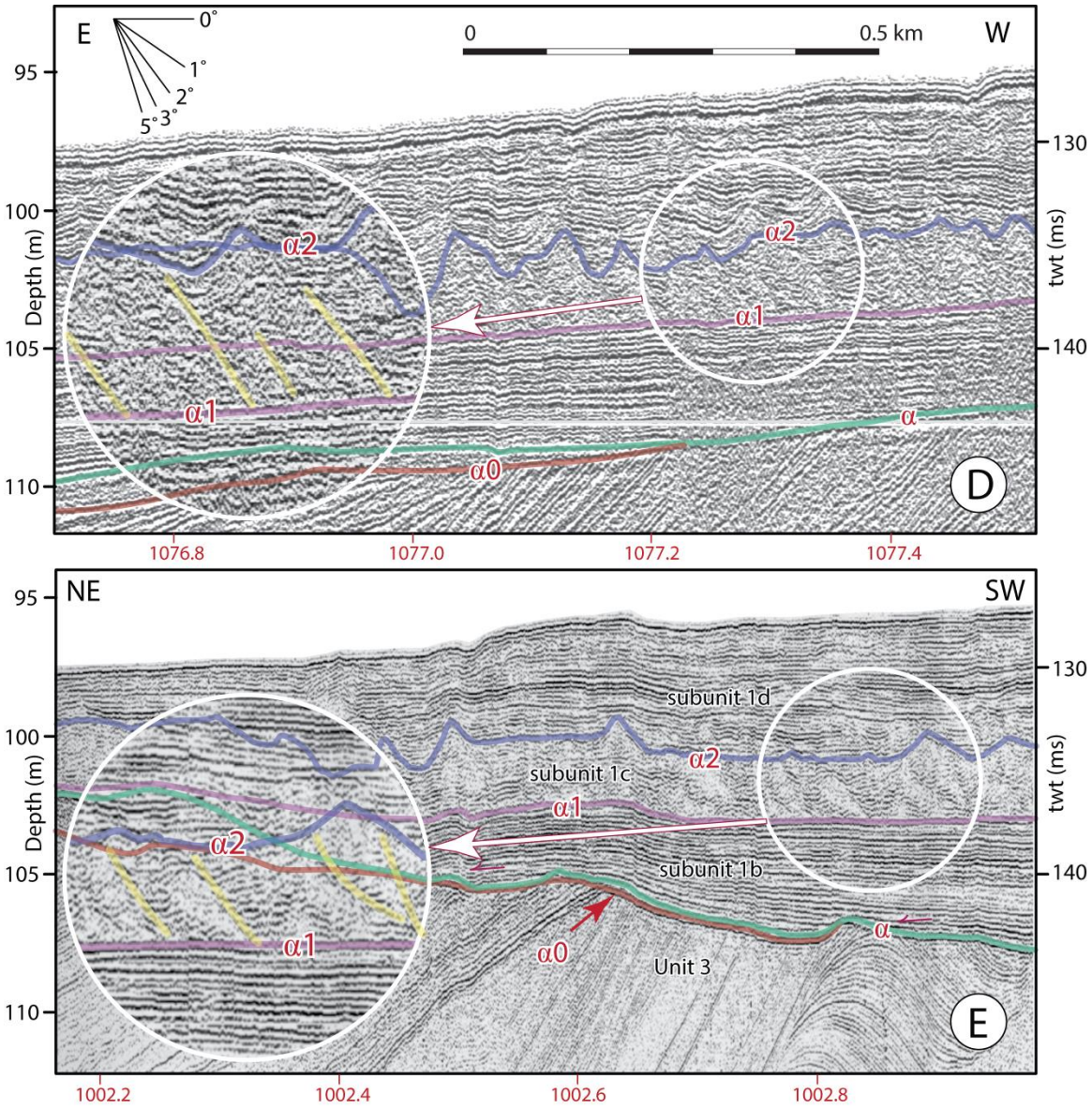

Figure 3.6. Huntec DTS seismic reflection profiles D and E showing the seismic stratigraphic architecture of subunit 1c across the northwestern sector of the study area. Note the west (D) and southwest (E) inclined seismic architecture of the unit, interpreted as growth patterns of mollusc colonies (explained in the text). Water depth and sediment thicknesses are calculated using an acoustic velocity of 1500 m s^{-1}. Red numbers with vertical ticks are navigation fix positions. Location is given in Figure 2.1.

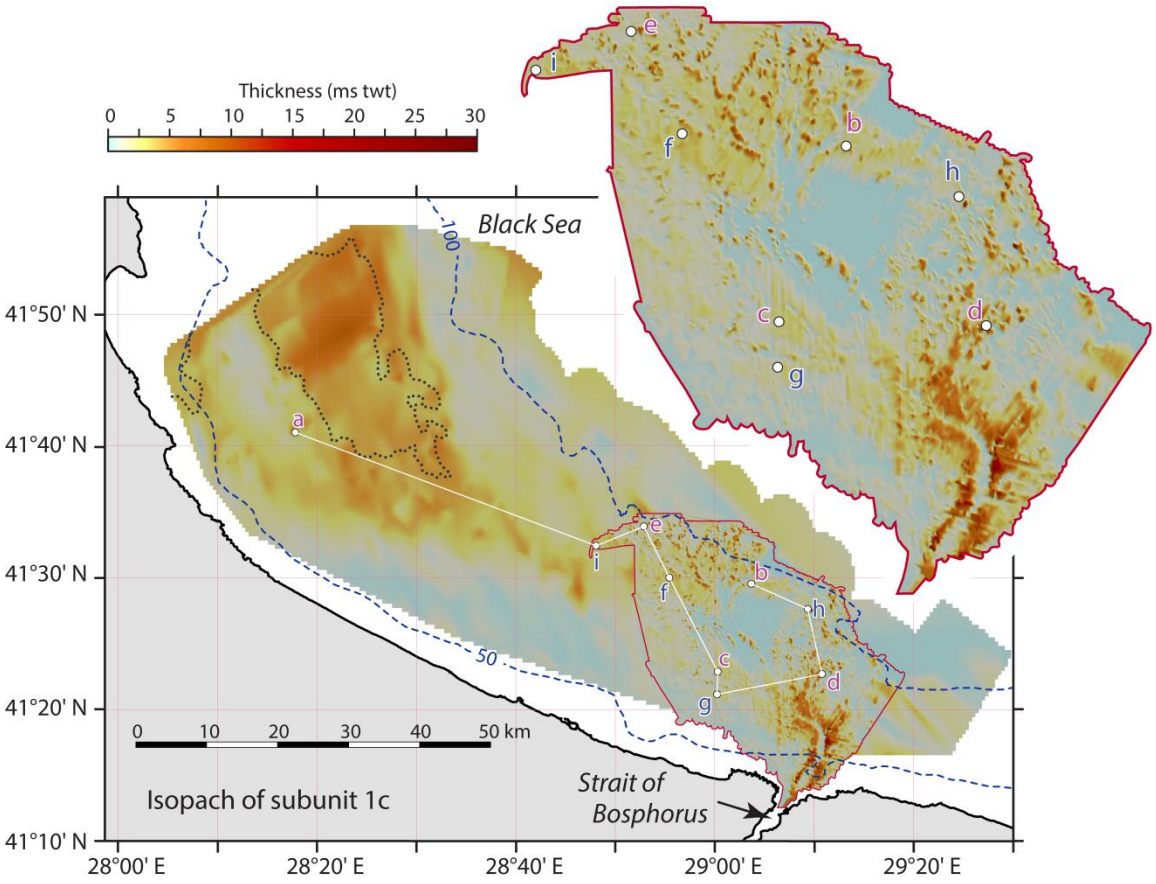

Figure 3.7. Isopach map of the middle Holocene subunit 1c (in ms twt) across the southwestern Black Sea. Coastline and rivers are from NOAA National Geophysical Data Center (http://www.ngdc.noaa.gov/mgg/shorelines/shorelines.html). The data are contoured using Global Mapper v14. The –50 m and –100 m isobaths are from IOC (1981). Small white circles are composite key and reference cores discussed in the text.

3.1.5. Seismic stratigraphic subunit 1d

Subunit 1d is present almost everywhere at the modern seabed, and so it belongs to the contemporary highstand systems tract (Aksu et al., 2002a). It is characterized by a strongly reflective, laterally continuous package of high-frequency reflections. The base of the subunit shows subtle and gradual onlap over the α2 unconformity (e.g., Fig. 3.11). In some areas, large stretches of the seafloor are erosional with reflector truncation at the

sediment-water interface, such as east of the saline channel system in water depths of 80–90 m (Flood et al., 2009, their figure 7).

The regional distribution of subunit 1d resembles that of subunit 1c (Fig. 3.8). There is a prominent northwest–southeast-trending arcuate tongue in the northwestern sector of the study area where subunit 1d is 10–15 ms thick (7.5–11.25 m @ 1500 m s^{-1}; Fig. 3.8). The subunit narrows toward the southeast, becoming largely confined to mid-shelf areas and thinning to <7 ms around the western margin of the saline underflow channel. There is also a narrow but relatively thick sediment accumulation immediately northeast of the present-day coastline around the –50 m isobath (Fig. 3.8), which is separated from the prominent thick arcuate accumulation by a northwest–southeast-trending zone of very thin subunit 1d sediments. Farther to the southeast, there is a very local accumulation of subunit 1d immediately north of the Strait of Bosphorus on the eastern and western levées of the saline channel system (Fig. 3.8). The floor of the saline underflow channel in this area is barren of subunit 1d sediment.

3.2. Allostratigraphy and lithological makeup of cores

The key seismic reflections (i.e., α0, α, α1 and α2) are acoustic returns from unconformities, passing laterally (and locally) into correlative disconformities/paraconformities or correlative surfaces with no perceptible break in deposition, but nevertheless with a relatively strong impedance contrast to explain good reflection strength and continuity. The sediments themselves can be viewed, therefore, as laterally extensive units and subunits separated by these unconformities and their correlative surfaces. Hence, each sedimentary unit or subunit conforms to the definition of

an allostratigraphic unit (henceforth 'allounit'). The North American Commission on Stratigraphic Nomenclature (2005) defines an allostratigraphic unit as "a mappable body of rock that is defined and identified on the basis of its bounding discontinuities".

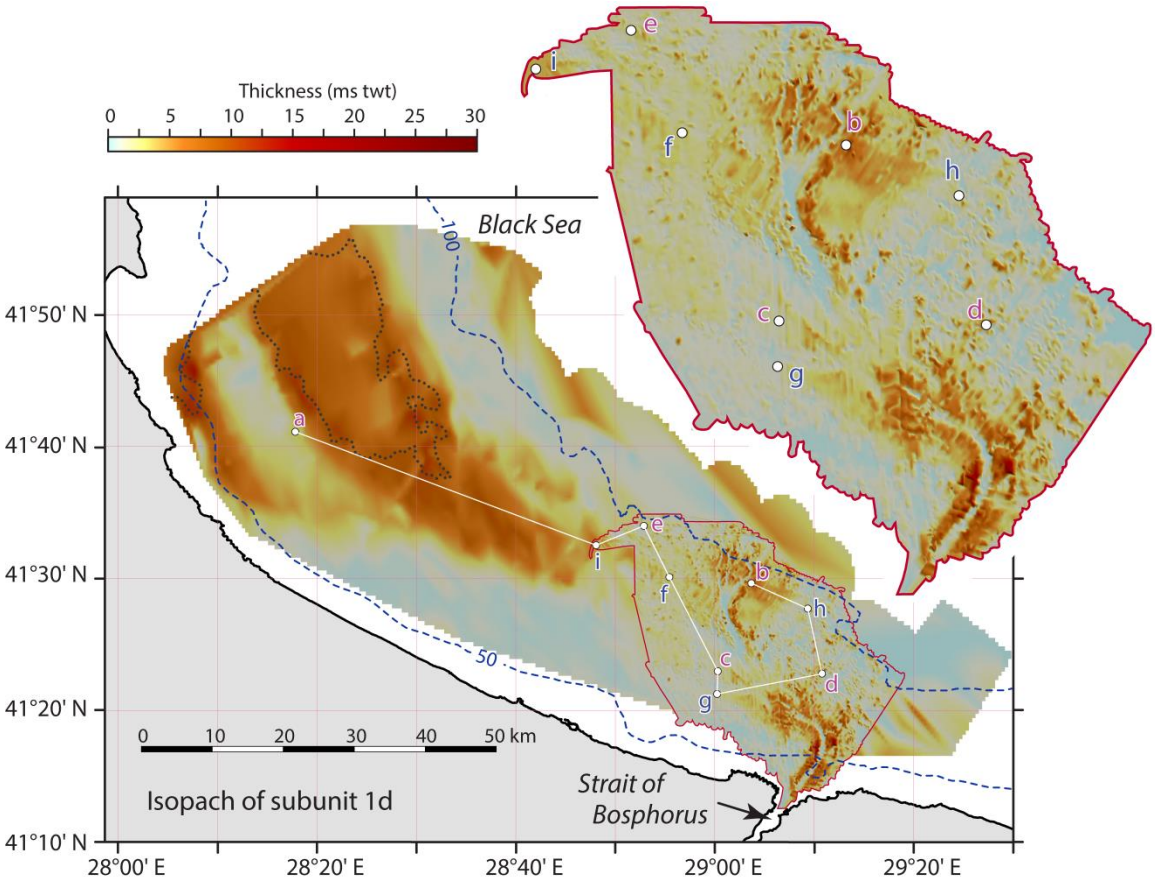

Figure 3.8. Isopach map of the upper Holocene subunit 1d (in ms twt) across the southwestern Black Sea. Coastline and rivers are from NOAA National Geophysical Data Center (http://www.ngdc.noaa.gov/mgg/shorelines/shorelines.html). The data are contoured using Global Mapper v14. The –50 m and –100 m isobaths are from IOC (1981). Small white circles are composite key and reference cores discussed in text.

Physical, chemical and paleontological characteristics of an allounit may vary laterally and vertically through the unit (see also Bhattacharya and Posamentier, 1994; Bhattacharya, 2001). The allounits and their subunits recognized in this thesis are informal.

They can be mapped in very high-resolution seismic profiles, but would not be discernible in industry-scale multichannel seismic data.

The seismic stratigraphic units can be 'mapped' one-for-one on to equivalent allounits with identical names because of the nature of the bounding surfaces (i.e., seismic subunit 1c corresponds to sedimentary allounit 1c). The facies and ages of allounits 1b–1d (and locally 1a) can be assessed using cores collected across the study area by supervisors Aksu and Hiscott.

Seventy-two gravity and 25 piston cores were collected from the southwestern Black Sea shelf, mainly concentrated in two critical regions: (a) the northwestern sector of the study area which is oceanographically under the influence of the Bosphorus anticyclonic surface-water gyre, and (b) the area around the saline underflow channel (Figs. 3.9). These two regions exhibit thick blankets of Holocene sediment (Figs. 3.5, 3.7, 3.8). Five key composite cores are emphasized in this thesis. At each key site, a composite stratigraphy was constructed using the lithological descriptions of co-located piston (P), trigger-weight (T) or independently collected gravity cores (G), multi-sensor core logs (where available) and calibrated radiocarbon ages acquired from shells in the cores. The key cores (named in bold) are (a) **M02-45** (composite of M02-45P, M02-45T, M05-03P), (b) **M05-50** (composite of M05-50P, M05-51G), (c) **M11-23** (composite of M11-08T, M11-23P), (d) **M11-16** (composite of M11-15G, M11-16P), and (e) **M05-19** (composite of M05-19P, M05-19T) (Fig. 3.9). Four additional long composite reference cores with few or no radiocarbon dates are used to further constrain the character of the various allounits: (f) M11-29G/M11-30P, (g) M11-09T/M11-22P, (g)M11-29G/M11-30P, (h) M05-

44G/M05-44P, and (i) M05-22T/M05-22P (Fig. 2.1). Summary characteristics of key and reference cores are presented in Table 3.1, and the correlation of allounits between the five key core sites is presented in Figure 3.9.

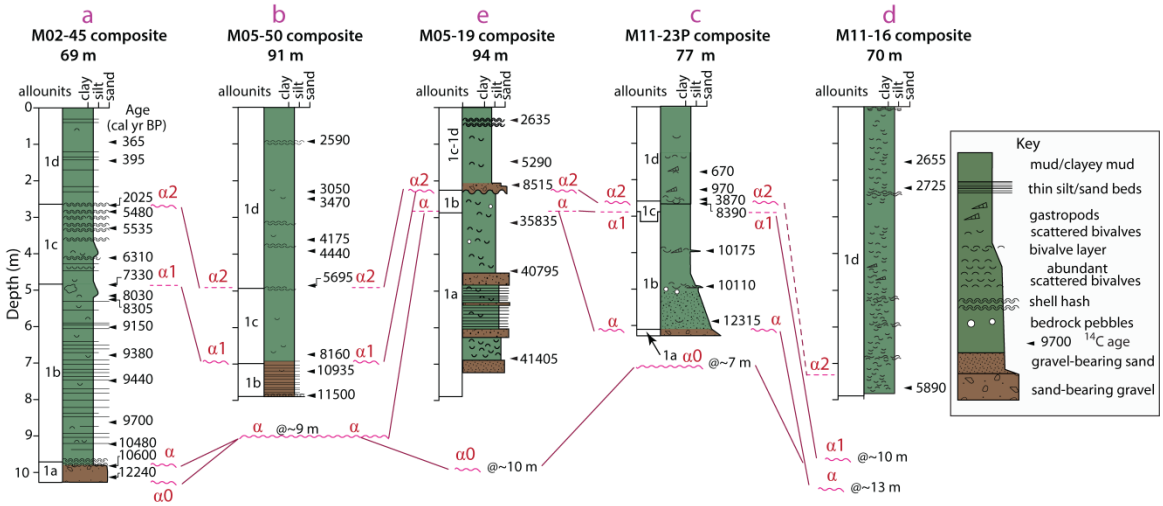

Figure 3.9. Allostratigraphy of the key cores across the southwestern Black Sea. α0 and α are major shelf-crossing unconformities, whereas α1 and α2 are unconformities and their correlative disconformities/conformities. Numbers with horizontal arrow-heads are radiocarbon ages given as calendar years before present, cal yr BP (see Table 3.2 for data). Locations are shown in Figure 2.1.

The North American Commission on Stratigraphic Nomenclature (2005) recommends the specification of type sections for allostratigraphic units. The vicinity of core M02-45 is selected as the type area for allounits 1d, 1c and 1b, and for bounding surface α2. The vicinity of core M05-50 is proposed as a reference section/area for allounit 1b and the type area for bounding surface α1. Core M05-19 provides a type section for allounit 1a. Bounding surface α0 directly overlies tilted, consolidated or lithified sediments of mainly Unit 3, and has not been sampled.

The primary descriptions of all cores presented in the thesis were completed by thesis supervisors Aksu and Hiscott prior to the start of the thesis research. Several cores

had magnetic susceptibility measured prior to splitting to assist assessment of core-top losses in the piston cores, using a Bartington™ MS2E point sensor integrated into a Geotek™ Model 95 multi-sensor core logger. Cores M02-45P and M05-50P have been subjected to various multi-proxy and paleontological analyses (Hiscott et al., 2007b, 2010; Marret et al., 2009; Bradley et al., 2012; Mertens et al., 2012; Lister et al., 2015; Williams et al., 2018; Ankindinova et al., 2019a,b) whereas the other cores described below have not been described in open literature or used for stratigraphic studies.

Table 3.1. Summary characteristics of key and reference cores. α1 and α2 surfaces at the sites are either conformities (C) or unconformities (U).

Core identifier	**Water**	**Allounit thickness (cm)**				**Character**	
Key cores	**depth (m)**	**1d**	**1c**	**1b**	**1a**	**α2**	**α1**
M02-45 (M02-45T, M02-45P, M05-03P)	69	265	220	490	55	U	C
M05-50 (M05-50P, M05-51G)	91	490	208	92	---	C	U
M11-23 (M11-08T, M11-23P)	77	260	28	322	19	U	U
M11-16(M11-15G, M11-16P)	70	795	---	---	---	C	--
M05-19 (M05-19T, M05-19P)	94	160	50	20	560	U	U
Reference cores							
M11-30 (M11-29G, M11-30P)	83	133	349	---	240	U	U
M11-22 (M11-09T, M11-22P	75	100	135	93	---	U	U
M05-22 (M05-22T, M05-22P)	86	445	145	144	---	U	U
M05-44 (M05-44T, M05-44P)	82	970	---	---	---	C	--

3.2.1. Composite key core M02-45

Core M02-45P, its trigger-weight gravity core M02-45T and core M05-03P were collected from the middle shelf in 69 m of water (a in Fig. 2.1.). A detailed description of

the full 1028 cm-long composite core M02-45 has been published by Williams et al. (2018). The allostratigraphy of the core is summarized below. Four allounits are recognized (Figs.3.9, 3.10). The oldest allounit 1a extends from the base of the core to 970 cm composite depth. The base of the allounit must be very close to the seismic reflector α0 (α in Williams et al., 2018; Fig. 3.10). The lowermost 10 cm of allounit 1a consists of mud with scattered pebbles and cobbles, and is succeeded by alternating horizons of sandy mud, shell hash and very coarse sand and gravel. Allounit 1b extends from 970 cm to a composite depth of 480 cm. Its top correlates to seismic reflector α1 which is a conformable surface at this site, or potentially a subtle disconformity or paraconformity with no discernible hiatus at the resolution of the available radiocarbon dates (Figs. 3.9, 3.10). Allounit 1b consists of colour-banded mud with graded laminae and 0.5–2.5 cm-thick graded beds of silt to very fine sand (Fig. 3.10), and scattered shells of *Euxinipyrgul*a sp., *Theodoxus* sp., *Monodacna pontica*, *Didacna* spp., *Dreissena polymorpha* and *D. rostriformis* (Hiscott et al., 2010). It was designated as lithologic Unit C by Hiscott et al. (2007b); those authors divided the unit into subunit C1 below 615 cm and subunit C2 above that depth based on geochemistry. Allounit 1c extends upward from 480 cm to 270 cm, the latter just below a <5 cm-thick shelly horizon which correlates in seismic profiles to unconformity α2. This allounit consists of alternating horizons of mud and shelly mud (Figs. 3.9, 3.10). The abundance of bioclastic sand locally exceeds 20%. The mollusc assemblage includes *Mytilus galloprovincialis*, *Abra alba*, *Euxinipyrgul*a sp., *Parvicardium exiguum*, *Rissoa* sp. and *Modiolus phaseolinus* (Hiscott et al., 2007b). *M. galloprovincialis* and *A. alba* dominate the shelly layers in the upper part of the allounit. Allounit 1d represents the youngest sediments in the composite core. It consists of colour-mottled/banded, burrowed

mud with silt laminae and scattered shells of several immigrant Mediterranean molluscs: *Bittium reticulatum, Spisula subtruncata, Acanthocardia paucicostata, A. alba, M. galloprovincialis* and *Turritella communis*.

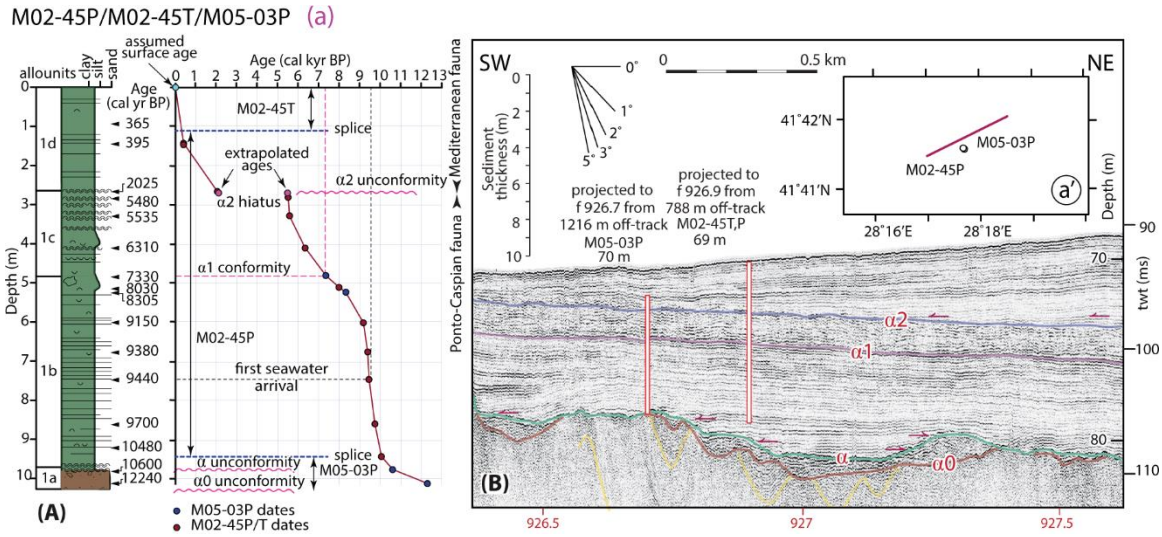

Figure 3.10. **(A)** Simplified stratigraphy of composite core M02-45 showing the positions of the allounits (discussed in text) and radiocarbon dates (shown as calendar years before present, cal yr BP). The age versus depth plot shows the 3025-year hiatus at the α2 unconformity in this core. Note that the α2 reflector is a local unconformity at core site M02-45, whereas the α1 reflector is a conformable surface at this core site. Key to core description is given in Figure 3.9. Locations are shown in Figure 2.1. **(B)** Huntec DTS boomer profile showing the acoustic character of the Holocene sedimentary successions across the southwestern Black Sea and the along-strike projections of core sites M02-45P/T and M05-03P to this line. Reflectors α, α1 and α2 are unconformities discussed in text. Water depth and sediment thicknesses are calculated using an acoustic velocity of 1500 m s^{-1}. Red numbers with ticks are navigation fix positions. Location is shown in the inset. **(C, next page)** Typical facies of allosubunit 1b, site M02-45, showing one sharp-based graded bed of very fine sand to silt with bedding-parallel parting but no clear internal lamination, and several discontinuous silt laminae and beds, partly mixed into surrounding mud by burrowers. **(D, next page)** Concentration of *Mytilus galloprovincialis* shells in allosubunit 1c, site M02-45; interleaved mud is bioturbated. **(E, next page)** Typical homogenized, bioturbated mud of allosubunit 1d at site M02-45; burrow-mottling is very subtle and there are scattered small open tunnels.

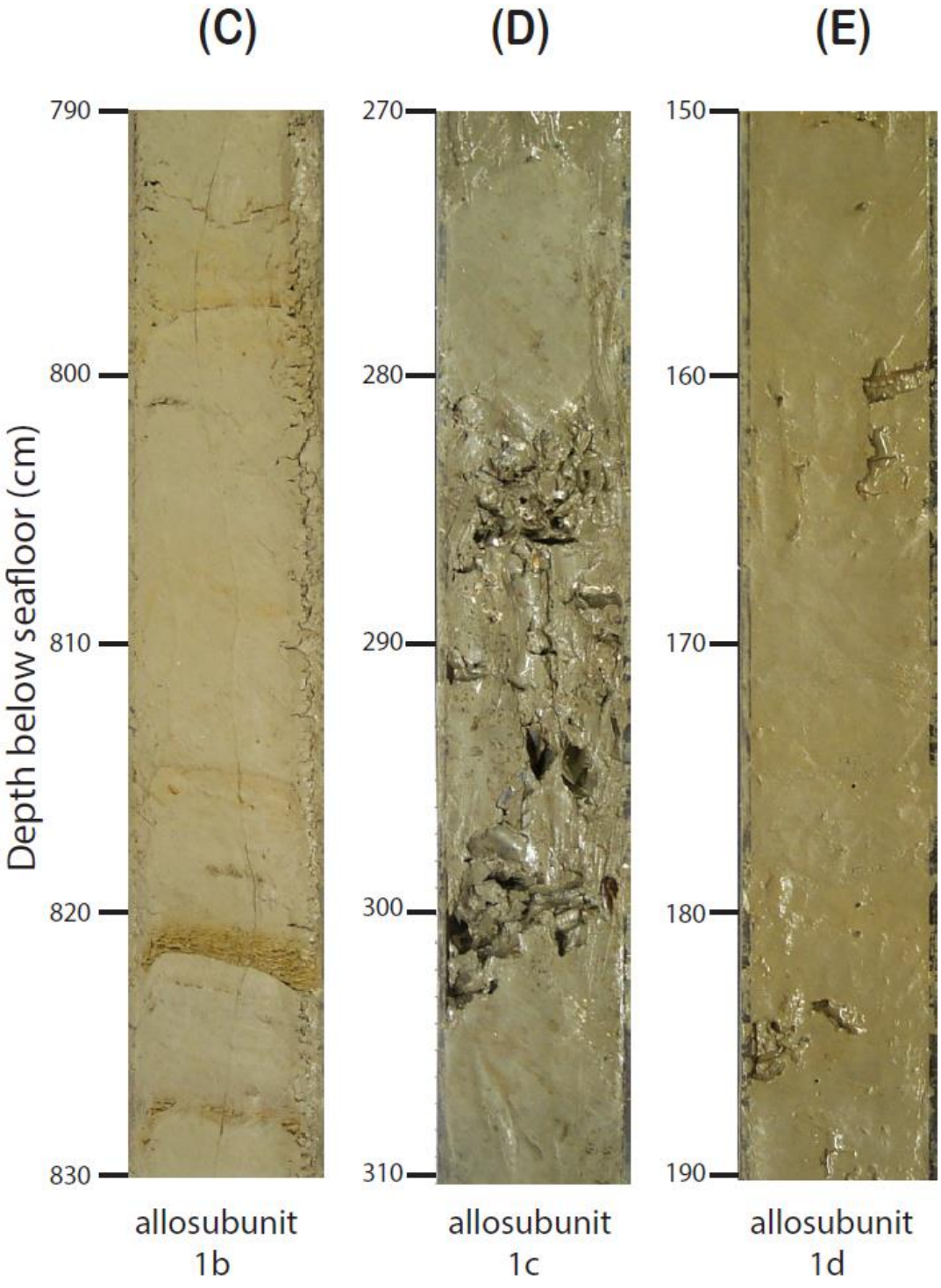
(C)
(D)
(E)
Depth below seafloor (cm)
790
800
810
820
830
270
280
290
300
310
150
160
170
180
190
allosubunit 1b
allosubunit 1c
allosubunit 1d

3.2.2. Composite key core M05-50

Core M05-50P and its nearby gravity core M05-51G were collected from the eastern levée of the saline underflow channel north of the Bosphorus exit (b in Fig. 2.1; Flood et al., 2009; Hiscott et al., 2013). A detailed description of the 787 cm-long composite core is available in Williams et al. (2018). Three allounits are defined. Allounit 1b extends from the base of the composite core to an unconformity at 695 cm depth which corresponds to the α1 reflection in high-resolution seismic data (Figs. 3.9, 3.11).

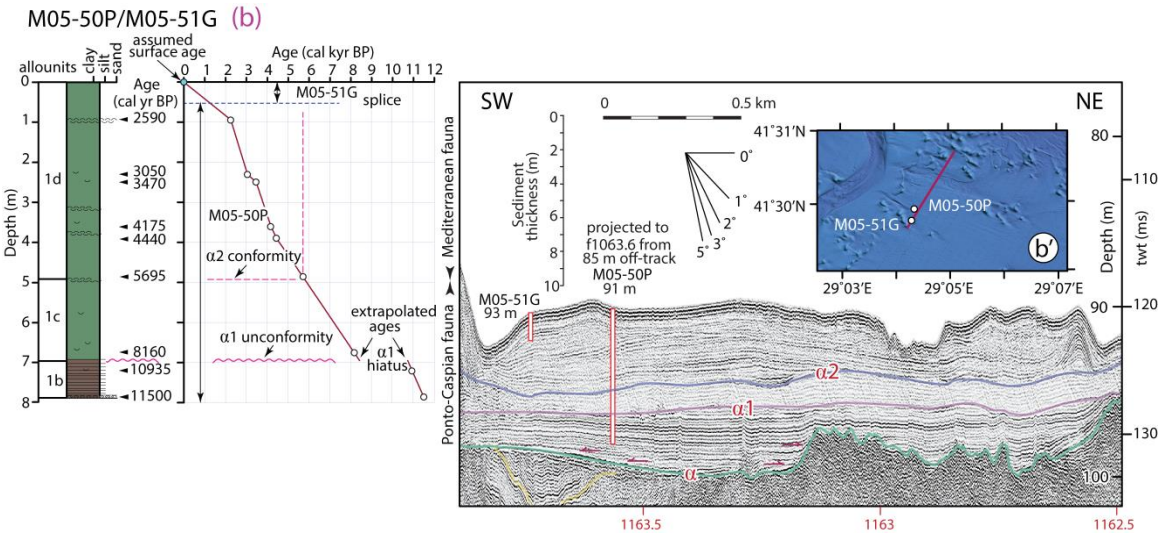

Figure 3.11. **(Left)** Simplified stratigraphy of the composite core M05-50 showing the positions of the allounits (discussed in the text) and radiocarbon dates (shown as calendar years before present, cal yr BP). The age versus depth plots show the 2305-year hiatus at the α1 unconformity in this core. Note that the α2 reflector is apparently a conformable surface at core site M05-50, whereas the α1 reflector is a local unconformity at this core site. Key to core description is given in Figure 3.9. Locations are shown in Figure 2.1. **(Right)** Huntec DTS boomer profile showing the acoustic character of the Holocene sedimentary successions across the southwestern Black Sea and the along-strike projections of core sites M05-50P and M05-51G to this line. Reflectors α, α1 and α2 are unconformities discussed in the text. Water depth and sediment thicknesses are calculated using an acoustic velocity of 1500 m s^{-1}. Red numbers with ticks are navigation fix positions. Location is shown in the inset.

Huntec DTS profiles show clear erosional truncation at the α1 level. Allounit 1b is comprised of interbedded silty mud and graded beds (0.5–2.5 cm thick) of coarse silt to mainly very fine sand, and therefore is almost identical in facies to the same allounit at core site M02-45. The brackish-water bivalve *Dreissena* is abundant in some of the graded beds (Flood et al., 2009). Allounit 1c extends from the α1 unconformity at 695 cm to the α2 conformable surface at 490 cm and consists of moderately bioturbated calcareous silty mud (≤ 10% sand) with a single specimen of the marine gastropod *Cyclope donovania* at 513 cm core depth. Allounit 1d extends from 490 cm composite depth to the core top, and is also bioturbated calcareous silty mud, transitioning to colour-banded silty mud in the upper 95 cm (Figs. 3.9, 3.11). There are scattered marine mollusc shells identified as *Mytilus galloprovincialis*, *Spisula subtruncata*, *Cyclope donovania* and *Abra alba*.

3.2.3. Composite key core M11-23

Trigger-weight core M11-08T and piston core M11-23P were acquired from 77 m water depth in an area of unconfined saline underflow just west of the saline channel complex (Fig. 3.12). This location beneath a persistent saline bottom-hugging gravity current (~0.5 m s^{-1}; Hiscott et al., 2013) surely accounts for the thick wavy-bedded deposits above α2. Allounit 1a forms the lowermost 18 cm of the core and is undated. The sediment consists of pebble-sized gravel with rounded clasts to 3 cm diameter, rare broken (reworked) shells and sand matrix. Based on the associated seismic profile (Fig. 3.12), allounit 1b extends from 607 cm to 290 cm composite depth, but there is no obvious facies change in the core at the inferred top of the allounit. Nevertheless, truncation of seismic reflectors at α1 indicates that there must be an unconformity at this level. From 490 cm to

290 cm depth, allounit 1b consists of burrowed calcareous silty mud. A 2 cm-thick shelly layer at 395 cm depth contains brackish-water fauna (*Dreissena* sp., *Theodoxus* sp.); a similar layer interrupts the muddy succession at ~495 cm depth. Below this, to 607 cm depth, the sediment consists of downward-coarsening sand (fine sand to granule grade) with scattered pebbles and rare shell fragments.

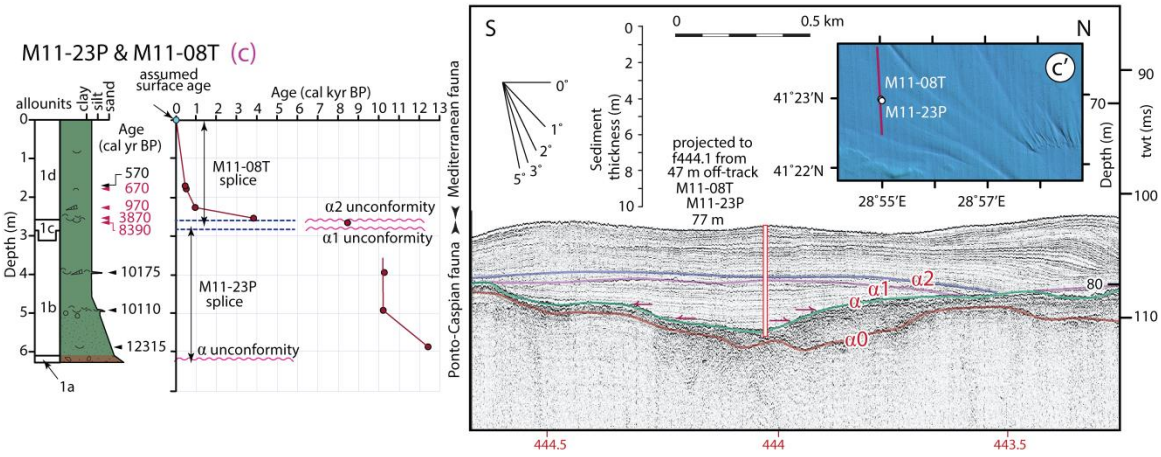

Figure 3.12 **(Left)** Simplified stratigraphy of the composite core M11-23 showing the positions of the allounits (discussed in the text) and radiocarbon dates (shown as calendar years before present, cal yr BP). The composite core is constructed using the lithologies and ^{14}C dates (red numbers) from the near co-located gravity core M11-08G. Note that there is ~4520-year hiatus at the α2 unconformity, whereas α1 is a conformable surface at this core site. Key to core description is given in Figure 3.9. Locations are shown in Figure 2.1. **(Right)** Huntec DTS boomer profile showing the acoustic character of the Holocene sedimentary successions across the southwestern Black Sea and the along-strike projections of core sites M11-23P and M11-08G to this line. Reflectors α, α1 and α2 are unconformities discussed in the text. Water depth and sediment thicknesses are calculated using an acoustic velocity of 1500 m s^{-1}. Red numbers with ticks are navigation fix positions. Location is shown in the inset

Allounit 1c is thin in the seismic profile and is correlated to 290–260 cm depth in the composite core. There is subtle erosional truncation at α2 in the associated seismic profile (Fig. 3.12); a hiatus of ~4000 years based on radiocarbon ages confirms this break in sedimentation. The allounit consists entirely of bioturbated calcareous silty mud.

Monodacna sp. and *Dreissena* sp. are present. *Chondrites* burrows are abundant. Allounit 1d begins at 260 cm in the composite succession, extends to the core top and is younger than ~4.0 cal ka. It consists of bioturbated, colour-mottled to subtly colour-banded calcareous silty mud with *Chondrites* burrows and mostly scattered Mediterranean species of molluscs (*Abra alba*, *Mytilus galloprovincialis*, *Nuculana commutata*, *Cyclope donovania*).

3.2.4. Composite key core M11-16

Gravity core M11-15G and piston core M11-16P were raised from the crest of a levée associated with an active secondary saline underflow channel (Fig. 3.13).

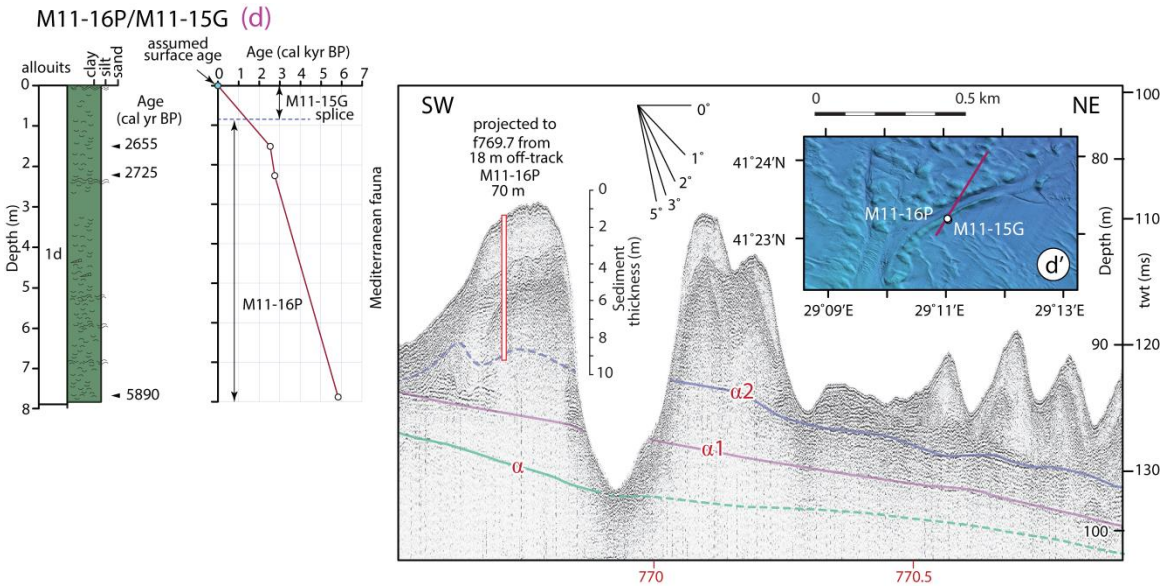

Figure 3.13**. (Left)** Simplified stratigraphy of the composite core M11-16 showing the positions of the youngest allounit (discussed in the text) and radiocarbon dates (shown as calendar years before present, cal yr BP). The composite section is constructed splicing 80 cm from the co-located gravity core M11-15G. Note that the α2 and α1 reflectors are not penetrated at this core site. Key to core description is given in Figure 3.9. Locations are shown in Figure 2.1. **(Right)** Huntec DTS boomer profile showing the acoustic character of the Holocene sedimentary successions across the southwestern Black Sea and the along-strike projections of core sites M11-16P and M11-15G to this line. Reflectors α, α1 and α2 are unconformities discussed in the text. Water depth and sediment thicknesses are

calculated using an acoustic velocity of 1500 m s^{-1}. Red numbers with ticks are navigation fix positions.

This secondary channel extends northward from a crevasse in the right-hand levée of the main saline underflow channel ~12 km from the Bosphorus exit (Flood et al., 2009; Hiscott et al., 2013). The sediments are entirely younger than 6.0 cal ka. Seismic data suggest that the very base of the core might have penetrated to the α2 level, although there is no facies change to support a break in sedimentation. For all practical purposes, the entire core can be considered as representative of allounit 1d at this location. In the upper ~250 cm of the composite core, calcareous silty mud contains clusters of large articulated bivalves, mainly *Mytilus galloprovincialis*. The remainder of the core consists of alternating shell-rich and mud-rich (but still shell-bearing) horizons. Some levels contain 50–70% mollusc shells, mainly *Mytilus galloprovincialis*, but also *Trophon muricatus*, *Cyclope donovania*, *Parvicardium exiguum*, and *Mysia undata*.

3.2.5. Composite key core M05-19

Piston core M05-19P and its associated trigger-weight core M05-19T were acquired near the shelf edge in an attempt to recover sediments from a buried shelf-edge channel in 94 m of water (Fig. 3.14). The channel fill is at an elevation below –100 m, so might have remained below the level of the Neoeuxine Lake even at its LGM lowstand. The core-to-seismic correlation for this core site is difficult. Radiocarbon dates suggest no core-top loss, yet a sharp facies change to gravel at 209–230 cm core depth is inconsistent with this being the α0 surface, which was initially expected to lie at a seismic depth of ~410 cm. Instead, it is believed that the gravel rests on a merged, composite α/α1/α2 unconformity

(Fig. 3.14), with multiply reworked pebbles and encrusted shells below that level and down to the top of the channel fill, found at 453 cm in the core (so somewhat offset from the apparent seismic depth). As interpreted, allounit 1a includes both the channel fill (here called 1a1) and an overlying tapered veneer (called 1a2) that is separated from the channel fill by a prominent truncation surface within allounit 1a.

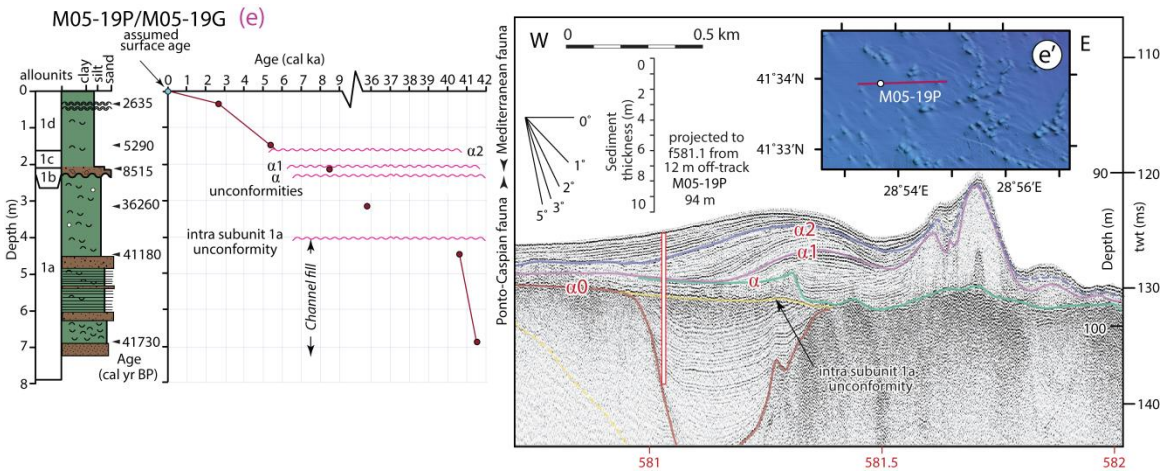

Figure 3.14. **(Left)** Simplified stratigraphy of the composite core M05-19 showing the positions of the allounits (discussed in the text) and radiocarbon dates (shown as calendar years before present, cal yr BP). The composite section is constructed using the lithologies and ^{14}C dates from the trigger weight core M05-19T. Note that at this core site the α2, α1 and α unconformities nearly converge. Also note that there is a prominent intra-allounit 1a unconformity at the core site. Key to core description is given in Figure 3.9. Locations are shown in Figure 2.1. **(Right)** Huntec DTS boomer profile showing the acoustic character of the Holocene sedimentary successions across the southwestern Black Sea and the along-strike projections of core sites M05-19P and M05-19T to this line. Reflectors α, α1 and α2 are unconformities discussed in the text. Water depth and sediment thicknesses are calculated using an acoustic velocity of 1500 m s^{-1}. Red numbers with ticks are navigation fix positions.

Allounit 1a1 consists of alternating thin to medium beds of medium-grained sand to fine-grained muddy sand, and sandy mud with frequent very thin graded beds and laminae of fine-grained sand and silt. Overall, this interval from the base of the core to 453 cm is very sand-prone. From 453 cm to 230 cm (allounit 1a2), the sediment consists of

shell-rich, pebble-bearing sandy mud. The shells are heavy, robust, specimens of *Didacna praetrigonoides*, commonly encrusted by calcareous red algae. There are also many *Dreissena polymorpha* shells. Some of the encrusted bivalves are articulated.

Allounit 1d (209 cm core depth to core top) consists of subtly colour-mottled, bioturbated silty mud with a few thin horizons having concentrations of small bivalves, including *Cerastoderma lamarcki* and *Mactra corallina*. This site is the provisional type locality for allounit 1a, but it is not necessarily typical of more typical of thinner, more lenticular occurrences on the middle shelf. More core sites are needed to confirm what might be a typical facies. It is worth mentioning, however, that reworked material on the α surface where it is exposed on the floor of the saline underflow channel consists of a very similar mixture of sand, pebbles and large reworked bivalves (Aksu et al., 2002a, their plate I).

3.2.6. Composite reference core M11-30

Piston core M11-30P and its associated gravity core M11-29G were acquired in 83 m of water on the landward side of a shore-parallel ridge ~7 km west of the main saline underflow channel (Fig. 3.15). Magnetic-susceptibility profiles indicate 60 cm core-top loss in the piston core. The shore-parallel ridge developed because of erosion of allounit 1b beneath the α1 unconformity, with younger allounits draping the erosional relief. The composite core is 715 cm long. The oldest sediment in the core is an ~1 m-thick coquina straddling the shelf-crossing, transgressive α unconformity. This coquina forms the basal ~1/3 of allounit 1b. The bivalve shells are mostly strongly fragmented to <5 mm size, except for scattered large worn speciments of *Didacna* spp. There are rounded quartz pebbles toward the base. The remainder of allounit 1b up to a composite core depth of 481

cm consists of burrowed calcareous silty mud. The predominant trace fossil is *Chondrites*. Allounit 1c (481–133 cm depth) has a basal bioclastic sand with silty mud matrix, ~15 cm thick, resting on the α1 unconformity. There are a few *Modiolus* sp. mussel shells in the sand, implying a basal age of no more than ~7.5 cal ka (cf. Ryan et al., 1997).

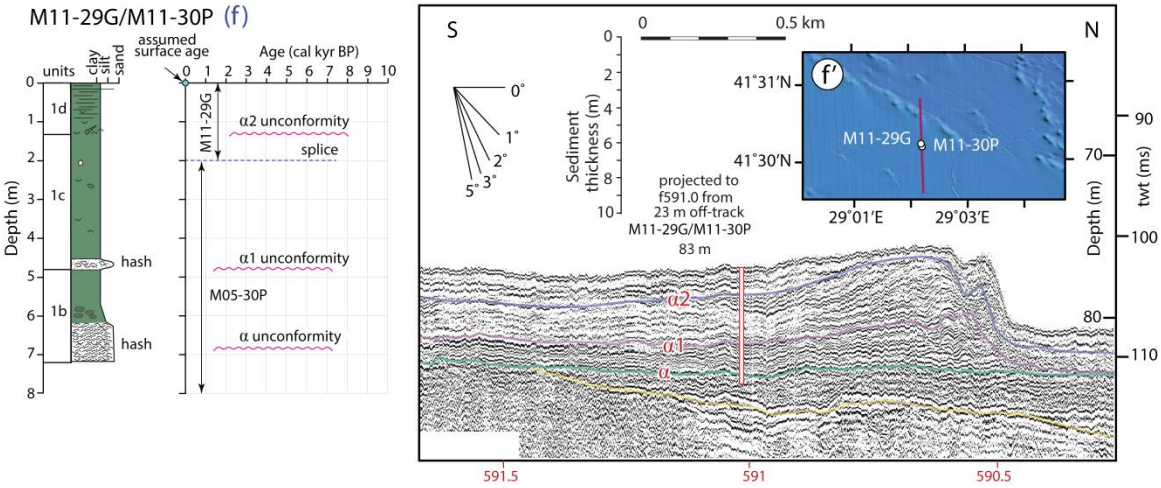

Figure 3.15. **(Left)** Simplified stratigraphy of the composite core M11-30 showing the positions of the allounits. The composite section is constructed using the lithologies from the separate gravity core M11-29G. Key to core description is given in Figure 3.9. Locations are shown in Figure 2.1. **(Right)** Huntec DTS boomer profile showing the acoustic character of the Holocene sedimentary successions across the southwestern Black Sea and the along-strike projections of core sites M11-29G and M11-30P to this line. Reflectors α, α1 and α2 are unconformities. Water depth and sediment thicknesses are calculated using an acoustic velocity of 1500 m s^{-1}. Red numbers with ticks are navigation fix positions. Location is shown in the inset.

The remainder of allounit 1c is bioturbated calcareous silty mud with rare marine bivalve shells, including articulated *Abra alba* and *Corbula gibba*. Allounit 1d (133 cm to core top) is burrow-mottled, subtly colour-banded, calcareous silty mud with spaced clusters of euryhaline bivalves (*Mytilus galloprovincialis, Spisula subtruncata, Parvicardium exiguum*) and gastropods (*Cyclope donovania*).

3.2.7. Composite reference core M11-22

Piston core M11-22P is paired with nearby gravity core M11-09T, the latter acquired during an earlier attempt to sample the sedimentary succession at this site. These cores were acquired 49 m apart in 75 m water ~5 km west of the main saline underflow channel, and landward of a prominent ridge along an erosional shore-parallel high beneath the α unconformity (Fig. 3.16). Today, this ridge splits overspilling saline bottom water into two threads which have an ~3 m difference in surface elevation just west of the M11-22 site (Hiscott et al., 2013, their fig. 16B). The relief was also present during the Holocene transgression of the southwestern shelf. Core-top loss (from radiocarbon dates, facies and magnetic susceptibility) is 40 cm.

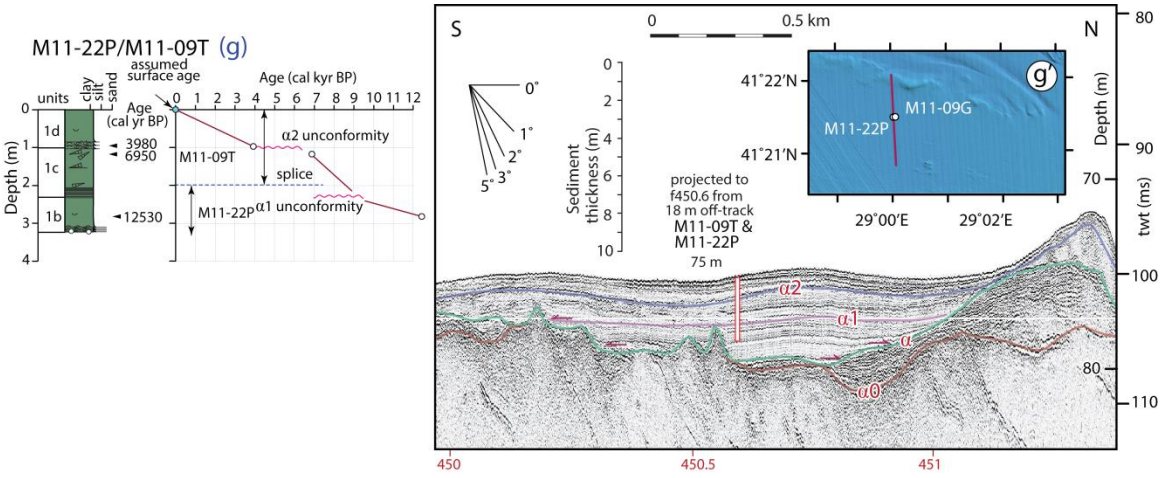

Figure 3.16. **(Left)** Simplified stratigraphy of the composite core M11-22 showing the positions of the allounits and radiocarbon dates (shown as calendar years before present, cal yr BP). The composite section is constructed using the lithologies and ^{14}C dates from the trigger weight core M11-09T and M11-22P. Note that at this core site the α1 and α2 are unconformities. Locations are shown in Figure 2.1. **(Right)** Huntec DTS boomer profile showing the acoustic character of the Holocene sedimentary successions across the southwestern Black Sea and the along-strike projections of core sites M11-09T and M11-22P to this line. Reflectors α, α1 and α2 are unconformities discussed in the text. Water depth and sediment thicknesses are calculated using an acoustic velocity of 1500 m s−1. Red numbers with ticks are navigation fix positions.

Allounit 1b forms the basal 88 cm of the composite core (319–231 cm core depth). Seismic profiles (e.g., Fig. 3.16) suggest that this is about half of the total allounit thickness at the site, but the location is very close to bedrock highs (Unit 2 of Aksu et al., 2002a) so caution must be exercised with the tie to the seismic data. Allounit 1b begins at the base of the core with ~20 cm of silty mud interbedded with ~60% sharp-based graded sand layers rich in shell fragments and ~1 cm-diameter quartz pebbles in the lowest sand bed. The remainder of this allounit is silty mud, burrow-mottled (mostly by the trace fossil *Chondrites*), with scattered brackish-water mollusc shells (*Dreissena polymorpha*, *Turricaspia* sp.) and one bedrock pebble floating in the mud. Allounit 1c (231–205 cm core depth) begins with pinstripe-laminated silty mud (1–3 mm laminae) identical to sapropel deposits seen elsewhere in the region. There are a few *Chondrites* burrows in this interval. The remainder of the allounit (205–103 cm core depth) consists of burrow-mottled, locally subtly colour-banded calcareous silty clay with very thin bands of small bivalve shells and scattered grains of bioclastic sand. Shells include *Mytilus galloprovincialis*, *Cyclope donovania* and *Calyptrea chinensis*. *Chondrites* remains the predominant trace fossil.

There is a significant hiatus at the $\alpha 2$ level (103 cm core depth; Fig. 3.16), above which allounit 1d consists of burrow-mottled calcareous silty mud with three sharp-based muddy bioclastic sand layers at the base (103–84 cm depth). Marine molluscs are diverse: *Mytilus galloprovincialis*, *Corbula gibba*, *Gouldia minima*, *Timoclea ovata*, *Cyclopedonovania*, *Trophon muricatus*.

3.2.8. Composite reference core M05-44

Piston core M05-44P and its trigger-weight gravity core M05-44T penetrated the crest of a large conical mound that has been interpreted by Flood et al. (2009) to coincide with a site of fluid venting, perhaps with mud extrusion or intrusion/diapirism (Fig. 3.17).

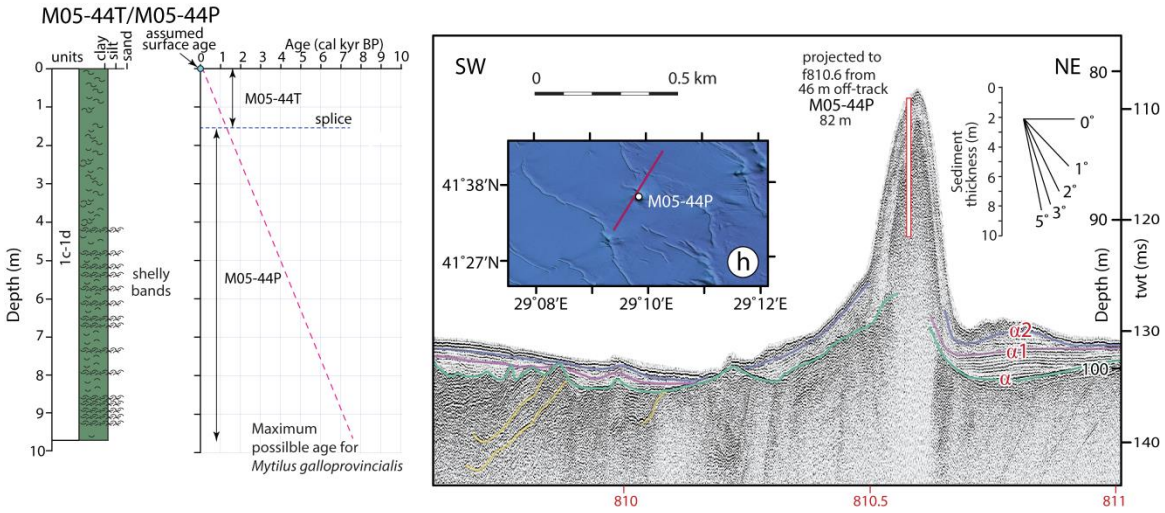

Figure 3.17. **(Left)** Simplified stratigraphy of the composite core M05-44 retrieved from the crestal region of a mud volcano. The composite section is constructed using the lithologies from the trigger weight core M05-44T. Note that all shells encountered in this core are *M. galloprovincialis*, a marine mollusc with a maximum possible age in the Black Sea of ~7.5 cal ka. Locations are shown in Figure 2.1. **(Right)** Huntec DTS boomer profile showing the acoustic character of the Holocene sedimentary successions across the southwestern Black Sea and the along-strike projections of core sites MAR05-44P and MAR05-44T to this line. Reflectors α, α1 and α2 are unconformities discussed in the text. Water depth and sediment thicknesses are calculated using an acoustic velocity of 1500 m s−1. Red numbers with ticks are navigation fix positions.

Water depth at the core site is 82 m whereas the surrounding seabed is ~18 m deeper, emphasizing the large scale of this mound. At a few similar mounds on the southwestern shelf, gas can be seen rising through the water column in high-resolution seismic profiles. Seismic markers cannot be traced with confidence into the centre of these mounds because of blanking by gas in near-surface sediments. The presence of numerous *Mytilis*

galloprovincialis shells from the seabed right to the base of the 970 cm composite core strongly suggests, however, that only allounits 1c and 1d are present, and perhaps only the latter. Magnetic susceptibility measurements indicate ~60 cm core-top loss in the piston core.

Throughout, the sediment is colour-mottled (burrowed) to colour-banded calcareous silty mud with many scattered bivalves above a core depth of ~4 m, and both scattered shells and shell layers/beds deeper in the core, where there are also numerous silt laminae and sand-filled burrows.

3.2.9. Composite reference core M05-22

Piston core M05-22P and its trigger-weight gravity core M05-22T were acquired ~17 km west of the distal distributaries of the saline underflow channel network on the outer shelf, in a water depth of 86 m. Core-top loss in M05- 22P is estimated to be 60 cm from visual descriptions. The only radiocarbon dates are in a basal sand bed (10380±115 cal yr BP for an *in situ* shell; 35065±265 cal yr BP for a shell reworked from below the merged α and α0 unconformities).

The core reached allounit 1b (Fig. 3.18), which has ~10 cm of bioclastic sand at the base followed upward by burrowed silty mud with numerous laminae and very thin beds of graded silt and sand/silt-filled burrows. Mollusc shells are very small (<0.5–1 cm) *Dreissena polymorpha*, *Euxinipyrgula* sp. and *Theodoxus pallasi*. The placement of the α1 surface (~590 cm core depth) is taken from the seismic interpretation with no clear feature in the core to mark this level. Hence allounit 1c (590–410 cm core depth) is lithologically

similar to 1b, with numerous silt/sand laminae and layers rich in comminuted shells, the last of which occur at the top of the allounit (i.e., at the inferred α2 level).

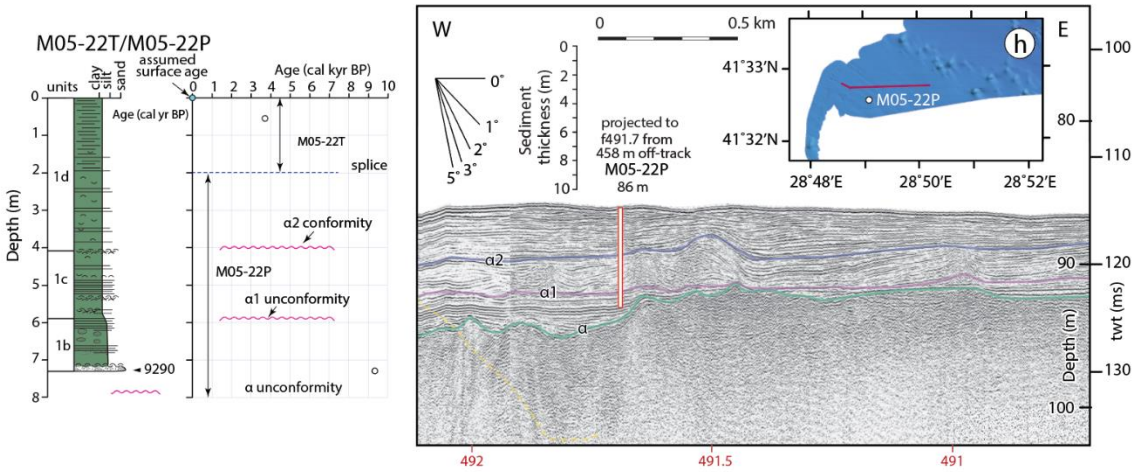

Figure 3.18. **(Left)** Simplified stratigraphy of the composite core M05-22 showing the positions of the allounits and two radiocarbon dates (shown as calendar years before present, cal yr BP). The composite section is constructed using the lithologies from the trigger weight core M05- 22T. Locations are shown in Figure 2.1. **(Right)** Huntec DTSboomer profile showing the acoustic character of the Holocene sedimentary successions across the southwestern Black Sea and the along-strike projections of core sites M05-22P and M05-22T to this line. Reflectors α, α1 and α2 are unconformities discussed in the text. Water depth and sediment thicknesses are calculated using an acoustic velocity of 1500 m s^{-1}. Red numbers with ticks are navigation fix positions.

Below 440 cm composite depth, the shells are brackish-water species *Dreissena polymorpha*, *Euxinipyrgula* sp. and possibly *Dreissena bugensis*, whereas above this depth and into allounit 1d molluscs are euryhaline species *Mytilus galloprovincialis*, *Spisula subtruncata* and *Parvicardium exiguum*. Allounit 1d (410 cm to core top) lacks the many layers of comminuted shells found in deeper sediments, but is otherwise similar to 1c with spaced silt laminae in a background of burrowed calcareous silty mud, and with scattered shells of euryhaline molluscs (Fig. 3.18). Above ~190 cm core depth, there is also subtle to locally better defined colour banding.

3.3. Chronology

Thesis supervisors Aksu and Hiscott provided a total of 56 radiocarbon ages from composite cores M05-50 (13 dates), M02-45 (20 dates), M11-23 (8 dates), M05-19 (9 dates), M11-16 (3 dates) and M11-22 (3 dates; Table 3.2). Eight and thirteen of the uncalibrated dates from M05-50 and M02-45 were originally published by Flood et al. (2009) and Hiscott et al. (2013), respectively. The chronology of the cores is based on 56 radiocarbon dates (Table 3.2), calibrated to calendar years using the Marine13 calibration curve (Reimer et al., 2013) and reservoir ages, *R*, justified in detail by Williams et al. (2018) and Section 2.2.

The temporal and relative spatial arrangements of the four allounits across the southwestern Black Sea plotted alongside relative sea-level curves for the Black Sea (Fig. 19), reveal two important observations: (a) the hiatus at the α unconformity correlates well with the time when the Neoeuxine Lake had been drawn down by evaporation to a level below –100 m (Ryan et al., 2003; Major et al., 2006; Cohen et al., 2011), whereas (b) the hiatuses at the α1 and α2 unconformities developed after the Black Sea was reconnected with the global ocean and its level was above the Bosphorus sill (Hiscott et al., 2002, 2017; Aksu et al., 2016). Thus, the development of the α unconformity can readily be ascribed to subaerial exposure and erosion during and shortly after the last glacial maximum when the Neoeuxine Lake level was low (Ryan et al., 2003; Major et al., 2006; Cohen et al., 2011), modified by ravinement during the post-glacial sea level rise. However, the development of the α1 and α2 unconformities occurring under tens of meters of water after the Holocene transgression was well under way (Fig. 3.19).

Table 3.2. Radiocarbon ages reported as uncalibrated conventional ^{14}C dates in yrBP (half-life of 5568 years; errors represent 68.3% confidence limits). Laboratory numbers with (1) TO prefix = IsoTrace Radiocarbon Laboratory, Accelerator Mass Spectrometry Facility, University of Toronto, (2) BE or BETA prefix = Beta Analytic Inc., Miami Florida, USA, (3) UCIAMS prefix = Radiocarbon Dating Laboratory, Université Laval, via KECK Carbon Cycle AMS Facility, University of California, Irvine (4) OXFORD prefix are University of Oxford Radiocarbon Laboratory, (5) UGAMS prefix = Radiocarbon Dating Laboratory, Université Laval via Centre for Applied Isotope Studies, The University of Georgia. Errors attached to the calibrated calendar years represent 95% confidence limits, but do not account for analytical errors of the ^{14}C dates. Core suffixes G= independent gravity core, P= piston core, T= gravity core as a trigger weight (co-located). Calibrated to calendar years using the Marine13 data set and reservoir ages justified in Williams et al. (2018).

Core	**Depth (cm)**		**Material dated**	**Raw date**		***ΔR***	**Calibrated date**		
	raw	**composite**		**^{14}C yr BP**		**^{14}C yr**	**cal yr BP**		**Lab No:**
MAR 02-45T	92	92	*Spisula subtruncata*	730	±50	+10	365	±50	TO -11433
MAR 02-45T	145	145	*Spisula subtruncata*	770	±50	+10	395	±55	TO-11434
MAR 02-45P	33	143	*Spisula subtruncata*	730	±40	+10	365	±45	TO-11435
MAR 02-45P	158	268	*Mytilus edulis*	2400	±60	+10	2025	±80	TO 11006
MAR 02-45P	174	284	*Mytilus galloprovincialis*	5115	±20	+10	5480	±40	UCIAMS-85907
MAR 02-45P	220	330	*Mytilus edulis*	5190	±50	+10	5535	±55	TO-11436
MAR 02-45P	302	412	*Mytilus galloprovincialis*	5900	±60	+10	6310	±65	TO-11437
MAR 02-45P	406	516	*Monodacna pontica*	7560	±60	–12	8030	±70	TO-11438
MAR 02-45P	495	605	*Euxinipyrgula* spp.	8380	±70	–145	9150	±100	TO-11142
MAR 02-45P	569	679	*Didacna ?praetrigonoides*	8570	±70	–141	9380	±80	TO-11439
MAR 02-45P	639	749	*Didacna* spp.	8620	±70	–143	9440	±70	TO-11440
MAR 02-45P	700	810	sediment (carbonate)	13570	±35		16000		UGAMS-24289
MAR 02-45P	754	864	*Dreissena rostiformis*	8840	±70	–184	9700	±120	TO-11441
MAR 02-45P	810	920	*Dreissena rostiformis*	9370	±70	–234	10480	±100	TO 11007
MAR 02-45P	822	932	*Dreissena polymorpha*	9340	±70	–238	10450	±100	TO-11442
MAR 02-45P	835	945	*Theodoxus* spp.	9070	±70	–127	10010	±115	TO-11443
MAR 05-03P	183	485	*Cardium edule*	6810	±25	+10	7330	±35	UCIAMS-85908
MAR 05-03P	226	528	*Adacna ?laeviuscula*	7785	±25	–42	8305	±45	UCIAMS-85911
MAR 05-03P	342	644	*Monodacna caspia*	8340	±25	–135	9070	±55	UCIAMS-85910
MAR 05-03P	678	980	*Dreissena* spp.	9510	±25	–191	10600	±45	UCIAMS-85909
MAR 05-03P	712	1014	*Dreissena* spp.	10475	±30	–306	12240	±120	UCIAMS-85912

Table 3.2 continued

Composite M05-19									
MAR 05-19G	31	31	*Cerastoderma lamarcki*	2230	±60	+10	1820	±75	TO 12722
MAR 05-19G	132	132	*Mactra corallina*	4390	±50	+10	4535	±80	TO 12723
MAR 05-19P	36	36	*Cerastoderma lamarcki*	2880	±50	+10	2620	±75	TO 12725
MAR 05-19P	149	149	*Mactra coralline*	4960	±60	+10	5285	±95	TO 12724
MAR 05-19P	211	211	white mussels	8070	±60	–58	8605	±90	TO 12726
MAR 05-19P	318	318	*Dreissena r. distincta*	32360	±290	–405	36245	±330	TO 12727
MAR 05-19P	445	445	*Dreissena r. distincta*	36590	±440	–405	41210	±425	TO 12728
MAR 05-19P	556	556	bivalve fragments	32040	±280	–405	35940	±295	TO 12729
MAR 05-19P	685	685	*Dreissena r. distincta*	37260	±430	–405	41745	±325	TO 12730
Composite M05-50									
MAR 05-50P	44	94	*Mytilus galloprovincialis*	2590	±90	+10	2255	±120	TO 13095
MAR 05-50P	180	230	*Mytilus galloprovincialis*	3240	±50	+10	3045	±75	TO 13096
MAR 05-50P	200	250	*Mytilus galloprovincialis*	3590	±15	+10	3470	±35	UCIAMS-96128
MAR 05-50P	279	329	*Mytilus galloprovincialis*	3250	±70	+10	3055	±120	TO 13097
MAR 05-50P	310	360	*Mytilus galloprovincialis*	4130	±20	+10	4175	±45	UCIAMS-96127
MAR 05-50P	340	390	*Mytilus galloprovincialis*	4320	±60	+10	4435	±90	TO 13098
MAR 05-50P	435	485	*Mytilus galloprovincialis*	5330	±70	+10	5695	±80	TO 13099
MAR 05-50P	550	600	foraminifera/ostracod	7710	±40	–50	8235	±55	BETA305920
MAR 05-50P	620	670	foraminifera/ostracod	8540	±50	–110	9320	±70	BETA305921
MAR 05-50P	625	675	foraminifera/ostracod	7570	±40	–12	8040	±60	BETA307981
MAR 05-50P	670	720	*Dreissena polymorpha*	9880	±110	–231	11095	±135	TO 13100
MAR 05-50P	737	785	*Dreissena* spp.	10270	±90	–385	12010	±204	TO 12915
MAR 05-51G	145	145	*Mytilus galloprovincialis*	3280	±60	+10	3095	±95	TO 13101
Composite M11-16									
MAR 11-15G	223	223	*Mytilus galloprovincialis*	2955	±15	+10	2726	±15	UCIAMS-116467
MAR 11-16P	68	208	*Mytilus galloprovincialis*	2865	±10	+10	2640	±45	UCIAMS-116468

MAR 11-16P	689	829	*Mytilus galloprovincialis*	5510	±20	+10	5885	±30	UCIAMS-116469

Table 3.2 continued

Composite M11-22

M11-09T	117	117	*Cyclopes* ?spp.	6470	±20	+10	6950	±40	UCIAMS-116459
MAR 11-22P	51	91	*Spisula subtruncata*	3990	±20	+10	3980	±50	UCIAMS-116470
MAR 11-22P	239	279	*Dreissena rostiformis*	10670	±25	–281	12530	±45	UCIAMS-116471

Composite M11-23

M11-08T	178	178	*Abra alba*	1130	±20	+10	670	±20	UCIAMS-209113
M11-08T	227	227	*Cyclope donovania*	1445	±20	+10	970	±35	UCIAMS-209114
M11-08T	253	253	*Nuculana commutate*	3910	±15	+10	3870	±35	UCIAMS-209117
M11-08T	264	264	*Monodacna pontica*	7870	±20	+10	8390	±25	UCIAMS-116458
MAR 11-23P	45	170	*Cyclopes* spp?	990	±25	+10	570	±30	UCIAMS-116472
MAR 11-23P	270	395	*Cyclopes* spp?	9190	±25	–156	10190	±25	UCIAMS-116473
MAR 11-23P	366	491	*Dreissena polymorpha*	9105	±25	–135	10090	±60	UCIAMS-209118
MAR 11-23P	464	589	*Dreissena polymorpha*	10555	±25	–254	12320	±105	UCIAMS-116474

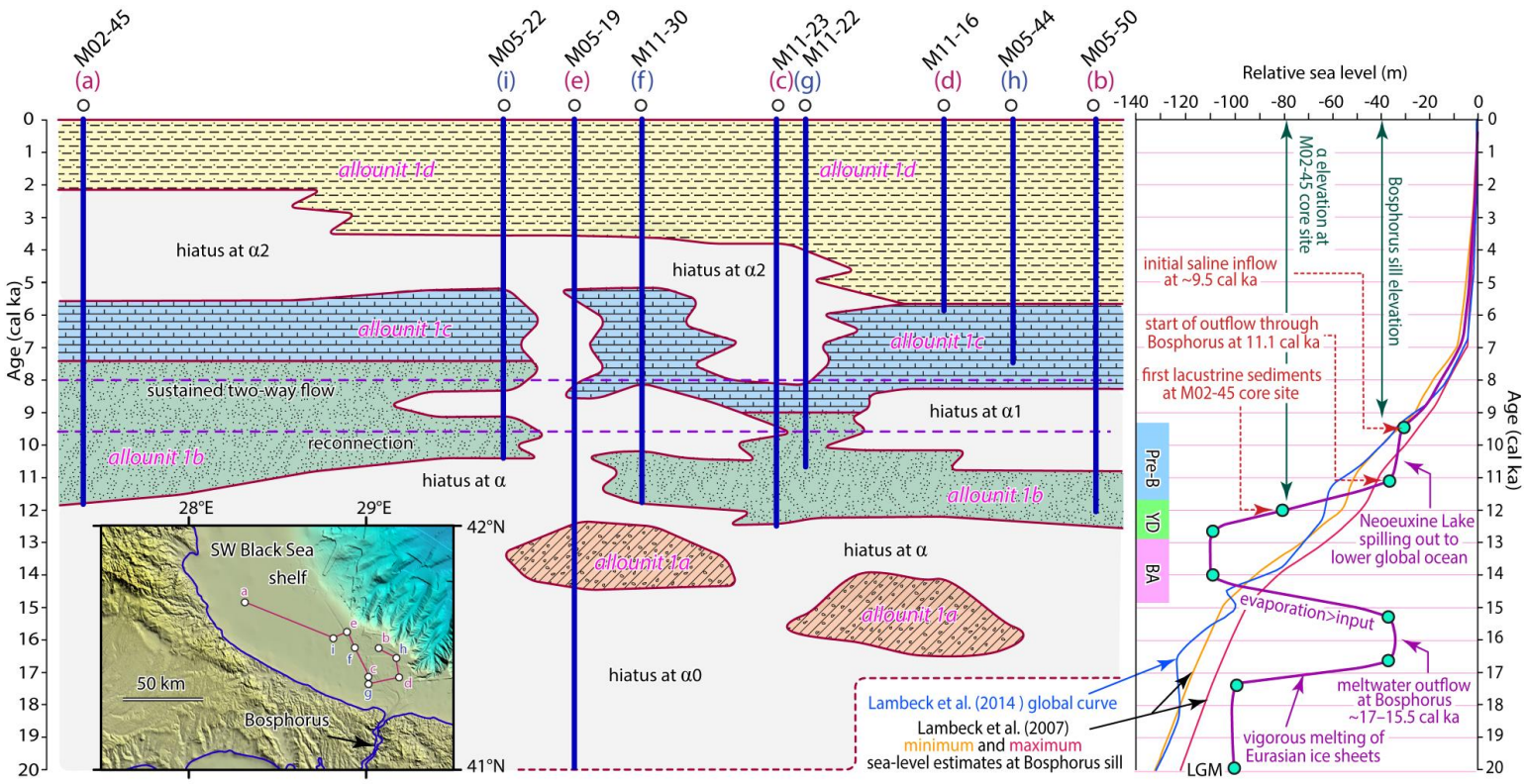

Figure. 3.19. Chronostratigraphic chart, representing the unconformity-bounded sequences across the southwestern Black Sea. The base level curves for the Black Sea, the global ocean and at Bosphorus sill are from Hiscott et al. (2007b), Lambeck et al. (2014) and Lambeck et al. (2007), respectively. The time of reconnection at ~9465 cal yr BP and the development of sustained two-way flow across the Strait of Bosphorus at ~8000 cal yr BP are from Ankindinova et al. (2019a). The evaporative drawdown of the Black Sea is from Ryan et al. (2003), Major et al. (2006) and Cohen et al. (2011). Note that the Bosphorus sill was at –40 m when a salt wedge penetrated sufficiently deeply into the southern end of the strait that bedload supply to the Holocene delta lobe in the northeastern Marmara Sea ceased (from Aksu et al. 2016). Also note that the α unconformity was developed during the low base level associated with the LGM, whereas the α1 and α2 unconformities were developed when the relevant parts of the southwestern Black Sea shelf were fully submerged. Pre-B= Preboreal; YD= Younger Dryas; BA= Bølling–Allerød.

3.4. Interpretation

Subunit 1a is a lowstand systems tract deposit (Aksu et al., 2002a). Landward of the lowstand shoreline, the scattered erosional remnants of this subunit are interpreted to have escaped erosion during the LGM lowstand when the shelf was subaerially exposed, as well as erosion by ravinement during the subsequent latest Quaternary base level rise. Based on the Holocene age of subunit 1b where cored (Hiscott et al., 2007b) and Sr-isotopic evidence within the subunit for reconnection to the global ocean as water levels were rising (Ankindinova et al., 2019a), subunit 1b is interpreted as the lowermost portion of a transgressive systems tract. Subunit 1c constitutes the upper portion of the same TST and accumulated after euryhaline molluscs had invaded the Black Sea. Subunit 1d is present almost everywhere at the modern seabed so belongs to the highstand systems tract (Aksu et al., 2002a).

Once reconnection with the global ocean occurred at ~9.5 cal ka (Yanchilina et al., 2017; Ankindinova et al., 2019a), base level must have coincided with the MIS1 water-level rise in the global ocean (e.g., Lambeck et al., 2007). Why, then, did post-reconnection accumulation over significant portions of the southwestern shelf occur in spurts (upper part of 1b, 1c, 1d) interrupted by widespread hiatuses that must have been generated by subaqueous erosion, since the elevations of α1 and α2 are well below the contemporary water levels?

In the following sections, the conditions that might have controlled net accumulation (or erosion) are considered for each major step of the latest Pleistocene to Holocene transgression.

3.4.1. Development, recognition and timing of unconformities

In a contemporary shallow marine shelf setting, such as the southwestern Black Sea, there is a delicate balance between deposition and non-deposition/erosion. In such a setting, an erosional unconformity will occur if the long term (i.e., decadal–centennial) rate of sediment removal is greater than the rate of sediment supply. However, in an adjacent part of the same environment, the rate of sediment removal might be less than the rate of sediment supply so that an unconformity will not develop. In seismic stratigraphic nomenclature, this second set of conditions creates what is referred to as "the correlative conformity of the unconformity" (Mitchum, 1977). The correlative conformity surface can be traced into the unconformity by following the defining seismic reflections.

One's ability to identify an unconformity in the marine realm is a "horizontal and vertical scale problem". In marine surveys, the fire rate determines the horizontal resolution. For example, a 40 in^3 (655 cm^3) survey that fires every 10 seconds at a ship speed of 5 knots (9.25 km/hour) will only image the seafloor and subsurface every 28 m. During the same survey, a Huntec deep-tow system firing at 0.25 second intervals will obtain reflections from the seafloor every 0.7 m, providing much better definition of the lateral continuity of seismic reflectors.

Vertical resolution is also critical to the accurate mapping of stratal surfaces including unconformities. In seismic reflection profiles, the reflections are returned from interfaces where there is significant acoustic impedance contrast, which is a function of the density of the media through which the waves propagate and the P-wave velocity of the acoustic pulse within these media. The wavelength of the acoustic pulse determines the

shortest vertical spacing that the system can resolve between levels with significant acoustic impedance contrast. A common heuteristic is that two closely-spaced reflectors only can be resolved if they are separated by at least one quarter of the dominant wavelength of the source signal (Sheriff and Geldart, 1995). Wavelength (λ) is controlled by the dominant frequency of the source (f) and the P-wave velocity within the medium (v) according to the relationship:

$$v = f \times \lambda \qquad (3.1)$$

For example, if the medium is soft unconsolidated sediment with an average v of 2000 m s^{-1}, and a dominant source frequency of 1000 Hz, the dominant λ is 2 m. Then, the best vertical resolution achievable (using the quarter λ criterion) is 0.5 m.

In seismic reflection profiles, the vertical resolution varies from >20 m in industry multichannel data, to ~5.5 m in high-resolution multichannel data used by academics or for well-site surveys, to <20 cm in ultra-high-resolution boomer/sparker/chirp data, each dependent on the dominant frequency of the outgoing pulse. In the southwestern Black Sea, the uppermost Pleistocene–Holocene sediments are thin, ranging from <1 m to ~15 m (locally and rarely reaching 30 m). In these water-laden soft sediments, the P-wave velocity ranges from 1500–1650 m s^{-1}. The Memorial University of Newfoundland Huntec deep-tow system, operated with a boomer acoustic source, provides a broadband pulse with dominant frequencies between 2000 and 6000 Hz. This setup provides a vertical resolution between ~20 cm and 6 cm (http://www.geoforcegroup.com/wp-content/uploads/2018/06/Geoforce-DTS-specs-andata.pdf). In the same survey area, a 40 in^3 single-channel airgun emitting a dominant pulse with a frequency of 150– 250 Hz

(Traband, 1984) will only provide ~1.5–3.0 m vertical resolution. The vertical resolution will further deteriorate as the source size increases and the dominant frequency decreases to ~20 Hz (or ~21 m vertical resolution), such as in industry seismic profiles. Thus, closely spaced unconformities readily visible in Huntec DTS data may be missed in single-channel airgun profiles, but certainly will not be recognizable in industry seismic reflection data. If one could achieve progressively greater vertical resolution, it might be possible to detect more and more hiatuses within a seemingly conformable succession as the scale of observation becomes smaller and smaller. There might actually be many geologically very short intervals during which sediment accumulation ceased, or there was minor erosion, so that the succession could really be composed of a number of vertically-stacked mini-unconformities separating conformable intervals (cf. Miall, 1994, his figure 4). Mini-unconformities could be generated by storm waves sweeping the seabed, with a frequency dependent on wave climate and water depth, but they would go unnoticed if below the vertical resolution of survey techniques. Thus, in many shelf settings, the vertical resolution of the seismic reflection profiles and the smallest temporal resolution of radiometric dates in cores collectively control whether or not an unconformity can be delineated. If the sediment is bioturbated, the vertical mixing and homogenization of detritus by burrowers could further degrade evidence of depositional breaks of annual or even decadal duration (e.g., very thin storm event-beds).

3.4.2. Allounit 1b net accumulation

By 11.1 cal ka, the Neoeuxine Lake was flowing outward through the Strait of Bosphorus and creating a climbing delta lobe in the northeastern Marmara Sea (Aksu et al.,

2016). In its type area around the M02-45 core site, allounit 1b forms a tongue-shaped lobe which extends to the northwest, beyond the study area (Fig. 3.4). The volume alone requires sediment supply from major river(s) which are not available along the nearby Turkish coastline. Lister et al. (2015) concluded that the Danube and possibly Kamchiya rivers must have contributed the bulk of the silty mud found in allounit 1b, probably in the form of an elongate along-shelf mud belt with analogues today in east Asia (Liu et al., 2018). According to Giosan et al. (2006) and Vespremeanu-Stroe et al. (2017) the Danube River only began to build a delta into its flooded (transgressed) coastal embayment at ~8.0 cal ka, although Constantinescu et al. (2015) demonstrate that significant sediment from the Danube river ceased reaching its submarine fan by ~11.7 cal ka. In the intervening ~3700 years (i.e., 11.7–8.0 cal ka), no delta lobe was created in the mouth of the Danube River in spite of the fact that sediment discharge must have continued. It is postulated that suspended muds during this period moved predominantly away from the river mouth and along the shelf toward the south and southeast, as they do today (Panin and Jipa, 2002). In the early Holocene, the lower salinity of surface waters ($S \leq 10$) made rapid flocculation less likely (Sutherland et al., 2015), so that fine clays and silts could be maintained in transport for long distances. An abundance of reworked loess, now removed from the drainage basins of the Danube and Kamchiya rivers (Smalley and Leach, 1978; Haase et al., 2007) would have swollen the volume of suspended sediment relative to today (Lister et al., 2015). Deposition toward what are now Bulgarian and Turkish waters might have been promoted by water-column stratification (across the seasonal thermocline), as explained by Liu et al. (2018).

There surely would have been episodic non-deposition and/or minor erosion associated with the emplacement of storm event beds found at various allounit 1b sites, but the high rates of supply and accumulation (e.g., Fig. 3.10) ensured net deposition and prevented any significant hiatuses in the western part of the study area and in depressions behind relict ridges on the shelf.

3.4.3. α1 unconformity and its correlative conformity

Several previous studies reported the presence of local unconformities within the Holocene successions of the southwestern Black Sea (e.g., Aksu et al., 2002a; Ryan et al., 2003; Hiscott et al., 2007a; Konerding, 2009; Lister et al., 2015). Algan et al. (2002) recognized the α1 unconformity in the Sakarya River delta region to the east of the study area considered in this thesis. Hiscott et al. (2007a) suggested that these unconformities might have developed where surface currents were sufficiently strong to prevent deposition across shallow shelves. This hypothesis would require episodic shifts in the location of the strongest threads of available currents to explain temporal shifts from erosion/non-deposition to net accumulation.

Subsequently, Flood et al. (2009, their figure 7) recognized a local seabed unconformity forming today on the middle shelf east of the saline underflow channel, lending support for the interpretation of Hiscott et al. (2007a). Ryan et al., (2003) proposed that Holocene water level changes in the Black Sea (e.g., Chepalyga, 1984; Balabanov, 2006; Ivanov and Kakaranza 2006) might explain the Holocene unconformities, but did not further elaborate as to how base-level changes can create extensive erosional surfaces

unless the water depth becomes very shallow or there is subaerial exposure. Neither situation existed at the time of α1 development (Fig. 3.20).

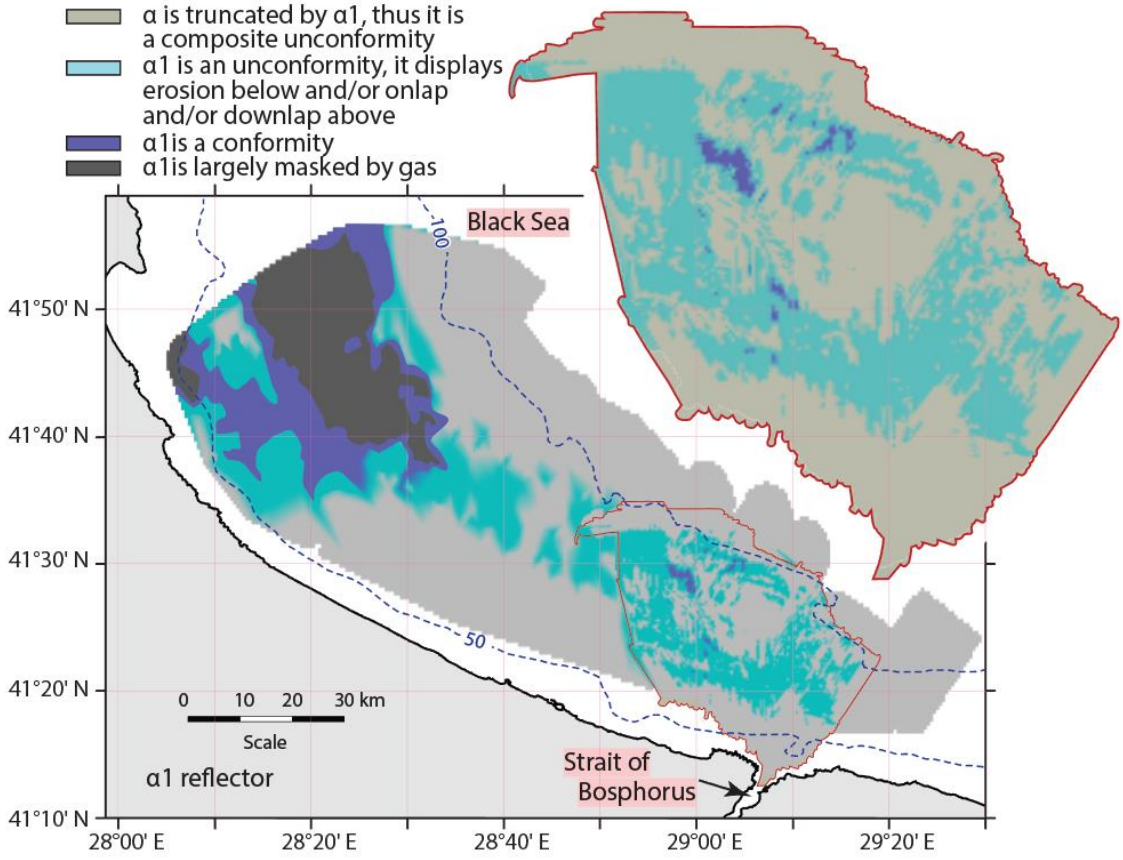

Figure 3.20. The distribution and characteristics of the α1 reflector across the southwestern Black Sea shelf. The unconformity at the α1 level is delineated by the erosional truncation below and/or onlap and/or downlap terminations above the reflector. Note that in regions where the α unconformity is truncated by the α1 reflector, the latter defines a composite unconformity. Also note that across the northwestern sector of the study area the α1 reflector is a conformable surface. The –50 m and –100 m isobaths (blue dashed lines) are from IOC (1981). Small white circles are composite key and reference cores discussed in the text.

The α1 surface is a prominent unconformity across most of the southwestern Black Sea, except where it laterally transitions into a correlative conformity with age of ~7.5 cal

ka across the northwestern sector of the study area (Fig. 3.10), and sporadically in small isolated enclaves in the saline channel region (Fig. 3.21).

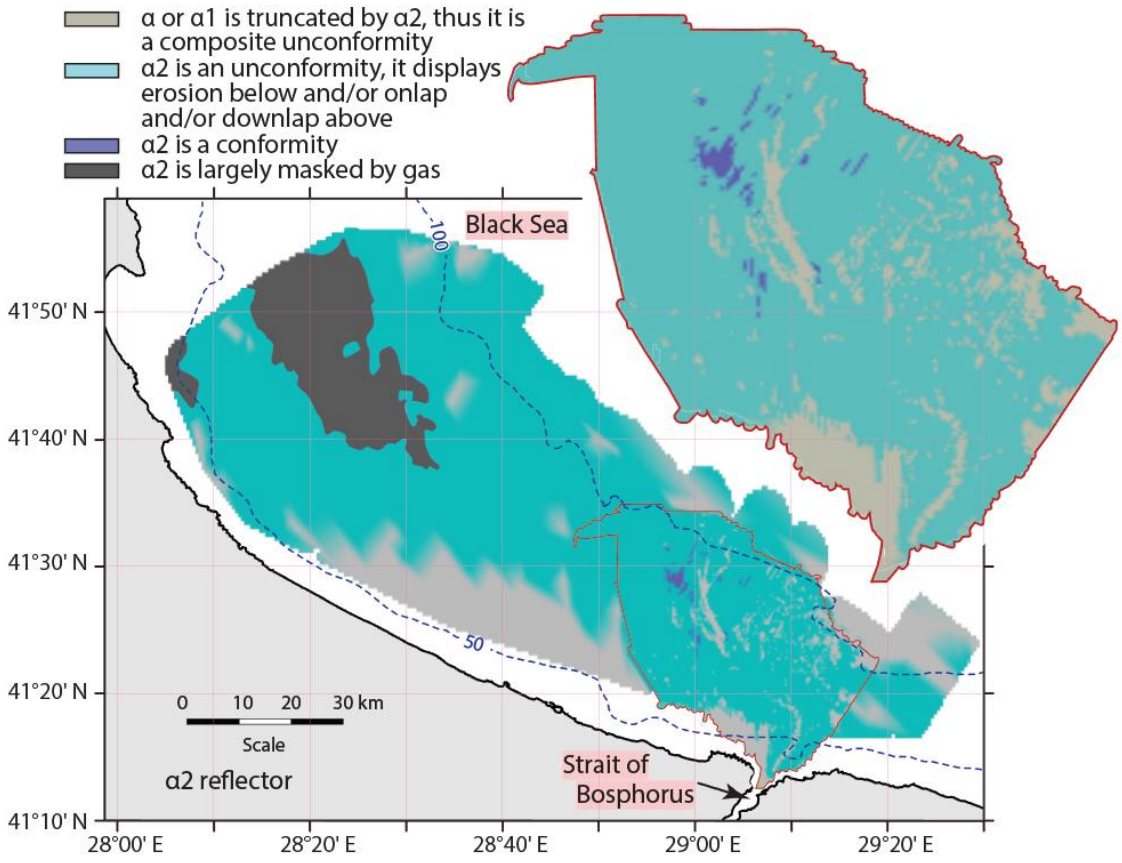

Figure 3.21. The distribution and characteristics of the α2 reflector across the southwestern Black Sea shelf. The unconformity at the α2 level is delineated by the erosional truncation below and/or onlap and/or downlap terminations above the reflector. Note that in regions where the α and/or α1 unconformities are truncated by the α2 reflector, the latter defines a composite unconformity. Also note that across small pockets in the saline channel area the α2 reflector is a conformable surface. The –50 m and –100 m isobaths (blue dashed lines) are from IOC (1981). Small white circles are composite key and reference cores discussed in the text.

In seismic reflection profiles α1 is characterized by notable downcutting at its base into subunit 1b and mild onlap by reflectors of subunit 1c above (e.g., Figs. 3.11, 3.12,

3.14). In cores, α1 is generally characterized by a significant hiatus overlain by sediments as old as ~8.2 cal ka (e.g., Figs. 3.11, 3.12, 3.14). A large region in the northwest, north of 41º 40'N latitude and west of 28º 30'E longitude is characterized by gas-charged sediments where subunits 1b, 1c and α1 are largely masked in Huntec DTS profiles. Here the subunits can only be discerned in airgun profiles. Southeast of the gas-charged sediments there is a distinct trend in the character of the α1 surface: in nearshore and shelf-edge seismic profiles, the α1 surface is a composite unconformity truncating the older shelf-crossing major unconformity α (Fig. 3.21).

Sediments below an erosional unconformity do not indicate the time of onset of the erosion. The time of development of α1 is instead given by the age of the correlative conformity. Except in unusual cases of diachronous development the erosional phase precedes the age of the oldest sediments covering the unconformity. These two indicators of age might be different from place to place if the erosion was diachronous, for example if the axis of an erosive current shifted through time. For example, several locations along the boomer profile that crosses the M05-50 core site show that there is ~1.5 m of missing section in the α1 unconformity around this site (Fig. 3.11). This simply tells us that the erosion started sometime after the youngest of the preserved layers accumulated, because even younger sediment could have been removed everywhere. The only constraints available for the youngest possible age of the erosional episode that resulted in the development of the α1 unconformity are provided by (a) the age of the correlative conformity if it exists, and/or (b) the age of the oldest sediment on top of the unconformity. For the α1 unconformity, these two constraints give an age range of 7.5–8.2 cal ka,

suggesting that the unconformity might be slightly diachronous, because the 8.2 cal ka determination is for sediments on top of the α1 surface. Unless the unconformity is diachronous, sediment on top of α1 should never be older than the age of the correlative conformity (Cross and Lessenger, 1988).

At ~8.2 cal ka, the Black Sea level was ~20 m lower than today (Fig. 3.22; Lambeck et al., 2007), whereas at ~7.5 cal ka it was ~10 m lower than today. As a compromise, a map of the paleo-water depth over α1 has been drawn assuming a water level 15 m lower than today (Fig. 3.22). Most locations where α1 is mapped would have been at water depths >40 m (and more if erosion started earlier). Today, the seabed at water depths <40m is devoid of seismically measureable Holocene sediment because of wave erosion/resuspension (Aksu et al., 2002a). This makes it difficult to explain the α1 hiatus entirely as a consequence of increased storminess. Other processes that might have contributed to preventing accumulation or cutting into the seabed are eddies associated with a paleo-Rim Current, or possibly the breaking of internal waves along the seasonal thermocline as they impinge upon the seabed. Internal waves in the modern Black Sea are mostly restricted to areas of fluvial discharge (Lavrova et al., 2017) and the seasonal thermocline is generally shallower than ~ –50 m, so breaking will only occur quite close to shore rather than on the middle to outer shelf.

It is possible that the initiation of growth of a lobe of the Danube Delta in the flooded river entrance at ~8.0 cal ka (Vespremeanu-Stroe et al., 2017) consumed a larger portion of the suspended load of the river (perhaps induced by enhanced flocculation as salinity increased; Syvitski et al., 1985; Sutherland et al., 2015). This might account for a drop in

accumulation rate of mud even at site M02-45 (Fig. 3.10) and a cross-over between net accumulation where allounit 1b is present and either non-deposition or erosion by processes that earlier were not able to keep up with the high sediment flux.

Finally, it should be noted that at least half of allounit 1b at site M02-45 was deposited before the first arrival of Mediterranean water at ~9.5 cal ka, and the base of the levées of the saline underflow channel are apparently no older than ~8.2 cal ka (immediately atop α1). Hence, any influence of saline inflow on the development of α1 is discounted.

3.4.4. Allounit 1c net accumulation

What might have ended a period of reduced deposition (or indeed erosion) at α1 so that the rather widespread allounit 1c could accumulate? Water depth was continuing to increase as base level rose (Fig. 3.21). This deepening of the seabed would have reduced the erosive capabilities of storm waves for the predominantly muddy substrates in the study area. In the area of the saline underflow channel, scouring along the main thread of the underflow would have transferred mud to the banks and overbank areas, as is the case today (Hiscott et al., 2013). Once the suspended mud carried into this area by the Rim Current and its associated eddies settles into the top of overspilling saline water, it more rapidly flocculates and becomes trapped near the seabed, leading to enhanced accumulation. This possibly explains why subunits 1c (and 1d) thin quickly to the east of the saline channel network (Figs. 3.7, 3.8).

In western portions of the study area, subunit 1c displays strongly crenulated ('crinkly') reflections, and the sediment contains numerous bands rich in mussel shells

(*Mytilus* and *Modiolus*). The crenulations are mound-shaped in three dimensions and in some cases climb upward through the section (Fig. 3.6). The mounds and crenulations are interpreted as mussel banks; i.e., low-relief bioherms. Today in the northwestern Black Sea, communities of *Mytilus galloprovincialis* are widespread to water depths of ~65 m (Shurova and Gomoiu, 2014), whereas on the Romanian shelf colonies dominated by *Modiolus phaseolinus* cover 40% of the seabed to depths of 120 m (Begun et al., 2010). The euryhaline mussels in allounit 1c apparently capitalized on a new opportunity when the salinity of the Black Sea rose to a level conducive to marine faunas, and rapidly colonized the seabed over the southwestern shelf. Like mussel and oyster banks throughout the world, the rugose seabed created by the bivalves would have acted as a baffle to trap suspended sediment in the water column, inducing deposition. The mussels themselves generate faecal matter which contributes to the sediment load. It is indeed possible that the mussel colonies were responsible for renewed net accumulation across much of the southwestern shelf (Fig. 3.21).

3.4.5. α2 unconformity and its correlative conformity

The α2 surface is the younger of the two intra-Holocene unconformities/ correlative conformities (Fig. 3.23). In seismic reflection profiles it is characterized by downlap and onlap of subunit 1d reflectors from above, and minor erosional downcutting of the α2 surface into subunit 1c below (Fig. 3.11). In the northwestern core M02-45, α2 is represented by a hiatus from 5480 to 2025 cal yr BP (Figs. 3.10, 3.19). The correlative

conformity at the M05-50 core site has an age of ~5695 cal yr BP (Figs. 3.11, 3.19).

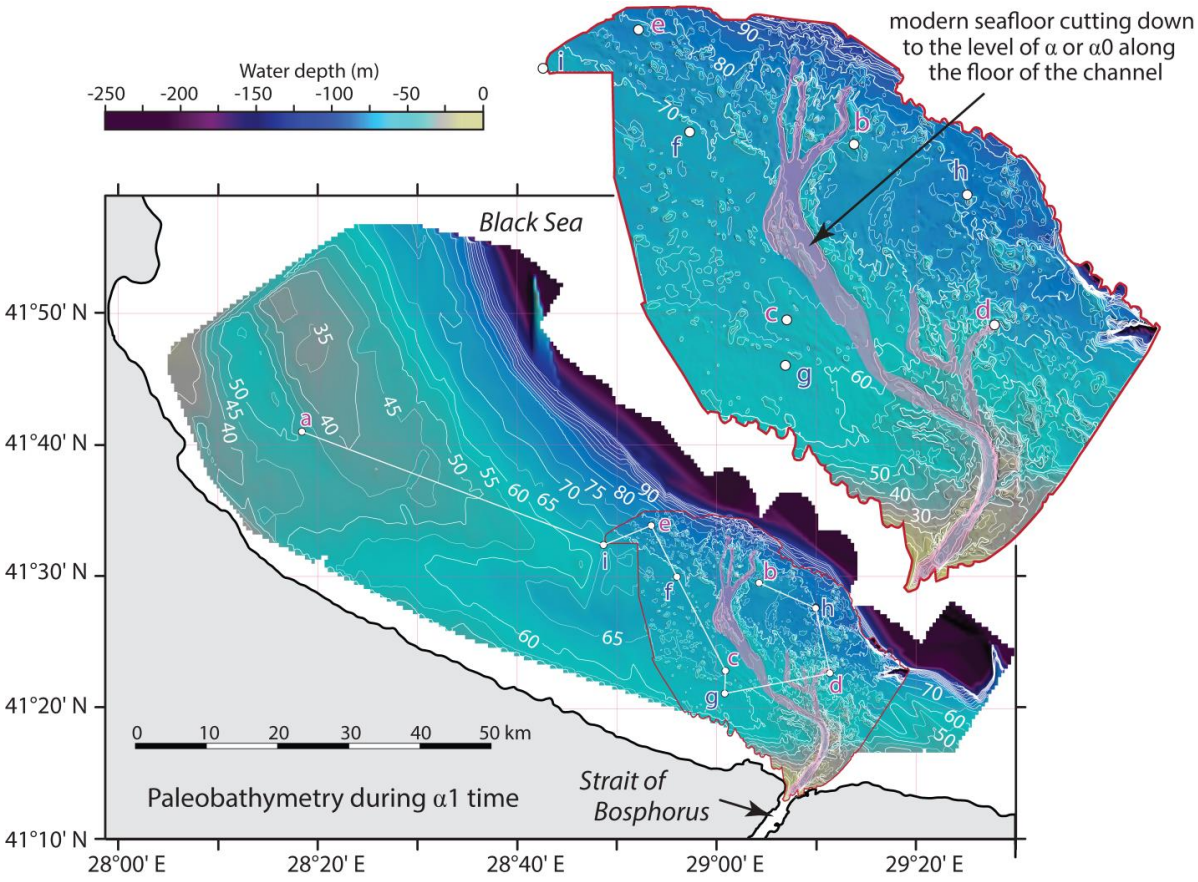

Figure 3.22. Paleobathymetry during α1 time, in meters. At this time (8.4–7.3 cal ka), sea level was ~15m lower than today (Lambeck et al., 2007), but subunits 1d and 1c had not yet been deposited. The map shows, in depth, what a time-structure map would show in acoustic two-way travel time. Hence, the water depth at every point on the map was calculated by subtracting 15m from today's depth, then adding the combined thicknesses of subunits 1d and 1c. The map was then compiled using Global Mapper and contoured. Small white circles with purple and blue lettering a through i are composite key and reference cores, respectively, discussed in the text. The pale pink mask over the saline channel demarcates the region where the modern seafloor has been eroded below the α1 level (to α or α0), creating a morphology that did not exist during α1 time.

Base level during the development of the α2 unconformity was ~5 m below the present-day sea level, so this episode of non-deposition and erosion developed under many tens of meters of water on the shelf (Fig. 3.23). The existence of seafloor relief (e.g., mussel

banks, vent/seep-related conical mounds, older bedrock ridges) might have provided an opportunity for flow separation and scouring under the shoreward margin of the Rim Current or its associated anticyclonic eddies. With increased water depth, breaking internal waves associated with the permanent pycnocline/halocline might have intersected the deeper parts of the shelf, maintaining sediment in suspension.

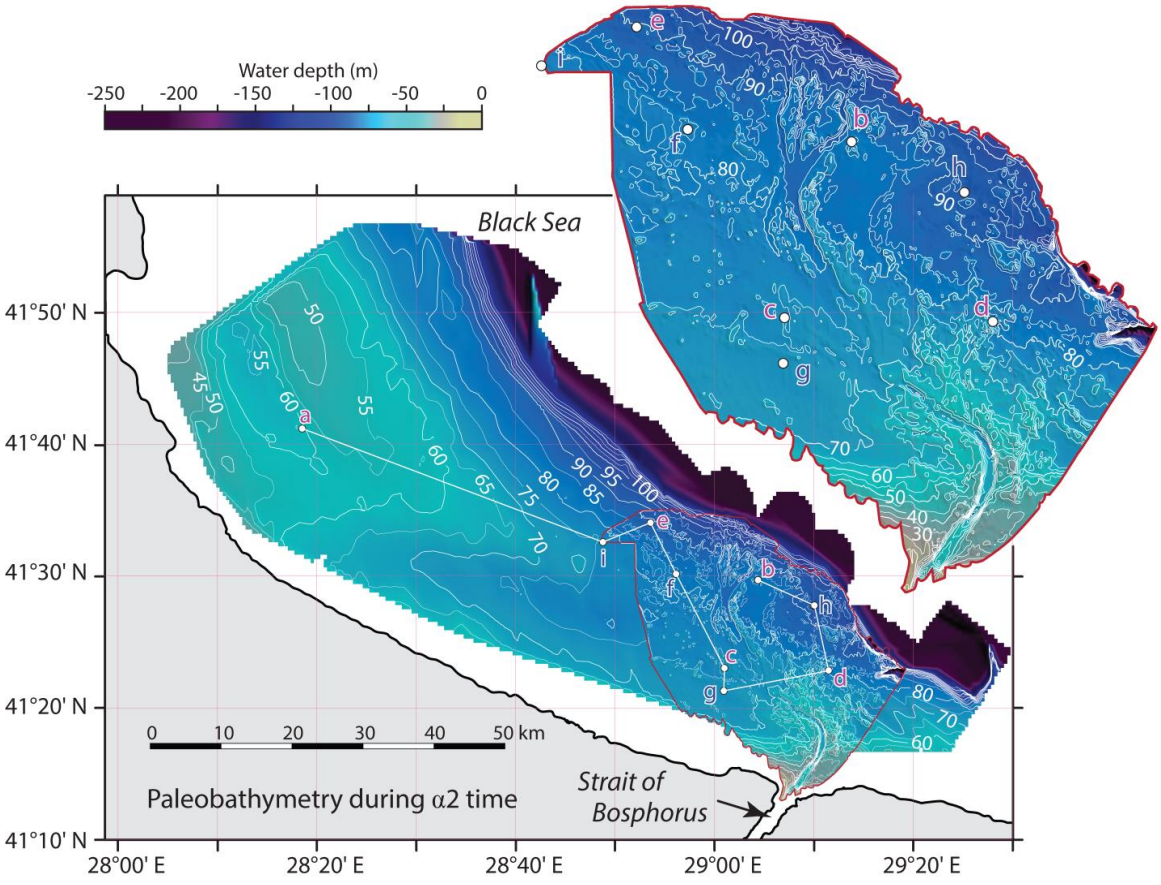

Figure 3.23. Paleobathymetry during α2 time in meters. At this time (~5.7 cal ka), sea level was ~5m lower than today (Lambeck et al., 2007; Fig. 19), but subunit 1d had not yet been deposited. Hence, the water depth at every point on the map was calculated by subtracting 5m from today's depth, then adding the thickness of subunit 1d. The map was then compiled using Global Mapper and contoured.

At ~5.7 cal ka, coincident with the α2 correlative conformity, deposition on the Danube Delta switched from infilling of the precursor coastal embayment to progradation of an external lobe exposed to shelf currents and waves (Vespremeanu-Stroe et al., 2017). The coincidence of this transition with the α2 drop in net accumulation on the southwestern shelf might implicate delta dynamics in the development of the α2 unconformity, but the writer of this thesis cannot point to an obvious cause-and-effect relationship.

3.4.6. Allounit 1d net accumulation

Allounit 1d is accumulating today under modern conditions. The Rim Current advects sediment along the shelf from the Danube Delta, and is inferred to be the main source of new detritus. The saline underflow is not laden with suspended sediment as it exits the Strait of Bosphorus, so is more important as an agent of sediment suspension and redistribution along the channel network. A high terrigenous fraction of the total organic carbon in allounit 1d (Hiscott et al., 2007b) points to a strengthening of the sediment flux from the Danube and possibly Bulgarian sources during the latest Holocene.

3.5. Summary

An extensive grid of high-resolution Huntec deep-tow seismic reflection profiles (~9150 line-km), complemented with several long piston cores (72 gravity + 25 piston cores) reveals that the sedimentary architecture of the southwestern Black Sea above the prominent shelf-crossing unconformity α is characterized by three distinctive allounits (1b, 1c, 1d), separated by two regional unconformities and their correlative conformities, α1 and α2. A fourth allounit (1a) occurs as patchy remnants between the α and α0 unconformities. The chronology is established using 56 radiocarbon dates in five key cores. The α

unconformity developed as a ravinement surface during the transgression associated with the transition from the Last Glacial Maximum to Holocene, thus defines the base of the Holocene successions. The α0 unconformity is older and is overlain by pre-last-transgression Pleistocene deposits. Allounit 1b is bounded at its base and top by the α and α1 unconformities/correlative conformities. It was deposited between ~12.5 and ~7.4 cal ka, but shows a notably patchy but widespread distribution across the southwestern Black Sea. Allounit 1c is bounded at its base and top by the α1 and α2 unconformities/correlative conformities. It was deposited between ~7.4 and ~5.3 cal ka, and also shows marked thickness variations across the shelf. Allounit 1d has developed above the α2 unconformity/correlative conformity since ~5.3 cal ka.

Interpretation of the well-dated cores and several detailed regional maps reveals that the widespread occurrence of ~11.0–7.5 cal ka deposits (allounit 1b) across the middle and outer shelf provides no possibility for a Holocene evaporative drawdown of the Neoeuxine Lake to a lowstand elevation of –120 m at 9.4 cal ka as suggested by Yanchilina et al. (2017). There is no evidence from any of the core sites which have recovered allounit 1b that they were located in limans (local term for a coastal pond, isolated from the main water body by a natural barrier and potentially at a higher elevation), rather than on a transgressed shelf which had been flooded by post-glacial meltwater and enhanced river runoff as the climate became more humid in the early Holocene. The development of the subaqueous unconformities/correlative conformities α1 and α2 was most likely facilitated by breaking internal waves, storm-induced wave erosion, transport and erosion under the Rim Current and its anticyclonic eddies.

Chapter 4. Strontium isotopic composition of shells from the M02-45 composite core

At the time of the Last Glacial Maximum (LGM), the Aegean Sea, the Propontis Lake (today's Marmara Sea) and Neoeuxine Lake (today's Black Sea) were 100–150 m lower than today, with the Propontis Lake and the Neoeuxine Lake being landlocked water bodies characterized by very low salinity (practical salinity <~12; Chepalyga, 2007; Mudie et al., 2007; Marret et al., 2009; Bradley et al., 2012; Mertens et al., 2012; Yanko-Hombach et al., 2014) and strontium isotopic ratios distinctly lower than open marine values (Major et al., 2006; Yanchilina et al., 2017). In the case of the Neoeuxine Lake, initial marine inflow occurred when global sea level reached, then exceeded, the ~ –40 m elevation of the sill in the Strait of Bosphorus, leading to a rapid rise in the $^{87}Sr/^{86}Sr$ ratio in shell carbonate (Yanchilina et al., 2017). Subsequent salination to the modern practical salinity of 17–20 on Black Sea shelves (~22 overall; Leonov, 2005) can be tracked using strontium isotopes and the progressive replacement of fresh- and brackish-water species by euryhaline species (Ryan et al., 1997, 2003; Hiscott et al., 2007a; Yanko-Hombach, 2007b; Marret et al., 2009; Ivanova et al., 2012; Williams et al., 2018).

The recent synthesis of Yanchilina et al. (2017) provides a rich compendium of isotopic data for the latest Pleistocene, the initial marine inflow, and the subsequent period of Black Sea salination, but suffers from the fact that the analysed shells predominantly come from coquina layers in short, low-resolution cores collected along the modern shelf edge and upper slope rather than from a conformable stratigraphic succession, ideally of sufficient thickness to provide a temporal resolution of ~100 years or less between samples during the time of reconnection of the formerly isolated Neoeuxine Lake to the global

ocean. The coquinas are transgressive lags created by wave action, and contain shells of variable age. The shells might have been transferred basinward during transgressive reworking, and the principle of superposition cannot be used to judge the true sequence of events whenever the error bars of radiocarbon-dated shells overlap. An additional problem with low-resolution cores is establishing accurate ties to nearby seismic profiles. In a low-resolution core, a 10 cm error in the tracing of a seismic reflection to the core site might lead to an error of several hundred years in the assignment of an age to the seismic event.

Hiscott et al. (2007a) described an ~10 m-long high-resolution piston core (M02-45P) with trigger-weight gravity core (M02-45T) from the southwestern Black Sea shelf (–69 m water depth). The composite core M02-45 samples all but the earliest Holocene – the only gap is a hiatus from 5445–2055 cal yr BP (Section 3.2.1). There is a complete record of the initial marine inflow and the period of salination. A follow-up piston core (M05-03P) was collected ~480 m away from the M02-45 site and extends the stratigraphic record down to the transgressive gravel along the basal unconformity (Fig. 3.10). This basal unconformity was called α by Aksu et al. (2002). Two younger unconformities, α1 and α2, are locally developed on the southwestern shelf and have been interpreted as submarine erosional surfaces because they both post-date the initial marine inflow (Flood et al., 2009). At the M02-45 and M05-03 core sites, α1 is apparently a conformable surface, but elsewhere is associated with a hiatus and could be a subtle disconformity or paraconformity in the M02-45 area.

The Holocene succession at the M02-45 and M05-03P sites provides a major advantage over upper-slope coquinas for unravelling the timing, pace and causes of the

Holocene transgression in the Black Sea basin. The accumulation rate on this part of the middle shelf was ~55 cm/100 yr at the time of the initial marine inflow, so samples 10 cm apart potentially provide a temporal resolution of ~20 years. As a result, short-duration changes in marine influence can be accurately tracked by isotopic proxies, providing reliable input to mixing models designed to test whether the reconnection involved the introduction of saline water into a brim-full basin already spilling into the Marmara Sea (*Outflow Model* of Hiscott et al., 2007b) or rapid infilling of what was still an evaporative lowstand lake by saline water from the Mediterranean Sea (*Flood Model* consistent with Ryan et al., 2003, and Yanchilina et al., 2017). The high accumulation rate also ensures that bioturbation could not have mixed shells of significantly different age to lie at the same level in the core.

This chapter presents the Sr-isotopic investigation of the three near co-located cores at the M02-45 site, extending from the basal transgressive unconformity to the sea floor. The results of this study also have been published in the international journal *Marine Geology* (Ankindinova et al., 2019a). No other comparable study with the same degree of stratigraphic and age control is available. Methods are found in Section 2.3.

4.1. Precision

The $^{87}Sr/^{86}Sr$ ratios for separate shells from the same core depth have standard deviations of 0.000011 and 0.000013, respectively (Table 4.1). The within-shell standard deviations are 0.000011 and 0.000012 for the 140 cm (sub-seafloor) and 920 cm samples (Table 4.1). These 1σ uncertainties (i.e., ±0.000011–0.000013) are effectively identical to the long-term uncertainty in SRM987 determinations at the Memorial University of

Newfoundland laboratory (i.e., ±0.000014; 1σ). Hence, there is no evidence that additional uncertainty might have been introduced by selecting particular shells, or by analysing only small portions of larger shells (or shell fragments). For this reason, the uncertainty that should be attached to $^{87}Sr/^{86}Sr$ ratios in this study is not a summation, but is simply ±0.000014 (1σ).

Table 4.1. Replicate analyses of single shells from a common depth, and separate pieces of one of these same shells, from two depths in composite core M02-45.

Sample	**Single shell**	**Pieces of one shell**	**All results**
M02-45 140-1	0.709145		0.709145
M02-45 140-3	0.709120		0.709120
M02-45 140-2	0.709126		0.709126
M02-45 140-4	0.709139		0.709139
M02-45 140-5-1	0.709120	0.709120	0.709120
M02-45 140-5-2		0.709121	0.709121
M02-45 140-5-3		0.709110	0.709110
M02-45 140-5-4		0.709119	0.709119
M02-45 140-5-5		0.709137	0.709137
Mean	**0.709130**	**0.709121**	**0.709126**
1 s	**0.000011**	**0.000010**	**0.000011**
M02-45 810-1	0.708870		0.708870
M02-45 810-2	0.708869		0.708869
M02-45 810-3	0.708881		0.708881
M02-45 810-5-1	0.708897	0.708897	0.708897
M02-45 810-5-2		0.708871	0.708871
M02-45 810-5-4		0.708874	0.708874
M02-45 810-5-5		0.708875	0.708875
Mean	**0.708879**	**0.708879**	**0.708870**
1 s	**0.000013**	**0.000012**	**0.000012**

4.2. Baseline parameters and a variable to track the progress of Holocene salination

$^{87}Sr/^{86}Sr$ ratios measured in Holocene shells from the M02-45 site provide a record of the timing and degree of mixing of contemporary marine, lacustrine and river waters during the reconnection of the Neoeuxine Lake to the world ocean. An appreciation of the strontium concentrations and isotopic ratios of these different waters provides useful guidance and context to the results of this study. First consider Mediterranean seawater. Major et al. (2006) used a seawater $^{87}Sr/^{86}Sr$ ratio of 0.709155 and Sr concentration of 7.62 ppm for their mixing calculations. They also estimated values of 0.708792 for $^{87}Sr/^{86}Sr$ and 0.24 ppm for the average strontium concentration of modern rivers entering the Black Sea, dominated by the Danube River. However, a survey of the literature indicates that some of these parameters are not known to the implied accuracies (e.g., Bernat et al., 1972; Vasiliev et al., 2010; Kuznetsov et al., 2012; Khaska et al., 2013). As an alternative approach, the published $^{87}Sr/^{86}Sr$ and Sr concentrations for seawater and modern Black Sea rivers are extracted from the literature (Table 4.2), then randomly selected values within the range for each parameter to compare with the strontium characteristics of the modern Black Sea. Random selection was accomplished using the Microsoft Excel™ function RANDBETWEEN. For the Black Sea itself, the range of isotopic ratios in the youngest M02-45 molluscs was used (Table 4.3, supplemented by data from Kuznetsov et al. [2012] after normalization of their values to SRM987 = 0.710240).

Table 4.2. Upper block: ranges of strontium concentrations and $^{87}Sr/^{86}Sr$ ratios used in Monte Carlo simulations. Lower block: the 0.1% of Equation 4.1 solutions most consistent with the modern depth-averaged practical salinity of the Black Sea (22; Leonov, 2005). These are the values used in mixing models.

Parameter	**Symbol**	**Units**	**Range**	**Source(s)**
$^{87}Sr/^{86}Sr$ ratio seawater	X_{SW}	none	0.709155–0.709170	Henderson et al. (1994); Major et al. (2006); Vasiliev et al. (2010); Kuznetsov et al. (2012); Khaska et al. (2013)
Sr concentration, seawater	C_{SW}	ppm	7.45–8.25	Henderson et al. (1994); Vasiliev et al. (2010); Brass and Turekian (1972); Bernat et al. (1972); Kuznetsov et al. (2012)
$^{87}Sr/^{86}Sr$ ratio, modern rivers	X_{BSR}	none	0.708792–0.70900	Palmer and Edmond (1989); Major et al. (2006); Pawellek et al. (2002); Zitek et al. (2015)
Sr concentration, rivers	C_{BSR}	ppm	0.2175–0.242	Palmer and Edmond (1989); Major et al. (2006)
$^{87}Sr/^{86}Sr$ ratio, modern Black Sea	X_M	none	0.709120–0.709155	This thesis, recent molluscs; Kuznetsov et al. (2012)
Author $^{87}Sr/^{86}Sr$ ratio, seawater	X_{SW}	none	0.709158 ± 0.000002	Equation 4.1
Author Sr concentration, seawater	C_{SW}	ppm	7.81 ± 0.20	Equation 4.1
Author $^{87}Sr/^{86}Sr$ ratio, modern rivers	X_{BSR}	none	0.708863 ± 0.000054	Equation 4.1
Author Sr concentration, rivers	C_{BSR}	ppm	0.230 ± 0.007	Equation 4.1
Author $^{87}Sr/^{86}Sr$ ratio, modern Black Sea	X_M	none	0.709152 ± 0.000002	Equation 4.1

Table 4.3 $^{87}Sr/^{86}Sr$ data for the M02-45 composite-core and from Yanchilina et al. (2017), the latter in italics. All results have been corrected to SRM987 = 0.710240. Calendar ages are presented without uncertainties, and for M02-45 are mostly interpolated between Table 3.1 results. Yanchilina et al. (2017) ages were determined by recalibration of their original radiocarbon dates using reservoir corrections explained in Williams et al. (2018), so are consistent with Table 3.1 calibrations. All ages are rounded to the nearest 5 years.

Core	**Depth (cm)**		**Age**	**$^{87}Sr/^{86}Sr$**	**Age Yanchilina et al. (2017)**	**$^{87}Sr/^{86}Sr$ Yanchilina et al. (2017)**
	Raw	**Composite**	**cal yr BP**			
M02-45T	60	60	240	0.709120	100	0.709163
M02-45T	115	115	380	0.709130	825	0.709140
M02-45T	130	130	385	0.709147	2925	0.709135
M02-45P	40	150	460	0.709080	3390	0.709133
M02-45T	160	160	595	0.709129	4280	0.709138
M02-45T	170	170	725	0.709129	5190	0.709127
M02-45P	90	200	1125	0.709122	6070	0.709127
M02-45P	158	268	2025	0.709138	6345	0.709111
M02-45P	174	284	5480	0.709122	7110	0.709105
M02-45P	220	330	5535	0.709155	7200	0.709086
M02-45P	230	340	5630	0.709114	7290	0.709046
M02-45P	250	360	5820	0.709096	7300	0.709046
M02-45P	270	380	6010	0.709110	7310	0.709041
M02-45P	290	400	6195	0.709108	7340	0.709041
M02-45P	302	412	6310	0.709105	7390	0.709083
M02-45P	340	450	6840	0.709115	7395	0.709083
M02-45P	360	470	7120	0.709100	7535	0.709092
M02-45P	380	490	7445	0.709060	7590	0.709128
M02-45P	406	516	8030	0.709071	7665	0.709083
M02-45P	430	540	8435	0.709075	7815	0.709115
M02-45P	430	540	8435	0.709059	8150	0.709097
M02-45P	460	570	8765	0.709042	8455	0.709089
M02-45P	480	590	8985	0.708972	8825	0.708992
M02-45P	490	600	9095	0.709022	8935	0.708948
M02-45P	495	605	9150	0.708980	9005	0.708973
M02-45P	500	610	9165	0.708963	9155	0.708988
M02-45P	520	630	9230	0.708959	9175	0.708966
M02-45P	530	640	9260	0.708966	9195	0.708898
M02-45P	540	650	9290	0.708959	9255	0.709060
M02-45P	550	660	9320	0.708934	9270	0.708942
M02-45P	560	670	9350	0.708950	9350	0.708939
M02-45P	569	679	9380	0.708965	9455	0.708945
M02-45P	570	680	9380	0.708962	9505	0.708966

Table 4.3 continued

M02-45P	600	710	9405	0.708917	9505	0.708962
M02-45P	610	720	9415	0.708907	9510	0.708980
M02-45P	620	730	9425	0.708942	9515	0.708939
M02-45P	620	730	9425	0.708899	9575	0.708907
M02-45P	630	740	9430	0.708942	9585	0.708942
M02-45P	640	750	9440	0.708924	10430	0.708914
M02-45P	650	760	9465	0.708894	11415	0.708870
M02-45P	680	790	9535	0.708843	12065	0.708889
M02-45P	700	810	9580	0.708875	12200	0.708920
M02-45P	740	850	9670	0.708881	12290	0.708904
M02-45P	754	864	9700	0.708872	12350	0.708919
M02-45P	810	920	9915	0.708871	12520	0.708916
M02-45P	820	930	9955	0.708853	12590	0.708949
M02-45P	822	932	9960	0.708873	12645	0.708898
M05-03P	680	982	10695	0.708865	12670	0.708941
M05-03P	690	992	11180	0.708873	12860	0.708939
M05-03P	700	1002	11660	0.708841	12870	0.708935
M05-03P	700	1002	11660	0.708859	12870	0.708895
M05-03P	710	1012	12145	0.708847	12880	0.708963
					12890	0.708924
					12915	0.708920
					12920	0.708946
					12925	0.708937
					12950	0.708898
					13460	0.708964

The mollusc ratios are proxies for the Sr-isotopic composition of modern/recent Black Sea water, because Sr-isotopes are not offset by a 'vital effect' when strontium is incorporated into biogenic carbonate (Reinhardt et al., 1999). The random selection procedure was repeated 50,000 times as a Monte Carlo simulation and the parameter-set from each trial was used to calculate the proportion of river water (relative to marine water) consistent with the isotopic ratio of the Black Sea in the associated trial, using Equation 4.1 modified from Mills et al. (1998). In this equation, F = decimal fraction of the least saline

water in a thoroughly mixed basin, $X = {}^{87}Sr/{}^{86}Sr$, C = Sr concentration. Subscripts *SW*, *BSR* and *M* indicate seawater, Black Sea rivers and modern/recent molluscs, respectively.

$$F_{BSR} = \frac{C_{SW}(X_{SW} - X_M)}{C_{SW}(X_{SW} - X_M) + C_{BSR}(X_M - X_{BSR})} \quad (4.1)$$

F_{BSR} can be directly converted to salinity if seawater and river practical salinities are set to 38 and zero, respectively. The sets of randomly selected input parameters for seawater and river water that yielded mixtures with practical salinities closest to 22 (i.e., the depth averaged salinity of the modern Black Sea; Leonov, 2005) are believed to provide the best estimates for these parameters. Practical salinity of 22 corresponds to $F_{BSR} = 0.421$. From the 50,000 Monte Carlo trials, the 50 parameter sets (0.1%) yielding values of F_{BSR} closest to 0.421 were averaged (Table 4.2); the averages are used to characterize the strontium characteristics of Holocene rivers and seawater.

As expected, the best estimate for seawater $^{87}Sr/^{86}Sr$ (0.709158) is slightly greater than all measurements on M02-45 mollusc shells. The lowest $^{87}Sr/^{86}Sr$ value in the Holocene section (0.708841; Table 4.3) is slightly less than the estimated ratio for major rivers entering the Black Sea (0.708863). These minimum and maximum values are used in the remainder of the chapter to track, in relative terms (i.e., from 0–1), the progress of the $^{87}Sr/^{86}Sr$ increase which occurred at site M02-45 through the Holocene. The $^{87}Sr/^{86}Sr$ increase is a proxy for climbing salinity as greater and greater volumes of Mediterranean water entered the Black Sea and mixed with residual lacustrine waters of the Neoeuxine Lake and contemporary river water. A scaling variable called ξ is introduced here which varies linearly from 0.00 for the lowest $^{87}Sr/^{86}Sr$ ratio recorded in this study (i.e., 0.00ξ =

0.708841) to 1.00 for the Sr-isotopic ratio in modern seawater (i.e., 1.00ξ = 0.709158). ξ values are presented in brackets wherever $^{87}Sr/^{86}Sr$ values are reported so that readers can appreciate the progress from lacustrine to marine isotopic values. Of course the relationship between ξ and absolute salinity is not linear, because a small amount of seawater will induce a far greater increase in ξ than in salinity, owing to the greater concentration of Sr in seawater than in river water or lake water.

4.3. 12.1 cal ka to modern isotopic record

The $^{87}Sr/^{86}Sr$ record for the last 12,000 years spans the range 0.708841 to 0.709152 (ξ = 0.00–0.98) and can be subdivided into four isotopically distinctive intervals, A through D (Table 4.3; Figs. 4.1, 4.2). A smoothed trendline has been superimposed on the 52 data points for the M02-45 composite core to accentuate the most significant variations, and to de-emphasize small up/down excursions which are attributed to short-duration (perhaps decadal) environmental fluctuations on the Holocene shelf, perhaps some transport of shells by stronger storms, or to uncertainties in the measurements themselves. A line connecting data points proceeds in stratigraphic order from oldest to youngest honouring the principal of superposition. Ages are largely interpolated between dated shells (Tables 3.1, 4.3).

Interval A spans 12,145–9580 cal yr BP: here the Sr-isotope ratio varies from 0.708847 to 0.708881 (ξ = 0.02–0.13), and reflects average Neoeuxine Lake values published by Major (2002), Major et al. (2006) and Yanchilina et al. (2017). Interval B from 9580–9490 cal yr BP reflects a drop in $^{87}Sr/^{86}Sr$ values ranging between 0.708841 and 0.708843 (ξ = 0.00–0.01).

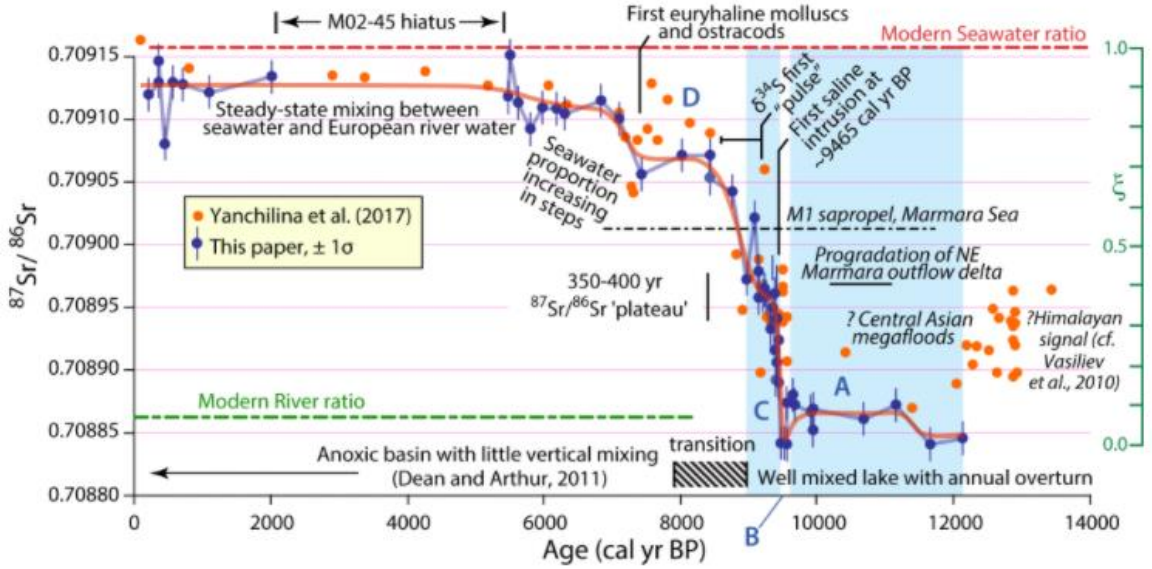

Figure 4.1. M02-45 $^{87}Sr/^{86}Sr$ data (blue points; 1σ error bars = ±0.000014) compared with Yanchilina et al. (2017) data mostly from coquina layers and listed in Table 4.3. Bold orange line represents smoothed $^{87}Sr/^{86}Sr$ evolution of basin water. Marked/labelled local and regional events are discussed in the text. ζ is defined in Section 4.2.

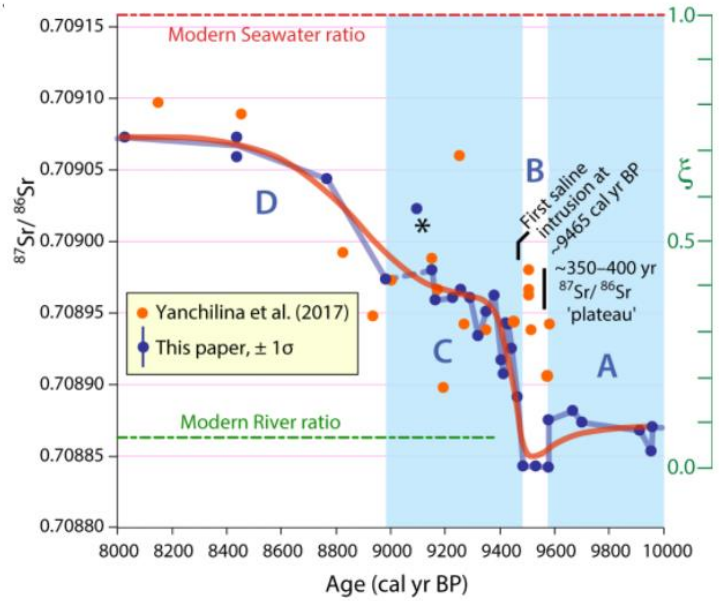

Figure 4.2. Detail of 8–11 cal ka portion of the $^{87}Sr/^{86}Sr$ data to better portray the initial sharp rise in the isotopic ratio and the character of the older 'plateau' used in modelling exercises. One data point (*) falls off the smoothed trend and is considered an outlier. A–D segments of the plot are alternately colored and are explained as evolutionary stages in the text. ζ is defined in Section 4.2.

The third interval C starts at 9465–9490 cal yr BP with an abrupt increase in $^{87}Sr/^{86}Sr$ terminating in a relatively flat 'plateau' along which ratios stall and/or climb very slowly from 0.708962–0.708972 (ξ = 0.38–0.41) through ~9380–8985 cal yr BP. The last interval D starts at ~8985 cal yr BP and is characterized by a step-wise rise of Sr-isotopic values toward modern Black Sea ratios. There is little variation after ~7000 cal yr BP.

Sr isotopic data from previous studies (Ryan et al., 1997; Major et al., 2006; Yanchilina et al. 2017) are also considered (Figs. 4.1, 4.2; Table 4.3). These follow a similar pattern of Sr isotopic evolution during the last 12,000 cal yr BP, but are more scattered than the M02-45 data and come from many different cores so cannot be placed in a stratigraphic sequence. The distinctive 'plateaux' of this study are not visible in the point scatter defined by the data of Yanchilina et al. (2017). Nevertheless, the broad similarity of the M02-45 results with those of Yanchilina et al. (2017) argues against the conjecture of those authors that the M02-45 site was in a topographically high, isolated pond above the level of the Neoeuxine Lake, rather than on the transgressed and submerged shelf of a rising Neoeuxine Lake prior to incursion of saline water from the Mediterranean Sea.

4.4. Interpretation

12,045–9465 cal yr BP corresponds to the Younger Dryas and earliest Holocene when various studies suggest increased precipitation, river runoff via major rivers entering the Neoeuxine Lake and possible ice-dam outburst floods from central–east Asia (Mudie et al., 2002; Thom, 2010; Aksu et al., 2016; Hiscott et. al., 2017). The data indicate that these sources maintained a rather stable Sr-isotopic composition of water in the Neoeuxine Lake (Fig. 4.1). According to Aksu et al. (2016) and Hiscott et al. (2017), the lake was

flowing outward carrying bedload and suspended load into the Marmara Sea from ~11.1–10.2 cal ka, and suspended load afterward until at least ~6.0 cal ka.

Around 9465–9490 cal yr BP, there was a sharp rise in the $^{87}Sr/^{86}Sr$ ratio that is interpreted as a first pulse of saline water intrusion into the Black Sea from the Mediterranean Sea (Fig. 4.2). Considering the large difference between the Sr concentration in seawater (~7.5–8.0 ppm) and in rivers entering the Black Sea (~0.25 ppm today; Major et al., 2006), even a small amount of seawater will cause a significant rise in the $^{87}Sr/^{86}Sr$ ratio; in contrast, quite large amounts of fresh water have little effect on a mixed water body because the concentration in river water is very low.

9380 cal yr BP is an important milestone because it signifies the termination of a first pulse of marine water, after which there was apparently a steady state for ~350–400 years, during which the proportions of newly arriving Mediterranean water and hinterland (river) water were balanced to maintain an approximately constant Sr-isotopic ratio in basinal waters. In this particular case and with the concentrations and isotopic compositions for marine and river water presented in Table 4.2, the annual river discharge to maintain the Sr-isotopic plateau would have been about 60 times the annual saline inflow, when averaged over one to several decades (Fig. 4.2). This plateau cannot be attributed to a hiatus in saline inflow, because in that circumstance the continued discharge of rivers into the young Black Sea would have diluted the marine strontium and perhaps caused a slow drop in the $^{87}Sr/^{86}Sr$ ratio, which is not evident. Also, by 9380 cal yr BP, global sea level was ~20 m above the sill in the Strait of Bosphorus (Lambeck et al., 2007), so there must have been a growing opportunity for further marine inflow. It is possible that

marine access to the Black Sea was impeded for several hundred years by strong outflow of brackish surface waters caused by an increase in precipitation and river runoff into the sea, or by the draining of remnant glacial lakes into the Caspian Sea and then to the Black Sea. The transition from the last glacial (Weichselian/Würm) to the Holocene was characterized by a marked increase in precipitation across the entire Mediterranean region starting as early as 12 ka (Guiot et al., 1993; Harrison et al., 1993, 1996). Similar wetter conditions are also recorded in Europe about 1500 yr later (Aksu et al., 2002a,b). Geogievski and Stanev (2006, their table 5) and Thom (2010) summarize evidence for an increase in the discharge of rivers entering the Black Sea basin through the Preboreal period (11,900–9300 cal yr BP) and into the middle Holocene, consistent with an increase in fresh to brackish outflow through the Strait of Bosphorus over several millennia. The Sr-isotopic data suggest that average fluvial discharge might have varied on time scales of decades to a few centuries, in order to account for the 2–3 observed interruptions in the salination process (Fig. 4.1). One cannot look to paleoclimate models for evidence of such fluctuations because the time steps in such models are invariably coarser than a few centuries.

In the following sections, elevation of the Bosphorus sill and bathymetry of the Black Sea basin are not adjusted for the possible isostatic impacts of changing water loads stemming from base level changes (e.g., Goldberg et al., 2016). These isostatic adjustments are assumed to have little effect on calculations involving base level changes of many tens of meters. The magnitude of isostatic changes in this area depends on sychroneity (or not)

between water level changes in the Aegean and Black seas, mantle viscosity, and flexural rigidity of the underlying lithosphere; these aspects are beyond the scope of this thesis.

4.4.1. Implications of $^{87}Sr/^{86}Sr$ data for a catastrophic marine inflow

This section examines how the new $^{87}Sr/^{86}Sr$ data might fit the hypothesis of a sudden inundation of the Neoeuxine Lake by Mediterranean seawater, raising its level from ~ –120 m to ~ –30 m. In ~110 yr, the Sr-isotopic ratio rose sharply from ~0.708842 to ~0.708962 (ξ = 0.00–0.38), after which the ratio stalled at ~0.708962–0.708972 (ξ = 0.38–0.41) for 350–400 yr (Figs. 4.1, 4.2). What volume of seawater could account for this shift in the strontium isotopic ratio, and is it consistent with the base-level rise proposed by Ryan et al. (2003) and Yanchilina et al. (2017)? The $^{87}Sr/^{86}Sr$ ratio that would result from mixing lake water and seawater depends on three parameters: (a) the $^{87}Sr/^{86}Sr$ ratio and Sr concentration of contemporary seawater, (b) the $^{87}Sr/^{86}Sr$ ratio and Sr concentration of the pre-reconnection Neoeuxine Lake, and (c) the proportions of lake water and seawater in the mixture.

Leonov (2005) tabulates water volumes within selected depth intervals in the Black Sea – each 10 m from today's level to –50 m depth, from –50 to –100 m, and at wider intervals beyond the shelf edge. For water depths shallower than –200 m, the volume of water (in km^3) below any level z is reliably calculated by Equation 4.2, fitted to the data of Leonov (2005) using Microsoft Excel™ trendline options:

$$Vol_z = 0.001044z^3 + 0.610905z^2 + 425.25z + 538716 \qquad (4.2)$$

where z retains its negative sign in the calculation. This equation permits the conversion of seawater volumes added to the lowstand lake into meters of base-level rise.

In order to estimate the effect of adding various volumes of saline marine water to the Neoeuxine Lake at the time of the initial marine inflow, it is necessary to have reliable estimates of contemporary water-mass characteristics, and to consider underlying assumptions. For X_{SW} and C_{SW} average values from the Monte Carlo simulations were used (Table 4.2), assuming that global and Mediterranean seawater strontium characteristics have been constant through the Holocene. For X_{NL}, the best estimate of the isotopic ratio immediately before the initial marine inflow comes from mollusc shells having an age of 9485–9580 cal yr BP, so ~0.708843 (ξ = 0.01).

The parameter that is most poorly known is the concentration of strontium in the Neoeuxine Lake. Major et al. (2006) assumed that modern river concentrations provide an acceptable proxy. However, the Neoeuxine Lake was evaporative for perhaps ~3000–5000 years in the Late Pleistocene after it was last flushed by meltwater from the Scandinavian ice sheet (Tudryn et al., 2016). During its subsequent drawdown to ~ -120 m depth and extended lowstand, river water would have evaporated, leaving behind strontium and other solutes. This would have increased the concentration above that of contemporary rivers. The same process likely explains why the modern evaporative Caspian Sea has a Sr concentration of ~10 ppm (greater than modern seawater) even though it has a salinity ~1/3 of seawater. The larger modern rivers entering the Black Sea supply ~350 km^3 yr^{-1} of water (Oğuz et al., 2004), which would be sufficient to entirely replace the volume of the lowstand Neoeuxine Lake each ~1400 years, so ~4.5 times over ~5000 yr of evaporative conditions.

If all solutes were left behind without incorporation into sediments, the Sr concentration could have increased by this factor relative to river concentrations (so reaching ~0.23×4.5 = 1.04 ppm).

There is a counteracting effect in any isolated basin like the Neoeuxine Lake because of the removal of Sr in carbonates. For example, Upper Pleistocene lacustrine muds in the Black Sea contain ~250 ppm Sr (Piper and Calvert, 2011). If the water column contained only 0.25 ppm Sr, then each meter of ~70% porosity sediment (Opreanu, 2003/2004) would have been capable of sequestering all of the Sr from ~300 m of the overlying water column, assuming no resupply from river inflow.

In order to cover a realistic range of possible Late Pleistocene strontium concentrations in the Neoeuxine Lake, values from approximately those of modern rivers (~0.2 ppm) up to ~1.5 ppm are considered in separate sets of calculations. The 1.5 ppm concentration allows for uncertainty in river concentrations before initial marine inflow, and the duration of evaporative conditions.

Using the concentrations and isotopic ratios for seawater and lake water outlined above and in Table 4.2, the time-varying $^{87}Sr/^{86}Sr$ ratio that might have developed during the transition from the Neoeuxine Lake to the nascent Black Sea can be calculated. First, the scenario of rising water level from –120 m to –30 m (10 m above the sill in the Strait of Bosphorus) is examined to assess whether the $^{87}Sr/^{86}Sr$ 'plateau' at ~0.708965 ($\xi = 0.39$) is consistent with the catastrophic flood proposed by Yanchilina et al. (2017). A level of –30 m is consistent with the ~9.4 cal ka marine water level in the vicinity of the southern

entrance of the Strait of Bosphorus (–25 to –30 m; Lambeck et al., 2007). An equation to calculate a set of ratios for each possible Sr concentration in the pre-reconnection lake is:

$$X_{120-z} = \frac{(1.027\ V_{SW(z)} \times\ C_{SW} \times X_{SW}) + (V_{NL} \times C_{NL} \times X_{NL})}{(1.027\ V_{SW(z)} \times C_{SW}) + (V_{NL} \times C_{NL})} \quad (4.3)$$

where V = volume in km^3, z = elevation of the sea surface after addition of seawater to the precursor –120 m Neoeuxine Lake, *NL* = Neoeuxine Lake values immediately before initial marine inflow – other variables are defined above. The results (Table 4.4, Fig. 4.3) indicate that the Sr concentration of the pre-reconnection lake must have been ~0.85 ppm for the $^{87}Sr/^{86}Sr$ ratio to be consistent with an instantaneous input of ~32,500 km^3 of seawater leading to a water level rise to ~ –30 m depth. This conclusion depends upon water column homogenization after arrival of the seawater; otherwise, surface waters at the M02-45 site after a rise to ~ –30 m could have attained a $^{87}Sr/^{86}Sr$ value close to 0.708965 (ξ = 0.39) in spite of the Sr concentration in the Neoeuxine Lake (C_{NL}) being considerably less than 0.85 ppm. Yanchilina et al. (2017) argue that saline inflow into the lowstand Neoeuxine Lake would have descended to depth and taken significant time to mix with the overlying fresher water mass. This is not an obvious conclusion, because for several centuries after the start of saline inflow, winter chilling likely made the surface waters of the Black Sea denser than the deeper layer(s), which would have initiated downwelling, upwelling (to compensate) in other parts of the sea, thus greater vertical mixing than today (Myers et al., 2003). Even today, winter cooling of surface waters enhances convection and ventilation (Ostrovskii and Zatsepin, 2016). The density structure of the full water column during progressive salination has been modelled by Leonov (2005).

Table 4.4. Modelled $^{87}Sr/^{86}Sr$ ratios based on thorough mixing of Neoeuxine Lake water at –120 m elevation with 10 m-thick increments of Mediterranean water (see text for input parameters). Bold entries bracket the target 'plateau' ratio of 0.708965. The plateau is not reached for Sr concentration in the Neoeuxine Lake, CNL = 1.5 ppm. CNL of 0.84 ppm results in a ratio of exactly 0.708965.

SE	**Volume of**	**<——— ——— CNL alternatives ——— ———>**				
(m)	**lake/sea (km3)**	**0.2 ppm**	**0.3 ppm**	**0.5 ppm**	**1.0 ppm**	**1.5 ppm**
–120	494645	0.708843	0.708843	0.708843	0.708843	0.708843
–110	498055	0.708910	0.708891	0.708874	0.708859	0.708854
–100	501504	0.708954	0.708927	0.708899	0.708874	0.708864
–90	504996	0.708985	0.708955	0.708921	0.708887	0.708874
–80	508532	0.709008	0.708977	0.708940	0.708900	0.708884
–70	512115	0.709027	0.708995	0.708956	0.708912	0.708892
–60	515747	0.709041	0.709010	0.708970	0.708923	0.708901
–50	519431	0.709053	0.709023	0.708983	0.708933	0.708909
–40	523169	0.709063	0.709034	0.708994	0.708943	0.708917
–30	526964	0.709071	0.709044	0.709005	0.708952	0.708925

Calculations based on values for surface- and deep-water salinity extracted from his graphs and modern summer/winter temperature profiles predict seasonal density instability for 2–3 millenia after initial marine inflow. When coupled with surface circulation patterns (precursors to the modern western and eastern gyres), seasonal deeply penetrating convective overturning like that which characterizes modern Lake Baikal (Troitskaya et al., 2015) can be anticipated. Thus, the assumption of rapid vertical homogenization of Sr concentrations and isotopic values during the early phases of the reconnection process is considered to be reasonable, but a full analysis is beyond the scope of this thesis. Why has

this modelling not included the effects of the addition of river water to the Black Sea during the 110 yr postulated entry of saline Mediterranean water?

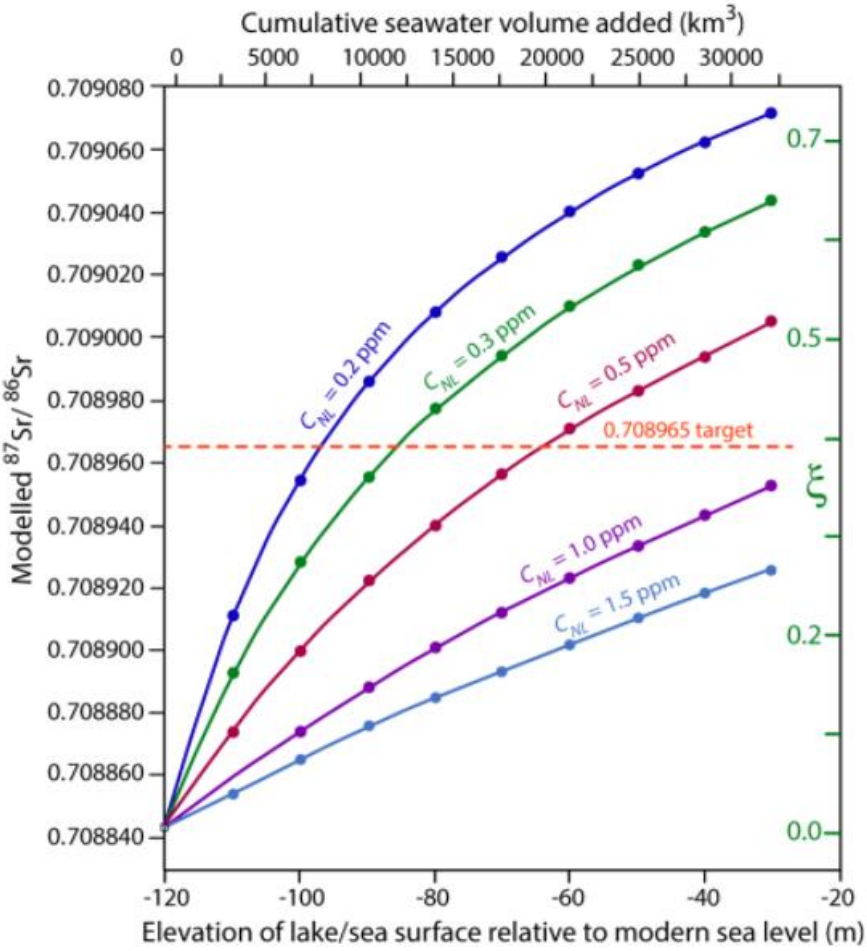

Figure 4.3. Modelled $^{87}Sr/^{86}Sr$ ratios of mixtures of lowstand Neoeuxine Lake water (volume set at its hypthetical –120 m elevation) and increasing amounts of Mediterranean seawater (in 10 m-thick aliquots) until reaching –30 m elevation. Each curve corresponds to a different initial concentration of Sr in the pre-reconnection lake. Assuming the ~350–400 yr-long steady state 'plateau' in isotopic ratio (Figs. 4.1, 4.2) marks the end of a proposed basin-filling inundation (*Flood Hypothesis* of Ryan et al., 2003; Yanchilina et al., 2017), the initial concentration, C_{NL}, must have been slightly less than 1.0 ppm, so significantly higher than the ratio in modern rivers entering the Black Sea. ζ is defined in Section 4.2.

One important tenet of the *Flood Hypothesis* (Ryan et al., 2003) is that the Neoeuxine Lake remained low until the initial marine inflow began, because evaporation

balanced river inflow and direct precipitation onto the lake surface. For this test of the viability of the *Flood Hypothesis*, such a balance has been extended through the entire 110 years required to reach the Sr-isotopic 'plateau' (Figs. 4.1, 4.2). The 'plateau' itself is sufficiently long in duration that it must mark the end of the first phase of filling of the basin. According to the *Flood Hypothesis* (Ryan et al., 2003; Yanchilina et al., 2017), this filling event runs to completion once initiated, because there would be no way to stop the saline inflow rushing down the Bosphorus valley.

4.4.2. Implications of $^{87}Sr/^{86}Sr$ data for marine inflow into a high Neoeuxine Lake

Core M02-45 was raised from a water depth of –69 m yet has a record of Sr-isotopic variation effectively identical (within uncertainty) to trends and values of Yanchilina et al. (2017). The first evidence of marine incursion at this site comes from a sub-seafloor elevation of –76.6 m, ~50 m above the widely accepted lowstand elevation. Hiscott et al. (2007a) have argued from facies descriptions that sedimentation at the M02-45 site was below storm wavebase; they place the effective wavebase today at ~ –40 m. It is therefore a reasonable hypothesis that the ~9.4 cal ka lake level was at, or near, the sill depth in the Strait of Bosphorus, having risen from its late Pleistocene lowstand as river discharges increased and perhaps as the last of a number of ice-dams collapsed in the Altay region of east-central Asia (Hiscott et al., 2017, their supplementary material). This high water level is strongly supported by the secure dating of an outflow delta at the southern exit of the strait to 11.1–10.2 cal ka (Aksu et al., 2016), leaving a gap of only 800 yr between the cessation of delta advance and the first documented arrival of saline water in the Neoeuxine

Lake (Fig. 4.1). Hiscott et al. (2017) have argued that this 800 yr time interval coincided with the advance of a 'salt wedge' up the strait until saline water was eventually able to penetrate into the lake. A water depth in the strait of ~10 m at this time is consistent with requirements for the start of effective two-way flow (Lane-Serff et al., 1997).

Equation 4.3 was used to evaluate the conditions under which underflow into an already high lake could have shifted the $^{87}Sr/^{86}Sr$ ratio from ~0.708843 (ξ = 0.01) to ~0.708965 (ξ = 0.39; the ratio attained at the onset of the 350–400 yr-long 'plateau'). The total volume was fixed throughout these simulations to the volume of the Black Sea basin below –30 m, so $V_{NL} + V_{SW} = 526{,}964$ km^3. Increasing amounts of marine water were added to the modelled lake, displacing and expelling fresh water to maintain a constant total volume. A number of possible pre-reconnection Sr concentrations were tested. This approach does not account for Sr loss in the outflow, but the analysis is only concerned with the first ~110 yr of saline inflow so ignoring the outflow with its rather low Sr concentration is deemed acceptable.

Required volumes of saline inflow range, respectively, from 53,500–7800 km^3 for C_{NL} of 1.5–0.2 ppm (Fig. 4.4). With a ~110 yr duration to reach the 'plateau', discharges of saline water consistent with these volumes are ~485–70 km^3 yr^{-1}, equivalent to ~15,420–2250 m^3 s^{-1}.

As explained in Section 4.4.1, it is reasonable to assume rapid homogenization of the water column because of weak stratification, making the water column susceptible to localized downwelling and upwelling.

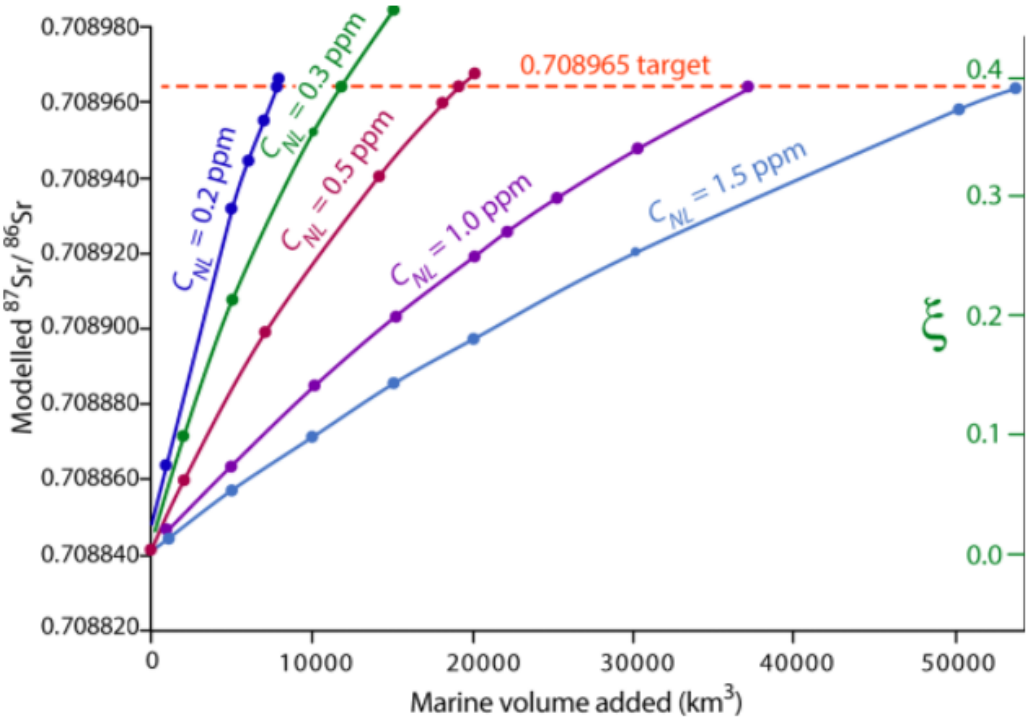

Figure 4.4. Modelled $^{87}Sr/^{86}Sr$ ratios calculated for replacement of increasingly larger volumes of Neoeuxine water by saline Mediterranean water (via underflow) when the Black Sea was at the same level as the global ocean. A simplifying assumption is that the fresh/brackish water expelled to accommodate the inflowing saline water had not mixed with any Mediterranean water. Small volumes of Mediterranean water are able to shift the basinwide isotopic ratio to the ~350–400 yr-long steady state 'plateau' (Figs. 4.1, 4.2) if the initial pre-reconnection Sr concentration in the lake was low, similar to the concentration in modern rivers. ζ is defined in Section 4.2. Plateaux existed from ~9380–9100 cal yr BP and from ~8450–7400 cal yr BP.

Average significant storm wave lengths in the area are <100 m (Aksu et al., 2002b), so wavebase for most of the year is shallower than the modern –50 m contour. Except during severe storms, sea-surface waves are therefore unable to augment the degree of mixing of saline and ambient water beyond that caused by interfacial shear and shedding of eddies from the top of the underflow (Hiscott et al., 2013). At the time of the initial marine inflow, however, water depths on the inner to middle shelf would have been mostly shallower than 50 m and the saline underflow would have been unconfined by high levées,

making wave-enhanced mixing far more likely. As a result, minimally diluted saline water could not reach the slope or deep basins and the water column would have been much better mixed than today.

Regardless of the veracity of the *Flood Hypothesis* or the *Outflow Hypothesis* (Hiscott et al., 2007b), after 9380 cal yr BP there is consensus that the Black Sea was at essentially the same level as the Aegean and Marmara seas, and that there was ongoing and increasing exchange of water across the Strait of Bosphorus. Seawater, being more dense than lower salinity water of the Neoeuxine Lake, would tend to flow northward as a gravity current, initiating two-way exchange flow like today. Twice, for durations of ~350–400 yr and ~1000 yr, the $^{87}Sr/^{86}Sr$ ratios of molluscs stopped increasing (or increased only very slowly), creating what the authors call 'plateaux' in the smoothed isotopic curve (Figs. 4.1, 4.2). At these times, the proportions of river water and saline water in the Black Sea (i.e., the former Neoeuxine Lake) remained more-or-less fixed. Evaporation would have been of no consequence to the Sr-isotopic ratio of the water, since solutes are excluded from the vapour phase. What might have caused the ~9380–8985 and ~8450–7400 cal yr BP interruptions in the evolution of the Black Sea?

Modern conditions can be viewed as a late Holocene steady state which began at ~5 cal ka (Fig. 4.1), characterized by a stable $^{87}Sr/^{86}Sr$ ratio. The modern situation provides guidance on what might have been required to maintain a constant or near-constant $^{87}Sr/^{86}Sr$ ratio in the past. Today, inflow of seawater with practical salinity of ~38 is balanced by brackish outflow (practical salinity ~19). The volume of the outflow is almost exactly double the volume of the inflow (Oğuz et al., 2004). The result is an annual export of the

same amount of seawater that enters, albeit diluted by half before it exists the basin. This is what accounts for the modern steady state.

In the early to middle Holocene, salinity and the $^{87}Sr/^{86}Sr$ ratio rose whenever seawater inflow exceeded the amount of diluted seawater carried through the strait system in the outflow. It would have been quite difficult to reach a balance at those times because the proportion of the saline end-member in the outflow (as part of a diluted mixture) would have been much lower than today, requiring a much stronger outflow than the contemporary inflow. Global sea level rise was continuous through the early Holocene so the only way to restrict seawater inflow (in either absolute or relative terms) would have been for river supply to have increased sufficiently to maintain a strong low-salinity discharge through the Strait of Bosphorus. This would have had two reinforcing consequences. First, a stronger outflow would increase the amount of marine salts and marine strontium leaving the basin, more effectively counteracting contributions from the contemporary undiluted saline inflow along the bottom. Second, a stronger outflow is potentially more effective in blocking or seriously impeding the inflow of Mediterranean water, as sometimes happens even today when particularly strong outflowing currents generated by storm surges and strong winds can reduce the saline inflow to zero (Özsoy et al., 2002). This is because drag along the upper interface of the saline underflow transiting the strait can arrest its forward movement regardless of the presence of a favourable bottom slope. If fully blocked for an extended time, one might anticipate a slow drop in the $^{87}Sr/^{86}Sr$ ratio of molluscs. Prolonged blockage might explain the minor apparent $^{87}Sr/^{86}Sr$ decline in the younger plateau around 7400 cal yr BP (Fig. 4.1). The older plateau is

characterized by a very slow rise in $^{87}Sr/^{86}Sr$ ratio (Fig. 4.2), although there may have been steady-state conditions for decades at a time.

What if the pre-reconnection Neoeuxine Lake had a strontium concentration closer to 0.85 ppm rather than the ~0.23 ppm of modern rivers? River inflow through the Holocene would gradually reduce the strontium contribution of the fresh-water component of mixed basin waters. Even if the proportion of Mediterranean water remained constant (i.e., a steady-state condition for salinity), the $^{87}Sr/^{86}Sr$ ratio would continue to increase because of a progressive reduction in the strontium concentration in the fluvial component. Such a situation would make it even more difficult to reach and maintain a steady strontium isotopic ratio, and might account for the slow rise in $^{87}Sr/^{86}Sr$ during the time of the older plateau (Fig. 4.2) when a shallower water depth in the strait (~20–25 m shallower than today; Lambeck et al., 2007) would have favoured episodic blockage of Mediterranean inflow. Blockage of the saline inflow might have been seasonal – less blockage in autumn–winter when river discharges tend to be lower and greater blockage in spring when rivers reach peak discharge (Esin et al., 2016).

Between the first and second plateaux, from ~8985–8450 cal yr BP, the $^{87}Sr/^{86}Sr$ ratio rose rapidly (Fig. 4.1), indicating renewed and temporarily strong entry of saline water into the Black Sea. This time interval overlaps with the "first pulse" of significant seawater entry into the Black Sea, sufficient to leave a record of elevated total sulfur (as sedimentary sulfides) and enrichment in $\delta^{34}S$ to ~+30‰ (Hiscott et al., 2007a). The sulfur stable-isotope values indicate that the sulfate delivered by this pulse of marine water was entirely consumed by sulfate-reducing bacteria in the accumulating sediments. The final sulfur

isotopic ratio eventually climbed upward to seawater values because the entire pool of sulfate was consumed, preventing isotopic fractionation. This consumption of available sulfate likely occurred during the early stages of the second plateau when new seawater (and additional sulfate) was largely blocked from entering the basin.

4.5. Summary

The 10 m-thick Holocene succession at core site M02-45 (41°41.17N, 28°19.08E, −69m water depth) has key advantages for investigation of the Sr-isotopic evolution of the Holocene Black Sea. Earlier studies have focussed on thinner successions and coquinas. At the M02-45 site (augmented by nearby core M05-03P), $^{87}Sr/^{86}Sr$ determinations on mollusc shells extracted at mostly 10–20 cm depth increments provide a temporal resolution mostly <200 years in sediment older than ~5500 cal yr BP, and ~20–25 years for the early Holocene reconnection between the Neoeuxine Lake (today's Black Sea) and the global ocean. Isotopic measurements are in stratigraphic order, so temporal trends are unambiguous. Measurements were made using a Neptune multi-collector inductively coupled plasma mass spectrometer (MC-ICPMS) and have 1σ uncertainties of ~±0.000015. There are four stages of $^{87}Sr/^{86}Sr$ increase and salination associated with the reconnection. From 12,145–9580 cal yr BP (stage A), before first Mediterranean inflow, the Sr-isotopic ratio varied from 0.708847–0.708881. Modelling suggests that the Sr concentration in the Neoeuxine Lake might have been several times higher than modern river values because of evaporative concentration. For ~100 years immediately before reconnection (9580–9490 cal yr BP, stage B), $^{87}Sr/^{86}Sr$ values dropped to their lowest levels: 0.708841–0.708843. Abruptly (in geological terms), $^{87}Sr/^{86}Sr$ then began to climb starting 9465–9490 cal yr BP

and reached a quasi-steady-state 'plateau' with ratios ~0.708965 by ~9380 cal yr BP (stage C). The sharp $^{87}Sr/^{86}Sr$ increase marks the first significant intrusion of saline water into a previously isolated Neoeuxine Lake.

The quasi-steady-state condition lasted 350–400 years. Subsequently, starting ~8985 cal yr BP and proceeding to the present day, there was a step-wise rise of $^{87}Sr/^{86}Sr$ to modern levels (stage D), during which a salinity threshold was passed that allowed widespread replacement of brackish-water faunas by Mediterranean species. Modelling suggests that the lake/sea level likely did not, and could not, rise from −120m to −30m between 9490 and 9380 cal yr BP unless (a) the Sr concentration in the pre-reconnection Neoeuxine Lake was 3–4 times higher than today, or (b) the water column was strongly stratified during first entry of saline water. The second alternative is very unlikely because of seasonal vertical mixing (downwelling/upwelling) in what was then a rather homogeneous temperate lake. Catastrophic flooding of a lowstand lake would require an average discharge through the Strait of Bosphorus of ~9500 $m^3\ s^{-1}$, whereas saline entry of Mediterranean water as an underflow into an already high lake could reproduce the first stage of $^{87}Sr/^{86}Sr$ increase with an average discharge as low as ~2200 $m^3\ s^{-1}$. Because the M02-45 site is ~50m above the Late Pleistocene lowstand shoreline and contains sub-wavebase sediments with $^{87}Sr/^{86}Sr$ values that record the first entry of saline water into the Neoeuxine Lake, the surface of the lake must have been significantly higher than −70m at the time of the reconnection. Two prominent 'plateaux' which punctuate the long-term $^{87}Sr/^{86}Sr$ increase are attributed to decadal to centennial periods of increased discharge from

European rivers, creating a positive hydrological balance and effectively blocking or seriously impeding saline-water advance up the Strait of Bosphorus toward the Black Sea.

Chapter 5. Oxygen and carbon isotopes and trace element/Ca ratios in ostracods Loxoconcha lepida and Palmoconcha agilis in composite cores M02-45 and M05-50

Ostracods are found in almost all aquatic environments and even on damp-vegetation (Schornikov, 1969; De Deckker, 1980; Horne et al., 2004). They can be divided into marine, brackish and freshwater types. In addition to being ubiquitous in aquatic environments, ostracods leave an excellent fossil record. The strongly calcified carapace or valve is typically the only part of the ostracod that is preserved as a fossil. Laboratory experiments as well as studies in natural environments show that the stable isotope geochemistry of ostracod shells accurately records environmental conditions (e.g., Heaton et al., 1995; Decrouy, 2009;). Two long composite cores together provide a complete latest Pleistocene–Holocene sedimentary record, with 16 radiocarbon-dated mollusc shells in core M02-45 (Section 3.2.1) and 9 in core M05-50 (Section 3.2.2).

This chapter presents stable-isotopic and trace-element data on ostracod shells from composite cores M02-45 and M05-50 and offers environmental interpretations for the southwestern Black Sea shelf based on these results. A peer-reviewed paper based on the same work and data has been published in the international journal *Palaeogeography, Palaeoclimatology, Palaeoecology* (Ankindinova et al., 2019b).

5.1 Constructing oxygen and carbon isotopic curves

Stable isotopic values are listed in Table 5.1. Analytical methods are described in Sections 2.4.2–2.4.4. Because both composite cores recovered sedimentary successions

that contain the brackish Neoeuxine Lake stage as well as the post-reconnection marine stage (Hiscott et al., 2007a,b; Williams et al., 2018; Ankindinova et al., 2019a), the oxygen and carbon isotopic values could not be obtained using a single species of ostracod. Williams et al. (2018) document two dominant species in these cores: *Palmoconcha agilis* dominates the marine sediments (including the contemporary sediments in the Black Sea), whereas *Loxoconcha lepida* dominates the lower Holocene and uppermost Pleistocene lacustrine sediments. The oxygen and carbon isotopic data were acquired on these two species, which precludes the construction of a single oxygen or carbon isotopic curve for each core unless isotopic offsets between the two species are known. The literature is mute regarding the vital effects (i.e., species-dependent deviations from oxygen and carbon isotopic equilibria) for *P. agilis* and *L. lepida*. The remedy selected for this study was to obtain and compare pairs of oxygen and carbon isotopic measurements on both species in samples where they co-occur at the same core depths. Williams et al. (2018) showed that the lacustrine to marine transition in core M05-50 occurs across a 90 cm-thick zone where both marine and brackish fauna co-occur; the transition is thinner (60 cm) in core M02-45. Both *P. agilis* and L. *lepida* were collected in 15 samples across these transitional intervals to quantify stable isotopic offsets between the two species. Comparison of the results for the different species provides an estimate of the vital effect for $\delta^{18}O$ and $\delta^{13}C$: the $\delta^{18}O$ values for *P. agilis* are determined to be ~2.6‰ more positive than determinations on coeval *L. lepida* (i.e., 2.56 ±0.83‰), and its $\delta^{13}C$ values are ~1.7‰ more negative than determinations on coeval *L. lepida* (i.e., 1.72 ±0.50‰). The $\delta^{18}O$ and $\delta^{13}C$ data are plotted against time (Fig. 5.1); the raw data are given in Table 5.1. The scales for *P. agilis* and *L. lepida* are shifted relative to one another to account for the differences in vital effect (Fig.

5.1). However, to allow a coherent description of isotopic variations for the entire Holocene section, all $\delta^{18}O$ and $\delta^{13}C$ values in the rest of the paper are assessed relative to the scales for *P. agilis* (with corresponding measurements on *L. lepida* in brackets).

Table 5.1. Oxygen and carbon isotopic composition of samples from composite cores M02-45 and M05-50. Values are shown relative to the standard PDB. Ages are rounded to the nearest 5 years. See text for explanations.

M02-45 composite

Core	Age	Depth (cm)		P. agilis	L. lepida	P. agilis	L. lepida
	Cal yrBP	Composite	Raw	$\delta^{13}C$	$\delta^{13}C$	$\delta^{18}O$	$\delta^{18}O$
M02-45T	0	0	0	-4.64		-2.30	
M02-45T	120	30	30	-4.09		-0.33	
M02-45T	160	40	40	-4.21		0.59	
M02-45T	240	60	60	-4.76		-1.06	
M02-45T	280	70	70	-4.14		-0.21	
M02-45T	315	80	80	-4.90		-2.02	
M02-45T	355	90	90	-4.19		0.06	
M02-45T	370	100	100	-3.66		0.10	
M02-45P	375	110	0	-4.24		0.01	
M02-45P	380	120	10	-4.06		0.50	
M02-45P	390	140	30	-4.03		-0.10	
M02-45P	460	150	40	-3.54		-0.12	
M02-45P	595	160	50	-3.74		0.10	
M02-45P	725	170	60	-4.28		0.56	
M02-45P	860	180	70	-4.40		-0.62	
M02-45P	1125	200	90	-3.93		-0.10	
M02-45P	1255	210	100	-3.85		0.02	
M02-45P	1390	220	110	-3.77		0.44	
M02-45P	1520	230	120	-4.59		-0.25	
M02-45P	1785	250	140	-3.48		0.82	
M02-45P	1920	260	150	-4.37		-0.34	
M02-45P	2050	270	160	-4.26		0.36	
M02-45P	5475	280	170	-5.59		0.67	
M02-45P	5485	290	180	-4.32		0.20	
M02-45P	5500	300	190	-5.21		-0.39	
M02-45P	5535	330	220	-5.23		0.57	
M02-45P	5630	340	230	-5.60		-1.22	
M02-45P	5725	350	240	-5.65		-1.80	

Table 5.1 continued

M02-45P	5820	360	250	-4.77		0.51	
M02-45P	6195	400	290	-5.79		0.23	
M02-45P	6290	410	300	-5.78		2.07	
M02-45P	6610	430	320	-5.45		0.94	
M02-45P	7115	460	350		-4.06		1.82
M02-45P	7285	470	360		-3.44		3.42
M02-45P	7450	480	370		-3.21		0.88
M02-45P	7620	490	380		-2.63		2.19
M02-45P	7785	500	390	-2.92	1.76		
M02-45P	7955	510	400	-3.70	2.32		
M02-45P	8105	520	410	-3.36	1.83		
M02-45P	8225	530	420	-3.36	0.37		
M02-45P	8460	550	440	-3.31	3.33		
M02-45P	8580	560	450	-3.36	3.06		
M02-45P	8940	590	480	-2.95	0.99		
M02-45P	9165	620	510	-3.84	-0.74		
M02-45P	9195	630	520	-3.18	-0.76		
M02-45P	9220	640	530	-2.90	-2.49		
M02-45P	9430	770	660	-3.96	-3.16		
M02-45P	9450	780	670	-3.30	-3.50		
M02-45P	9475	790	680	-3.74	-2.30		
M02-45P	9520	810	700	-3.14	-3.40		
M02-45P	9560	830	720	-3.06	-3.58		
M02-45P	9605	850	740	-3.26	-3.34		
M02-45P	9710	870	760	-3.13	-3.97		
M02-45P	9960	890	780	-3.28	-2.65		
M02-45P	10210	910	800	-3.39	-4.91		
M02-45P	10360	930	820	-2.91	-3.80		
M05-03P	10390	942	640	-2.76	-3.72		
M05-03P	10420	952	650	-2.99	-3.98		
M05-03P	10470	972	670	-2.86	-5.22		
M05-03P	10570	982	680	-2.37	-4.28		
M05-03P	10975	992	690	-2.90	-3.16		
M05-03P	11375	1002	700	-2.15	-4.83		
M05-03P	11780	1012	710	-3.12	-4.06		

M05-50 composite

Core	**Age**	**Depth (cm)**		**P. agilis**	**L. lepida**	**P. agilis**	**L. lepida**
	Cal yrBP	**Composite**	**Raw**	**$\delta^{13}C$**	**$\delta^{13}C$**	**$\delta^{18}O$**	**$\delta^{18}O$**
M05-50P	5755	440	490	-4.26		1.07	
M05-50P	5880	450	500	-4.12		0.78	

Table 5.1 continued

M05-50P	6005	460	510	-5.16		0.68	
M05-50P	6125	470	520	-4.78		0.63	
M05-50P	6250	480	530	-4.74		0.5	
M05-50P	6375	490	540		-3.74		-2.03
M05-50P	6620	510	560	-4.53		0.54	
M05-50P	6620	510	560	-5.47		0.25	
M05-50P	6620	510	560		-2.92		-1.92
M05-50P	6745	520	570		-3.1		-3.2
M05-50P	6745	520	570	-4.19		0.2	
M05-50P	6745	520	570		-3.13		-3.06
M05-50P	6865	530	580		-2.68		-0.59
M05-50P	6990	540	590		-3.39		-3.24
M05-50P	6990	540	590	-5.4		0.99	
M05-50P	7115	550	600		-2.88		-1.32
M05-50P	7115	550	600	-4.78		1.36	
M05-50P	7115	550	600		-2.98		-1.18
M05-50P	7240	560	610		-2.73		-1.99
M05-50P	7360	570	620		-2.82		-3.53
M05-50P	7485	580	630	-5.26		1.2	
M05-50P	7610	590	640		-2.71		-2.08
M05-50P	7730	600	650		-3.23		-2.4
M05-50P	7855	610	660		-3.02		-0.6
M05-50P	7980	620	670		-3.29		-1.42
M05-50P	7980	620	670		-2.83		-0.43
M05-50P	8100	630	680		-2.95		-0.88
M05-50P	8100	630	680		-2.99		-1.22
M05-50P	8225	640	690		-3.28		-1.12
M05-50P	8225	640	690		-3.32		-1.6
M05-50P	10820	650	700	-5.12		1.67	
M05-50P	10820	650	700		-2.54		-3.14
M05-50P	10820	650	700		-3.42		-1.5
M05-50P	10960	660	710		-2.54		-2.06
M05-50P	10960	660	710		-2.94		-1.33
M05-50P	11095	670	720		-3.38		-2.73
M05-50P	11095	670	720		-2.72		-2.8
M05-50P	11230	680	730		-2.73		-3.71
M05-50P	11370	690	740		-3.05		-0.76
M05-50P	11505	700	750		-2.74		-1.18
M05-50P	11505	700	750		-3.31		-2.81
M05-50P	11640	710	760		-2.98		-1.25
M05-50P	11780	720	770		-3.33		-1.74
M05-50P	11915	730	780		-2.91		-1.54
M05-50P	12025	750	788		-3.26		-2.52

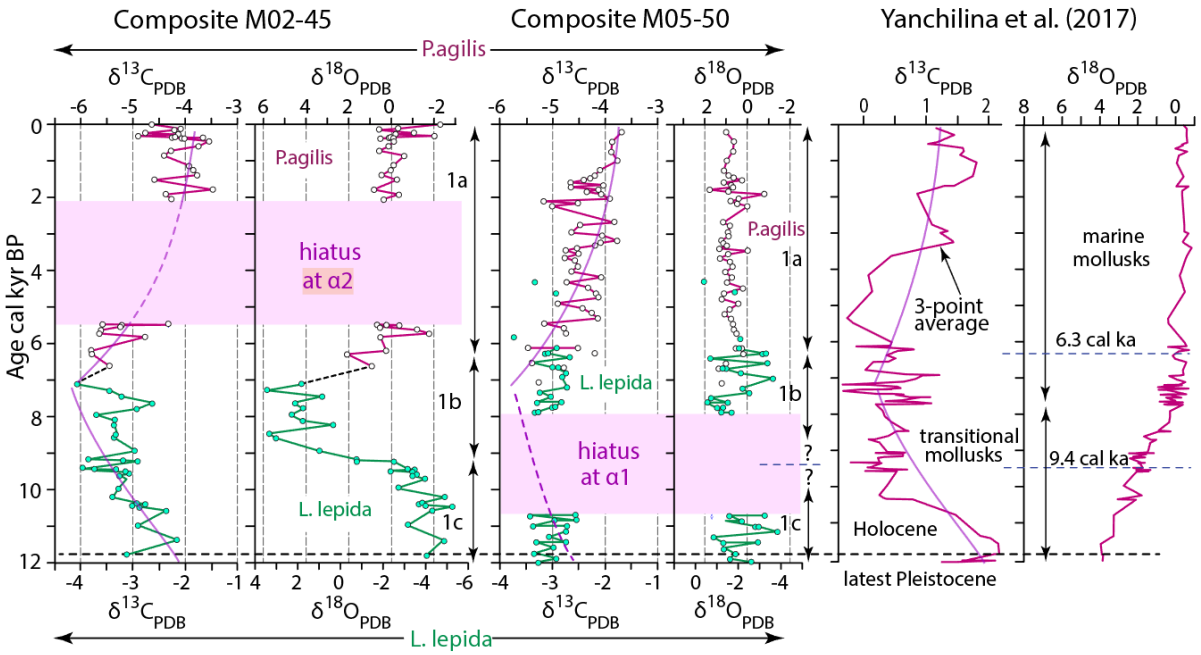

Figure 5.1 Oxygen ($\delta^{18}O$) and carbon ($\delta^{13}C$) isotopic compositions relative to Pee Dee Belemnite (PDB) plotted against age (cal ka) in composite cores M02-45 and M05-50. Replicates of $\delta^{18}O$ and $\delta^{13}C$ measurements have average reproducibility of ~0.5‰. Also shown are $\delta^{18}O$ and $\delta^{13}C$ for mollusc shells (data from Yanchilina et al., 2017, their Supplementary material 3; converted to calibrated ages using the reservoir corrections of Williams et al., 2018). Hiatuses at α_1 and α_2 are described in the text. Pleistocene–Holocene boundary is placed at 11.7 cal ka (Walker et al., 2009). Isotopic substages 1a–1c are described in the text.

5.2 Oxygen isotopes

Three distinct oxygen isotopic substages are recognized (Fig. 5.1), labeled 1c–1a in accordance with isotopic stage and substage labeling conventions (e.g., Lisiecki and Raymo, 2005). Substage 1c is identified between the deepest and oldest sample near the base of core M02-45 at ~12.1 cal ka and the substage top at ~9.1 cal ka. Most of substage 1c in core M02-45 has $\delta^{18}O$ values in the range 0‰ to –2.0‰ (*L. lepida* values of ~ –3.0‰ to –5.0‰), increasing slowly and irregularly upward. A large portion of this substage straddles the hiatus at α1 in core M05-50. Substage 1b occurs from 9.1–6.3 cal ka in core

M02-45, but a large portion of the substage is not represented in core M05-50 because of the 10.7–8.3 cal ka hiatus across the α1 unconformity at that site. Across the transition from substage 1c into the lower part of substage 1b in core M02-45, there is a major increase in $\delta^{18}O$ values from ~ –1.5‰ to +6.0‰ (*L. lepida* values of ~ –3.5‰ to +3.5‰). Values then decrease slightly to ~ +5.0‰ to +3.0‰ (*P. agilis* scale), remaining approximately static from ~8.2–7.4 cal ka, before sharply decreasing upward to +1.0‰ to +2.0‰ at the top of substage 1b. The character of substage 1b observed in core M02-45 is not apparent in core M50-50, perhaps because sediments equivalent in age to the lower part of substage 1b and the top of substage 1c are missing at the α1 unconformity. Substage 1a extends from ~6.3 cal ka to the tops of both cores and exhibits near-constant $\delta^{18}O$ values around 0.0 to +1.0‰ (Fig. 5.1). Substage 1a straddles the α2 hiatus in core M02-45, but this interval (from ~6.3–1.2 cal ka) is conformable at the M05-50 site.

5.3 Carbon isotopes

Substage 1c in core M02-45 has $\delta^{13}C$ values of ~ –4.3‰ to –5.0‰ (*P. agilis* scale) in the lower part decreasing to mostly ~ –5.0‰ to –5.5‰ at the top (Fig. 5.1). In core M05-50, substage 1c is largely within the hiatus at α1 but where preserved shows rather consistent values of –4.5‰ to –5.5‰ (*P. agilis* scale). Substage 1b resembles 1c in core M05-50, but in core M02-45 there are several peaks and troughs between –5.0‰ and –6.0‰ (*P. agilis* scale) with no apparent trend (*L. lepida* values of ~ –4‰ to –3‰). The upward passage into substage 1a (from ~6.3 cal ka to Present) is characterised by $\delta^{13}C$ values ranging from –5.0‰ to –5.5‰ at the base of the substage to ~ –3.5‰ to –4.5‰ at

the tops of the cores (Fig. 5.1). A large portion of this substage is masked by the hiatus at α2 in core M02-45.

5.4 Trace-element concentrations and element/Ca ratios

Minor- and trace-element data are listed in Table 5.1. Methods are described in Section 2.4.5–2.4.6. The individual analyses carried out on 4–6 valves at each sampling depth show scatter around mean values that significantly exceeds analytical error (as quantified in Table 5.2 and shown by standard deviations in Table 5.3). For several element/Ca ratios, such as B*, Ba*, Fe*, La*, Mg* and Sr*, envelopes one standard deviation wide around mean downcore trends (Figs. 5.2, 5.3) define narrow bands, yet for others, such as Cd*, Ce*, Mo*, V*, Zn* and Zr*, these bands are relatively broad. Correlation coefficients based on primary data (Table 5.1) indicate that V* shows a clear reciprocal relationship to Mg* and Sr* ($r < -0.5$) in core M02-45, whereas many elements – Ba*, Cd*, Ce*, Fe*, La*, Mo*, Rb*, U*, Zn* and Zr* – behave this way in core M05-50. In core M02-45, Mg* and Sr* have weak reciprocal relationships with Ba*, Fe* and Rb*.

In core M02-45 (Fig. 5.2) most element/Ca ratios are lowest before reconnection, climb during the ~9.4–6.3 cal ka environmental transition to conditions agreeable to marine faunas, then either remain rather steady (Ce*, La*, Mo*, Sr*, Ti*, U*, Zr*) or increase further toward the Present (B*, Cd*, Cu*, Pb*, Zn*). A few elements in core M02-45 have relatively high ratios before reconnection (Ba*, Fe*, V*). Mg* and Sr* are considerably higher after ~6.3 cal ka than before. Many elements show spiky variations in abundance just before to just after reconnection (during ~10.0–8.5 cal ka).

Table 5.2. Quantification of the degree of scatter determined by plotting standard deviation at each depth against average abundance at that depth (both in ppm), and fitting a regression line passing through (0,0) to obtain a relationship between 'amount present' and 'average scatter', expressed here as a percentage of the amount present.

Element	Range in valves (ppm)	Average scatter as % of amount present
B	7.8 – 99	± 13.3
Ba	34 – 92	± 14.4
Cd	0.03 – 0.83	± 46.5
Ce	0.82 – 81	± 36.0
Cu	2.8 – 330	± 46.8
Fe	154 – 5728	± 45.4
La	0.82 – 32.3	± 13.3
Mg	4182 – 9127	± 13.4
Mn	239 – 1504	± 23.4
Mo	0.13 – 0.36	± 78.3
P	121 – 7345	± 26.7
Pb	0.48 – 25.4	± 34.1
Rb	0.07 – 4.6	± 71.2
Sr	1483 – 3561	± 8.5
Ti	0.66 – 68.6	± 43.4
U	0.06 – 1.76	± 27.9
V	0.13 – 5.1	± 55.1
Zn	9.8 – 279	± 42.5
Zr	0.04 – 5.2	± 42.7

Table 5.3. Molar ratios of trace elements (mmole/[mol Ca]) in composite cores M02-45 and M05-50 shown as element*. Composite Depth (cm), Age (cal yr BP), Core identifiers T = trigger weight core, P = piston core.

Core	Species	Depth	Age	Temp	B*	Mg*	P*	Ti*	V*	Mn*	Fe*	Cu*	Zn*
M02-45T	P. agilis	60	240	21.84328	0.65665	37.68894	7.96383	0.08240	0.00248	0.97564	2.62400	0.22837	0.43406
M02-45T	P. agilis	80	320	21.35375	0.94741	36.92881	7.22343	0.07095	0.00166	0.82129	3.56049	0.14356	0.37196
M02-45T	P. agilis	100	370	16.87897	0.61469	29.98038	6.47248	0.15864	0.00331	1.05013	1.23909	0.21145	0.29115
M02-45P	P. agilis	120	380	18.69515	0.62640	32.80054	8.63100	0.06566	0.00166	1.05589	2.77095	0.60280	0.77311
M02-45P	P. agilis	140	390	23.07269	0.96692	39.59797	9.09417	0.08483	0.00083	0.90864	2.91545	0.21742	0.34325
M02-45P	P. agilis	160	595	16.65209	0.56688	29.62808	6.94144	0.12912	0.00207	0.79921	3.03294	0.15103	0.29873
M02-45P	P. agilis	180	860	18.46463	0.82740	32.44259	6.32195	0.06434	0.00083	0.75832	2.33047	0.08614	0.23405
M02-45P	P. agilis	200	1125	13.16279	0.48297	24.20992	5.97593	0.07800	0.00041	0.81150	2.08851	0.10456	0.32728
M02-45P	P. agilis	220	1390	19.05838	0.48785	33.36457	6.85732	0.07910	0.00062	0.98966	2.22790	0.19966	0.45003
M02-45P	P. agilis	230	1520	18.41573	0.70348	32.36667	7.03271	0.10730	0.00083	0.97468	2.92584	0.09875	0.28389
M02-45P	P. agilis	270	2050	21.21907	0.69177	36.71968	6.86243	0.09430	0.00041	1.21101	1.87526	0.06191	0.12565
M02-45P	P. agilis	290	5485	15.68672	0.64884	28.12906	12.58975	0.09144	0.00062	2.17839	2.24774	0.15518	0.27211
M02-45P	P. agilis	330	5535	14.07563	0.40492	25.62737	9.14083	0.08879	0.00269	1.32044	2.76037	0.08149	0.16711
M02-45P	P. agilis	350	5725	13.68669	0.47712	25.02343	25.01467	0.15115	0.00145	1.58537	5.55852	0.16049	0.28292
M02-45P	P. agilis	400	6195	15.72779	0.46053	28.19284	5.40276	0.09474	0.00145	0.98102	1.27838	0.07103	0.16469
M02-45P	P. agilis	410	6290	15.37573	0.41955	27.64617	3.56642	0.05751	0.00124	0.96182	1.11707	0.12282	0.23453
M02-45P	P. agilis	430	6560	10.52710	0.49566	20.11723	9.19021	0.12537	0.00228	1.25708	2.64818	0.09095	0.18969
M02-45P	P. agilis	480	7260	14.15470	0.44882	25.75016	6.58248	0.06852	0.00166	2.88795	2.87295	0.06489	0.09242
M02-45P	P. agilis	490	7445	13.39554	0.53566	24.57133	3.58822	0.05024	0.00166	1.89254	2.94661	0.02523	0.04468
M02-45P	P. agilis	500	7670	14.08485	0.49663	25.64169	4.71549	0.09254	0.00393	2.08068	3.65682	0.04166	0.06129
M02-45P	P. agilis	530	8325	13.86830	0.44882	25.30544	4.54862	0.07425	0.00269	1.29087	2.50840	0.04813	0.07597
M02-45P	L.lepida	560	8655	13.12171	0.37077	24.14614	10.17172	0.05266	0.00145	1.10964	0.83299	0.12896	0.19243
M02-45P	L.lepida	580	8875	9.86573	0.35321	19.09026	7.13829	0.03151	0.00352	0.64832	1.67353	0.13410	0.20969
M02-45P	L.lepida	600	9095	12.54808	0.42248	23.25541	5.59893	0.02600	0.00186	1.04821	1.06626	0.06954	0.17307
M02-45P	L.lepida	620	9195	12.81352	0.41272	23.66758	6.33455	0.02600	0.00269	1.05685	2.38185	0.09958	0.08000
M02-45P	L.lepida	640	9260	10.77382	0.46834	20.50034	7.05655	0.01278	0.00352	0.86199	3.72577	0.07552	0.11033

Table 5.3 continue

Core	Species	Depth	Age	Temp	B*	Mg*	P*	Ti*	V*	Mn*	Fe*	Cu*	Zn*
M02-45P	L.lepida	660	9320	12.64867	0.34833	23.41160	5.51855	0.04120	0.00290	0.89578	3.15061	0.07518	0.06581
M02-45P	L.lepida	680	9380	13.41426	0.27417	24.60040	4.68212	0.04230	0.00663	0.94166	4.55837	0.15751	0.13146
M02-45P	L.lepida	700	9400	12.71573	0.35516	23.51573	7.55208	0.03790	0.00393	1.08430	3.49910	0.12946	0.13307
M02-45P	L.lepida	720	9415	13.77051	0.32686	25.15359	9.30600	0.03613	0.00642	0.93494	4.50813	0.21576	0.22485
M02-45P	L.lepida	740	9430	13.89625	0.28295	25.34883	7.08891	0.05751	0.00621	0.98870	4.81847	0.11717	0.13291
M02-45P	L.lepida	770	9485	14.28742	0.35516	25.95624	6.59849	0.01586	0.00414	1.00751	2.90412	0.07635	0.15694
M02-45P	L.lepida	780	9510	11.39551	0.34833	21.46570	6.64889	0.03569	0.00497	0.79672	3.70877	0.10141	0.12243
M02-45P	L.lepida	800	9555	11.82161	0.29759	22.12735	8.05442	0.03481	0.00932	0.99772	5.76101	0.11137	0.07920
M02-45P	L.lepida	820	9600	12.47823	0.31710	23.14694	9.33154	0.08835	0.01284	1.15668	11.79590	0.12166	0.17582
M02-45P	L.lepida	840	9645	14.57382	0.33467	26.40096	8.64360	0.07954	0.01180	1.09524	10.81842	0.08282	0.07629
M02-45P	L.lepida	860	9690	10.04734	0.34442	19.37227	7.16111	0.06941	0.00745	1.27379	6.54167	0.06904	0.05162
M02-45P	L.lepida	880	9760	15.82642	0.32589	28.34600	7.78639	0.03834	0.01160	0.81342	15.24306	0.06572	0.08855
M02-45P	L.lepida	900	9840	12.47544	0.38345	23.14260	7.36919	0.07249	0.01056	1.31314	7.20409	0.04282	0.04565
M02-45P	L.lepida	920	9915	13.65651	0.34345	24.97657	6.79432	0.07403	0.00704	1.10254	5.42101	0.06606	0.09065
M02-45P	L.lepida	930	9955	12.40838	0.12030	23.03847	4.63938	0.05603	0.00557	1.63605	4.92991	0.04669	0.19266
M05-03P	L.lepida	942	10000	17.56073	0.17036	31.03903	1.18177	0.03420	0.00661	0.69305	3.13550	0.03577	0.37234
M05-03P	L.lepida	952	10090	15.41485	0.16441	27.70691	0.75674	0.03162	0.00828	0.97641	4.27826	0.04133	0.13430
M05-03P	L.lepida	962	10205	16.58279	0.10489	29.52048	0.74244	0.03041	0.00408	1.85990	2.62022	0.01998	0.12420
M05-03P	L.lepida	972	10320	13.12786	0.16080	24.15569	0.56602	0.02212	0.00331	0.94108	2.41396	0.02503	0.13572
M05-03P	L.lepida	982	10695	13.91161	0.13035	25.37269	0.61030	0.03591	0.00497	0.73720	2.11117	0.02400	0.14304
M05-03P	L.lepida	992	11180	12.06191	0.09055	22.50047	0.41277	0.01472	0.00416	0.91690	2.99308	0.01605	0.03649
M05-03P	L.lepida	1002	11660	11.74896	0.07884	22.01454	0.66683	0.01575	0.00282	1.22829	3.84231	0.01090	0.03468
M05-03P	L.lepida	1012	12145	13.63220	0.07610	24.93882	0.41958	0.01681	0.00234	1.29740	2.08624	0.01037	0.03007

Core	Species	Depth	Age	Rb*	Sr*	Zr*	Mo*	Cd*	Ba*	La*	Ce*	Pb*	U*
M02-45T	P. agilis	60	240	0.00099	3.98108	0.00266	0.00011	0.00056	0.05200	0.01913	0.04750	0.01049	0.00033
M02-45T	P. agilis	80	320	0.00173	3.90621	0.00208	0.00044	0.00028	0.05038	0.01222	0.02747	0.01013	0.00032

Table 5.3 continued

Core	Species	Depth	Age	Rb*	Sr*	Zr*	Mo*	Cd*	Ba*	La*	Ce*	Pb*	U*
M02-45T	P. agilis	100	370	0.00000	4.16141	0.00139	0.00011	0.00028	0.05561	0.01602	0.04065	0.02520	0.00026
M02-45P	P. agilis	120	380	0.00000	4.06065	0.00197	0.00044	0.00000	0.05415	0.01602	0.03990	0.03100	0.00033
M02-45P	P. agilis	140	390	0.00185	4.05367	0.00173	0.00033	0.00075	0.05322	0.00562	0.01046	0.01293	0.00029
M02-45P	P. agilis	160	595	0.00568	3.88418	0.00254	0.00055	0.00028	0.04831	0.01222	0.01957	0.01145	0.00029
M02-45P	P. agilis	180	860	0.00136	4.10603	0.00127	0.00022	0.00028	0.04677	0.00987	0.02108	0.00906	0.00024
M02-45P	P. agilis	200	1125	0.00000	3.88334	0.00220	0.00000	0.00019	0.04631	0.01777	0.04426	0.01924	0.00047
M02-45P	P. agilis	220	1390	0.00074	4.06306	0.00173	0.00033	0.00028	0.05430	0.02012	0.05043	0.00886	0.00043
M02-45P	P. agilis	230	1520	0.00037	4.14901	0.00220	0.00000	0.00019	0.05246	0.01724	0.02845	0.01049	0.00042
M02-45P	P. agilis	270	2050	0.00025	3.66401	0.00312	0.00022	0.00047	0.03786	0.01632	0.03448	0.00825	0.00078
M02-45P	P. agilis	290	5485	0.00136	4.18909	0.00428	0.00022	0.00066	0.05868	0.01040	0.02183	0.01094	0.00040
M02-45P	P. agilis	330	5535	0.00099	3.87130	0.00312	0.00011	0.00038	0.05568	0.01238	0.02921	0.00596	0.00027
M02-45P	P. agilis	350	5725	0.00136	4.30646	0.00439	0.00033	0.00038	0.07058	0.01336	0.02838	0.00962	0.00044
M02-45P	P. agilis	400	6195	0.00099	3.82580	0.00382	0.00022	0.00038	0.06405	0.02453	0.06097	0.00799	0.00059
M02-45P	P. agilis	410	6290	0.00074	4.25891	0.00254	0.00011	0.00028	0.06989	0.02270	0.05615	0.00606	0.00035
M02-45P	P. agilis	430	6560	0.00099	3.25497	0.00451	0.00000	0.00047	0.04424	0.01762	0.04381	0.00743	0.00073
M02-45P	P. agilis	480	7260	0.00111	2.86953	0.00370	0.00011	0.00028	0.06482	0.01534	0.04110	0.00596	0.00062
M02-45P	P. agilis	490	7445	0.00136	2.94657	0.00162	0.00011	0.00019	0.05246	0.01116	0.02544	0.00489	0.00038
M02-45P	P. agilis	500	7670	0.00185	2.91551	0.00324	0.00022	0.00028	0.05622	0.01017	0.02522	0.00479	0.00078
M02-45P	P. agilis	530	8325	0.00173	2.93670	0.00266	0.00011	0.00038	0.05100	0.01147	0.03131	0.00479	0.00047
M02-45P	L.lepida	560	8655	0.00025	2.53633	0.00243	0.00022	0.00019	0.04601	0.00949	0.02522	0.00468	0.00027
M02-45P	L.lepida	580	8875	0.00222	2.22732	0.00254	0.00000	0.00028	0.04416	0.00691	0.01528	0.00534	0.00012
M02-45P	L.lepida	600	9095	0.00049	2.43642	0.00139	0.00000	0.00028	0.04992	0.00767	0.01490	0.00428	0.00009
M02-45P	L.lepida	620	9195	0.00136	2.43461	0.00231	0.00011	0.00047	0.04869	0.00790	0.01889	0.00336	0.00008
M02-45P	L.lepida	640	9260	0.00074	2.41571	0.00231	0.00011	0.00019	0.05138	0.00676	0.01362	0.00260	0.00010
M02-45P	L.lepida	660	9320	0.00160	2.54500	0.00266	0.00011	0.00047	0.04777	0.00691	0.01648	0.00285	0.00008
M02-45P	L.lepida	680	9380	0.00259	2.43642	0.00266	0.00011	0.00019	0.04892	0.00630	0.01091	0.00626	0.00007
M02-45P	L.lepida	700	9400	0.00136	2.50659	0.00301	0.00011	0.00019	0.05392	0.00759	0.01709	0.00672	0.00010
M02-45P	L.lepida	720	9415	0.00420	2.48192	0.00358	0.00033	0.00019	0.05261	0.00516	0.01182	0.00499	0.00013

Table 5.3 continued

Core	Species	Depth	Age	Rb*	Sr*	Zr*	Mo*	Cd*	Ba*	La*	Ce*	Pb*	U*
M02-45P	L.lepida	740	9430	0.00271	2.45544	0.00301	0.00011	0.00056	0.06582	0.00774	0.01679	0.00468	0.00009
M02-45P	L.lepida	770	9485	0.00383	2.39428	0.00243	0.00022	0.00056	0.06282	0.00638	0.01347	0.00484	0.00006
M02-45P	L.lepida	780	9510	0.00259	2.13945	0.00254	0.00011	0.00047	0.05008	0.00721	0.01378	0.00519	0.00008
M02-45P	L.lepida	800	9555	0.00173	2.44087	0.00405	0.00022	0.00056	0.05906	0.00721	0.01498	0.00529	0.00012
M02-45P	L.lepida	820	9600	0.00284	2.29919	0.00497	0.00055	0.00047	0.05960	0.00866	0.01581	0.00519	0.00012
M02-45P	L.lepida	840	9645	0.00333	2.28474	0.00601	0.00022	0.00028	0.06405	0.00759	0.01656	0.00667	0.00013
M02-45P	L.lepida	860	9690	0.00111	2.29594	0.00648	0.00000	0.00066	0.05760	0.00721	0.01468	0.00453	0.00007
M02-45P	L.lepida	880	9760	0.00234	2.34336	0.00474	0.00044	0.00056	0.06390	0.00691	0.01408	0.00641	0.00014
M02-45P	L.lepida	900	9840	0.00333	2.36010	0.00416	0.00022	0.00047	0.06252	0.00706	0.01814	0.00448	0.00010
M02-45P	L.lepida	920	9915	0.00346	2.20048	0.00393	0.00011	0.00056	0.06137	0.00828	0.01904	0.00316	0.00010
M02-45P	L.lepida	930	9955	0.00148	2.29028	0.00282	0.00018	0.00022	0.06444	0.00783	0.02019	0.00263	0.00014
M05-03P	L.lepida	942	10000	0.00188	2.53994	0.00148	0.00025	0.00034	0.06602	0.00604	0.01391	0.00264	0.00005
M05-03P	L.lepida	952	10090	0.00111	2.45086	0.00202	0.00024	0.00020	0.06067	0.00702	0.01764	0.00320	0.00005
M05-03P	L.lepida	962	10205	0.00130	2.38321	0.00119	0.00019	0.00032	0.06812	0.00976	0.02174	0.00237	0.00006
M05-03P	L.lepida	972	10320	0.00095	2.50383	0.00104	0.00024	0.00023	0.05722	0.00600	0.01588	0.00145	0.00004
M05-03P	L.lepida	982	10695	0.00111	2.13668	0.00095	0.00008	0.00029	0.05665	0.00576	0.01203	0.00160	0.00004
M05-03P	L.lepida	992	11180	0.00094	1.80384	0.00083	0.00013	0.00015	0.05717	0.00540	0.01234	0.00177	0.00007
M05-03P	L.lepida	1002	11660	0.00083	2.19085	0.00084	0.00009	0.00021	0.06479	0.00560	0.01119	0.00146	0.00008
M05-03P	L.lepida	1012	12145	0.00075	2.26548	0.00096	0.00031	0.00027	0.06370	0.00486	0.00934	0.00135	0.00004

Core	Species	Depth	Age	Temp	B*	Mg*	P*	Ti*	V*	Mn*	Fe*	Cu*	Zn*
M05-50P	P. agilis	50	1195	17.32044	0.81276	30.66590	3.06085	0.00637	0.00137	0.64371	0.84998	0.54737	0.15594
M05-50P	P. agilis	80	1915	18.68397	0.79286	32.78318	2.86690	0.01143	0.00130	0.95088	1.35658	0.11757	0.09259
M05-50P	P. agilis	100	2285	17.25338	0.32510	30.56177	2.04953	0.02479	0.00195	0.81822	1.46122	0.04020	0.05249

Table 5.3 continued

M05-50P	P. agilis	110	2345	19.79603	0.28627	34.50998	1.50463	0.00460	0.00079	1.05205	0.93574	0.01361	0.03900
M05-50P	P. agilis	120	2405	18.56103	0.31125	32.59228	1.61361	0.01697	0.00155	1.25401	1.00412	0.01700	0.05697
M05-50P	P. agilis	130	2460	17.29809	0.27651	30.63119	2.14762	0.01255	0.00159	1.12116	0.81939	0.05268	0.11614
M05-50P	P. agilis	160	2640	18.61691	0.26773	32.67905	2.81717	0.00290	0.00097	1.59631	1.16240	0.04402	0.15715
M05-50P	P. agilis	180	2755	16.47382	0.31496	29.35127	1.96235	0.00243	0.00041	0.75102	0.67054	0.01917	0.04820
M05-50P	P. agilis	210	2930	17.28691	0.27203	30.61383	1.28734	0.00412	0.00035	1.18144	0.63050	0.01842	0.05087
M05-50P	P. agilis	230	3050	16.92367	0.33037	30.04980	1.93783	0.00490	0.00081	1.22925	0.78387	0.02035	0.03055
M05-50P	P. agilis	260	3535	16.21956	0.30442	28.95645	2.01871	0.00550	0.00093	1.17127	0.81976	0.01190	0.03668
M05-50P	P. agilis	290	3725	18.67838	0.29291	32.77450	2.18644	0.00146	0.00120	0.84625	0.65581	0.02531	0.03068
M05-50P	P. agilis	320	3920	19.41603	0.26305	33.91992	1.53391	0.00542	0.00077	0.75448	0.86188	0.02762	0.01855
M05-50P	P. agilis	340	4045	19.49985	0.23241	34.05008	1.32889	0.00426	0.00077	0.70034	0.93121	0.01661	0.02329
M05-50P	P. agilis	360	4175	20.46243	0.26617	35.54476	1.93102	0.00494	0.00079	0.64908	0.78387	0.03731	0.05202
M05-50P	P. agilis	380	4350	17.62639	0.20197	31.14099	1.29552	0.00201	0.00027	0.64563	0.71021	0.01691	0.01576
M05-50P	P. agilis	400	4570	17.00470	0.57235	30.17563	1.21378	0.00879	0.00068	0.79595	1.02376	0.00602	0.02205
M05-50P	P. agilis	420	4835	17.44897	0.49624	30.86548	0.97947	0.00953	0.00048	0.45960	0.67734	0.00456	0.01826
M05-50P	P. agilis	440	5100	21.40544	0.44356	37.00907	0.93656	0.00896	0.00054	0.69497	0.28994	0.05587	0.03758
M05-50P	P. agilis	460	5365	17.33720	0.42697	30.69193	1.28649	0.00783	0.00056	0.58093	0.49904	0.00772	0.01724
M05-50P	P. agilis	480	5630	16.15250	0.46190	28.85232	1.86178	0.02850	0.00145	0.84490	0.75403	0.02719	0.04291
M05-50P	P. agilis	500	5880	17.55514	0.45390	31.03035	1.48760	0.02023	0.00118	0.84279	0.88115	0.01779	0.04736
M05-50P	P. agilis	510	6005	17.24779	0.41487	30.55309	2.61215	0.03520	0.00104	0.62816	0.49488	0.01862	0.02678
M05-50P	P. agilis	530	6250	18.98015	0.46170	33.24308	1.58432	0.00554	0.00029	0.72069	0.35813	0.01582	0.02765
M05-50P	L.lepida	540	6375	12.19407	0.42911	22.70569	2.35730	0.05427	0.00199	0.79192	1.12349	0.03187	0.08449
M05-50P	L.lepida	550	6495	11.14488	0.29154	21.07651	1.61429	0.01243	0.00195	0.60666	0.98409	0.25121	0.10151
M05-50P	L.lepida	560	6620	10.57348	0.28315	20.18925	6.31752	0.03358	0.00207	0.87581	1.10271	0.03671	0.12475
M05-50P	L.lepida	570	6745	9.82661	0.26207	19.02952	5.67600	0.04164	0.00172	0.63699	0.82411	0.03960	0.09304
M05-50P	L.lepida	580	6865	10.57124	0.24919	20.18578	5.03444	0.00636	0.00048	0.70207	0.82014	0.09103	0.10630
M05-50P	L.lepida	590	6990	10.06132	0.26734	19.39397	3.91516	0.03107	0.00124	0.54714	1.27838	0.27674	0.15136
M05-50P	L.lepida	600	7115	12.88338	0.29232	23.77605	2.52701	0.03650	0.00292	0.94915	1.90699	0.04491	0.19840
M05-50P	L.lepida	610	7240	10.53632	0.25759	20.13155	3.19725	0.00756	0.00089	0.88579	1.02810	0.12096	0.12788

M05-50P	L.lepida	620	7360	10.63411	0.23788	20.28340	2.83624	0.03350	0.00199	0.96950	1.31351	0.04976	0.13375
M05-50P	L.lepida	630	7485	9.99258	0.22617	19.28724	2.02638	0.02172	0.00110	1.02556	1.15031	0.03231	0.10401
M05-50P	L.lepida	640	7610	10.44690	0.25173	19.99271	2.59376	0.03575	0.00302	0.75218	1.43742	0.05351	0.10046

Table 5.3 continued

Core	**Species**	**Depth**	**Age**	**Temp**	**B***	**Mg***	**P***	**Ti***	**V***	**Mn***	**Fe***	**Cu***	**Zn***
M05-50P	L.lepida	640	7610	9.25661	0.14597	18.14442	2.00662	0.01009	0.00079	1.09140	1.22436	0.04458	0.15194
M05-50P	L.lepida	650	7730	13.05102	0.23671	24.03637	2.08291	0.01227	0.00137	0.80401	1.18167	0.05165	0.13775
M05-50P	L.lepida	660	7855	11.72661	0.25720	21.97983	2.90300	0.02437	0.00259	0.93264	1.72604	0.02964	0.07726
M05-50P	L.lepida	660	7855	11.25720	0.25817	21.25093	2.01360	0.01564	0.00170	0.82935	1.20698	0.02775	0.07904
M05-50P	L.lepida	670	7980	10.78080	0.19377	20.51118	2.16465	0.01347	0.00255	1.11348	2.15178	0.02221	0.13981
M05-50P	L.lepida	680	8100	10.22896	0.26344	19.65429	2.53382	0.04352	0.00219	1.28396	1.66937	0.03157	0.09139
M05-50P	L.lepida	690	8225	11.17338	0.12684	21.12077	1.71237	0.01183	0.00209	1.32312	2.13365	0.03333	0.05376
M05-50P	L.lepida	700	10820	13.12926	0.19299	24.15786	2.08291	0.01318	0.00104	1.00751	1.14578	0.03200	0.15178
M05-50P	L.lepida	720	11095	14.02897	0.29232	25.55492	2.19325	0.00697	0.00170	1.10926	1.45782	0.03660	0.15151
M05-50P	L.lepida	740	11370	12.85544	0.17758	23.73266	3.03514	0.01658	0.00255	0.98582	2.34143	0.04880	0.18069
M05-50P	L.lepida	750	11505	10.74671	0.45370	20.45825	3.09916	0.04828	0.00246	1.37458	1.87507	0.31038	0.09046
M05-50P	L.lepida	760	11640	12.88338	0.15562	23.77605	3.00721	0.01443	0.00356	0.93206	3.03237	0.05465	0.17162
M05-50P	L.lepida	770	11780	9.57514	0.27808	18.63904	2.89823	0.01311	0.00402	1.26399	3.27679	0.03031	0.19082
M05-50P	L.lepida	780	11915	10.15911	0.47741	19.54582	2.35758	0.02804	0.00356	1.36690	1.41192	0.02071	0.09646
M05-50P	L.lepida	787	12010	9.82102	0.15543	19.02084	2.77086	0.01166	0.00217	1.07797	2.22375	0.02992	0.12901

Core	**Species**	**Depth**	**Age**	**Rb***	**Sr***	**Zr***	**Mo***	**Cd***	**Ba***	**La***	**Ce***	**Pb***	**U***
M05-50P	P. agilis	50	1195	0.00067	3.86215	0.00044	0.00000	0.00000	0.03005	0.00416	0.00870	0.00489	0.00023
M05-50P	P. agilis	80	1915	0.00074	3.81545	0.00033	0.00000	0.00000	0.03402	0.00773	0.00724	0.00268	0.00012
M05-50P	P. agilis	100	2285	0.00041	3.69964	0.00028	0.00005	0.00010	0.03852	0.00650	0.01080	0.00170	0.00014
M05-50P	P. agilis	110	2345	0.00014	3.84530	0.00013	0.00005	0.00010	0.03206	0.00293	0.00518	0.00125	0.00016
M05-50P	P. agilis	120	2405	0.00069	3.82508	0.00032	0.00005	0.00010	0.03808	0.00518	0.01097	0.00134	0.00020
M05-50P	P. agilis	130	2460	0.00039	3.75405	0.00028	0.00007	0.00010	0.03140	0.01050	0.02321	0.00219	0.00021

M05-50P	P. agilis	160	2640	0.00016	4.14143	0.00043	0.00008	0.00011	0.04336	0.01252	0.02721	0.00204	0.00025
M05-50P	P. agilis	180	2755	0.00002	3.76368	0.00014	0.00006	0.00003	0.03674	0.00829	0.01627	0.00075	0.00012
M05-50P	P. agilis	210	2930	0.00011	3.79378	0.00005	0.00010	0.00005	0.03157	0.00093	0.00193	0.00066	0.00004
M05-50P	P. agilis	230	3050	0.00022	3.92427	0.00014	0.00013	0.00008	0.03203	0.00290	0.00606	0.00094	0.00012

Table 5.3 continued

Core	**Species**	**Depth**	**Age**	**Rb***	**Sr***	**Zr***	**Mo***	**Cd***	**Ba***	**La***	**Ce***	**Pb***	**U***
M05-50P	P. agilis	260	3535	0.00020	3.81039	0.00013	0.00011	0.00008	0.02653	0.00168	0.00365	0.00116	0.00012
M05-50P	P. agilis	290	3725	0.00011	3.92691	0.00005	0.00009	0.00009	0.02740	0.00341	0.00614	0.00114	0.00027
M05-50P	P. agilis	320	3920	0.00009	3.75381	0.00011	0.00001	0.00003	0.02509	0.00116	0.00246	0.00109	0.00004
M05-50P	P. agilis	340	4045	0.00028	3.91825	0.00018	0.00007	0.00003	0.03303	0.00183	0.00380	0.00103	0.00003
M05-50P	P. agilis	360	4175	0.00027	3.92282	0.00020	0.00007	0.00008	0.03146	0.00286	0.00324	0.00118	0.00007
M05-50P	P. agilis	380	4350	0.00023	3.61755	0.00009	0.00006	0.00005	0.03988	0.00294	0.00389	0.00071	0.00004
M05-50P	P. agilis	400	4570	0.00026	3.97073	0.00012	0.00004	0.00004	0.03482	0.00177	0.00105	0.00072	0.00003
M05-50P	P. agilis	420	4835	0.00020	3.79715	0.00009	0.00005	0.00006	0.03032	0.00064	0.00061	0.00024	0.00003
M05-50P	P. agilis	440	5100	0.00015	4.08220	0.00009	0.00019	0.00007	0.02624	0.00142	0.00291	0.00111	0.00005
M05-50P	P. agilis	460	5365	0.00027	3.96929	0.00010	0.00009	0.00004	0.03502	0.00062	0.00117	0.00038	0.00003
M05-50P	P. agilis	480	5630	0.00102	3.79089	0.00043	0.00007	0.00008	0.03794	0.00524	0.00980	0.00083	0.00027
M05-50P	P. agilis	500	5880	0.00047	3.85950	0.00038	0.00007	0.00008	0.03218	0.00199	0.00367	0.00077	0.00016
M05-50P	P. agilis	510	6005	0.00078	4.02394	0.00024	0.00007	0.00003	0.03216	0.00091	0.00194	0.00072	0.00021
M05-50P	P. agilis	530	6250	0.00019	3.77933	0.00026	0.00008	0.00012	0.03164	0.00650	0.01413	0.00027	0.00029
M05-50P	L.lepida	540	6375	0.00165	2.79249	0.00066	0.00024	0.00012	0.03779	0.00660	0.01517	0.00146	0.00019
M05-50P	L.lepida	550	6495	0.00091	2.58207	0.00083	0.00037	0.00030	0.04286	0.00731	0.01675	0.00491	0.00018
M05-50P	L.lepida	560	6620	0.00139	2.68656	0.00120	0.00014	0.00029	0.05140	0.00814	0.01904	0.00166	0.00023
M05-50P	L.lepida	570	6745	0.00193	2.44821	0.00070	0.00019	0.00019	0.04961	0.00685	0.01449	0.00147	0.00025
M05-50P	L.lepida	580	6865	0.00027	2.41150	0.00061	0.00031	0.00024	0.05294	0.00784	0.01752	0.00243	0.00018
M05-50P	L.lepida	590	6990	0.00060	2.48505	0.00062	0.00028	0.00023	0.06823	0.00526	0.01099	0.00253	0.00016
M05-50P	L.lepida	600	7115	0.00131	2.56161	0.00106	0.00030	0.00026	0.05049	0.00922	0.02114	0.00290	0.00028
M05-50P	L.lepida	610	7240	0.00178	2.77323	0.00098	0.00011	0.00023	0.05213	0.00882	0.01825	0.00389	0.00026

M05-50P	L.lepida	620	7360	0.00126	2.43184	0.00130	0.00013	0.00025	0.05347	0.00993	0.01989	0.00278	0.00023
M05-50P	L.lepida	630	7485	0.00049	2.61505	0.00096	0.00013	0.00011	0.04536	0.00959	0.02231	0.00264	0.00030
M05-50P	L.lepida	640	7610	0.00131	2.48457	0.00092	0.00011	0.00021	0.05177	0.00704	0.01483	0.00278	0.00029
M05-50P	L.lepida	640	7610	0.00052	2.71617	0.00086	0.00009	0.00020	0.05473	0.00749	0.01603	0.00300	0.00025
M05-50P	L.lepida	650	7730	0.00101	2.62420	0.00096	0.00014	0.00033	0.04424	0.00576	0.01332	0.00153	0.00029
M05-50P	L.lepida	660	7855	0.00135	2.82740	0.00100	0.00013	0.00017	0.04130	0.00618	0.01372	0.00248	0.00030

Table 5.3 continued

Core	Species	Depth	Age	Rb*	Sr*	Zr*	Mo*	Cd*	Ba*	La*	Ce*	Pb*	U*
M05-50P	L.lepida	660	7855	0.00085	2.70461	0.00084	0.00015	0.00019	0.04061	0.00639	0.01385	0.00233	0.00027
M05-50P	L.lepida	670	7980	0.00125	2.63143	0.00103	0.00023	0.00022	0.04912	0.00536	0.01236	0.00169	0.00024
M05-50P	L.lepida	680	8100	0.00123	2.86110	0.00114	0.00013	0.00023	0.03018	0.00776	0.01723	0.00227	0.00028
M05-50P	L.lepida	690	8225	0.00100	2.86736	0.00124	0.00026	0.00015	0.04806	0.00496	0.01095	0.00185	0.00020
M05-50P	L.lepida	700	10820	0.00047	2.66513	0.00101	0.00038	0.00023	0.04777	0.00798	0.01867	0.00192	0.00026
M05-50P	L.lepida	720	11095	0.00028	2.47072	0.00151	0.00017	0.00016	0.04353	0.00487	0.01135	0.00189	0.00010
M05-50P	L.lepida	740	11370	0.00046	2.55198	0.00169	0.00013	0.00014	0.05209	0.00660	0.01466	0.00289	0.00014
M05-50P	L.lepida	750	11505	0.00059	2.65466	0.00151	0.00003	0.00032	0.06024	0.00856	0.01753	0.00339	0.00022
M05-50P	L.lepida	760	11640	0.00115	2.57124	0.00193	0.00023	0.00026	0.05326	0.00475	0.01026	0.00315	0.00013
M05-50P	L.lepida	770	11780	0.00053	2.42919	0.00190	0.00017	0.00030	0.05991	0.00753	0.01599	0.00262	0.00013
M05-50P	L.lepida	780	11915	0.00101	2.30677	0.00106	0.00011	0.00033	0.06526	0.00677	0.01469	0.00227	0.00020
M05-50P	L.lepida	787	12010	0.00049	2.53753	0.00124	0.00015	0.00015	0.05706	0.00616	0.01345	0.00167	0.00023

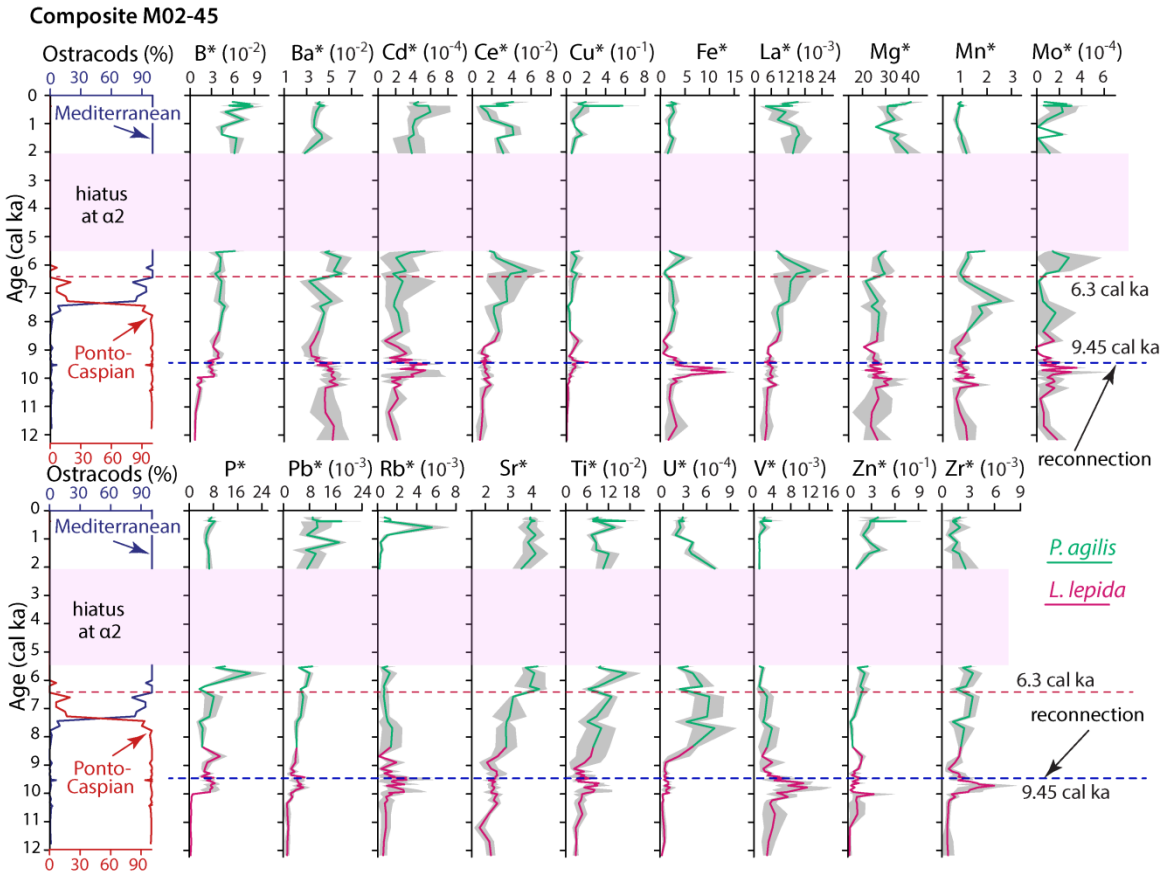

Figure 5.2 Downcore plots of element/Ca ratios (shown with the symbol of the element followed by an asterisk) against age (cal ka) for ostracod valves of *P. agilis* (aquamarine) and *L. lepida* (burgundy) in core M02-45. Hiatuses at α2 and α1 are highlighted. The gray bands represent the scatter in the element/Ca ratios calculated as the standard deviation of the analyses at each sample depth for all elements. The Mediterranean and Ponto–Caspian ostracod assemblages are taken from Williams et al. (2018). Blue dashed line shows the time of reconnection at ~9.45–9.40 cal ka (Section 4.4; Ankindinova et al., 2019a).

The data for core M05-50 (Fig. 5.3) suggest two primary trends: (a) higher element/Ca ratios before ~6.3 cal ka (Ba*, Cd*, Ce*, Fe*, La*, Mo*, Pb*, Rb*, Ti*, U*, V*, Zn*, Zr*) with some cases of a slight increase after ~3.0 cal ka, or (b) higher ratios after ~6.3 cal ka (B*, Mg*, Sr*). A few elements show little change with time or have

rather spiky profiles (Cu*, Mn*, P*). Before reconnection (i.e., below the α1 unconformity) some element/Ca ratios are quite variable (B*, Ba*, Cu*, Mo*).

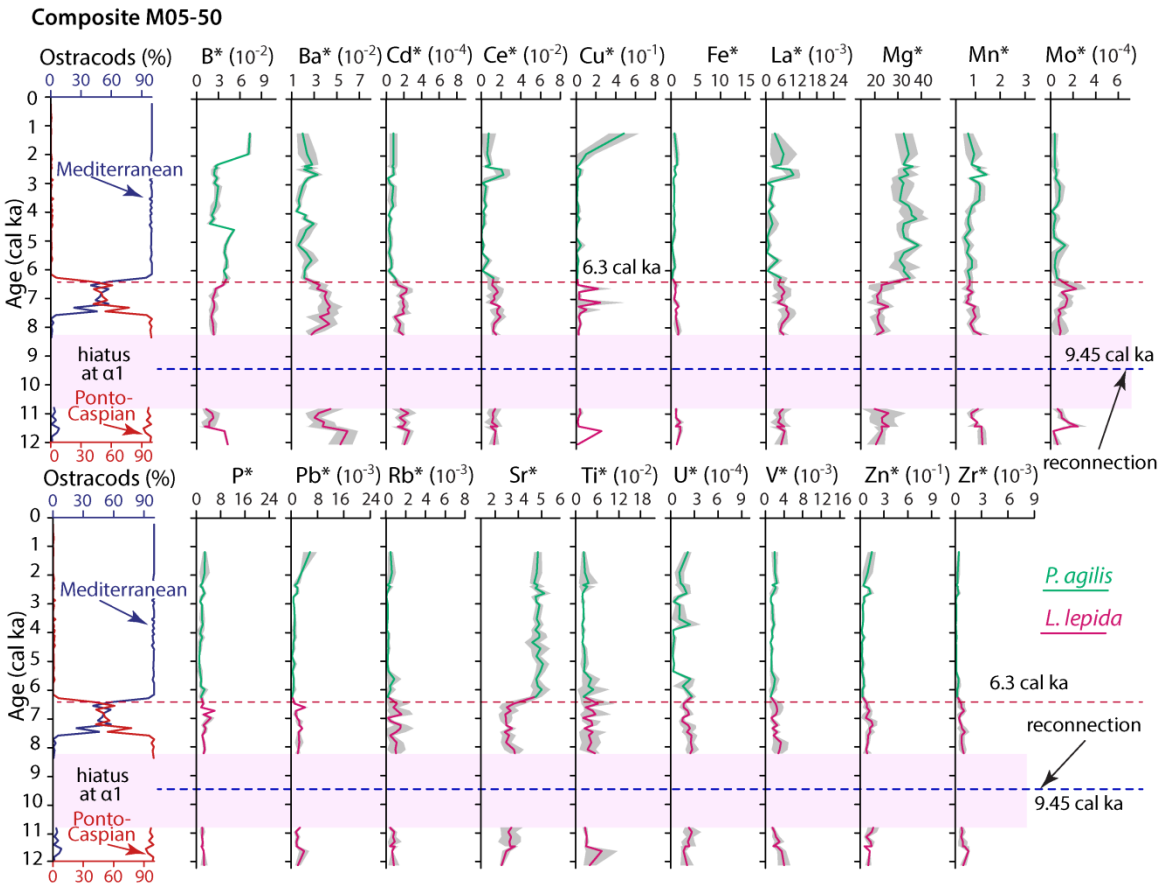

Figure5.3 Downcore plots of element/Ca ratios (shown with the symbol of the element followed by an asterisk) against age (cal ka) for ostracod valves of *P. agilis* (aquamarine) and *L. lepida* (burgundy) in core M05-50. Hiatuses at α2 and α1 are highlighted. The gray bands represent the scatter in the element/Ca ratios calculated as the standard deviation of the analyses at each sample depth for all elements. The Mediterranean and Ponto-Caspian ostracod assemblages are taken from Williams et al. (2018). Blue dashed line shows the time of reconnection at ~9.45–9.40 cal ka (Section 4.4; Ankindinova et al., 2019a).

5.4.1. Cluster analysis

Cluster analysis reveals five Q-clusters and three Q-super-clusters in each core (Figs. 5.4, 5.5). The super-clusters identify three distinct populations with ages of >12.0–

9.50 cal ka (interpolated sample ages 12.1–9.50 cal ka in core M02-45 and >10.8 cal ka in core M05-50), 9.45–6.3 cal ka (sample ages 9.45–7.3 cal ka in core M02-45 and 8.2–6.4 cal ka in core M05-50) and 6.3 cal ka to Present (sample ages 6.3–0.4 cal ka in core M02-45 and 6.3–1.2 cal ka in core M05-50).

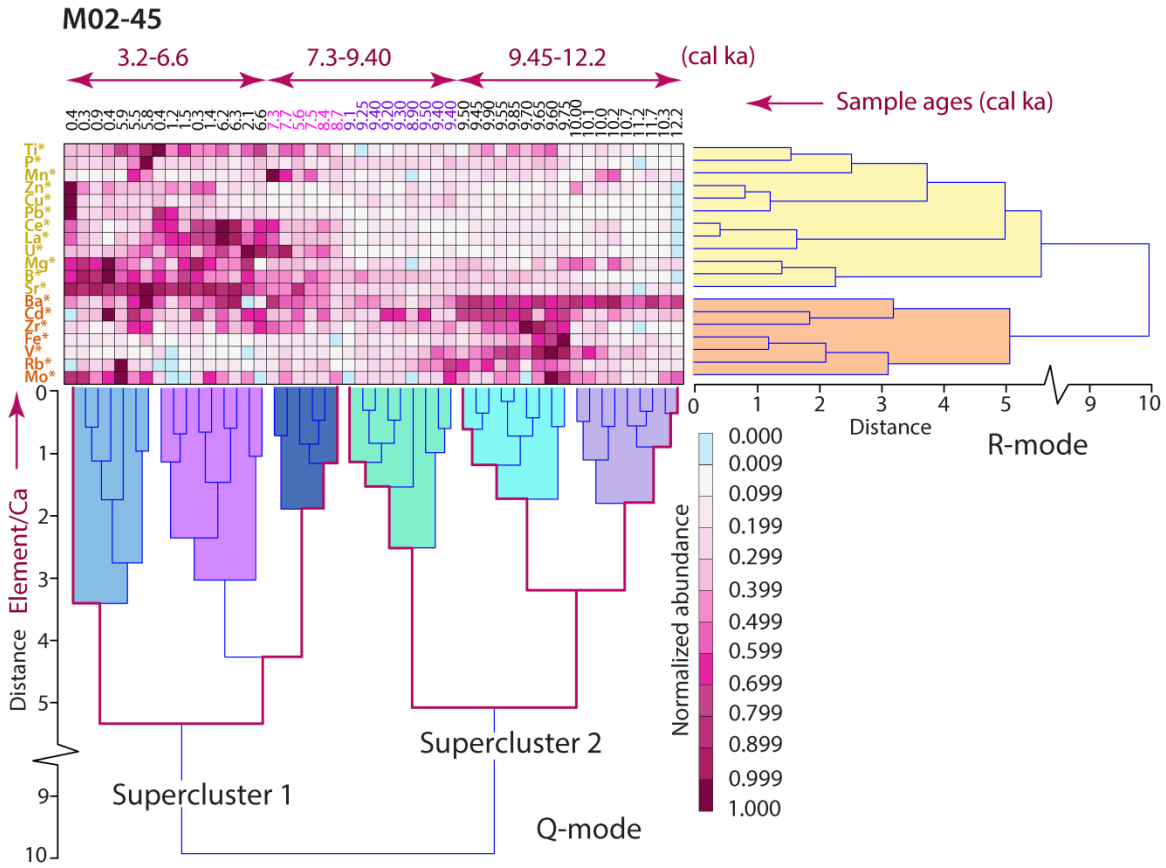

Figure 5.4. Ward's two-way cluster dendrograms of samples, each shown by its age in cal ka (Q-mode) and by its element/Ca ratio (R-mode) for core M02-45. Using sample ages, the sub-seafloor depth of each sample can be obtained from Table 5.3. Note three distinct age groupings of samples, explained in the text. Two outliers, grouped improperly with samples all of distinctly different age, are not plotted.

5.4.2 Factor analysis

Factor analysis extracted three factors in the combined matrix for cores M02-45 and M05-50, accounting for 87% of the total variance in the trace-element compositional data (Fig. 5.6a).

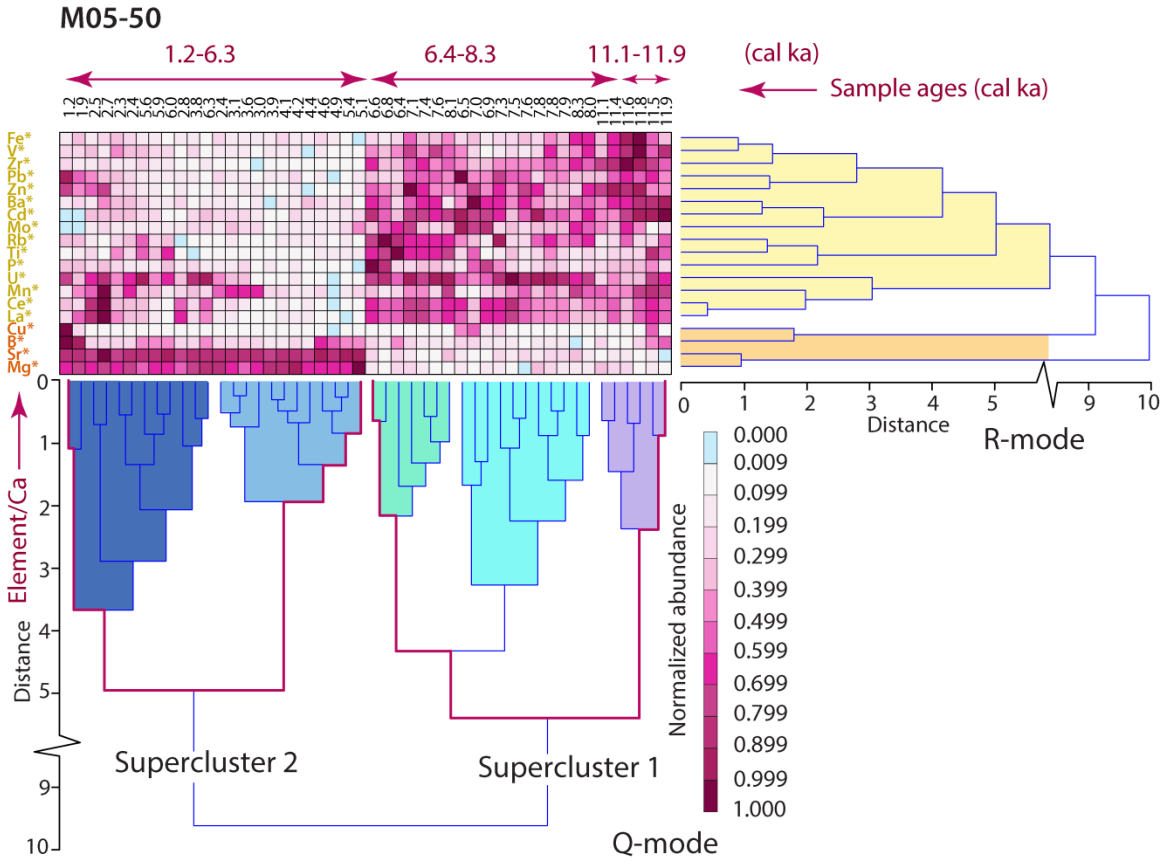

Figure 5.5. Ward's two-way cluster dendrograms of samples, each shown by its age in cal ka (Q-mode) and by its element/Ca ratio (R-mode) for core M05-50. Using sample ages, the sub-seafloor depth of each sample can be obtained from Table 5.3. Note three distinct age groupings of samples, explained in the text. Two outliers, grouped improperly with samples all of distinctly different age, are not plotted.

Factor 1 accounts for 70% of the total variance (Fig. 5.6a) and is characterized by significant R-factor loadings on Cd*, Ce*, La*, Pb*, Ti*, U*, Zn* and Zr*. Factor 2

accounts for 10% of the total variance and is characterized by very high negative loadings on B*, Mg* and Sr* (Fig. 5.6b).

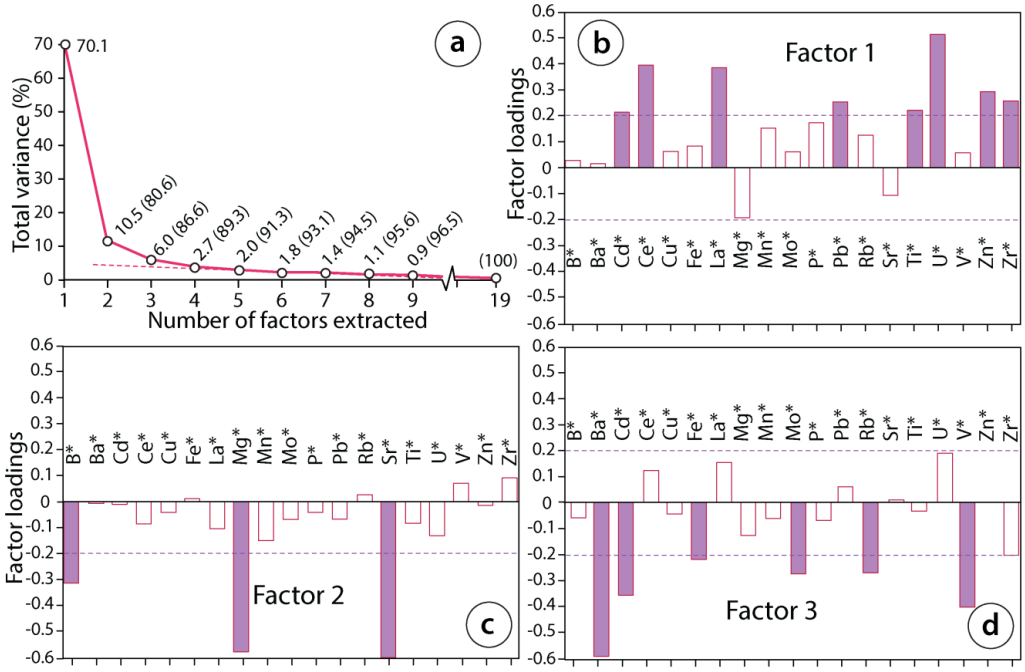

Figure 5.6. CABFAC factor analysis results. (a) Number of factors extracted and the proportion of the total variance accounted for by each factor. Three factors account for 87% of the total variance; the remaining 13% of the variance is distributed among several additional extracted factors and is considered to be uninterpretable noise. (b–d) Element/Ca composition of the three extracted R-factors. Factor loadings >0.2 or <−2.0 are considered statistically significant.

Factor 3 accounts for 6% of the total variance, exhibiting statistically significant loadings on Ba*, Cd*, Fe*, Mo*, Rb* and V*, (Fig. 5.6d). Several trace-elements (as element/Ca ratios) do not have significant loadings on any of the three factors, so are missing from the lists above. This is because their inclusion would not have increased the proportion of total variance accounted for by the particular factor, but this does not mean that these variables do not vary in parallel with some of the included variables. Based on the primary data (Table 5.3), it can be shown that several variables with high loadings on

F1–F3 correlate well ($r > 0.6$) with some of the variables which are not prominent in Figure 5.6 (Table 5.4).

Table 5.4. Element/Ca variables which have correlation coefficients of 0.6 or greater with highly loaded variables associated with factors F1–F3. For example, at site M02-45, Cu* and Sr* correlate at $r \geq 0.6$ with the factor F1 key variables Pb* and Zn*. Variables that appear more than twice in columns (2) and (3) for a single factor are set in ***italics-bold***, as they must play an important role whenever that factor is important.

	(1)	(2)	(3)
Factor	**Key variable**	**Other variables correlated to these at $r \geq 0.6$ M02-45 set**	**M05-50 set**
F1	Ce*	***Sr****	***Cd****
	La*	***Sr****	—
	Pb*	B*, ***Cu****, ***Sr****	***Cu****
	Ti*	***Sr****	***Fe****
	U*	***Sr****	—
	Zn*	***Cu****, ***Sr****	Ba*, ***Cd****, ***Fe****
	Zr*	***Fe****	Ba*, ***Cd****, ***Fe****
F2	B*	Pb*	—
	Mg*	Zn*	—
	Sr*	Ce*, La*, Pb*, Ti*, U*, Zn	—
F3	Ba*	—	***Zn****, ***Zr****
	Cd*	—	Ce*, ***Zn****, ***Zr****
	Fe*	***Zr****	Ti*, ***Zn****, ***Zr****
	Mo*	—	—
	Rb*	—	—
	V*	—	—

5.5. Interpretation of the results

The small-scale fluctuations in the oxygen and carbon isotopic values (Table 5.1) and the scatter about average values at individual core depths in the trace-element data

(Table 5.3) can be attributed to analyzing different valves which might have grown at different times while composition of the basin water fluctuated, or in different seasons associated with different ambient temperatures and fresh-water influxes. Also, water in contact with the growing ostracods might have included a contribution from near-surface pore water having its own characteristics. The ostracods in each sample could be different in age by many tens of years based on accumulation rates (Figs. 3.10, 3.11), the 1–2 cm stratigraphic thickness of the samples themselves, and bioturbational mixing on a scale of perhaps 5–10 cm. Finally, the observed scatter could include a contribution from systematic sub-micron-scale compositional variations within the mineral grains and inter-granular matrix of the valve ultrastructure (similar to what is determined by X-ray microscopy of the marine deep water ostracod *Krithe* by Branson et al., 2018).

5.5.1. Oxygen isotopes

The most notable characteristic of the oxygen isotope profile for core M02-45 is the very large range in the $\delta^{18}O$ values (~6–8‰; Fig. 5.1). The $\delta^{18}O$ record of mollusc shells from the northwestern Black Sea shelf and slope (Yanchilina et al., 2017) is shown for comparison (Fig. 5.1). The mollusc $\delta^{18}O$ record is composite, constructed using oxygen isotopic data obtained from dated shells in several cores and surface samples (see Yanchilina et al., 2017; their supplementary material 3). The mollusc record and the M02-45 and M05-50 data sets are surprisingly dissimilar from ~12.0–6.0 cal ka (Fig. 5.1). The mollusc $\delta^{18}O$ values decrease rather steadily from +4.0‰ to 0‰. Ostracod values in core M05-50 show no trend but rather vary irregularly over a range of ~+2‰ to –1‰ where not obscured by the α1 hiatus. Values at site M02-45 show a large ~+7–8‰ increase centered

on a high spanning the ages of ~8.5–7.0 cal ka, followed upward by an equally large decrease to values of ~0‰ by ~6.0 cal ka. After ~6.0 cal ka and to the Present, however, the mollusc and ostracod records are very similar to each other (Fig. 5.1), being tightly disposed around 0‰ (molluscs and M02-45) and +1‰ (M05-50).

In open-ocean deep-sea cores, Holocene isotopic records generally show 0.1–0.4‰ oscillations with a maximum shift of ~1.5‰ at the MIS 2–1 transition (Lisiecki and Raymo, 2005). The oxygen isotopic records of inland seas that became isolated from the global ocean during glacial periods often exhibit more dramatic oxygen-isotopic oscillations that can become exaggerated, particularly in bays and inlets that receive a near-constant inflow of glacial melt water (Ravelo and Hillaire-Marcel, 2007). The variations observed in cores M02-45 and to a lesser extent in M05-50 are 4–6 times the average for open-ocean records. Most of the mollusc shells in the Yanchilina et al. (2017) study come from the shelf edge and beyond. Perhaps coastal water supply from large rivers (particularly the Danube River) and the counterclockwise surface-water circulation contributed to the divergent trends between molluscs and ostracods living on the southwestern shelf of the Neoeuxine Lake and early post-reconnection Black Sea, but there is no obvious explanation for these differences.

An interpretation of $\delta^{18}O$ records simply in terms of mixing of watermasses will underestimate the influence of changes in the sources themselves, or processes that fractionate oxygen isotopes such as evaporation. The base-level changes inferred from drowned shorelines point to negative shifts in the hydrologic balance of the Neoeuxine Lake, indicating a relative increase in the influence of evaporation (e.g., Major et al., 2006).

During the LGM, central and eastern Europe were predominantly affected by southerly and easterly atmospheric flow patterns, leading to reduced rainfall in these regions (e.g., Ludwig et al., 2016). The drier conditions particularly in the drainage basins of major rivers must have contributed to the evaporative drawdown of the Black Sea. The associated evaporative concentration of ^{18}O might have been an important contributer to the observed isotopic shift. Although ~90% of the Pliocene–Quaternary $\delta^{18}O$ variations in the open ocean are controlled by global ice volume, there is a small but important contribution associated with the thermodynamic fractionation between ^{16}O and ^{18}O which occurs during precipitation of biogenic carbonate (Urey, 1947). Thus, increase in global ocean temperature during the Holocene must have affected the observed isotopic record in the composite cores. More specifically, an ~1‰ decrease in the $\delta^{18}O$ values of foraminiferal tests translates to an ~4ºC increase in the temperature of associated ocean water (e.g., Lisiecki and Raymo, 2005). Model simulations indicate that the LGM temperatures of the Black Sea region were 7–10ºC lower than modern values (e.g., Pollard and Barron, 2003). These results suggest that ~2‰ of the shift in the $\delta^{18}O$ record might be explained by the Holocene increase in Black Sea water temperature. Shifts in the oxygen-isotopic composition of meteoric water related to temperature variations also might have influenced the isotopic composition of basinal water through runoff and precipitation (e.g., von Grafenstein, 2002). The flux of meteoric water to the Black Sea during the Holocene is difficult to estimate. There are two important factors which influenced the supply of meteoric water: (a) temporal variations in atmospheric precipitation over river catchments, and (b) glacial meltwater from the northwestern European icesheet (e.g., Tudryn et al., 2016) as well as from the Altay and Sayan mountains of central Asia (e.g., Grosswald,

1980; Arkhipov, 1984; Rudoy and Baker, 1993; Rudoy, 1998). The $\delta^{18}O$ of atmospheric precipitation increases with increasing atmospheric temperature (e.g., Jouzel et al., 1994). However, glacial ice has notably low $\delta^{18}O$ values ranging between –20‰ and –35‰, controlled by the latitudinally-dependent temperature of precipitation (Dansgaard, 1964). Large meltwater influx into the Black Sea would have counteracted any increase associated with climbing atmospheric temperature, substantially lowering the isotopic composition of the sea/lake water.

The strongly negative $\delta^{18}O$ values of substage 1c in core M02-45 might reflect the isolation of the shelves of the pre-reconnection Neoeuxine Lake. Following the LGM, the lake periodically received large quantities of glacial melt water, either via large rivers (Tudryn et al., 2016) or from ice dam outburst floods from the central Asia (Grosswald, 1980; Arkhipov, 1984; Rudoy and Baker, 1993; Rudoy, 1998). However, the absence of a notably depleted isotopic interval in the mollusc record suggests the presence of regionally heterogeneous surface water masses across the Black Sea during this time. The base of substage 1b coincides closely with the ~9.45–9.40 cal ka reconnection of the Neoeuxine Lake (subsequently the Black Sea) with the Aegean Sea via the Marmara Sea Gateway. The trend toward higher oxygen isotopic values across the substage 1c/1b boundary potentially records the influence of Mediterranean water entering the isotopically depleted Neoeuxine Lake. The apparent absence of this signal at the M05-50 site is puzzling because the proximity of that core site to the Strait of Bosphorus should have ensured a greater oxygen isotopic enrichment as Mediterranean water entered the Black Sea. It is possible that the saline inflow took a more direct course to the shelf edge at that time, effectively

bypassing the M05-50 site. Furthermore, the fact that much of the substage 1b record is missing at the α1 unconformity further complicates an interpretation.

5.5.2. Carbon isotopes

The $\delta^{13}C$ of the ostracod shells reflects the carbon isotopic composition of dissolved inorganic carbon (DIC) in the water from which shell secretion occurs. There is often isotopic disequilibrium between the ambient water and the biogenic carbonate. Through longer intervals of geological time and across global scales, the average $\delta^{13}C_{DIC}$ in the global ocean reflects the global carbon cycle, particularly the partitioning of carbon in the ocean–atmosphere–terrestrial-biosphere reservoirs. The terrestrial biosphere is notably depleted in ^{13}C ($\delta^{13}C \sim -25‰$) because C3 plants predominantly use ^{12}C during their photosynthesis (Bender, 1971). The $\delta^{13}C$ records of ostracods can be influenced by several factors besides changes in the isotopic composition of the water body where they live. For example, the $\delta^{13}C_{DIC}$ of the water in the Black Sea and the Neoeuxine Lake could have been influenced by (a) changes in the balance between locally occurring aquatic photosynthesis and respiration, (b) the presence or absence of watermasses, particularly Mediterranean water, (c) large quantities of glacial meltwater entering the basin, and (d) changes in the original $\delta^{13}C_{DIC}$ signatures of watermasses reaching the core sites. In the surface ocean, photosynthesis dominates over respiration, thus the DIC is relatively low and $\delta^{13}C_{DIC}$ is relatively high reflecting the preference of marine flora to use ^{12}C during photosynthesis: the resulting net export of organic particulate matter has $\delta^{13}C$ values of –19‰ to –23‰ (Macko et al., 1994). In the deeper shelf depths of the Black Sea, where respiration predominates, DIC is relatively high and the $\delta^{13}C_{DIC}$ is relatively low. Thus, changes in

photosynthesis or respiration can impact the $\delta^{13}C_{DIC}$ of the ambient water, and these changes will be recorded in the $CaCO_3$ shells of invertebrates like ostracods. Because photosynthesis and respiration also influence major nutrient distributions in the ocean, the concentrations of, for example, dissolved phosphate or nitrate in the ocean are inversely related to the $\delta^{13}C_{DIC}$ (e.g., Ortiz et al., 2000). Both *P. agilis* and *L. lepida* are apparently epifaunal benthic species, thus may also have been affected by the chemical composition of the porewater.

There are other possible causes of local changes in the $\delta^{13}C_{DIC}$ linked to watermass formation and circulation. For example, the Mediterranean watermass found across deeper parts of the Marmara Sea acquired its $\delta^{13}C_{DIC}$ signature when it was a surface watermass in the eastern Aegean Sea. Although it becomes a deep watermass in the Marmara Sea, the Mediterranean inflow retains the $\delta^{13}C_{DIC}$ characteristics it acquired in the Aegean Sea. When the upper portion of this saline watermass enters the Black Sea as a bottom current through the Strait of Bosphorus, it proceeds to the shelf edge and descends to mid-depth over the slope where it forms interflows and mixes with ambient water. Today, a portion of this watermass spreads across parts of the southern shelf (cf. Hiscott et al., 2017, their figure 16), having $\delta^{13}C_{DIC}$ characteristics significantly different from those of the local watermass(es) in the contemporary Black Sea. Another possibility is the presence of methane in the environment. Today the Black Sea deep basinal waters are anoxic, with no dissolved oxygen (Murray et al., 2007), and euxinic where carbonate alkalinity occurs via sulfate reduction which, depending on the pathway, can lower the $\delta^{13}C$ of the DIC. Methane is ubiquitous across the Black Sea shelves and upper slope regions occurring as

seeps, mud volcanoes and gas hydrates (Popescu et al., 2007; Flood et al., 2009; Starostenko et al., 2010). In these regions, methane is predominantly abiogenic in origin, formed by the redeposited thermogenic hydrocarbons (e.g., Starostenko et al., 2010). Methane ebullition from deep Black Sea or shallow shelves will invariably affect the $\delta^{13}C$ in DIC: in regions of anaerobic methane oxidation mediated by bacteria, $\delta^{13}C$ DIC values as low as –48‰ are reported in the upper 4 cm of the sediment (e.g., Torres et al., 2003).

The high $\delta^{13}C$ values in substage 1c, ranging between –4‰ to –5‰ (*L. lepida* values of –2‰ to –3‰), are interpreted as indicators of vigorous lacustrine photosynthesis (relative to respiration) during the Neoeuxine Lake stage, when the flora preferentially used ^{12}C during photosynthesis (Fig. 5.1). The progressive decrease of the $\delta^{13}C$ values toward the substage 1c–1b transition and within substage 1b probably reflects the depleted $\delta^{13}C_{DIC}$ characteristics of the Mediterranean watermass entering the Black Sea following the reconnection. The subsequent progressive increase in the $\delta^{13}C$ values from ~ –5.5‰ at the base to ~ –3.5‰ at the top of substage 1a is interpreted to reflect an increase in marine photosynthetic production in the Black Sea following the establishment of two-way flow across the Strait of Bosphorus (Fig. 5.1).

The $\delta^{13}C$ profiles are very similar in their shape to the mollusc record of Yanchilina et al. (2017); those authors show a progressive decrease in the carbon isotopes from ~12.0–7.0 cal ka, followed by a progressive (although spiky) increase from ~6.0 cal ka to Present (Fig. 5.1). However, the ostracod record is shifted to lower values by approximately 5–6‰ relative to the mollusc record.

5.5.3 Correlation of $\delta^{18}O$ with $^{87}Sr/^{86}Sr$ in M02-45

$^{87}Sr/^{86}Sr$ data from mollusc shells are only available for core M02-45 (Fig. 4.1; Section 4; Ankindinova et al., 2019a). The $^{87}Sr/^{86}Sr$ signal can be readily correlated with the $\delta^{18}O$ variations (Fig. 5.7). For example, oxygen isotopic substage 1c correlates with intervals A–C in the $^{87}Sr/^{86}Sr$ downcore plot, with the sharp increase in the Sr isotopic ratios from ~0.708843 to ~0.708962 correlating with the equally sharp increase in the $\delta^{18}O$ values of ~ 7‰ across the substage 1c–1b transition (Fig. 5.7). The $\delta^{13}C$ downcore plot cannot be correlated with the $^{87}Sr/^{86}Sr$ values. The $\delta^{13}C$ data show some of the least negative values across substage 1c (Fig. 5.1), with progressively more negative values occurring near the substage 1c–1b transition. However, the abrupt increase in $^{87}Sr/^{86}Sr$ values across interval C is not represented in the carbon isotopic data obtained from the ostracod valves; instead, the $\delta^{13}C$ values vary between ~ –6‰ and –5‰ (*L. lepida* values of ~ –4‰ to –3‰).

5.5.4. Mg/Ca ratios and paleotemperatures

Mg/Ca temperature calibration for the ostracod genus *Loxoconcha* collected from Chesapeake Bay on the Atlantic coast of North America provides the following linear regression equation with $r^2 = 0.8051$ (Cronin et al., 2003).

$$y = 0.644\ x - 2.4284 \qquad (5.1)$$

where y = temperature, x = the Mg/Ca molar ratio in ostracod valves. Chesapeake Bay has been a semi-marine estuary (practical salinity 12–30) throughout the Holocene with a salinity similar to the Black Sea.

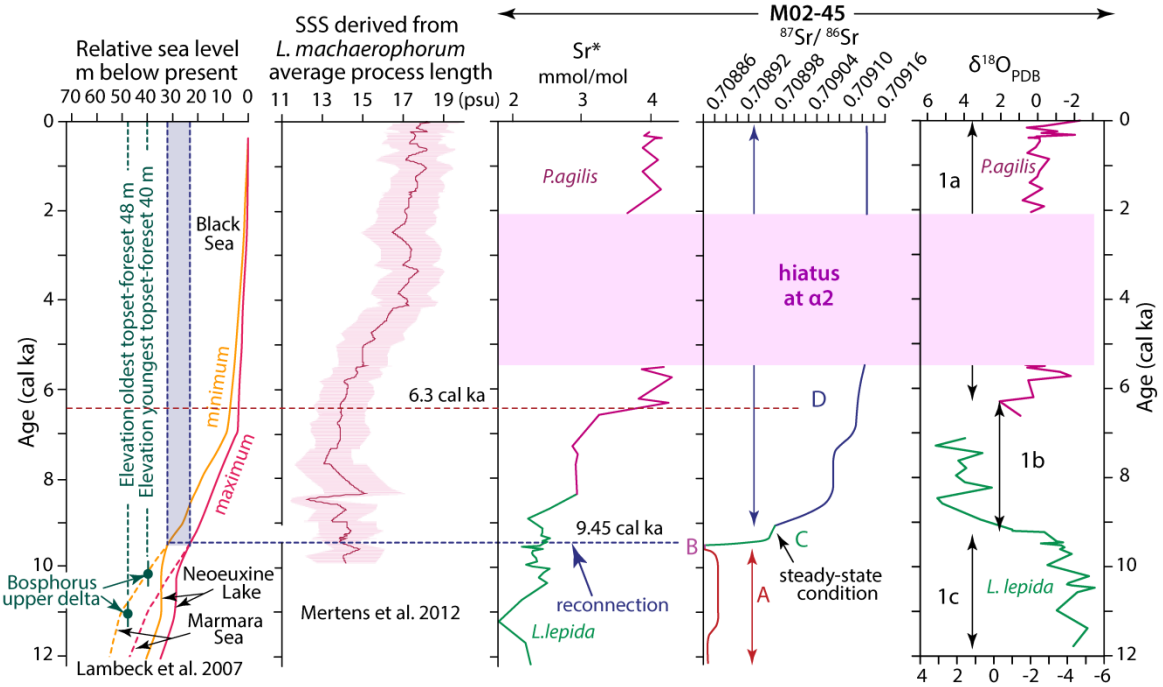

Figure 5.7. Temporal variations in $\delta^{18}O$, Sr*, and $^{87}Sr/^{86}Sr$ (from Fig. 4.1) for core M02-45. Replicates of $\delta^{18}O$ measurements have average reproducibility of ~0.5‰. Note the nearly synchronous and parallel development of sharp $\delta^{18}O$ and $^{87}Sr/^{86}Sr$ variations on the southwestern Black Sea shelf. Also note that there is a broad correlation with a sharp increase in Sr/Ca and a protracted increase in sea surface salinity (from Mertens et al., 2012). The relative sea level curve (from Lambeck et al., 2007) is shown as a reference for various oceanographic events discussed in the text. The hiatus at α2 is explained in the text. Blue dashed line shows the time of reconnection at ~9.45–9.40 cal ka (Section 4.4; Ankindinova et al., 2019a). Element symbol followed by an asterisk = element/Ca.

Both water bodies experience a temperate climate. Equation 5.1 is considered to be genus-dependent rather than species-dependent, thus probably can be used for all species of *Loxoconcha*. However, the literature is mute about a similar Mg/Ca calibration for the ostracod genus *Palmoconcha*. *Palmoconcha agilis* is very closely related to the genus *Loxoconcha*; in fact this species was first described as a *Loxoconcha (L. agilis,* Ruggieri, 1967, and *L.* aff. *agilis* Bonaduce et al., 1975). Its genus was reassigned to *Palmoconcha* only recently (Boomer et al., 2010). In the absence of Mg/Ca temperature calibration for

Palmoconcha, the *Loxoconcha* calibration equation was cautiously applied to *Palmoconcha agilis* in this study.

The Mg/Ca paleotemperature plots for both cores suggest that average bottom-water temperatures on the shelf were around 12–14ºC from the start of the Holocene until ~6.3 cal ka, when they sharply increased to 17–19ºC and remained in that range until the present. Today, winter temperatures on Black Sea shelves are ~7–9ºC and summer temperatures ~25ºC (Oğuz et al., 2004), suggesting that the Mg/Ca ratios in the ostracod valves primarily reflect summer and fall conditions before the onset of winter cooling. The inferred sharp increase in temperature correlates well with the last dwindling occurrences of Ponto–Caspian ostracod fauna in the cores, but also broadly corresponds to the shift of $\delta^{18}O$ values in core M02-45 from +2‰ to –2‰ (Figs. 10, 11), although detailed information on the relationship to paleotemperature has been lost at the α2 unconformity in this core. The ~6.3 cal ka sharp transition in temperature also broadly correlates with more gradual increases in total organic carbon (TOC), changes in the carbon isotopic composition of the TOC, and the proportion of marine organic carbon (Figs. 5.8, 5.9; Hiscott et al., 2007b; Linegar, 2012). These correlations collectively suggest the establishment of marine conditions across the southwestern Black Sea shelf by ~6.3 cal ka, coinciding with the establishment of a Mediterranean ostracod assemblage across the southwestern Black Sea dominated by *Palmoconcha agilis*, *Carinocythereis carinata*, *Hiltermannicythere rubra* and *Pterygocythereis jonesii* (Williams et al., 2018).

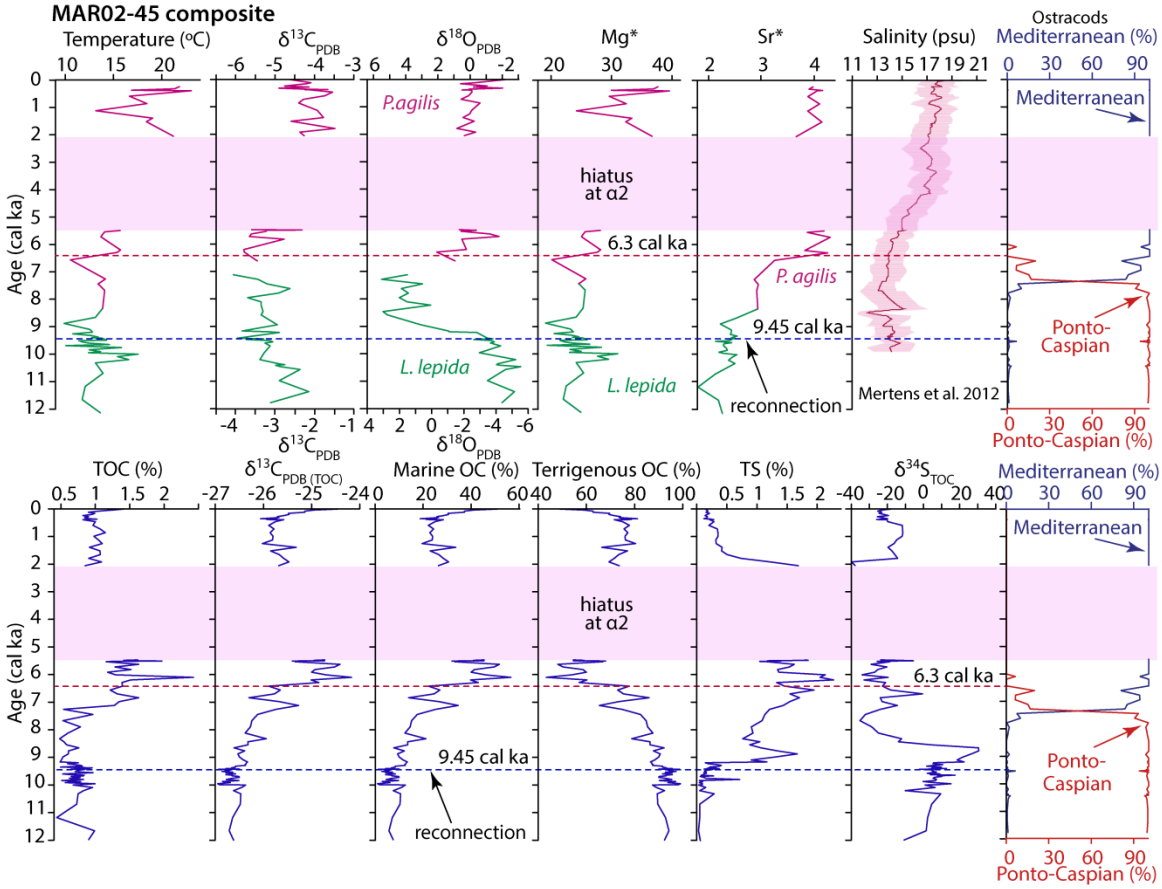

Figure 5.8. Summary of oxygen and carbon isotopes, Mg/Ca, Sr/Ca and paleotemperature in core M02-45, plotted against the Mediterranean and Ponto–Caspian ostracod assemblages from Williams et al. (2018). Replicates of $\delta^{18}O$ and $\delta^{13}C$ measurements have average reproducibility of ~0.5‰. The downcore variations in TOC, $\delta^{13}C_{TOC}$, marine and terrigenous organic carbon (OC), total sulfur (TS) and $\delta^{34}S$ of TS are from Hiscott et al. (2007b). The hiatus at α2 is explained in the text. Blue dashed line shows the time of reconnection at ~9.45–9.40 cal ka (Section 4.4; Ankindinova et al., 2019a). Element symbol followed by an asterisk = element/Ca.

5.5.5. Trace-element concentrations and element/Ca ratios

There is a growing volume of literature on trace-element incorporation into ostracod valves as new techniques allow the acquisition of progressively higher resolution data from single valves. Nevertheless, there is little information in the literature on the significance of Ba*, Cd*, Cu*, Mo*, Pb*, Rb*, Ti*, V*, Zn* and Zr* in ostracod valves.

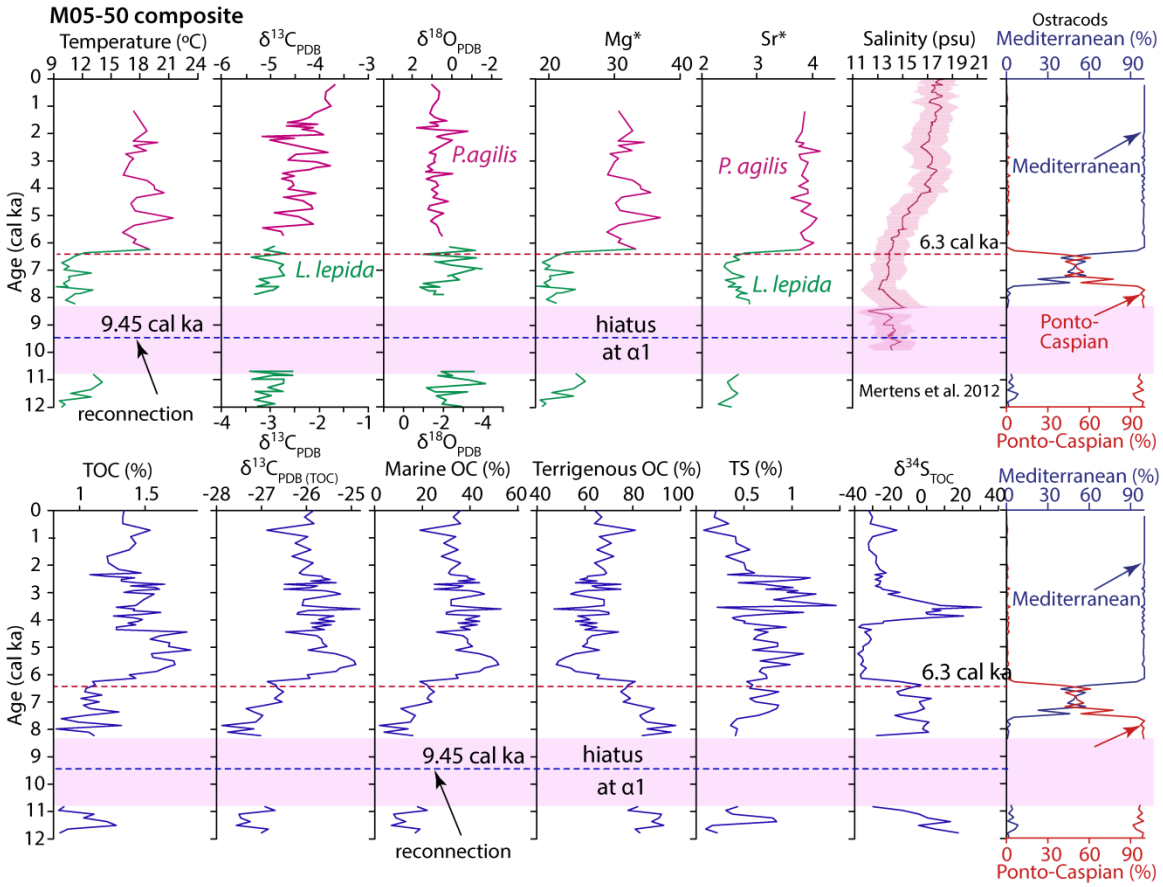

Figure 5.9. Summary of the oxygen and carbon isotopes, Mg/Ca, Sr/Ca and paleotemperature in core M05-50, plotted against the Mediterranean and Ponto–Caspian ostracod assemblages from Williams et al. (2018). Replicates of $\delta^{18}O$ and $\delta^{13}C$ measurements have average reproducibility of ~0.5‰. The downcore variations in TOC, $\delta^{13}C_{TOC}$, marine and terrigenous organic carbon (OC), total sulfur (TS) and $\delta^{34}S$ of TS are from Linegar (2012). The hiatus at α1 is explained in the text. Blue dashed line shows the time of reconnection at ~9.45–9.40 cal ka (Section 4.4; Ankindinova et al., 2019a). Element symbol followed by an asterisk = element/Ca.

Therefore, the significance of the incorporation (and amounts) of these elements in the ostracods from the southwestern Black Sea will be interpreted based on the better known behaviour of these elements in marine and lacustrine environments, and their associations with one another. As a starting point, it is assumed that the incorporation of trace elements into the $CaCO_3$ of M02-45 and M05-50 ostracods is predominantly

controlled by (a) the dissolved concentrations of trace elements in water, (b) the redox state of the water in which the fauna lived, and (c) the temperature, salinity and pH characteristics of the Black Sea/Neoeuxine Lake.

Cluster analysis indicates that the abundances of trace elements incorporated into ostracod valves were different (a) before reconnection of the Black Sea with the global ocean and up to ~9.4 cal ka, when compared with (b) a transitional period as salinity climbed to near-modern values (~9.4–6.3 cal ka), and (c) the recent past (~6.3 cal ka to Present; Figs. 5.4, 5.5). Immediately prior to reconnection at ~9.45–9.40 cal ka, ostracod valves show high levels of Ba*, Cd*, Fe*, Rb*, V* and Zr* at site M02-45; these higher values drop sharply after reconnection (Fig. 5.2). Site M05-50 does not have a record around the time of reconnection. Later, after ~7.2 cal ka and extending to the present, ostracod valves show increased levels of B*, Mg*, Mo*, Sr* and Ti* at site M02-45, joined in many samples by Ce*, La* and U*, although these latter element/Ca ratios are also higher downward into sediment as old as ~8.3 cal ka (Fig. 5.2). At site M05-50, many elements have their highest abundances in valves older than ~6.3 cal ka, followed upward by a sharp rise of Mg* and Sr*. In this same interval, some samples have enhanced Ce*, La*, Mn* and U*.

The downcore plots of the normalized Q-factor loadings show prominent temporal trends which can be readily correlated with downcore plots of individual trace-element/Ca values in both cores M02-45 and M05-50 (Fig. 5.10). For example, in both cores Factor 1 shows high loadings across the interval between ~9.40 cal ka and 6.3 cal ka, whereas Factor 2 shows high loadings across the interval between ~6.3 cal ka and the top of the cores at

~1.1–0.2 cal ka (Fig. 5.10b,c). Factor 3 is the dominant factor between the base of the cores at ~12.1 cal ka and ~9.40 cal ka (Fig. 5.10b,c). These time intervals are nearly identical to those deduced from cluster analysis (e.g., Figs. 5.4, 5.5).

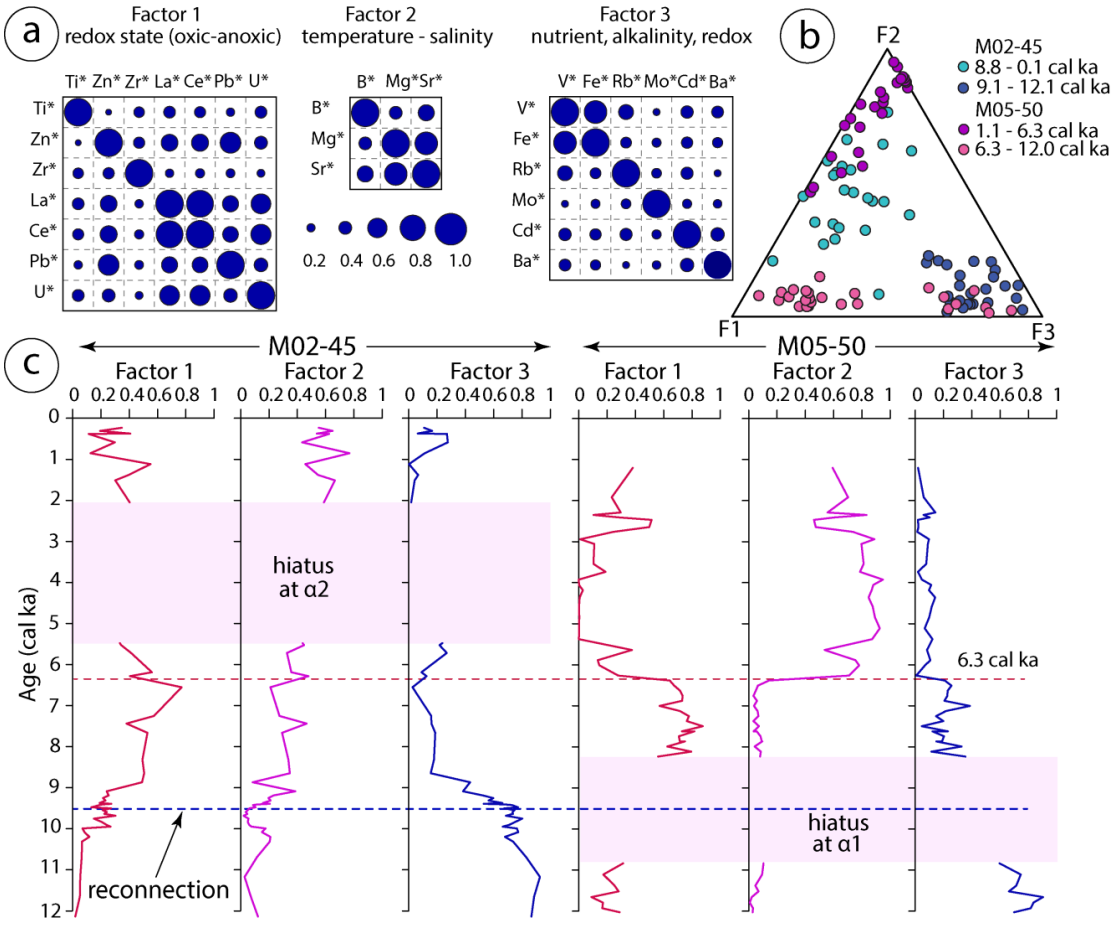

Figure 5.10. (a) Correlation coefficient matrices of the element/Ca ratios with statistically significant loadings on each factor. (b) Ternary plot of the Q-factors showing that the intervals <6.3 cal ka, 6.3–9.1 cal ka and 9.1–12.1 cal ka are dominated by Factor 2, Factor 1 and Factor 3, respectively. (c) Downcore plots of the three Q-factors in cores M02-45 and M05-50. Note the similarities in the downcore trends of Q-factor loadings between these two cores (further explained in the text). Blue dashed line in (c) shows the time of reconnection at ~9.45–9.40 cal ka (Section 4.4; Ankindinova et al., 2019a).

Trace-element concentrations in ostracod valves can be used to distinguish between open marine, brackish water, or continental influences (de Deckker et al., 1988; Janz and

Vennemann, 2005; Bahr et al., 2008; Jin et al., 2011; Ruiz et al., 2013). In enclosed basins, Mg/Ca and Sr/Ca can be used to reconstruct past salinity and to estimate changes in relative rates of evaporation versus precipitation (Tütken et al., 2006; de Deckker, 2017). The uptake of Sr in inorganic calcite depends on the Sr concentration in the ambient water and the appropriate partition coefficient (including both inorganic and biological effects).

The sharp boundary at ~6.3 cal ka in both cores (particularly M05-50) with distinctly higher Sr/Ca and Mg/Ca above this level must represent a significant oceanographic event, probably associated with the establishment of full and free water exchange between the Black Sea and the global ocean through the Marmara Sea Gateway. The quick upward change in Sr/Ca and Mg/Ca confirms, at least at this level in core M05-50 (Fig. 5.3), that bioturbational mixing has not smoothed the geochemical signatures at a 10 cm scale. 6.3 cal ka coincides with the termination of the transitional ostracod faunal turnover in cores M02-45 and M05-50, during which a mixed fauna consisting of Ponto–Caspian and selected Mediterranean species was replaced by a typical Mediterranean assemblage (Figs. 5.2, 5.3; Williams et al., 2018). This is also the time when modern Sr-isotopic ratios became the norm in Black Sea molluscs (Sections 4.3 and 4.4; Ankindinova et al., 2019a). Two previous studies have suggested that the salinity in the Black Sea rapidly increased at ~5.2 cal ka (Coolen et al., 2013; Eckert, 2014), somewhat consistent with Sr/Ca and Mg/Ca increases in the ostracod trace-element data.

Several researchers (e.g., Piper, 2016) have proposed that saline inflow filled the Black Sea basin from the bottom upward, only delivering a strong marine signal to the shallowest depths after ~ 7.8 cal ka. As argued in Section 4.4.1 and in Ankindinova et al.

(2019a), good vertical mixing was likely the norm in the first few centuries after reconnection when the seasonally-changing thermal structure of the water column had greater influence on upwelling/downwelling than salinity differences. It is certainly reasonable to believe that a stronger vertical gradient in salinity developed after ~9.0 cal ka. The onset of sapropel accumulation (at the Unit 3/2 boundary; ~7.9–7.8 cal ka; Dean and Arthur, 2011) signified nearly complete isolation of surface waters from oxygen-depleted (and more saline) deeper levels within which any Mediterranean immigrants (as larvae) would have perished. The quite rapid increase in Sr/Ca, Mg/Ca and temperature at ~6.3 cal ka on the southwestern shelf might reflect the rise of the halocline to at least the edge of the shelf, so that storm waves could more easily mix saline waters to the surface, allowing Mediterranean immigrants to colonize the shelf and, eventually, to flourish.

Conservative behaviour and long residence times in oxic seawater of redox-sensitive trace elements Mo and U, and Mn–Fe redox cycling within the water column, make these elements strong potential paleoproxies in marine and lacustrine environments (e.g., Tribovillard et al., 2006; Helz et al., 2011; Scholz et al., 2013), particularly in the delineation of oxic versus anoxic/euxinic environments (Algeo et al., 2012; Tribovillard et al., 2012; Börner et al., 2013). High Fe*, Mn* and U* before ~6.3 cal ka in both cores, but particularly in core M05-50 (e.g., Figs. 5.2, 5.3) might be associated with the onset of watermass stratification across the southwestern Black Sea as bottom waters progressively became suboxic following the reconnection with the Marmara Sea.

Several redox-sensitive trace elements such as Cu, Zn, Cd and Pb are delivered to the sediment mainly in association with organic matter and tend to be incorporated into Fe-

sulfides (eventually pyrite) following the decay of organic matter in reducing environments (e.g., de Deckker, 2017). Trace elements such as Ba and P are shown to have considerable potential as paleo-productivity proxies (Schoepfer et al., 2015).

Seawater in oxygenated oceans is generally depleted in dissolved Ce and La (and almost all rare earth elements, REE), largely because of their oxidative removal from the environment. However, these elements exhibit several-fold increases in anoxic environments (e.g., De Baar et al., 1988; German and Elderfield, 1990). Many REEs exhibit reductive dissolution in suboxic waters (or enrichments in deeper anoxic waters), very much like Mn and Fe in anoxic waters of the Black Sea (Westerlund, 1986), the Cariaco Trench (German and Elderfield, 1990) or Saanich Inlet (German and Elderfield, 1989). For example, in the Cariaco Trench all dissolved REEs exhibit low concentrations in the upper oxic waters, but show a sharp increase just at or below the oxic/anoxic interface, coincident with trends of dissolved Mn and Fe (German and Elderfield, 1990).

Dissolved Mo and V concentrations are high in the oxic surface waters of the Black Sea, but show a rapid decline across the redoxcline, and are scarce in deep waters because of rapid removal in sulfidic waters (Emerson and Huested, 1991; Colodner et al., 1995). However, dissolved Fe concentrations are very low in the oxic surface waters, high in the anoxic waters but notably low in the euxinic H_2S-rich deep waters (Colodner et al., 1995; Anderson and Raiswell, 2004).

Across the northwestern Black Sea shelf, dissolved Cd and Zn concentrations increase gradually with water depth suggesting that coupling with the cycle of production and decomposition of organic material is important and that dissolved Cd and Zn are

depleted in surface waters through uptake in phytoplankton and/or adsorption onto biogenic particles (Cullen et al., 1999; Tankéré et al., 2001). The similarities of Cd and Zn profiles suggest some interdependence in their cycles, in particular a common benthic source. Tankéré et al. (2001) showed high correlation coefficients between dissolved Cd and dissolved Mn and Fe, which are consistent with release of Cd and Zn adsorbed onto Mn- and Fe-oxides following reductive dissolution of the host phases.

The notably high Ba*, Cd*, Mo*, P* and Zn* ratios from ~8.3–6.3 cal ka in core M05-50 and from ~10.4–9.2 cal ka in core M02-45 may be interpreted as periods of high primary productivity in the southwestern Black Sea (Figs. 5.2, 5.3). This interpretation is based on comparison with studies that show Ba/Ca and Mo/Ca ratios associated with phytoplankton dynamics in coastal environments, where peaks in Ba/Ca and Mo/Ca are associated with diatom blooms that occur associated with nutrient increases in the ocean (Thébault et al., 2009). Similarly, some studies in marine sedimentary successions show close linkages between the accumulation patterns of authigenic carbonate and the incorporation of Ba, Cd and P, strongly suggesting close association of these elements with higher oceanic calcareous phytoplankton production (e.g., Wei et al., 2003).

Given the background information presented above, Factor 1 (9.40–6.3 cal ka) is interpreted as a redox indicator, particularly oxic-anoxic discrimination based on the tendency for dissolved Ce, La, Pb and U to be removed in oxygenated surface waters. Associated elements Cd, Cu and Fe are likewise sensitive to redox conditions. This factor is also affected by coupling between water depth and the cycle of production and decomposition of organic material. Specifically, Zn and Cd tend to be depleted in surface

waters because of uptake by phytoplankton and/or adsorption onto biogenic particles which eventually sink.

Factor 2 (6.3 cal ka to Present) is interpreted as a temperature and salinity indicator because Mg/Ca and Sr/Ca have been used for the reconstruction of past changes in ocean and lake temperatures and salinities (Chivas et al., 1985; 1986a,b; Holmes, 1996; de Deckker et al., 1999; Dwyer et al., 2002; Holmes and Chivas, 2002; Ito, 2002; Ito et al., 2003). Although previous studies have suggested that there are taxonomic differences in the biochemically moderated partition coefficients of trace elements in different ostracod species (e.g., Dettman and Dwyer, 2012), other studies have suggested that partition coefficients are either constant or very similar within genera or even closely related genera (e.g., Cadot and Kaesler, 1977; Chivas et al., 1986b; Engstrom and Nelson, 1991; Holmes and de Deckker, 2012).

Factor 3 (12.1–9.40 cal ka) with its statistically significant loadings on Ba*, Cd*, Fe*, Mo*, Rb*, U* and V* is interpreted as a complex factor involving nutrients, alkalinity and redox conditions in the southwestern Neoeuxine Lake, since its importance is greatest before reconnection with the global ocean (Fig. 5.10).

5.6. Summary

Oxygen and carbon isotopes and trace-element/Ca ratios measured in valves of benthic ostracods *Palmoconcha agilis* and *Loxoconcha lepida* provide a complete latest Pleistocene–Holocene record, with age constraints provided by 16 radiocarbon-dated shells in core M02-45 and 9 in core M05-50. Results reveal environmental changes and evolution of water chemistry associated with the last reconnection of the Black Sea to the global

ocean. The $\delta^{18}O$ values in composite cores M02-45 and M05-50 exhibit ranges of ~8.0‰ and ~3.0‰, respectively; $\delta^{13}C$ values show ranges of ~2.5‰ and ~2.0‰. There are three isotopic substages: (a) substage 1c (12.1–9.4 cal ka) represents conditions in the Neoeuxine Lake with relatively high $\delta^{13}C$ and low $\delta^{18}O$, (b) substage 1b (9.4–6.3 cal ka) represents the transition from lacustrine to marine conditions with an increase in $\delta^{18}O$ values as small amounts of Mediterranean water flowed into the Black Sea, and (c) substage 1a (6.3 cal ka to Present) represents the establishment of marine conditions like today with near-constant $\delta^{18}O$ values and a trend of slowly increasing $\delta^{13}C$. Trace-element/Ca ratios show downcore trends consistent with the three isotopic substages. Immediately prior to reconnection at ~9.45 cal ka, ostracod valves show high levels of Ba*, Cd*, Fe*, Rb*, V* and Zr* at site M02-45; these higher values drop sharply after reconnection. After ~7.2 cal ka and extending to the Present, ostracod valves show increased levels of B*, Mg*, Mo*, Sr* and Ti* at site M02-45, joined in many samples by Ce*, La* and U*, although these latter element/Ca ratios are also higher downward into sediment as old as ~8.3 cal ka. At site M05-50, many elements have their highest abundances in valves older than ~6.3 cal ka, followed upward by a sharp rise of Mg* and Sr*. In this same interval, some samples have enhanced Ce*, La*, Mn* and U*. The factor analysis distinguished three intervals that determined elemental behaviour (a). Factor 1 (9.40 cal ka) interpreted as a redox indicator, particularly oxic–anoxic discrimination based on the tendency for dissolved Ce, La, Pb and U to be removed in oxygenated surface waters. Associated elements Cd, Cu and Fe are likewise sensitive to redox conditions. Zn and Cd tend to be depleted in surface waters because of uptake by phytoplankton and/or adsorption onto biogenic particles which eventually sink. (b). Factor 2 (6.3 cal ka to Present) is interpreted as a temperature and

salinity indicator. In particular Mg/Ca ratio is suggesting an increase in water temperature from 12–14 ℃ to 17–19 ℃ after 6.3 cal ka BP. (c). Factor 3 (12.1 cal ka) with its statistically significant loadings on Ba*, Cd*, Fe*, Mo*, Rb*, U* and V* is interpreted as a complex factor involving nutrients, alkalinity and redox conditions in the southwestern Neoeuxine Lake, since its importance is greatest before reconnection with the global ocean.

Chapter 6. Discussion

6.1. Chronology, seismic-stratigraphy, detrital composition and mapping

It is more than 20 years since William Ryan, Walter Pitman and their collaborators proposed that the transition from a landlocked Neoeuxine Lake to the Holocene Black Sea involved a catastrophic inflow of Mediterranean water through the Strait of Bosphorus (Ryan et al., 1996, 1997; Ryan and Pitman, 1998). This proposal triggered a flurry of new research, and the emergence of strong advocates for and against what has become known as the "Flood Hypothesis" (Hiscott et al., 2007a). Despite valiant organizational efforts by Valentina Yanko-Hombach, in particular, to bring individuals with divergent views together via a number of dedicated conferences and special publications (Yanko-Hombach et al., 2007; Buynevich et al., 2011), there is still no agreement on the manner of reconnection of the Black Sea to the global ocean, although the timing is now settled to be ~9.4–9.5 cal ka based on the study of Sr isotopes in mollusc shells (Section 4.4 this thesis; Major et al., 2006; Yanchilina et al., 2017; Ankindinova et al., 2019a)

Ocakoğlu et al. (2018) provide a thorough historical summary of the debate which has taken place over the reconnection of the Black Sea to the global ocean. Those authors happen to support the "Flood Hypothesis" of Ryan et al. (2003) and Yanchilina et al. (2017). That perspective is not shared by the author of this thesis, so the following discussion focuses instead on issues relevant to the likelihood of a gradual reconnection of the Black Sea to the global ocean, during which there was a persistent outflow from a rising Neoeuxine Lake into, and through, the Marmara Sea Gateway and onward to the global ocean (cf. Hiscott et al., 2007a).

6.1.1 No evidence or time available for a Holocene lowstand

Yanchilina et al. (2017) proposed that the Neoeuxine Lake spilled out into the Marmara Sea and global ocean from ~16.3–15.0 cal ka, then experienced evaporative drawdown to a lowstand elevation of ~ –120 m by 9.4 cal ka, just before rapid inundation by saline Mediterranean water. The evidence from the southwestern shelf negates the possibility of a Holocene lowstand, because there are widespread ~ 11.0–7.5 cal ka deposits of allounit 1b across the middle and outer shelf (Figs. 3.10, 6.1d) with a cumulative volume that can only be explained if base level was sufficiently high to allow major distant rivers in Bulgaria and Romania (e.g., Kamchiya and Danube rivers) to contribute detritus through long-distance marine transport along a submerged shelf (Section 5.2; Lister et al., 2015). More importantly, the time when allounit 1b was accumulating overlaps fully with the time (11.1–10.2 cal ka) when a climbing delta lobe, sourced from the outspilling lake, was prograding into the northeastern Marmara Sea from the southern exit of the Strait of Bosphorus (Fig. 6.1b,d; Aksu et al., 2016). Mineral composition of the sand fraction in the delta lobe proves its provenance from the hillsides around the strait and from the shores of the Neoeuxine Lake (Hiscott et al., 2017). This leaves no opportunity for the Neoeuxine Lake to have evaporated to an early Holocene lowstand before the first incursion of saline water at ~9.5 cal ka (Fig. 6.1c,d). Instead, the lake must have been, and remained, above the spill depth into the Marmara Sea since ~11.0 cal ka. The flow of brackish water from the lake transported sediment along the strait to the advancing delta lobe at its southern end. Other researchers have realized that the shelves of the Neoeuxine Lake were flooded as early as ~11.7 cal ka and remained flooded until the Present, because after ~11.7 cal ka the

supply of coarse-grained detritus and turbidity currents to the Danube Fan ceased as expected during a transgression (Constantinescu et al., 2015, including a co-author of that paper, G. Lericolais, who previous supported the "Flood Hypothesis").

Unconformities α1 and α2 cannot originate from falls in base level because they both date from the middle to late Holocene when the Black Sea was fully connected to the global ocean (Fig. 6.1). The erosional surface named α1 by Yanchilina et al. (2017) on the Ukrainian and Romanian upper slope is older and likely unrelated to α1 of this paper, as it overlies Younger Dryas deposits rather than pre-reconnection Holocene deposits.

6.1.2. No indication of early Holocene limans on the southwestern shelf

To satisfy the "Flood Hypothesis", Yanchilina et al. (2017) suggested that lower Holocene successions at modern elevations shallower than –100 m (e.g. as at sites M02-45, M11-23) must have accumulated in perched ponds (referred to as limans) stranded above a lowstand Neoeuxine Lake. Ocakoğlu et al. (2018) inferred ponds of this origin offshore from Sinop, east of the study area, based on multibeam bathymetry but no sampling of sediments or dating. There are several reasons to exclude this possibility for the M02-45 site in particular, one of which is the wide distribution of allounit 1b deposits on the southwestern shelf (Fig. 3.4), all of which are above the lowstand elevation proposed by Ryan et al. (1997, 2003) and Yanchilina et al. (2017). Surely the entire shelf could not have been populated by perched ponds in an area with insignificant input from local rivers, and during a time when Cohen et al. (2011) propose dry, evaporative conditions in the Black Sea basin.

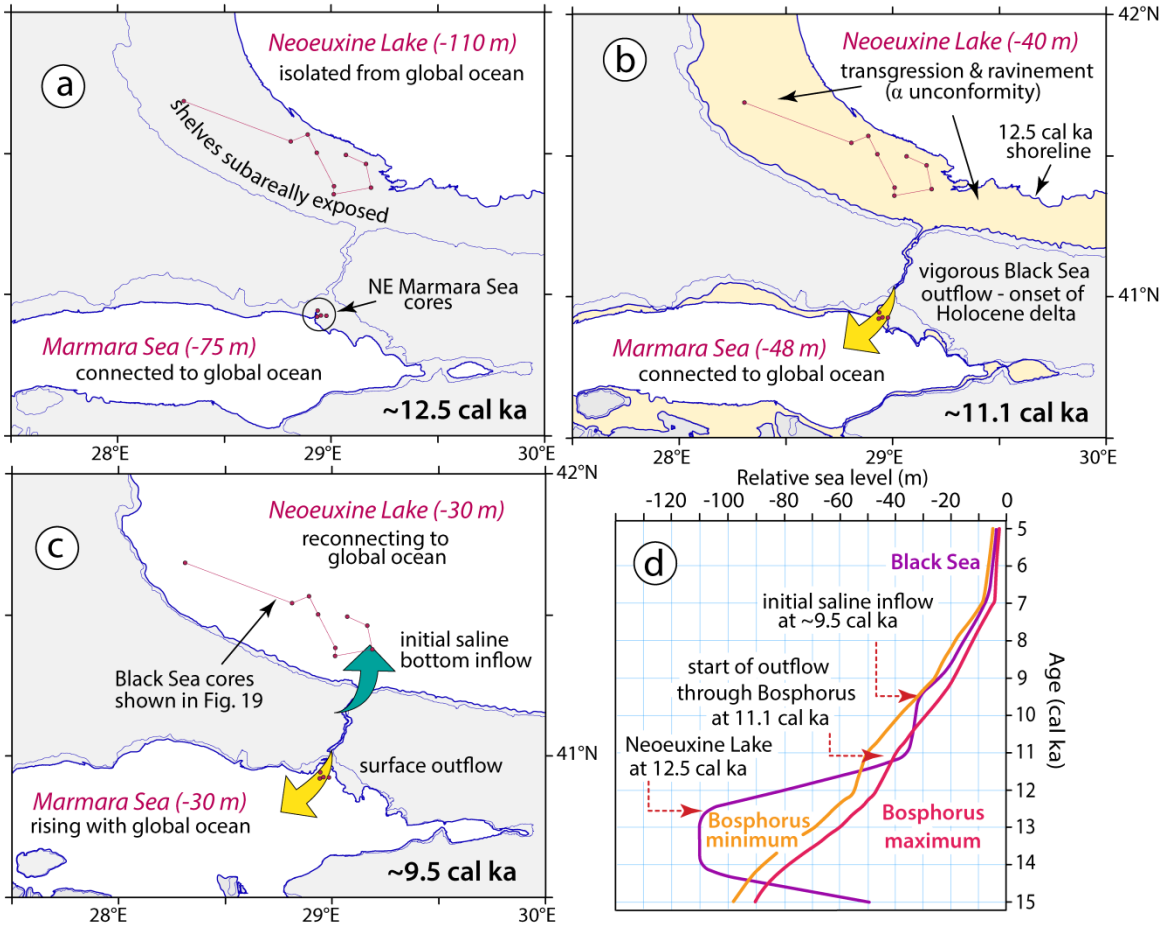

Figure 6.1. Maps showing the paleogeography of the southwestern Black Sea (Neoeuxine Lake) Marmara Sea during three critical intervals in the Holocene. (**a**) ~12.5 cal ka: the Neoeuxine Lake is isolated from the global ocean, when its level stood at –110 m below present sealevel, while the Marmara Sea was connected to the global ocean and stood at –75 m. (**b**) ~11.1 cal ka: the Neoeuxine Lake swells to –40 m below present sealevel and vigorous outflow starts into the Marmara Sea (yellow arrow) which stood at –48 m below present sealevel at this time. (**c**) ~9.5 cal ka: the time of reconnection with global ocean when the Neoeuxine Lake and the Marmara Sea were at –30 m below present sealevel. Saline inflow occurs as a bottom current (aquamarine arrow), while surface outflow continues across the Strait of Bosphorus (yellow arrow). (**d**) Sealevel curves for the Black Sea and the Bosphorus sill are from Hiscott et al. (2007b) and Lambeck et al. (2007), respectively.

Other arguments against isolation of the M02-45 site from the open Neoeuxine Lake are (a) no topographic barrier surrounding the site based on a structure-contour map at the level of the α1 unconformity (Aksu et al., 2002), (b) Sr-isotopic values through the earliest Holocene (Ankindinova et al., 2019a; Section 4.4) identical to those reported by Yanchilina et al. (2017) for the open lake, (c) dinoflagellate species and *Lingulodinium machaerophorum* process lengths indicating a pre-reconnection practical salinity at the M02-45 site of ~14, just like other sites in the open parts of the basin (Mertens et al., 2012), and (d) mineralogy of very fine sand fractions more similar to Danube detritus than detritus from local Turkish rivers (Sinclair, 2018). There really is no evidence that any of the core sites which have recovered allounit 1b on the southwestern shelf were located in limans, rather than on a transgressed shelf which had been flooded by post-glacial meltwater and enhanced river runoff as the climate became more humid in the early Holocene (Mudie et al., 2007).

6.1.3. Development of subaqueous unconformities

There are several potential physical oceanographic processes which might have contributed to the development of the α1 and α2 unconformities and their correlative conformities. These are breaking internal waves, storm-induced wave erosion, transport and erosion under the Rim Current and its anticyclonic eddies. The saline underflow is believed to have had less influence, because it is not a credible source of detritus nor agent of widespread erosion.

Internal gravity waves can form along density interfaces within stratified fluids under shear. On a shoaling seabed, internal waves will steepen and break (Lamb, 2014),

thereby generating turbulence, potentially preventing accumulation or even eroding the seabed. For example, internal waves have been determined to erode and re-suspend sediments on the Portuguese shelf to form a 10–15-m-thick bottom nepheloid layer (Quaresma et al., 2007). Similarly, internal waves are said to exhibit celerities high enough to re-suspend and maintain coarse silt to fine silt-clay in suspension along the deeper regions of the Bulgarian shelf (e.g., Dimitrov, 2014). These and other sources of water-column agitation are particularly important in explaining net accumulation versus offshore advection of muds, because cohesion makes it far more difficult to erode deposited mud than to keep it in suspension. In the southwestern Black Sea, the various processes listed above could keep suspended load moving along the shelf, away from its ultimate source in drainage basins of the Danube and other major rivers, to a point where topography, flocculation, or trapping near the seabed in a stratified water column might promote accumulation. Otherwise, the suspended load might continue to move toward the east, might be shunted off the shelf in the persistent saline underflow in front of the Strait of Bosphorus, or might be advected into central basinal areas to ultimately settle into deep anoxic waters.

Potentially small shifts in the balance between episodes or events of accumulation and erosion are believed to be responsible for the unconformities and sedimentary allounit development (Section 3.4.1). Such small shifts might be caused by switching between delta lobes of source rivers, or by climatic variations. A high resolution study of Central and Eastern Europe (Perșoiu et al., 2017) suggests that Holocene temperature increased in a gradual manner towards a mid-to-late-Holocene peak (between 4–2 cal ka), and then

decreased towards 0.8 cal ka with a minimum during the Little Ice Age (AD 1300–1850). In the earliest Holocene, it is even possible that the climate was sufficiently cold that parts of the Black Sea were frozen in the winter (cf. Yavuz et al., 2007), which might have protected the southwestern shelf from wave action during particularly violent winter storms (Arkhipkin et al., 2014). This would have enhanced mud accumulation relative to erosion and, although speculative, might help explain why allounit 1b experienced uninterrupted net accumulation from ~11.5–8.5 cal ka even though base level was lower at that time than during the development of both α1 and α2.

6.1.4. Potential contributions from European loess

Loess is widespread today as a deeply eroded blanket of Pleistocene windblown silt in the drainage basins of the Danube, Kamchiya and other Bulgarian rivers (Smalley and Leach, 1978; Haase et al., 2007; Marković et al., 2015). This loess would have been available to swell the volume of suspended sediment in southward-flowing early Holocene coastal currents, as suggested by Lister et al. (2015) to explain a high accumulation rate (Fig. 3.10) and the mineral content of allounit 1b. Allounit 1b contains 20–30% detrital calcite and minor detrital dolomite. The silt fraction of a sample from the allounit with depositional age 9.58 cal ka was digested in acid to isolate its calcite carbon (as carbonate species), and this separate was then radiocarbon dated, giving an age of 13570 ± 35 yr BP (UGAMS 24289, Radiocarbon Dating Laboratory, Université Laval). The calibrated age of this detrital calcite (IntCal13 calibration curve) is ~16.3 cal ka, within the range of younger loess sequences in the Danube basin and environs (Újvári et al., 2010; Marković et al., 2015; Rousseau et al., 2018). Much of the calcite in loess is diagenetic (Újvári et al.,

2010), so a Late Pleistocene age for the detrital calcite in allounit 1b opens the possibility that even older loess was eroded from major river basins as a source, in part, for allounit 1b.

6.1.5. Holocene sediment pathways from the Danube Delta to the Bosphorus

The seismic grid for this study lies in Turkish territorial waters, but the Holocene mud belt extends beyond the study area toward the northwest into Bulgarian waters (Fig. 6.2). Lister et al. (2015) quantified the sediment discharges of Turkish rivers in Thrace, and argued that their yields through the Holocene would have been insufficient to supply the successions on the nearby shelf. Assuming that Holocene marine muddy sediments in allounits 1b–1d exhibit ~65% porosity and that ~60% of river sediment discharge is retained at the associated deltas (Kukal, 1971), the local Turkish rivers and all Bulgarian rivers as far north as the Romanian border would take ~32 kyr to deliver the volume of Holocene sediment sequestered on the southwestern Turkish shelf (Table 6.1). Given that the Bulgarian shelf has its own thick blanket of Holocene muddy sediments, characterized by a 20–30 m-thick shore-parallel prominent belt between capes Kaliakra and Emine (Fig. 6.2, Hristova, 2006, 2007; Dimitrov, 2010, 2014), much of the sediment supply to the Turkish shelf must have come from a far larger source than these Turkish and Bulgarian rivers. First-order calculations support this conclusion. For example, the proportion of the detritus delivered by the combined Bulgarian and Turkish rivers into allounits 1b–1d can be estimated for two cases (Table 6.1). For the first case, 100% of the yield of the Bulgarian and Turkish rivers is assumed to have contributed to Allounit 1 in the study area on the Turkish shelf.

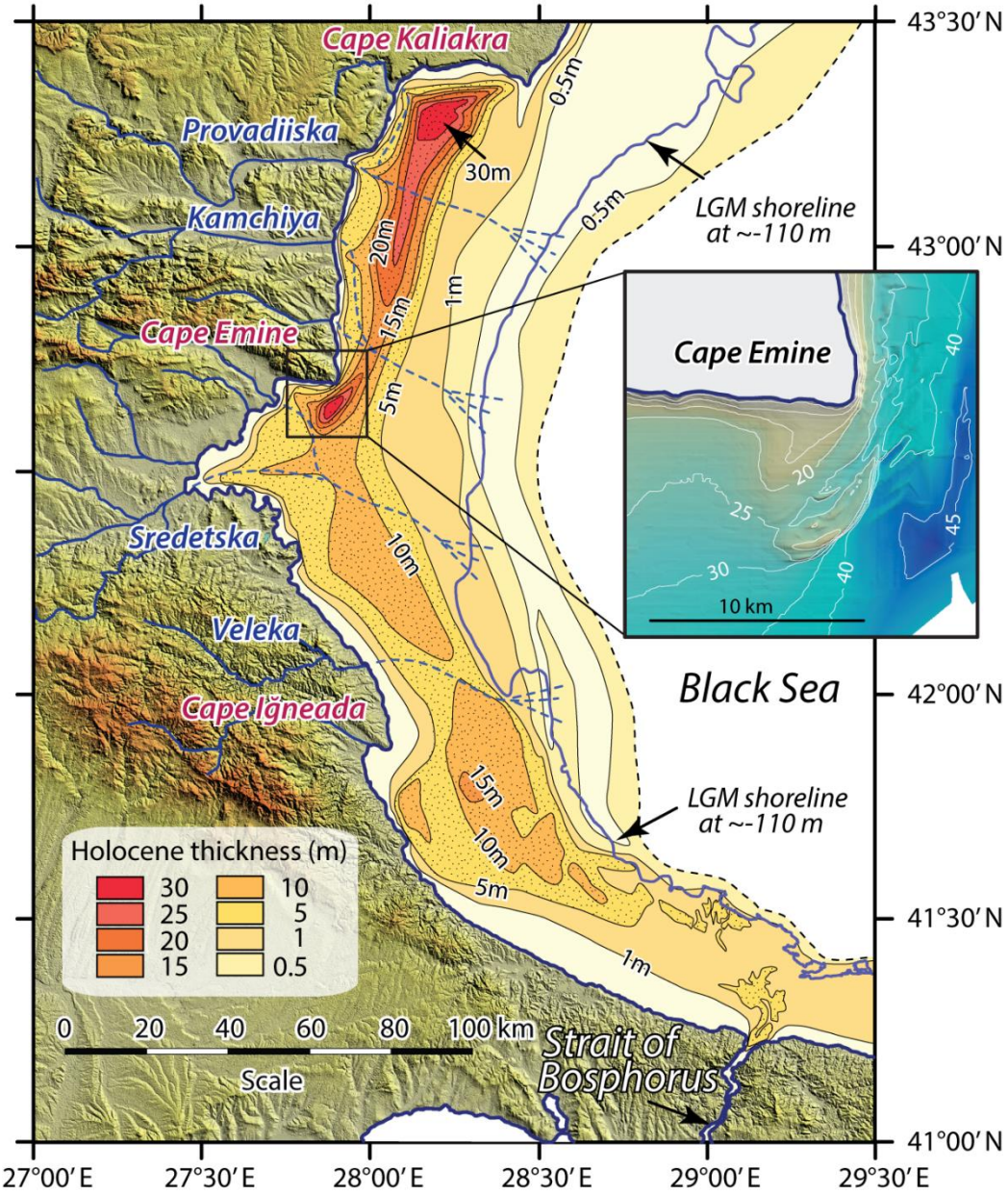

Figure 6.2. Map of the southwestern Black Sea showing the regional thickness distribution of Holocene deposits (Bulgarian shelf between capes Kaliakra and Iğneada is simplified and redrawn from Hristova, 2006, 2007; Dimitrov, 2010, 2014). The gridded xyz data for the multibeam inset were downloaded from the EMODnet Bathymetry Consortium site (http://doi.org/10.12770/18ff0d48-b203-4a65-94a9-5fd8b0ec35f6), and displayed and contoured using Global Mapper. The topography and –110 m isobath are extracted from GeoMapApp (Ryan et al., 2009), and compiled using Global Mapper. Coastline is from NOAA National Geophysical Data Center (http://www.ngdc.noaa.gov/mgg/shorelines/shorelines.html).

For the second case, only 30% of the available yield of the Bulgarian and Turkish rivers is assumed to have accumulated in the study area on the Turkish shelf. The estimates of the proportion of the total mass calculated for the various allounits (based on isopachs) that could have been supplied solely by Bulgarian and Turkish rivers under time constraints provided by radiocarbon dates range between ~32.5% (allounit 1d), 21.4% (allounit 1c), 87.1% (allounit 1b) for Case 1 (Table 6.1) and 11.3% (allounit 1d), 7.4% (allounit 1c) and 30.3% (allounit 1b), with an average Holocene value of 13.4% for Case 2. Case 1 is not a very realistic scenario because of the presence of a thick blanket of sediment across the Bulgarian shelf which must have sequestered some of the available detrital supply from local rivers.

Even if Case 1 were valid, the predicted mass of detritus is insufficient to account for the solids in the various allounits. The situation is considerably worse for Case 2 (Table 6.1). The only viable alternative is that the overwhelming proportion of the detritus found within Holocene allounits of the study area must have been supplied by point sources other than the Bulgarian and Turkish rivers. In the western Black Sea, the only reasonable source is the Danube River, which today has an annual sediment discharge ~140 times that of all Bulgarian rivers and Turkish streams in Thrace combined (i.e., 87.8×10^6 T yr^{-1} vs 6.2×10^5 T yr^{-1} ; Jaoshvili, 2002). Longshore transport from the Danube Delta is predominantly toward the south (Dinu et al., 2013). A multibeam map of the central Bulgarian shelf (inset in Fig. 6.2) reveals the presence of a prominent feature on the shallow shelf south of Cape Emine that strongly resembles a recurved spit, underlain by a 20–30 m-thick Holocene deposit (Fig. 6.2; Dimitrov, 2010, 2014).

Table 6.1. Volumetrics of allounits in the southwestern Black Sea. Volumes of sediments contained in allounits are calculated using Global Mapper 14. (**6.1.1**) A = sediment discharge rates for the Bulgarian and Turkish rivers taken from Jaoshvili (2002). B = sediment discharge rates calculated taking 40% of A, based on the suggestion that only 40% of the sediments associated with river discharge leave the immediate prodelta areas (Kukal, 1971). C = sediment discharge rates calculated taking 30% of B. (**6.1.2**) See text for explanations. (**6.1.3**) Case 1 and Case 2 assume that 100% and 30% of the sediments supplied by the Bulgarian and Bulgarian + Turkish rivers reach the Turkish sector of the southwestern Black Sea, respectively. (**6.1.4**) Percentages of accumulated mass accounted for by rivers using sediment discharge rates in columns C and B of part 4.1. The Danube River percentage contributions are calculated by subtracting the percentages of the total mass accounted for by Bulgarian + Turkish rivers from 100.

(6.1.1) Sediment discharge (T yr^{-1})

	A	**B**	**C**
Bulgarian Rivers	1445000	578000	173400
Turkish rivers	104520	41808	41808
Bulgarian + Turkish rivers	549520	619808	215208

(6.1.2) Volumetrics

allounit 1d	**allounit 1c**	**allounit 1b**	**allounit 1b-1d**	**units**
Raw volume	10.496	7.192	3.912	21.600	**km^3**
Volume at Φ = 65%	3.674	2.517	1.369	7.560	**km^3**
Weight at ρ = 2.65 t m^{-3}	9.735	6.670	3.628	20.034	**MT**
Duration of deposition	5100	2300	5100	12500	**years**
Sediment discharge rates to account for weight	1908858	2900180	711416	1602705	**T yr^{-1}**

(6.1.3) Time required to account for weight of allounits (years)

Case 1 (allounits)	**1d**	**1c**	**1b**	**1b-1d**
Bulgarian rivers	16843	11541	6277	34661
Turkish (Thrace) rivers	232854	159549	86783	479186
Bulgarian + Turkish rivers	15707	10762	5854	32323
Case 2				
Bulgarian rivers	56143	38468	20924	115535
Turkish (Thrace) rivers	232854	159549	86783	479186
Bulgarian + Turkish rivers	45236	30995	16859	93090

(6.1.4) Percentage of fill accounted for by rivers

Using values at 6.1.1 Column C	**1d**	**1c**	**1b**	**1b-1d**
Bulgarian rivers	9.1	6.0	24.4	10.8
Bulgarian + Turkish rivers	11.3	7.4	30.3	13.4
Danube River	88.7	92.6	69.7	86.6
Using values at 6.1.1 Column B	**1d**	**1c**	**1b**	**1b-1d**
Bulgarian rivers	30.2	19.9	81.2	36.1
Bulgarian + Turkish rivers	32.5	21.4	87.1	38.7
Danube River	67.5	78.6	12.9	61.3

The sedimentary feature is ~9.0–9.5 km long and at its central region it is ~0.9–1.1 km wide. It is presently located at ~30–35 m water depth. The characteristic morphology and location at a sharp change in orientation of the coastline justify interpretation of this feature as an abandoned spit from a time when base level was ~35 m lower than today, with the top of the spit being a subaerial beach-dune complex. Recurved spits form as a result of wave refraction where sand has accumulated by longshore drift. The presence of a spit in this area and at this water depth would require (a) that south-directed longshore transport away from the Danube Delta characterized the Neoeuxine Lake when it was at its spill depth into the Marmara Sea (i.e., –35 m elevation), and (b) that the stillstand at the spill depth lasted hundreds of years to account for growth of such a large spit which prograded ~9.5 km during the early Holocene. A mud belt (sensu Liu et al., 2018) is clearly evident extending from a constriction at Cape Kaliakra (where a narrow shelf might have focused shelf currents and induced bypass) to the vicinity of the northern exit of the Strait of Bosphorus (Fig. 6.2). Unimpeded along-shelf transport could only have existed if the level of the Neoeuxine Lake was above ~ –40 m to –35 m through the entire Holocene (see also Giosan et al., 2009). The transport pathway apparently did not end near the Bosphorus exit, but apparently continued southward through the strait to the delta lobe in the northeastern Marmara Sea (Aksu et al., 2016) that is contemporary with the lower portion of allounit 1b.

6.2. Implications of the Sr isotopic evolution

The only acceptable geological history of the study area must be consistent and compatible with observations elsewhere in the Black Sea, in the Marmara Sea, and in the Aegean Sea. For example, if there is good evidence of outflow from the Neoeuxine Lake

(today's Black Sea) into the Marmara Sea from 11.1–10.2 cal ka (Aksu et al., 2016), then it is not possible to believe that the Neoeuxine Lake remained at a lowstand well below its Bosphorus outlet through the earliest Holocene.

This part of the discussion is an attempt to fit the M02-45 Sr-isotopic story into a wider range of events in the Black Sea – Marmara Sea – Aegean Sea corridor preceding, during, and following the reconnection of the Black Sea to the global ocean.

6.2.1. Relationship of Sr-isotopic variations to other Black Sea events

The total sulfur peak and $\delta^{34}S$ excursion documented by Hiscott et al. (2007a) are found in sediments which accumulated between the developments of the two $^{87}Sr/^{8}6Sr$ plateaux (Fig. 4.1). These sulfur variations have been explained as the result of total microbial conversion of a limited supply of seawater sulfate to sedimentary sulfides, and imply a significant decrease or potentially a hiatus in seawater entry into the basin (so consistent with development of a plateau and possible $^{87}Sr/^{86}Sr$ decline). However, the sulfur anomalies occur in sediment ~1.5 kyr older than the apparent $^{87}Sr/^{86}Sr$ decline at ~7.5 cal ka (Fig. 4.1). This age difference is easily explained, because sulfate reduction is a diagenetic process which occurs in the shallow subsurface, so in sediment older than the contemporaneous seabed. Sulfate diffuses downward in the pore water within the shallowest sediments until it is reduced and fixed into monosulfides. In core M02-45, sediments deposited toward the end of the upper Sr-isotopic plateau are ~50–80 cm higher in the succession than sediments exhibiting excursions in total sulfur and $\delta^{34}S$ (Hiscott et al., 2007a their figure 7), and the oceanographic conditions associated with consumption

of the first pulse of seawater sulfate should be assigned to this younger time interval, ~8.0 cal ka.

The first euryhaline molluscs and ostracods do not appear until $^{87}Sr/^{8}6Sr$ climbs above 0.70907 (Fig. 4.1; $\xi = 0.72$), ~2000 years after the reconnection. This coincides rather closely with the onset of sapropel deposition in the Black Sea (Dean and Arthur, 2011). If the end members by this time were average Mediterranean seawater and average river waters (Table 4.1), the proportion of river water in the basin to account for the observed Sr-isotopic ratio would have been 93.5% (Eqn 4.1), leading to a practical salinity of 2.5. This is certainly incorrect, because other studies indicate that the Neoeuxine Lake has a pre-reconnections practical salinity of ~8–12 (Leonov, 2005; Mertens et al., 2012; Yanko-Hombach et al., 2014; More et al., 2018) and that the lake water was toxic to the first Mediterranean immigrants. The alternative scenario is that a considerable volume of Neoeuxine Lake water remained in the Black Sea long after the reconnection, augmenting its salinity without inflating the $^{87}Sr/^{8}6Sr$ ratio. This residual brackish water would have contributed to the development of a stratified water column and conditions for sapropel deposition because of its greater density than river water.

Several trials using Equation 4.1 confirm that a significant salinity rise by ~7.5 cal ka is not possible unless (1) the brackish component had an initial practical salinity of ~10, and (2) the Sr concentration in that component was ~0.5 ppm or higher, so at least double that of modern river sources (Table 4.1). For example, with modern seawater parameters and a practical salinity, Sr concentration and $^{87}Sr/^{8}6Sr$ ratio for the brackish component of 8–10, 0.5 ppm and 0.708853 (all after some dilution of pre-existing Neoeuxine Lake water

by river water; brackish $\xi = 0.04$), a mixed water body would attain a $^{87}Sr/^{8}6Sr$ ratio of 0.70907 ($\xi = 0.72$) when its practical salinity reached 13–15, with seawater accounting for ~13% of the water volume. A practical salinity of 13–15 at 7.5 cal ka is consistent with estimates based on dinoflagellate cyst process lengths (Mertens et al., 2012) and environmental requirements for successful replacement of *Dreissena*-dominated assemblages by euryhaline molluscs and ostracods (Orlova et al., 2005; Ivanova et al., 2015; Büyükmeriç, 2016).

6.2.2. Relationship of new data to down-system events in Marmara and Aegean seas

From the latest Pleistocene onward, the Black Sea must be viewed as part of the larger Mediterranean–Caspian network. In this section, features of the Sr-isotopic trend determined for basinal waters (Fig. 4.1) are considered with reference to events in the Marmara Sea, eastern Mediterranean Sea, and global ocean. Prior to first entry of saline water at ~9.5 cal ka, a climbing delta lobe accumulated at the southern end of the Strait of Bosphorus. This lobe is securely dated to 11.1–10.2 cal ka (Aksu et al., 2016) and is not of mid-Holocene age as proposed by Eriş et al. (2007) based on their incorrect ties between a Calypso piston-core site and vintage seismic profiles in the area. 13–10 cal ka is a time of declining $^{87}Sr/^{8}6Sr$ ratios in the Neoeuxine Lake (Fig. 4.1), reasonably explained by a growing discharge of fresh water into the lake. Other studies have identified this as a time of increased precipitation, river runoff via major rivers and possible enormous ice-dam outburst floods from central–east Asia (Mudie et al., 2002; Thom, 2010; Aksu et al., 2016). An influx of fresh water is consistent with a rise in the level of the lake and overspill into the Marmara Sea to create the climbing delta lobe. Overspill in this period is also consistent

with the onset of stratification and sapropel development in the Marmara Sea (M1) and eastern Mediterranean Sea (S1) (onsets ~11.8 cal ka and ~10.5 cal ka respectively; Çağatay et al., 2000; Rohling et al., 2015). Rohling et al. (2015) discounted Black Sea outflow as a factor in S1 initiation because reconnection between the global ocean and the Black Sea occurred later (~9.5 cal ka), but this is not a valid argument because water export from a high Neoeuxine Lake, via a spillway into the Marmara Sea, need not coincide with entry of saline water into that lake. Other researchers (Sperling et al., 2003; Vidal et al., 2010) have dismissed Black Sea outflow as a significant factor but their data might not have captured the existence of a brackish surface outflow toxic to marine organisms living below the contemporary pycnocline (Aksu et al., 2016).

The termination of deposition of sapropel M1 in the Marmara Sea occurred at ~6.9 cal ka (Çağatay et al., 2000). This coincides closely with a sharp rise in the $^{87}Sr/^{86}Sr$ signal in the Black Sea toward present-day marine values that could have been caused by a weakening of Black Sea outflow, reducing the severity of water-column stratification in the Marmara Sea to the point that its bottom waters ceased to be dysoxic to anoxic. A very similar termination age characterizes sapropel S1 in the Aegean Sea and eastern Mediterranean Sea (İşler et al., 2015; Rohling et al., 2015), and might have the same explanation.

The draining of glacial Lake Agassiz in North America has been identified as a globally significant event, inducing a rapid rise in global sealevel of ~1.4 m at ~8.4 cal ka (Turney and Brown, 2007; Herrle et al., 2018). In the Black Sea, this rapid rise should have introduced an additional ~565 km^3 of saline Mediterranean water and expelled an

equivalent amount of brackish surface water. In the M02-45 Sr-isotopic record, this event indeed corresponds with a portion of the rapid rise in $^{87}Sr/^{86}Sr$ from ~0.70897–0.70907 (Fig. 4.1; ξ = ~0.41–0.72). However, using a modified version of Equation 4.3 and an approximate 8.4 cal ka $^{87}Sr/^{86}Sr$ value for the evolving Black Sea of 0.70906 (ξ = 0.69), the instantaneous addition of a 1.4 m-thick basin-wide slab of Mediterranean seawater to the Black Sea (assuming it had a Sr concentration in the range 0.5–0.2 ppm) would only increase the isotopic ratio to 0.709062–0.709064 (ξ = 0.70 for both), too small a change to be resolvable in the M02-45 Sr-isotopic trend (Fig. 4.1).

6.3. Discussion of oxygen and carbon isotopic composition and trace elements in ostracod biogenic carbonate

New $\delta^{18}O$ and $\delta^{13}C$ and trace-element data acquired from ostracod carapaces reveal that significant environmental changes occurred across the southwestern shelf region during the transition from the Neoeuxine Lake stage into the present-day Black Sea stage (Fig. 5.1). Although $^{87}Sr/^{86}Sr$ data from core M02-45 (Ankindinova et al., 2019a; Section 4.4) suggest a transition to the modern Black Sea from ~9.40–7.0 cal ka, the trace-element/Ca, $\delta^{18}O$ and $\delta^{13}C$ isotopic data extend this transition to ~6.3 cal ka when saline waters fully impacted shelf ecosystems.

There are several sources of uncertainty to consider. The radiocarbon dates have 1σ errors of ±50–100 years, but any age uncertainty is more than compensated for by clear stratigraphic arrangement of the samples in the two continuously cored successions. Average accumulation rates and temporal resolution are well constrained. Bioturbational mixing certainly must have a smoothing effect on our results, because specimens in a

collection of ostracod valves at any core depth might differ in age by many tens to, locally, >100 years. This mixing probably explains the ~0.5‰ difference between replicate $\delta^{13}C$ and $\delta^{18}O$ measurements, and the scatter in trace-element concentrations. Fortunately, around the time of reconnection of the Black Sea to the world ocean the age difference between adjacent samples is <50 years (Fig. 3.10, 3.11). There is no evidence for deep burrowing, so it is believed that each sample contains ostracods spanning a unique and narrow range of ages, with no overlap. There is no way to sum the various sources of uncertainty into a single parameter to apply to the analysis of the Holocene history of the southwestern Black Sea shelf, so I merely alert the reader to these issues. In most cases, the time scales involved at the principal transitions are longer than 100 years and isotopic or trace-element shifts are larger than the potential cumulative uncertainty, so that general conclusions are considered to be robust.

6.3.1. Neoeuxine Lake (12.1–9.40 cal ka)

The level of the Neoeuxine Lake at ~12.1 cal ka was shallower than ~ –65 m below present sea-level, but rose to the –40 m to –35 m spill point into the Marmara Sea by 11.1 cal ka (Aksu et al., 2016), then to –32 to –23 m below present at 9.50–9.40 cal ka (Lambeck et al., 2007; Fig. 6.3). The modern – 69 m water depth at the M02-45 site, the sub-wavebase facies (Hiscott et al., 2007b), the presence of a 10.6–5.5 cal ka unbroken succession (Fig. 3.10, 3.11), and the Sr-isotopic record obtained from this site (Section 4.4; Ankindinova et al., 2019a) require a water level in the range of –40 m to –30 m when saline water first breached the Strait of Bosphorus at ~9.50 cal ka. Beforehand, the Neoeuxine Lake was completely disconnected from the Mediterranean Sea ($^{87}Sr/^{86}Sr$ ~0.70886; Ankindinova et

al., 2019a; Section 4.4). TOC values average 0.5–1.0% (Figs. 5.8, 5.9, 6.3), with $\delta^{13}C_{TOC}$ ranging from –26.5‰ to –27‰.

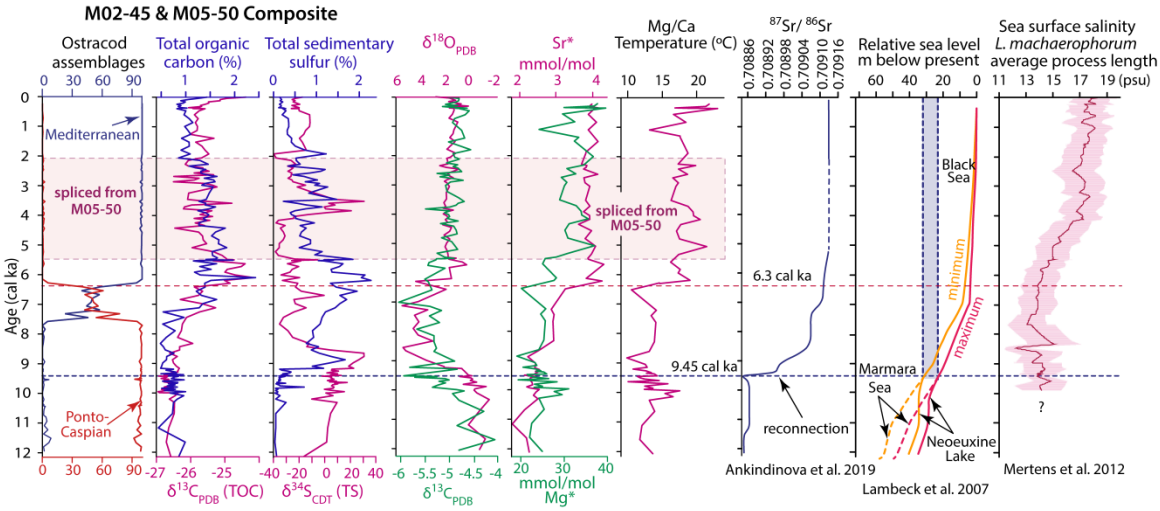

Figure 6.3. Downcore variations of various paleoproxies in a regional composite for the SW Black Sea. The records are largely from composite core M02-45, except for those variables across the α2 hiatus which are spliced from composite core M05-50. Blue dashed line shows the time of reconnection at ~9465–9380 cal yr BP.

Approximately 90% of the TOC apparently was terrigenous in origin, derived from C3 plants, with only ~10% marine (Figs. 5.8, 5.9, 6.3). Total preserved sulfur is very low (<0.5%) and $\delta^{34}S$ is uniform in the range 0 to +10‰ (Hiscott et al., 2007b). Elevated $\delta^{34}S$ values suggest that there was no influx of seawater sulfate to nourish sulfate-reducing bacteria – otherwise bacteria would have multiplied to reduce the sulfate to sulfide during early diagenesis, with a predicted sulfur isotopic shift of ~–40‰ (Habicht and Canfield, 1997; Canfield, 2001). Low $\delta^{18}O$ values in ostracod valves suggest that the region must have been isolated from the global ocean, receiving a near-constant influx of glacial melt water which promoted an isotopic decline of –5‰ to –6‰ (Figs. 5.8, 5.9, 6.3). During this interval, lake temperatures were low (ca. 12–15ºC) based on ostracod Mg/Ca ratios. Lake salinities were similarly low as suggested by ostracod Sr/Ca ratios.

Elevated Ba* in both cores M02-45 and M05-50, elevated Cd* in core M05-50 (Figs. 5.2, 5.3) and the predominance of Factor 3 (Fig. 5.10) across this time interval collectively suggest high biological productivity before ~9.40 cal ka, consistent with the TOC values of ~1% (Figs. 5.8, 5.9). This interval is also marked by notably elevated Fe*, Mn*, Ti* and Zr* in core M05-50 (c.f., Table 5.4), which probably suggests low oxygen conditions in the deeper portion of the shelf. Cycling of Fe* and Mn* is predominantly controlled by redox conditions, because in well oxygenated waters there is very little Fe or Mn present in solution (Holmes, 1998). Higher overall TOC values in core M05-50 compared to M02-45 probably indicates lower oxygen concentrations in the deeper portion of the southwestern shelf (cf. Figs. 5.8, 5.9).

The reconnection to the global ocean is marked by a dramatic increase in $^{87}Sr/^{86}Sr$ from 0.708843 to ~0.708965 (Fig. 4.1; Ankindinova et al., 2019a). This event occurred during the α1 hiatus at the M05-50 site (Figs. 5.2, 5.3). The trace-element/Ca ratios between ~10.0 cal ka and 9.45 cal ka, immediately before the reconnection, exhibit several notable features in core M02-45 (Fig. 5.2). For example, conspicuous spikes occur toward high values of Ba*, Cd*, Fe*, Mo*, Rb*, V* and Zr*, with smaller spikes in B*, Ti* and P*. These spikes become subdued and values sharply decline between ~9.45 and ~9.40 cal ka (Fig. 5.2). The sharp declines in Ba*, Cd*, Mo* and lesser declines in B* and P* suggest a sharp drop in biological productivity, possibly associated with a faunal/floral turnover in surface waters as saline Mediterranean water started to penetrate into the Neoeuxine Lake.

6.3.2. Transition to modern Black Sea (9.40–6.3 cal ka)

During 9.40 – 6.3 cal ka, TOC is ~0.5% and remains ~85–90% terrigenous in origin, while $\delta^{13}C_{TOC}$ is ~–26.5‰, so still dominated by C3 plants (Figs. 5.8, 5.9, 6.3). Total sulfur rises rapidly to >1%, reaching a peak of ~1.7% by ~8.9 cal ka, before declining to ~1%, but then rising to ~2% by ~6.0 cal ka. $\delta^{34}S$ increases progressively from ~9.50–6.9 cal ka, reaching values of ~+30‰ (Hiscott et al., 2007b). There is a dramatic decline in $\delta^{34}S$ across the interval 8.7–8.2 cal ka to values of ~ –20‰ (Figs. 5.8, 5.9; Hiscott et al., 2007b) signaling increased availability of seawater sulfate and the onset of early diagenetic, microbial sulfate reduction. This interval is also marked by a very large increase in $\delta^{18}O$ values and a reciprocal decrease in $\delta^{13}C$ values in ostracod valves. These changes are attributed to increasing communication between the Black Sea and the Mediterranean Sea via the Marmara Sea Gateway. Mg/Ca temperature estimates remained low (10–14ºC), whereas sea-surface salinities derived from the average process length of the dinoflagellate cyst *Lingulodinium machaerophorum* were 13–15 during this interval (Mertens et al., 2012). Bahr et al. (2008) presented Mg/Ca and Sr/Ca measurements on ostracod valves from the western Black Sea which indicated abrupt changes in the water chemistry concluded that there had been a temperature drop of 1–2 °C in the deep water of the Neoeuxine Lake during the Younger Dryas and that the reconnection of the lake with the Mediterranean Sea via the Sea of Marmara started at 9.3 cal ka coincident with a marked increase in these ratios. The dataset provided in this thesis do not indicate any dramatic changes in these ratios at this time. Geochemical studies of abyssal sediments also suggest first marine incursion and so the base of the transitional period at 9.4 cal ka as well as

increased communication between marine and brackish water, based on Mo concentrations, from 8.7–8.2 cal ka (Piper, 2016, his Fig. 8). A big geochemical shift occurred in deep water sediments around 7.8 cal ka interpreted as a disruption and subsequent rise of the shallow pycnocline. The onset of sapropel accumulation at this time confirms nearly complete isolation of the oxygen-depleted bottom water (Dean and Arthur, 2011). The elemental composition of the deep water sediments during this time interval (7.5–8 cal ka) shows similarity to the ostracod elemental trends on the southwestern shelf. The transition of ostracod communities from brackish-water to fully marine assemblages persisted until 6.3 cal ka (Williams et al., 2018) supported by the Sr-isotopic signature of the mollusc assemblage (Ankindinova et al., 2019). This possibly suggests that in deep waters the geochemical changes occurred perhaps 1000 years before sufficient salination on the shelf to allow Mediterranean organisms to flourish. It is also remarkable that the upward shifts for elements like Sr, U and Ti are smaller for the bulk sediment than they are in the ostracods, so perhaps the ostracods amplified some of these changes (Pipers, 2016 his Fig 8; this thesis, Fig. 5.2). Some other elements (e.g., V, Cu, Zr,) show big upward shifts at ~7.8 cal ka for abyssal sediments but do not display obvious shifts in the ostracods. This suggests more reducing conditions in the deep water at this time that did not extend onto the shelf.

The transition to modern Black Sea conditions is dominated by Factor 1 (Fig. 5.10b,c), which is primarily controlled by the redox-indicator elemental ratios La*, Ce*, U*, Zr* and Zn* (Fig. 5.10a), particularly critical in the distinction between oxic and anoxic conditions. Strongly correlated elemental ratios include Cd*, Cu* and Fe* with similar

significance (Table 5.4). In core M02-45, Factor 1 is of little importance until ~10.0 cal ka, just before the reconnection of the Neoeuxine Lake to the Marmara Sea. Factor 1 increases from ~10.0–9.0 cal ka, with a particularly sharp increase at ~9.40 cal ka. This trend might indicate the development of stratification leading to oxygen depletion and suboxic conditions. Factor 1 becomes particularly dominant at site M05-50 by ~8.0 cal ka, suggesting perhaps a greater importance of oxygen depletion in bottom waters at the deeper site (–91 m at site M05-50 versus –69 m at M02-45).

The Holocene evolution of the chemocline – the suboxic layer dividing the oxic surface water from anoxic and euxinic deep water in Black Sea – can be studied using high-resolution geochemical records of bulk parameters (carbonate, TOC, TS), trace metals (Cu, Mo, V), and δ^{56}Fe. Eckert et al. (2013) used the sedimentary concentrations of Fe/Al, Mo/Al and bulk TOC to suggest that the chemocline gradually rose as suboxic waters flooded the shelf for the first time, from ~8.0–5.6 cal ka (reported as a raw radiocarbon range of 7.6–5.3 ^{14}C ka BP; calibrated as set out in Section 2.2). The trace-element data and factor analysis results suggest that the rise of the chemocline might have started approximately 1000 yr earlier on, and adjacent to, the southwestern Black Sea shelf.

6.3.3. Modern Black Sea (6.3 cal ka to Present)

TOC values sharply increase by ~1% from ~7.0–5.5 cal ka in both studied cores (Figs. 5.8, 5.9). This increase coincides with a ~2‰ decrease in the $\delta^{13}C_{TOC}$, which indicates an increase in the proportion of marine organic carbon from ~10% to ~50% (Figs. 5.8, 5.9). Total sedimentary sulfur increases progressively from ~1.5% to ~2%, while δ^{34}S decreases from ~0‰, to –20‰ to –30‰ (Figs. 5.8, 5.9; Hiscott et al., 2007b). These

geochemical proxies signal the final transition to the modern Black Sea. After ~5.5 cal ka, TOC is uniform at ~1.0% in core M02-45 and ~1.5% in core M05-50 (Figs. 5.8, 5.9). 5.5–5.2 cal ka is also associated with a major transition in the pelagic plankton community structure (Coolen et al., 2013) and the anaerobic bacterial community (More et al., 2019), suggesting that salination was a gradual rather than abrupt process.

The interval from 6.3 cal ka to Present is dominated by Factor 2 (Fig. 5.10 b, c), which is strongly controlled by Mg/Ca, Sr/Ca and to a lesser extent by B*. Sr/Ca and Mg/Ca have strong linkages to salinity and temperature, respectively. Furthermore, element/Ca ratios in ostracod valves exhibit a major shift at ~6.3 cal ka when Ba*, Cd*, Ce*, Fe*, La*, Mo*, Rb*, U*, Zn* and Zr* show distinct declines, strongest in core M05-50 (Figs. 5.2, 5.3). These shifts are interpreted to represent the establishment of near-modern salinities and dissolved oxygen concentrations. Temperature calculations based on Mg/Ca suggest that temperatures in the Black Sea rapidly increased ~7–10ºC at ~6.3 cal ka (Figs. 5.8, 5.9). These observations suggest that the chemocline has deepened since 6.3 cal ka as indicated by downcore declines in redox sensitive elements (Fig. 5.2, 5.3). Trace metal and isotopic data presented by Eckert et al. (2013) similarly suggested a descent of the chemocline since the onset of brackish/marine conditions, before the present stable situation was established.

6.4. Summary

The widespread occurrence of ~12.5–7.4 cal ka deposits (allounit 1b) across the middle and outer shelf provides no possibility for a Holocene evaporative drawdown to a lowstand elevation of −120 m at 9.4 cal ka as suggested by Yanchilina et al. (2017).

Instead, the volume of detritus in allounit 1b can only be explained if base level was sufficiently high to allow major distant rivers in Bulgaria and Romania (e.g., Kamchiya, Danube) to contribute mud through long-distance marine transport along a submerged shelf. There is no evidence in any cores which sample allounit 1b that the sites were located in limans, rather than on a transgressed shelf which had been flooded by post-glacial meltwater and enhanced river runoff as the climate became more humid in the early Holocene. A prolonged stillstand at the spill depth controlled by the sill in the Strait of Bosphorus is confirmed by the elevation of a drowned recurved spit downdrift from Cape Emine, Bulgaria. The development of the subaqueous unconformities/correlative conformities α1 and α2 was facilitated by physical oceanographic processes. Volumetrics based on isopach maps and pre-industrial sediment discharge rates of various rivers entering the western and southwestern Black Sea suggest that the total sediment yields of Bulgarian and Turkish rivers can only account for ~13–14% of the total Holocene succession (allounits 1b–1d), and that major input from the Danube River via along-shelf long-distance transport must have occurred through the entire Holocene.

The sharp $^{87}Sr/^{86}Sr$ increase marks the first significant intrusion of saline water into a previously isolated Neoeuxine Lake around 9465–9490 cal yr BP. A quasi-steady-state condition lasted 350–400 years. Subsequently, starting ~8985 cal yr BP and proceeding to the present day, there was a step-wise rise of $^{87}Sr/^{86}Sr$ to modern levels, during which a salinity threshold was passed that allowed widespread replacement of brackish-water faunas by Mediterranean species. Modelling suggests that the lake/sea level likely did not, and could not, rise from −120m to −30m between 9490 and 9380 cal

yr BP unless (a) the Sr concentration in the pre-reconnection Neoeuxine Lake was 3–4 times higher than today, or (b) the water column was strongly stratified during first entry of saline water. The second alternative is very unlikely because of seasonal vertical mixing (downwelling/upwelling) in what was then a rather homogeneous temperate lake. Catastrophic flooding of a lowstand lake would require an average discharge through the Strait of Bosphorus of ~9500m3 s^{-1}, whereas saline entry of Mediterranean water as an underflow into an already high lake could reproduce the first stage of $^{87}Sr/^{86}Sr$ increase with an average discharge as low as ~2200m3 s^{-1}. Because the M02-45 site is ~50 m above the late Pleistocene lowstand shoreline and contains sub-wavebase sediments with $^{87}Sr/^{86}Sr$ values that record the first entry of saline water into the Neoeuxine Lake, the surface of the lake must have been significantly higher than −70 m at the time of the reconnection. Two prominent 'plateaux' which punctuate the long-term $^{87}Sr/^{86}Sr$ increase are attributed to decadal to centennial periods of increased discharge from European rivers, creating a positive hydrological balance and effectively blocking or seriously impeding saline-water advance up the Strait of Bosphorus toward the Black Sea. The Sr-isotopic signal can be readily correlated with oxygen and carbon isotopic signals reveal three isotopic substages in water chemistry evolution: 1c (12.1–9.4 cal ka) that represents conditions in the Neoeuxine Lake; (b) substage 1b (9.4–6.3 cal ka) that represents the transition from lacustrine to marine conditions, and (c) substage 1a (6.3 cal ka to Present) that represents the establishment of marine conditions like today. Trace-element/Ca ratios show downcore trends consistent with the three isotopic substages. At ~6.3 cal ka, isotopic data and trace-element/Ca ratios exhibit a major shift, with changes in the Mg/Ca ratio suggesting an increase in water temperature from 12–14 °C to 17–19 °C. These mid-

Holocene changes in ostracod-valve composition and environmental conditions coincide with the weakening of Black Sea outflow and the proliferation of marine organisms.

The data presented in this thesis provide evidence for a step-wise gradual reconnection of the Black Sea with the global ocean, in complete disagreement with the suggestion of a rapid inundation by saline water entering an evaporated, lowstand Neoeuxine lake as implied by the Flood Hypothesis of William Ryan and coworkers.

Chapter 7. Conclusions

This thesis is a complex multicomponent study of the SW Black Sea shelf area. It is underpinned by a high-resolution sequence-stratigraphic framework (Chapter 3) and and utilizes the geochemistry of mollusc and ostracod shells to reconstruct oceanographic and climatic events during the most recent post-glacial sea-level rise (Chapters 4 and 5). The results of this study have generated three peer reviewed manuscripts which have been accepted and published in the highly visible journals Marine Geology and Palaeogeography, Palaeoclimatology, Palaeoecology (Ankindinova et al., 2019a,b; 2020).

The approach taken was based on data sets and methods a–c, below:

a) the integrated interpretation of seismic reflection profiles, multibeam mosaics and the allostratigraphy of five key and four reference cores;

b) a comprehensive assessment of the Sr-isotopic evolution of Black Sea water during the last 12 cal ka with a tightly constrained age model for Sr-isotopic values in mollusc shells of the ~10 m-long composite core M02-45/M05-03P which permitted a detailed investigation of major events, some useful preliminary modelling, and a refined interpretation of the paleoceanography through the Late Quaternary transgression and subsequent salination, and

c) the acquisition and interpretation of oxygen and carbon stable-isotopic and trace-element data for ostracod valves of *L. lepida* and *P. agilis* in two key composite cores, M02-45 and M05-50.

The following are the salient conclusions of the thesis.

- Interpretation of the high-resolution Huntec DTS profiles revealed the presence of five units separated by five unconformities. Seismic stratigraphic Unit 1 is bounded at its base by the α unconformity and locally by the α0 unconformity. The α unconformity and two younger, regionally mappable, but less prominent unconformities and their correlative conformities called α1 and α2 divide seismic stratigraphic Unit 1 into four subunits (from oldest to youngest, 1a, 1b, 1c and 1d).
- The Black Sea continental shelf is a complex environment which reflects an interplay between riverine supply of detritus and a number of physical oceanographic processes, including coastal eddies of the Rim Current circulation, local wind-driven currents, fairweather and storm waves, internal waves along density interfaces, upwelling/downwelling, complex underlying bathymetry, and saline inflow of Mediterranean water via an anastomosing channel network which overspills onto adjacent levées and seabed.
- The counterclockwise-rotating Rim Current and longshore currents moved sediment from large western point sources (e.g., Danube River and Kamchiya and other Bulgarian rivers) along the shelf toward the southwest since the earliest Holocene, beginning before the first entry of Mediterranean water.
- Sedimentological and seismic stratigraphic data negate the proposal of Yanchilina et al. (2017) that the Neoeuxine Lake experienced evaporative drawdown to a lowstand elevation of ~ –120 m by 9.4 cal ka, just before rapid inundation by saline Mediterranean water. Instead, the data presented in this thesis show the widespread occurrence of lower Holocene deposits (i.e., allounit 1b) across the middle and outer shelf possessing a

cumulative volume that can only be explained if base level was sufficiently high to allow major distant rivers in Bulgaria and Romania to contribute detritus through long-distance marine transport along a submerged shelf.

- Unconformities α1 and α2 cannot originate from falls in base level because they both date from the middle to late Holocene when the Black Sea was fully connected to the global ocean. It is speculated that coastal eddies of the Rim Current circulation, local wind-driven currents, storm waves and/or internal waves along density interfaces are probably responsible for their development, and that subtle swings in the balance between long-term accumulation and bypass/erosion might be responsible for lateral passages from unconformity to conformity on the shelf.
- There is no evidence across the southwestern Black Sea for the wide-spread development of early Holocene perched ponds stranded above a lowstand Neoeuxine Lake (referred to as limans by Ryan et al., 1997, 2003; Yanchilina et al., 2017). Several well-dated core sites (e.g., M02-45, M11-23) are above the lowstand elevation of –100 m proposed by those authors and show thick development of allounit 1b. Furthermore, seismic stratigraphy clearly demonstrates the widespread presence of allounit 1b across the southwestern Black Sea and no topographic barrier(s) surrounding these core sites based on a structure-contour map at the level of the α1 unconformity. Instead, the data suggest that allounit 1b developed on a transgressed shelf which had been flooded by post-glacial meltwater and enhanced river runoff as the climate became more humid in the earliest Holocene.
- The seismic grid for this study lies on the Turkish shelf, but the Holocene mud belt extends toward the northwest into Bulgarian waters and beyond. Volumes of sediment contained

in the Holocene allounits 1b–1d and sediment discharge rates for Bulgarian and Turkish rivers (Thrace only) suggest that the contributions of all the Bulgarian and Turkish rivers would have been insufficient to account for the mass of detritus contained in the Holocene allounits. The only viable alternative is that the overwhelming proportion of detritus found across the southwestern Turkish shelf must have come from the Danube River, farther to the northwest.

- There is a 9.0–9.5 km-long, 0.9–1.1 km-wide relict recurved feature interpreted as a transgressed spit immediately south of Cape Emine, Bulgaria, in water depths of –30 m to –35 m. A spit in this location and water depth would confirm that south-directed longshore transport away from the Danube Delta characterized the Neoeuxine Lake when it was at its spill depth into the Marmara Sea (i.e., –35 m elevation), and that the stillstand at the spill depth lasted hundreds of years to account for growth of such a large spit which prograded 9.0–9.5 km during the early Holocene.
- The sedimentary and seismic stratigraphic data document that unimpeded along-shelf transport must have prevailed since the Neoeuxine Lake was above ~ –40 m to –35 m. The transport pathway continued southward through the Strait of Bosphorus to a delta lobe at the southern exit of the strait in the northeastern Marmara Sea (Aksu et al., 2016) that is contemporary with the lower portion of allounit 1b.
- The level of the Neoeuxine Lake at the time of first arrival of saline water was not in the range –100 m to –120 m, but instead was well above ~ –70 m. From 12,145–9490 cal yr BP, the Sr-isotopic ratio varied from 0.708841 to 0.708881 (ξ = 0.00–0.13, where ξ ranges from 0 to +1 and indicates the evolution from lacustrine $^{87}Sr/^{86}Sr$ values at ξ = 0 to modern

values at $\xi = 1$). Between 9465–9490 cal yr BP and ~9380 cal yr BP, molluscs from core M02-45 indicate a sharp rise in $^{87}Sr/^{86}Sr$ from ~0.708842 to ~0.708965 ($\xi = 0.00–0.39$) that is interpreted as evidence for the first intrusion of saline water into the previously isolated Neoeuxine Lake from the Mediterranean Sea. Beginning at ~9380 cal yr BP, an ~350–400 yr-long steady state developed with only a slight and slow rise in the $^{87}Sr/^{86}Sr$ ratio. A second period of stalled $^{87}Sr/^{86}Sr$ increase occurred later, from ~8450–7400 cal yr BP. These episodes are referred to as 'plateaux' interrupting the long-term $^{87}Sr/^{86}Sr$ rise identified in core M02-45. The plateaux are attributed to strong outflow through the Strait of Bosphorus of brackish surface waters caused by an increase in precipitation and runoff into the post-reconnection Black Sea. At those times, the balance between runoff and a reduced (or periodically blocked) saline supply maintained a nearly constant $^{87}Sr/^{86}Sr$ ratio.

- The suggestion that ~32,500 km^3 of seawater catastrophically filled the Black Sea basin from a lowstand of ~ –120 m to ~ –30 m in no more than a few decades is dismissed because of the elevation of the M02-45 site well above –120 m, the sub-wavebase pre-reconnection facies (Hiscott et al., 2007a), and the high strontium concentration (or poor mixing) in the Neoeuxine Lake needed to accord that *Flood Hypothesis* with the ~350–400 yr-long steady-state plateau during which $^{87}Sr/^{86}Sr \approx 0.708965$ ($\xi \approx 0.39$). When modelled as an underflow penetrating northward into an outspilling Black Sea, the volume of saline water needed to shift the $^{87}Sr/^{86}Sr$ ratio to ~0.708965 is 53,500–7800 km^3 for pre-reconnection strontium concentrations in the Neoeuxine Lake of 1.5–0.2 ppm. The saline discharge through the Strait of Bosphorus implied by this modelling is 485–70 $km^3\ yr^{-1}$ or 15,420–2250 $m^3\ s^{-1}$, lasting for ~110 years. The more likely lower end of this range is much less than the

discharge of ~9500 m^3 s^{-1} that would be required for catastrophic refilling from –120 m to –30 m over the same time interval.

- By ~7.5 cal ka, a broad range of Mediterranean species had successfully colonized the Black Sea shelves, requiring a shift in practical salinity to ~13–15. This salinity is only consistent with the observed $^{87}Sr/^{86}Sr$ ratio of ~0.70907 (ξ = 0.72) if the pre-reconnection Neoeuxine Lake had a practical salinity of ~10 and a strontium concentration of ~0.5 ppm. Apparently a considerable volume of brackish Neoeuxine Lake water remained in the Black Sea long after the reconnection, augmenting its salinity without inflating the $^{87}Sr/^{86}Sr$ ratio.
- The $\delta^{18}O$ and $\delta^{13}C$ composition and trace-element/Ca ratios in ostracods delineate three distinct intervals: (a) the Neoeuxine Lake stage from >12 cal ka to 9.4 cal ka when the Black Sea was isolated from the global ocean, (b) a transitional interval between 6.3 and 9.4 cal ka when the Black Sea became progressively reconnected with the global ocean and (c) the establishment of the Present-day marine conditions at 6.3 cal ka.
- Until the reconnection and first entry of saline water at ~9.490–9.465 cal ka, the Neoeuxine Lake was completely disconnected from the Mediterranean Sea. Elevated Ba* (* indicates a ratio to Ca molar abundance) and Cd* (i.e., Cd/Ca in mmol/mol) and high TOC suggest that the lake experienced high biological productivity and organic carbon preservation, dominated by C3 plants as indicated by the depleted $\delta^{13}C_{TOC}$ values ranging from –26.5‰ to –27‰. Elevated $\delta^{34}S$ values suggest that there was no influx of seawater sulfate to nourish sulfate-reducing bacteria. Depleted $\delta^{18}O$ values in ostracod valves suggest that the region must have been isolated from the global ocean, receiving a near-constant influx of glacial melt water which promoted an isotopic depletion of –5‰ to –6‰. Very low

$^{87}Sr/^{86}Sr$ (~0.70886) affirms no communication with the Mediterranean Sea. During this interval, lake temperatures were low (ca. 12–15ºC) as indicated by ostracod Mg/Ca ratios and the linear regression equation of Cronin et al. (2005) for the ostracod genus *Loxoconcha*. Lake salinities were similarly low as suggested by the ostracod Sr/Ca ratios. This interval is also marked by notably elevated Fe*, Mn*, Ti* and Zr* in core M05-50, which probably suggests low oxygen conditions in the deeper portion of the shelf.

- The reconnection with the global ocean is marked by a dramatic increase in $^{87}Sr/^{86}Sr$ from 0.708843 to ~0.708965 (Ankindinova et al., 2019a). The sharp declines in Ba*, Cd*, Mo* and lesser declines in B* and P* and the reduction of TOC to ~ 0.5% are ascribed to a sharp drop in biological productivity, possibly associated with a faunal/floral turnover during an interval when saline Mediterranean waters started to penetrate into the Neoeuxine Lake. This interval is also marked by a very large enrichment in the $\delta^{18}O$ values and a reciprocal depletion in the $\delta^{13}C$ values in ostracod valves. These changes are attributed to increasing communication between the Black Sea and the Mediterranean Sea, facilitating stronger advection of marine waters with distinctly enriched $\delta^{18}O$ values and depletion in $\delta^{13}C$.
- The transition to the modern Black Sea is dominated by the redox-indicator elemental ratios La*, Ce*, U*, Zr* and Zn*, which are particularly critical in the distinction between oxic and anoxic conditions. Sharp increases of these elemental ratios at ~9.4 cal ka might indicate the onset of stratification leading to oxygen depletion and suboxic conditions across the SW Black Sea shelf.
- TOC sharply increases to ~1% from ~7000 to 5500 cal yr BP, which mirrors a progressive decrease in the $\delta^{13}C_{TOC}$ indicating a significant increase in the proportion of marine organic

carbon. Similarly, total sedimentary sulfur increases progressively from ~1.5% to ~2%, while $\delta^{34}S$ decreases from ~0‰ to –30‰. The interval from 6.3 cal ka to the present is dominated by elevated Mg/Ca and Sr/Ca which have strong linkages to temperature and salinity, respectively. Furthermore, element/Ca ratios in ostracod valves exhibit a major shift at ~6.3 cal ka, when Ba*, Cd*, Ce*, Fe*, La*, Mo*, Rb*, U*, Zn* and Zr* show distinct declines, interpreted as the establishment of near-modern salinities and dissolved oxygen concentrations conducive to the replacement of remaining brackish/lacustrine species of various organisms with euryhaline Mediterranean species. The data presented in Chapter 5 suggest that the chemocline deepened since 6.3 cal ka.

References

Aksu, A.E., Yaşar, D., Mudie, P.J., Gillespie, H., 1995. Late glacial–Holocene paleoclimatic and paleoceanographic evolution of the Aegean Sea: micropaleontological and stable isotopic evidence. Marine Micropaleontology 25, 1–28.

Aksu, A.E., Hiscott, R.N., Yaşar, D., 1999. Oscillating Quaternary water levels of the Marmara Sea and vigorous outflow into the Aegean Sea from the Marmara Sea-Black Sea drainage corridor. Marine Geology, 153: 275–302.

Aksu, A.E., Hiscott, R.N., Yaşar, D., İşler, F.I., Marsh, S., 2002a. Seismic stratigraphy of Late Quaternary deposits from the southwestern Black Sea shelf: evidence for non-catastrophic variations in sea-level during the last ~10 000 yr. Marine Geology 190, 61–94.

Aksu, A.E., Hiscott, R.N., Kaminski, M.A., Mudie, P.J., Gillespie, H., Abrajano, T., Yaşar, D., 2002b. Late-Glacial-Holocene paleoceanography of the Black Sea and Marmara Sea: stable isotopic, foraminiferal and coccolith evidence. Marine Geology 190, 119–149.

Aksu, A.E., Hiscott, R.N., Yaltırak, C., 2016. Early Holocene age and provenance of a midshelf delta lobe south of the Strait of Bosphorus, Turkey, and its links to vigorous Black Sea outflow. Marine Geology 380, 113–137.

Algan, O., Gokaşan, E., Gazioğlu, C., Yucel, Z.Y., Alpar, B., Guneysu, C., Kirci, E., Demirel, S., Sarı, E., Ongan, D., 2002. A high-resolution seismic study in Sakarya Delta and submarine canyon, southern Black Sea shelf. Cont. Shelf Res. 22, 1511–1527.

Algeo, T.J., Morford, J., Cruse, A., 2012. Reprint of: new applications of trace metals as proxies in marine paleoenvironments. Chemical Geology, 324–325, 1–5.

Altınok, Y., 1999. Tsunamis along the coasts of the Black Sea. Istanbul: Second Balkan Geophysical Congress and Exhibition. pp. 46–47.

Anderson, T.F., Raiswell, R., 2004. Sources and mechanisms for the enrichment of highly reactive iron in euxinic Black Sea sediments. American Journal of Science, 304, 203–233.

Ankindinova, O., Hiscott, R.N., Aksu, A.E., Grimes, V, 2019a. Strontium isotopic composition of shells from the Black Sea and implications for the reconnection with the global ocean. Marine Geology, 407, 213–228

Ankindinova, O., Aksu, A.E., Hiscott, R.N., 2019b. Oxygen and carbon isotope and trace element/Ca ratios in Late Quaternary ostracodes *Loxoconcha lepida* and *Palmoconcha agilis* from the Black Sea: Holocene paleoclimatic and paleoceanographic implications. Palaeogeogr. Palaeoclimatol. Palaeoecol. 533, 1–21.

Ankindinova, O., Aksu, A.E., Hiscott, R.N., 2020. Holocene sedimentation in the southwestern Black Sea: Interplay between riverine supply, coastal eddies of the Rim Current, surface and internal waves, and saline underflow through the Strait of Bosphorus. Marine geology, 420, article 106092.

Arkhangel'skiy, A.D., Strakhov, N.M., 1938. Geological structure and history of the evolution of the Black Sea. Izv. Akad. Nauk SSSR. 10, 3–104.

Arkhipkin, V.S., Gippius, F.N., Koltermann, K.P., Surkova, G.V., 2014. Wind waves in the Black Sea: results of a hindcast study. Natural Hazards and Earth System Science 14, 2883–2897.

Arthur, M. A., and W. E. Dean (1998), Organic-matter production and preservation and evolution of anoxia in the Holocene Black Sea, Paleoceanography, 13, 395–411, doi:10.1029/98PA01161.

Avrametz, V.M., Kakaranza, S.D., Sibirchenko, M.G., Mokrjak, I.M., Shvez, L.K., Makovetskaja, I.M., Ju Eremina, L., 2007. Zvit z provedennja geologichnoi ziomky masshtabu 1:200,000 pivnichno-zakhidnoi chastyny shelfu Chornogo moria v mezhakh arkushiv L-36-XIII, L-36-XIV, L-36-XV, 1992–2007 (Report on Geological Survey

1:200,000 Within Card Segments L-36-XIII, L-36-XIV, L-36-XV). Prichonomorske DRGP, Odessa (399 pp., in Ukrainian).

Balabanov, I.P., 2006. Holocene sea-level changes in the northern Black Sea. In: IGCP 521 Second Plenary Meeting, Odessa, Ukraine, 20–28 August, Abstracts Volume, pp. 21–23.

Ballard, R.D., Coleman, D.F., Rosenberg, G., 2000. Further evidence of abrupt Holocene drowning of the Black Sea shelf. Mar. Geol. 170, 253–261.

Begun, T., Teacă, A., Gomoiu, M.-T., 2010. State of macrobenthos within Modiolus phaseolinus biocoenosis from Romanian Black Sea continental shelf. Geo-Eco-Marina 16, 5–18.

Badertscher, S., Fleitmann, D., Cheng, H., Edwards, R.L., Göktürk, O.M., Zumbühl, A., Leuenberger, M., Tüysüz, O., 2011. Pleistocene water intrusions from the Mediterranean and Caspian seas into the Black Sea. Nature Geoscience 4, 236–239.

Bahr, A., F. Lamy, H. W. Arz, C. Major, O. Kwiecien, G. Wefer, 2008. Abrupt changes of temperature and water chemistry in the late Pleistocene and early Holocene Black Sea, Geochemistry, Geophysics, Geosystems, 9, Q01004, doi:10.1029/2007GC001683.

Begun, T., Teacă, A., Gomoiu, M.-T., 2010. State of macrobenthos within *Modiolus phaseolinus* biocoenosis from Romanian Black Sea continental shelf. Geo-Eco-Marina 16, 5–18.

Bender, M.M., 1971. Variations in the $^{13}C/^{12}C$ ratios of plants in relation to the pathway of photosynthetic carbon dioxide fixation. Phytochemistry, 10, 1239–1244.

Bernat, M., Church, T, Allegré, C.J., 1972. Barium and strontium concentrations in Pacific and Mediterranean sea water profiles by direct isotope dilution mass spectrometry. Earth and Planetary Science Letters 16, 75–80.

Besiktepe, S., Sur, H.I., Özsoy E., Latif, M., A., Oguz, T., &. Ünluata, Ü., 1994. The circulation and hydrography of the Marmara Sea: Prog. Oceanogr. 34, p. 285-334.

Bhattacharya, J.P., 2001. Allostratigraphy versus sequence stratigraphy. In: APG Search and Discovery Article #90050. AAPG Hedberg Research Conference, Dallas, Texas, August 26–29, 2001.

Bhattacharya, J.P., Posamentier, H.W., 1994. Sequence stratigraphy and Allostratigraphic applications in the Alberta foreland basin. In: Mossop, G.D., Shetsen, I. (Eds.), Geological Atlas of the Western Canada Sedimentary Basin. Canadian Society of Petroleum Geologists and Alberta Research Council, pp. 407–412. (comp.). https:// ags.aer.ca/publications/chapter-25-sequence-and-allostratigraphic-applications.

Bogdanova, C., 1969, Seasonal fluctuations in the inflow and the distribution of the Mediterranean waters in the Black Sea. In: L.M. FOMIN (Ed.), Basic Features of the Geological Structure, the Hydrological Regime and Biology of the Mediterranean Sea: Academy of Science, USSR, Moscow. English translation by Institute of Modern Languages, Washington, DC, p. 131-139.

Börner, N., De Baere, B., Yang, Q., Jochum, K.P., Frenzel, P., Andreae, M.O., Schwalb, A., 2013. Ostracod shell chemistry as proxy for paleoenvironmental change. Quaternary International, 313–314, 17–37.

Bonaduce, G., Ciarnpo, G., Masoli, M., 1975. Distribution of Ostracoda in the Adriatic Sea. Naples: Stazione Zoologica di Napoli.

Boomer, I., Guichard, P., Lericolais, G., 2010. Late Pleistocene to Recent ostracod assemblages from the western Black Sea. Journal of Micropalaeontology, 29, 119-1 33.

Boomer, I., Horne, D.J., Slipper, I., 2003. The use of Ostracodes in Paleoenvironmental Studies, or What can you do with an ostracod shell? Paleontological Society Papers, 9, 153–180.

Bradley, L.R., Marret, F., Mudie, P.J., Aksu, A.E., Hiscott, R.N., 2012. Constraining Holocene sea-surface conditions in the south-western Black Sea using dinoflagellate cysts. Journal of Quaternary Science, 27, 835–843.

Branson, O., Redfern, S.A.T., Elmore, A.C., Read, E., Valencia, S., Elderfield, H., 2018. The distribution and coordination of trace elements in *Krithe* ostracods and their implications for paleothermometry. Geochimica et Cosmochimica Acta, 236, 230–239.

Brass, G.W., Turekian, K.K., 1972. Strontium distribution in sea water profiles from the Geosecs I (Pacific) and Geosecs II (Atlantic) test stations. Earth and Planetary Science Letters 16, 117–121.

Bradley, L.R., Marret, F., Mudie, P.J., Aksu, A.E., Hiscott, R.N., 2012. Constraining Holocene sea-surface conditions in the south-western Black Sea using dinoflagellate cysts. J. Quat. Sci. 27, 835–843.

Bronk Ramsey, C., 2019. Oxcal 4.3. at. https://c14.arch.ox.ac.uk/oxcal.html (WWW program).

Brujevich, S.V., 1952. Buried fresh water beneath the recent sediments in the Black Sea. Dokl. Acad. Nauk SSSR. 84 (3), 575–577.

Buynevich, I.V., Yanko-Hombach, V., Gilbert, A.S., Martin, R.E. (Eds.), 2011. Geology and Geoarchaeology of the Black Sea Regrion: Beyond the Flood Hypothesis. Geological Society of America (Special Paper 473).

Buynevich, I.V., Yanko-Hombach, V., Gilbert, A.S., Martin, R.E. (Eds.), 2011. Geology and Geoarchaeology of the Black Sea Region: beyond the Flood Hypothesis. Geological Society of America, Special Paper 473.

Büyükmeriç, Y., 2016. Postglacial floodings of the Marmara Sea: molluscs and sediments tell the story. Geo-Marine Letters 36, 307–321.

Cadot, H.M., Kaesler, R.L., 1977. Magnesium content in calcite in carapaces of benthic marine ostracods. Paleontological Contributions, University of Kansas, 87, 1–23.

Çağatay, M.N., Görür, N., Algan, O., Eastoe, C., Tchapalyga, A., Ongan, D., Kuhn, T., Kuşçu, İ., 2000. Late Glacial–Holocene palaeoceanography of the Sea of Marmara: timing of connections with the Mediterranean and Black seas. Marine Geology 167, 191–206.

Canfield, D.E., 2001. Isotope fractionation by natural populations of sulfate-reducing bacteria. Geochimica et Cosmochimica Acta, 65, 1117–1124.

Capet, A., Stanev, E. V., Beckers, J. M., Murray, J. W. and Gregoire, M., 2016, Decline of the Black Sea oxygen inventory, Biogeosciences 13, pp. 1287–1297.

Charlier B.L.A., Ginibre, C., Morgan, D., Nowell, G.M., Pearson, D.G., Davidson, J.P., Ottley, C.J., 2006. Methods for the microsampling and high-precision analysis of strontium and rubidium isotopes at single crystal scale for petrological and geochronological applications. Chemical Geology 232, 114–133.

Chepalyga, A. L., 1984, Inland sea basins. In: A. A. Velichko, H. E. J. Wright & W. Barnosky-Cathy (Eds.), Late Quaternary environments of the Soviet Union: Mineapolis, MN, United States, Univ. Minn. Press., p. 229-247.

Chepalyga, A.L., 2007. The late glacial great flood in the Ponto-Caspian basin, in: Yanko-Hombach, V., Gilbert, A.S., Panin, N., Dolukhanov, P.M. (Eds.), The Black Sea Flood Question: Changes in Coastline, Climate and Human Settlement. Springer, Dordrecht, pp. 119–148.

Chivas, A.R., de Deckker, P., Shelley, J.M.G., 1985. Strontium content of ostracods indicates lacustrine paleosalinity. Nature 316, 251–253.

Chivas A.R., de Deckker P., Shelley J.M.G., 1986a. Magnesium and strontium in non-marine ostracod shells as indicators of paleosalinity and paleotemperature. Hydrobiologia 143, 135–142.

Chivas A.R., de Deckker P., Shelley J.M.G., 1986b. Magnesium content of non-marine ostracod shells: a new paleosalinometer and paleothermometer. Palaeogeography, Palaeoclimatology, Palaeoecology 54, 43–61.

Cifci, G., Dondurur, D., Ergun, M., 2002. Sonar and high resolution seismic studies in the eastern Black Sea. Turk. J. Earth Sci. 11, 61–81.

Colodner, D., Edmond, J., Boyle, E., 1995. Rhenium in the Black Sea: comparison with molybdenum and uranium. Earth and Planetary Science Letters, 131, 1–15.

Coolen, M.J.L., Orsi, W.D., Balkema, C., Quince, C., Harris, K., Sylva, S.P., Filipova-Marinova, M., Giosan, L., 2013. Evolution of the plankton paleome in the Black Sea from the Deglacial to Anthropocene. PNAS, 110 (21) 8609–8614.

Cohen, D.M., Ryan, W.B.F., Major, C.O., Goldstein, S.L., Pena, L.D., Dimitrov, P., Dimitrov, D., 2011. Post glacial evaporative drawdown of the Black Sea lake. In: 3rd International Symposium on the Geology of the Black Sea Region Bucharest, 1–10 October 2011, Abstracts, Supplement to Geo-Eco-Marina. vol. 17. pp. 49–51

Constantinescu, A.M., Toucanne, S., Dennielou, B., Jorry, S.J., Mulder, T., Lericolais, G., 2015. Evolution of the Danube Deep-Sea Fan since the Last Glacial Maximum: new insights into Black Sea water-level fluctuations. Marine Geology 367, 50–68.

Copeland, S.R., Sponheimer, M., le Roux, P.J., Grimes, V., Lee-Throp, J.A., de Ruiter, D.J., Richards, M.P., 2008. Strontium isotope ratios ($^{87}Sr/^{86}Sr$) of tooth enamel: a comparison of solution and laser ablation multicollector inductively coupled plasma mass spectrometry methods. Rapid Communications in Mass Spectrometry 22, 3187–3194.

Cronin, T.M., Kamiya, T., Dwyer, G.S., Belkin, H., Vann, C.D., Schwede, S., Wagner, R., 2005. Ecology and shell chemistry of *Loxoconcha matagordensis*. Palaeogeography, Palaeoclimatology, Palaeoecology, 225, 14–67.

Cross TA, Lessenger MA. 1988. Seismic stratigraphy. Annu. Rev. Earth Planet. Sci. 16:319- 54

Cullen, J.T., Lane, T.W., Morel, F.M.M., Sherrell, R.M., 1999. Modulation of cadmium uptake in phytoplankton by CO_2 concentration. Nature 402, 165–167.

Dan, S., Walstra, D.-J.R., Stive, M.J.F., Panin, N., 2011. Processes controlling the development of a river mouth spit. Mar. Geol. 280, 116–129.

Deuser, W. G., Evolution of anoxic conditions 20, 757-760, 1992. in Black Sea during Holocene, iin The Black Calvert, S. E., H. G. Thode, D. Yeung, and R.E. Sea- Geology, Chemistry and Biology, edited Karlin, A stable isotope study of pyrite by E. T. Degens and D. A. Ross, Mem. Am. formation in the late Pleistocene and Assoc. Pet. Geol., 20, 133-136, 1974.

Dean, W.E., Arthur, M.A., 2011. Geochemical characteristics of Holocene laminated sapropel (unit II) and underlying lacustrine unit III in the Black Sea. U.S. Geological Survey Open-File Report 2010–1323, 29 p.

De Baar, H.J.W, German, C.R., Elderfield, H., van Gaans, P., 1988. Rare earth element distributions in anoxic waters of the Cariaco Trench.Geochimica et Cosmochimica Acta, 2, 1203–1219.

De Deckker, P., 2017. Trace elemental distribution in ostracod valves. From solution ICPMS and laser ablation ICPMS to microprobe mapping: a tribute to Rick Forester. Hydrobiologia, 786, 23–39.

De Deckker P., Chivas A.R., Shelley J.M.G., Torgersen T., 1988. Ostracod shell chemistry: a new paleoenvironmental indicator applied to a regressive/transgressive record from the Gulf of Carpentaria, Australia. Palaeogeography, Palaeoclimatology, Palaeoecolcology, 66, 231–241.

De Deckker, P., Chivas, A.R., Shelley, J.M.G., 1999. The uptake of Mg and Sr in the euryhaline ostracod Cyprideis determined from in vitro experiments. Palaeogeography, Palaeoclimatology, Palaeoecology 248: 105–116.

Decrouy, L., 2009. Environmental and biological controls on the geochemistry (δ18O, δ13C,Mg/Ca, and Sr/Ca) of living ostracods fromLake Geneva, PhD thesis Université de Lausanne, 112 pp.

Decrouy, L (2012) Biological and environmental controls onisotopes in ostracod shells. In: Horne DJ, Holmes J,Rodriguez Lazaro J, Viehberg FA (eds), Ostracoda asproxies for quaternary climate change. Developments in quaternary science. Vol. 17, Chapter 10, Amsterdam, Elsevier: pp. 165–18.

De Muynck, D., Huelga-Suarez, G., Van Heghe, L., Degryse, P., Vanhaecke, F., 2009. Systematic evaluation of a strontium-specific extraction chromatographic resin for obtaining a purified Sr fraction with quantitative recovery from complex and Ca-rich matrices. Journal of Analytical Atomic Spectrometry 24, 1498–1510.

Dettman, D.L., Dwyer, G.S., 2012. The calibration of environmental controls on elemental ratios in ostracod shell calcite: a critical assessment. *In*: D.J. Horne, J. Holmes, J. Rodriguez-Lazaro, F.A., Viehberg (Eds), Ostracoda as Proxies for Quaternary Climate Change. Developments in Quaternary Science 17, 145–163.

Dimitrov, P.S., 1982. Radiocarbon datings of bottom sediments from the Bulgarian Black Sea Shelf. Bulgarian Academy of Science, Oceanology 9, 45–53.

Dimitrov, D.P., 2010. Geology and Non-traditional Resources of the Black Sea. LAP Lambert Academic Publishing AG & Co., KG (253 pp).

Dimitrov, D., Dimitrov, P., 2004. Alternative resourced and energy sources from the Black Sea bottom. In: 1st Assemblage Wprkshop, pp. 23-26

Dimitrov, D., Dimitrov, P., Peychev, V., Tsaneva, M., 2014. Physical-Geographical and Geological-Lithological Characteristic a Trace of the Pipeline Southern Stream in the Bulgarian Economical Zone of Black Sea. (10 pp).

Dinu, I., Bajo, M., Lorenzetti, G., Umbiesser, G., Zaggia, L., Maximov, G., Stănică, A., 2013. Black Sea coast. Geo-Eco-Marina 19, 17–37.

Drozdov OA, Vasilyeva VA, Kobysheva NV et al. (1989) Climatology. Gidrometeoizdat, Leningrad, 568 pp (in Russian).

Dwyer G.S., Cronin T.M., Baker P.A., 2002. Trace elements in marine ostracodes. *In*: The Ostracoda: Applications in Quaternary Research. Geophysical Monograph Series, 131, American Geophysical Union, Washington, D.C., 313 pp.

Eckert, S., 2014. The past and present trace metal budget of the Black Sea – A comparison of the Holocene and Eemian marine ingression. PhD thesis, Carl von Ossietzky Universität, Oldenburg, Germany, 120 pp.

Eckert, S., Brumsack, H.-J., Schnetger, B., Severmann, S., Schnetger, B., März, C., Fröllje, H., 2013. Establishment of euxinic conditions in the Holocene Black Sea. Geology 41, 431–434.

Efimov, V.V., Belokopitov, V.N., Anisimov, A.E., 2011. Estimation of Water Balance Componentsin the Black Sea. Meteorologiya i Gidrologiya, 2012, No. 12, pp. 69–76.

Engstrom, D.R., Nelson, S.R., 1991. Paleosalinity from trace metals in fossil ostracods compared with observational records at Devil Lake, North Dakota, USA. Palaeogeography, Palaeoclimatology, Palaeoecology 83, 295–312.

Eriş, K.K., Ryan, W.B.F., Çağatay, M.N., Sancar, Ü., Lericolais, G., Ménot, G., Bard, E., 2007. The timing and evolution of the post-glacial transgression across the Sea of Marmara shelf south of İstanbul. Marine Geology 243, 57–76.

Esin, N.V., Esin, N.J., Yanko-Hombach, V., 2016. The Black Sea basin filling by the Mediterranean salt water during the Holocene. Quaternary International 409, 33–38. Evans, J.M. (2004). Noah's flood: Fact or fiction? A paleoenvironmental study of Holocene Black Sea Ostracoda (master's project report). University College London, London.

Fedorov, P. V., 1988. The problem of changes in the level of the Black Sea during the Pleistocene: International Geology Review, v. 30, no. 6, p. 635-641.

Filippov D. M., 1968. Circulation and Structure of the Waters in the Black Sea, Nauka, Moscow 136 pp. (in Russian).

Finetti, I., Bricchi, G., Del Ben, A., Pipan, M., & Xuan, Z., 1988. Geophysical study of the Black Sea area: Bolletino di Geofisica Teorica e Applicata, v. 30, no. 117-118, p. 197-324.

Finkenbinder, M.S., Abbott, M.B., Steinman, B.A., 2016. Holocene climate change in Newfoundland reconstructed using oxygen isotope analysis of lake sediment cores. Glob. Planet. Chang. 143, 251–261.

Flood, R.D., Hiscott, R.N., Aksu, A.E., 2009. Morphology and evolution of an anastomosed channel network where saline underflow enters the Black Sea. Sedimentology 56, 807–839.

Genov, I.D., 2004. Way and time of swell formation near the Bulgarian Black Sea shelf CR. Bulgarian Academy of Science 57 (6), 95–98.

Georgievski, G., Stanev, E.V., 2006. Paleo-evolution of the Black Sea watershed: sea level and water transport through the Bosphorus Straits as an indicator of the Late glacial – Holocene transition. Climate Dynamics 26, 631–644.

German, C.R., Elderfield, H., 1989. Rare earth elements in Saanich Inlet, British Columbia, a seasonally anoxic basin. Geochimica et Cosmochimica Acta, 53, 2561–2571.

German, C.R., Elderfield, H., 1990. Application of the Ce anomaly as a paleoredox indicator: the ground rules. Paleoceanography, 5, 823–833.

Giosan, L., Donnelly, J.P., Constantinescu, S., Filip, F., Ovejanu, I., Vespremeanu-Stroe, A., Vespremeanu, E., Duller, G.A.T., 2006. Young Danube Delta documents stable Black Sea level since the middle Holocene: Morphodynamic, paleogeographic, and archaeological implications. Geology 34, 757–760.

Giosan, L., Filip, F., Constatinescu, S., 2009. Was the Black Sea catastrophically flooded in the early Holocene. Quat. Sci. Rev. 28, 1–6.

Glenn, C.R., & Arthur, M.A., 1984. Sedimentary and geochemical indicators of productivity and oxygen contents in modern and ancient basins: the Holocene Black Sea as the "type" anoxic basin. *Chemical Geology, 48,* 325–354.

Gozhik, P.F., Karpov, V.A., Ivanov, V.G., Sibirchenko, M.G., 1987. Golotsen severozapadnoy chasti Chernogo moria (Holocene of the Northwestern Part of the Black Sea). Geologicheskii Institut Ukrainskoi Akademii Nauk (Pre-Print 87–41, in Russian).

Goldberg, S.L., Lau, H.C.P., Mitrovica, J.X., Latychev, K., 2016. The timing of the Black Sea flood event: insights from modeling of glacial isostatic adjustment. Earth and Planetary Science Letters 452, 178–184.

Gorur, N., 1988. Timing of opening of the Black Sea basin: Tectonophysics, 147, p. 247-262.

Guiot, J., Harrison, S., Prentice, I.C., 1993. Reconstruction of Holocene precipitation patterns in Europe using pollen and lake-level data. Quaternary Research 40, 139–149.

Gürbüz, A., Leroy, S.A.G., 2010. Science versus myth: was there a connection between the Marmara Sea and Lake Sapanca. Journal of Quaternary Science, 25, 103–114.

Haase, D., Fink, J., Haase, G., Ruske, R., Pecsi, M., Richter, H., Altermann, M., Jager, K.-D., 2007. Loess in Europe – its spatial distribution based on a European loess map, scale 1:2,500,000. Quat. Sci. Rev. 26, 1301–1312.

Habicht, K.S., Canfield, D.E., 1997. Sulfur isotope fractionation during bacterial sulfate reduction in organic-rich sediments. Geochimica et Cosmochimica Acta, 61, 5351–5361.

Harrison, S.P., Prentice, I.C., Guiot, J., 1993. Climatic controls of Holocene lake-level changes in Europe. Climate Dynamics 8, 189–200.

Harrison, S.P., Yu, G., Tarasov, P., 1996. Late Quaternary lake-level record from northern Eurasia. Quaternary Research 45, 138–159.

Heaton, T. H. E., Holmes, J. A., and Bridgwater, N. D., (1995). Carbon andoxygen isotope variations among lacustrine ostracods: Implications for paleoclimatic studies. *The Holocene* 5, 428–434.

Helz, G.R., Bura-Nakić, E., Mikac, N., Ciglenečki, I., 2011. New model for molybdenum behavior in euxinic waters. Chemical Geology, 284, 323–332.

Henderson, G.M., Martel, D.J., O'Nions, R.K., Shackleton, N.J., 1994. Evolution of seawater $^{87}Sr/^{86}Sr$ over the last 400-ka: the absence of glacial interglacial cycles. Earth and Planetary Science Letters 128, 643–651.

Herrle, J.O., Bollmann, J., Gebühr, C., Schulz, H., Sheward, R.M., Giesenberg, A., 2018. Black Sea outflow response to Holocene meltwater events. Nature, Scientific Reports, 8:4081, DOI:10.1038/s41598-018-22453-z.

Hiscott, R.N., Aksu, A.E., 2002. Late Quaternary history of the Marmara Sea and Black Sea from high-resolution seismic and gravity core studies. Marine Geology, 190: 261–282.

Hiscott, R.N., Aksu, A.E., Yaşar, D., Kaminski, M.A., Mudie, P.J., Kostylev, V., MacDonald, J., İşler, F.I., Lord, A.R., 2002. Deltas south of the Bosphorus Strait record persistent Black Sea outflow to the Marmara Sea since ~10 ka. Marine Geology 190, 95–118.

Hiscott, R.N., Aksu, A.E., Mudie, P.J., Marret, F., Abrajano, T., Kaminski, M.A., Evans, J., Çakıroğlu, A., Yaşar, D., 2007a. A gradual drowning of the southwestern Black Sea

shelf: evidence for a progressive rather than abrupt Holocene reconnection with the eastern Mediterranean Sea through the Marmara Sea Gateway. Quaternary International 167–168, 19–34.

Hiscott, R.N., Aksu, A.E., Mudie, P.J., Kaminski, M., Abrajano, T., Yaşar, D., Rochon, A., 2007b. The Marmara Sea Gateway since ~16 ka: non-catastrophic causes of paleoceanographic events in the Black Sea at 8.4 ka and 7.15 ka, in: Yanko- Hombach, V., Gilbert, A.S., Panin, N., Dolukhanov, P.M. (Eds.), The Black Sea Flood Question: Changes in Coastline, Climate and Human Settlement. Springer, Dordrecht, pp. 89–117.

Hiscott, R.N., Aksu, A.E., Mudie, P.J., Marret, F., Abrajano, T., Kaminski, M.A., Evans, J., Çakıroğlu, A., Yaşar, D., 2010. Corrigendum to "A gradual drowning of the southwestern Black Sea shelf: Evidence for a progressive rather than abrupt Holocene reconnection with the eastern Mediterranean Sea through the Marmara Sea Gateway" [Quaternary International, 167–168 (2007), 19–34]. Quaternary International, 226, 160.

Hiscott, R.N., Aksu, A.E., Flood, R.D., Kostylev, V., Yaşar, D., 2013. Widespread overspill from a saline density-current channel and its interaction with topography on the south-west Black Sea shelf. Sedimentology 60, 1639–1667.

Hiscott, R.N., Aksu, A.E., Yaltırak, C., 2017. Modelling the provenance of detritus flushed through the Strait of Bosphorus, Turkey, during early Holocene outflow from the Black Sea to the world ocean. Marine Geology 390, 147–169.

Holmes, J.A., 1996. Trace-element and stable-isotope geochemistry of non-marine ostracod shells in Quaternary palaeoenvironmental reconstruction. Journal of Paleolimnology 15, 223–235.

Holmes, J.A., 1998. The palaeoenvironmental significance of iron and manganese in non-marine ostracod shells: a preliminary analysis. *In* J.A. Holmes, K. Lynch (Eds.), The Kingston Papers, a Geographical perspective on the Environment, Economy and Society, pp. 198–212. School of Geography, Kingston University, United Kingdom.

Holmes, J.A., Chivas, A.R., 2002. Ostracod shell chemistry—overview. In: Holmes, J.A., Chivas, A.R. (Eds.). The Ostracoda: Applications in Quaternary Research. Geophysical Monograph, vol. 131. The American Geophysical Union, Washington, DC, pp. 185–204.

Holmes, J.A., de Deckker, P., 2012. The chemical composition of ostracod shells: application in Quaternary palaeoclimatology. *In*: D.J. Horne, J. Holmes, J. Rodriguez-Lazaro, F.A., Viehberg (Eds), Ostracoda as Proxies for Quaternary Climate Change. Developments in Quaternary Science 17, 131–143.

Hristova R., 2003 Biostratigraphical analysis and paleoecolgical conditions in the Bulgarian Black Sea zone during the Quaternary. Trudy Instituta Okeanologii, Varna, 4, 36-41.

Hristova, R., 2006. Palaeogeographical reconstruction of the Bulgarian Black Sea shelf and coastal zone during the Quaternary. Comptes rendus de l'Academie bulgare des sciences: sciences mathematiques et naturelles 59 (12), 1275–1282.

Hristova, R., 2007. Marine Holocene sediments from the Bulgarian Black Sea coast. Comptes rendus de l'Academie bulgare des sciences: sciences mathematiques et naturelles 60 (4), 429–434.

Hristova, R., 2015 Lithostratigraphic and spatial relationship of the Upper Quaternary sediments on the boundary shelfcontinental slope in the Bulgarian sector of the Black Sea. Compt. rend. bulg. Acad. Sci. 68 (3), 351-358.

Hristova, R., 2018. Climate change and paleoenvironmental events in the Bulgarian Black Sea zone during the Late Pleistocene. International Scientific refered online journal with impacy factor. Issue 42. ISSN 2367-5721.

Imbrie, J., Hays, J.D., Martinson, D.G., McIntype, A., Mix, A.C., Morley, J.J., Pisias, N.G., Prell, W.L. & Shackleton, N.J., 1984. The orbital theory of Pleistocene climate: Support from a revised chronology of the marine δ18O record. In: A.L. Berger, J. Imbrie, J., Hays, J.D., G., Kukla, G., & Saltzman, B., (Eds.): Milankovitch and Climate, Part I, Reidel, The

Netherlands, p. 269-305. Intergovernmental Oceanographic Commission (IOC), 1981. International Bathymetric Chart of the Mediterranean (Published by the Head Department of Navigation and Oceanography, Russia under the authority of IOC, 10 sheets).

İşler, B.E., Hiscott, R.N., Aksu, A.E., 2015. Late Quaternary chronostratigraphy of the Aegean Sea sediments: special reference to the ages of sapropels S1–S5. Turkish Journal of Earth Sciences 25, 1–18.

Ito, E., 2002. Mg/Ca, Sr/Ca, $\delta^{18}O$ and $\delta^{13}C$ chemistry of Quaternary lacustrine ostracode shells from the North American continental interior. In: Holmes, J.A., Chivas, A.R. (Eds.), The Ostracoda: Applications in Quaternary Research. Geophysical Monograph, vol. 131. The American Geophysical Union, Washington, DC, pp. 267–278.

Ito, E., de Deckker, P., Eggins, S.M., 2003. Ostracodes and their shell chemistry: implications for paleohydrologic and paleoclimatologic applications. Paleontological Society Papers 9, 119–152.

Ivanov, V.A., Belokopytov, V.N., 2011. Oceanography of the Black Sea. National Academy of Science of Ukraine, Marine Hydrophysical Institute, Sevastopol, ECOSY-Gidrofizika, 210 pp.

Ivanov, V.G., Kakaranza, S.D., 2006. Major stages of Late Pleistocene–Holocene evolution of the northwestern Black Sea. In: IGCP 521 Second Plenary Meeting, Odessa, Ukraine, 20–28 August, Abstracts Volume, pp. 75–80.

Ivanova, E.V., Murdmaa, I.O., Karpuk, M.S., Schornikov, E.I., Marret, F., Cronin, T.M., Buynevich, I.V., Platonova, E.A., 2012. Paleoenvironmental changes on the northeastern and southwestern Black Sea shelves during the Holocene. Quaternary International 261, 91–104.

Ivanova, E.V., Marret, F., Zenina, M.A., Murdmaa, I.O., Chepalyga, A.I., Bradley, L.R., Schornikov, E.I., Levchenko, O.V., Zyryanova, M.I., 2015. The Holocene Black Sea

reconnection to the Mediterranean Sea: New insights from the northeastern Caucasian shelf. Palaeogeography Palaeoclimatology Palaeoecology 427, 41–61.

Janz, H., Vennemann, T.W., 2005. Isotopic composition (O, C, Sr, and Nd) and trace element ratios (Sr/Ca, Mg/Ca) of Miocene marine and brackish ostracods from North Alpine Foreland deposits (Germany and Austria) as indicators for palaeoclimate. Palaeogeography Palaeoclimatology Palaeoecology, 225, 216–247.

Jin, Z.D., Bickle, M.J., Chapman, H.J., Yu, J., An, Z., Wang, S., Greaves, M.J. 2011. Ostracod Mg/Sr/Ca and $^{87}Sr/^{86}Sr$ geochemistry from Tibetan lake sediments: Implications for early to mid-Pleistocene Indian monsoon and catchment weathering. Boreas, 40, 320–331.

Johnson, C.M., Lipman, P.W., Czamanske, G.K., 1990. H, O, Sr, Nd, and Pb isotope geochemistry of the Latir volcanic field and cogenetic intrusions, New Mexico, and relations between evolution of a continental magmatic center and modifications of the lithosphere. Contributions to Mineralogy and Petrology 104, 99–124.

Kaminski, M.A., Aksu, A.E., Box, M., Hiscott, R.N., Filipescu, S., & Al-Salameen, M. (2002). Late glacial to Holocene benthic foraminifera in the Marmara Sea: Implications for Black Sea-Mediterranean Sea connections following the last deglaciation. *Marine Geology, 190*, 165–202.

Karpov, V.A., Ivanov, V.G., Sibirchenko, M.G., et al., 1978. Otchet o geologicheskom izuchenii s s'emke Odesskogo zaliva Chernogo moria masshtaba 1:50,000m (List 36- 51-A, C, G), 1976–1978. Report on Geological Investigation and Survey 1:50,000 Within Odessa Bay of the Black Sea.

Kerey, I.E., Meriç, E., Tunoğlu, C., Kelling, G., Brenner, R.L., Doğan, A.U., 2004. Black Sea–Marmara Sea Quaternary connections: new data from the Bosphorus, İstanbul, Turkey. Palaeogeography, Palaeoclimatology, Palaeoecology, 204, 277–295.

Khaska, M., La Salle, C. Le-G., Lancelot, J., ASTER team, Mohamad, A., Verdoux, P., Noret, A., Simler, R., 2013. Origin of groundwater salinity (current seawater vs. saline deep water in a coastal karst aquifer based on Sr and Cl isotopes. Case study of the La Clape massif (southern France). Applied Geochemistry 37, 212–227.

Kırcı-Elmas, E., Algan, O., Özkar-Öngen, İ., Struck, U., Altenbach, A.V., Sagular, E.K., Nazik, A., 2008. Palaeoenvironmental investigation of sapropelic sediments from the Marmara Sea: a biostratigraphic approach to palaeoceanographic history during the Last Glacial–Holocene. Turkish Journal of Earth Sciences 17, 129–168.

Konerding, P., 2009. Quaternary Tectonics and Seismic Stratigraphy of the Western Black Sea Shelf. PhD Dissertation. Hamburg University (170 pp).

Konovalov, S.K. and J.W. Murray (2001) Variations in the chemistry of the Black Sea on a time scale of decades (1960-1995). Journal of Marine Systems, 31, 217-243

Köprülü, K., Alpar, B., Vardar, D., 2016. Late Glacial–Holocene stratigraphic development at the Marmara Sea exit of the Bosphorus Strait, Turkey. Marine Geophysical Researches 37, 21–35.

Kouli, K., Brinkhuis, H., Dale, B., 2001. Spiniferites cruciformis: a fresh water dinoflagellate cyst? Rev. Palaeobot. Palynol. 113 (4):273–286.

Kosarev, A.N., Arkhipkin VS, Surkova GV (2008) Hydrometeorological Conditions. In: Kostianoy A, Kosarev A (eds) The Black Sea Environment. The Handbook of Environmental Chemistry. Vol. 5, Part Q, Springer–Verlag, Berlin Heidelberg, pp 135–158.

Kukal, Z., 1971. Geology of Recent Sediments. Academic Press, London (490 pp).

Kuznetsov, A.B., Semikhatov, M.A., Gorokhov, I.M., 2012. Isotope composition of the world ocean, marginal and inland seas: implications for the Sr isotope stratigraphy. Stratigraphy and Geological Correlation 20, 501–515.

Kvasov, D.D., 1968. Paleohydrology of Eastern Europe in late Quaternary time. Yezhegodnkkh Chetniyakh Pamyati L.S. Berga Doklady Izd. Nauka, Leningrad, pp. 65–81.

Kwiecien, O., Arz, H.W., Lamy, F., Wulf, S., Bahr, A., Röhl, U., Haug, G.H., 2008. Estimated reservoir ages of the Black Sea since the Last Glacial. Radiocarbon 50, 99–118.

Lavrova, O., Mityagina, M., 2017. Satellite survey of internal waves in the Black and Caspian seas. Remote Sens. 9, 892.

Lambeck, K., Sivan, D., Purcell, A., 2007. Timing of the last Mediterranean Sea–Black Sea connection from isostatic models and regional sea-level data, in: Yanko-Hombach, V., Gilbert, A.S., Panin, N., Dolukhanov, P.M. (Eds.), The Black Sea Flood Question: Changes in Coastline, Climate and Human Settlement. Springer, The Netherlands, pp. 797–808.

Latif, MA, Özsoy, E, Oguz, T, Ünlüata, Ü., 1991. Observations of the Mediterranean inflow into the Black Sea. Deep Sea Res38 (Suppl 2):S711–S723.

Lane-Serff, G.F., Rohling, E.J., 1997. Postglacial connection of the Black Sea to the Mediterranean and its relation to the timing of sapropel formation. Paleoceanography 12, 169–174.

Lee B-S, J.L. Bullister, J.W. Murray, R.E. Sonnerup (2002) Anthropogenic chlorofluorocarbons in the Black sea and the Sea of Marmara. Deep-Sea Research 49, 895-913.

Leonov AK (1960) Regional oceanography, Part 1. The Bering Sea, the Okhotsk Sea, the Japan Sea, the Caspian Sea and the Black Sea. Gidrometeoizdat, Leningrad, 765 pp (in Russian).

Leonov, A.V., 2005. Variations in the Black Sea water salinity from its latest salinization to the present state: estimation based on mathematical modeling. Water Resources 32, 134–144.

Lericolais, G., Le Drezen, E., Nouzé, H., Gillet, H., Ergun, M., Çifçi, G., Avcıi, M., Dondurur, D., Okay, S., 2002. Recent canyon heads evidenced at the Bosporus outlet. EOS transactions, AGU Fall Meet. Suppl. 83(47), Abstract PP71B-0409.

Lericolais, G., Suc, J.-P., Guichard, F., Wong, H.K., Panin, N., Dinu, C., Dimitrov, D.P., Stanev, E.V., Staneva, J., Martinez-Ruiz, F., Morigi, C., 2006. High frequency sea level fluctuations recorded in the Black Sea since the LGM, *in* Sealaix '06—International Symposium "Sea Level Changes: Records, Processes and Modelling" (Giens, France): Paris, France, Association des Sédimentologues de France, 55, 132–133.

Lericolais, G., Popescu, I., Guichard, F., 2007a. A Black Sea lowstand at 8500 year BP indicated by a relict coastal dune system at a depth of 90m below sea level. *In*: Harff, J., Hay, W.W., Tetzlaff, D.M. (Eds.), Coastline Changes: Interrelation of Climate and Geological Processes. GSA Books. Allen Press, Inc., pp. 171–188.

Lericolais, G., Guichard, F., Morigi, C., Popescu, I., Bulois, C., Gillet, H., Ryan, W.B.F., 2011. Assessment of Black Sea water-level fluctuations since the Last Glacial Maximum. In: Buynevich, I., Yanko-Hombach, V., Gilbert, A.S., Martin, R.E. (Eds.), Geology and Geoarchaeology of the Black Sea Region: Beyond the Flood Hypothesis: Geological Society of America Special Paper. vol. 473. pp. 1–18.

Liu, J.T., Hsu, R.T., Yang, R.J., Wang, Y.P., Wu, H., Du, X., Li, A., Chien, S.C., Lee, J., Yang, S., Zhu, J., Su, C.-C., Chang, Y., Huh, C.-A., 2018. A comprehensive sediment dynamics study of a major mud belt system on the inner shelf along an energetic coast. Nat. Sci. Rep. 8, 4229. https://doi.org/10.1038/s41598-018-22696-w. (14 p).

Lericolais, G., Popescu, I., Guichard, F., Popescu, S.M. and Manolakakis, L., 2007b. Water-level fluctuations in the Black Sea since the Last Glacial Maximum. In: V. Yanko-Hombach, A.S. Gilbert, N. Panin and P.M. Dolukhanov (Editors), The Black Sea Flood Question: Changes in Coastline, Climate, and Human Settlement. Springer, pp. 437-452.

Lericolais, G., Guichard, F., Morigi, C., Minereau, A., Popescu, I., Radan, S., 2010. A post Younger Dryas Black Sea regression identified from sequence stratigraphy correlated to core analysis and dating. Quaternary International, 225, 199-209.

Lericolais, G., Bulois, C., Gillet, H., Guichard, F., 2009. High frequency sea level fluctuations recorded in the Black Sea since the LGM. Global and Planetary Change 66, 65–75.

Lericolais, G., Guichard, F., Morigi, C., Minereau, A., Popescu, I., Radan, S., 2010. A post Younger Dryas Black Sea regression identified from sequence stratigraphy correlated to core analysis and dating. Quaternary International, 225, 199-209.

Lericolais, G., Guichard, F., Morigi, C., Popescu, I., Bulois, C., Gillet, H., Ryan, W.B.F., 2011. Assessment of Black Sea water-level fluctuations since the Last Glacial Maximum, in: Buynevich, I.V., Yanko-Hombach, V., Gilbert, A.S., Martin, R.E. (Eds.), Geology and Geoarchaeology of the Black Sea Region: Beyond the Flood Hypothesis. Geological Society of America, Special Paper 473, 1–18.

Letouzey, J., Biju-Duva, B., Dorkel, A., Gonnard, R., Kristchev, K., Montadert, L., & Sungurlu, O., 1977, The Black Sea: A marginal basin - Geophysical and geological data. In: B. Biju-Duval & L. Montadert (Eds.): International Symposium on the structural history of the Mediterranean basins: Split. Paris, p. 363-376.

Linegar, A.E., 2012. Paleo-environmental history of the southwestern Black Sea during the late Holocene: an elemental and stable isotopic study. Unpublished MSc thesis, Memorial University of Newfoundland, 156 pp.

Lisiecki, L.E., Raymo, M.E., 2005. A Pliocene-Pleistocene stack of 57 globally distributed benthic $\delta^{18}O$ records. Paleoceanography, 20, 1–17.

Lister, C.J., Hiscott, R.N., Aksu, A.E., Mudie, P.J., 2015. Compositional trends through the Holocene mud succession of the southwestern Black Sea shelf: Implications for sedimentary provenance and water-level history. Sedimentary Geology 316, 13–25.

Liu, J.T., Hsu, R.T., Yang, R.J., Wang, Y.P., Wu, H., Du, X., Li, A., Chien, S.C., Lee, J., Yang, S., Zhu, J., Su, C.-C., Chang, Y., Huh, C.-A., 2018. A comprehensive sediment dynamics study of a major mud belt system on the inner shelf along an energetic coast. Nat. Sci. Rep. 8, 4229.

Londeix, L., Herreyre, Y., Turon, J.-L., Fletcher, W., 2009. Last Glacial to Holocene hydrology of the Marmara Sea inferred from dinoflagellate cyst record. Reviews of Palaeobotony and Palynology 158, 52–71.

Lyons, T. W. (1991), Upper Holocene sediments of the Black Sea: Summary of Leg 4 box cores (1988 Black Sea Expedition), in Black Sea Oceanographys, edited by E. Izdar and J. W. Murray, pp. 401–411, Springer, New York.

Macko, S.A., Engle, M.H., Quian, Y., 1994. Early diagenesis and organic matter preservation: A molecular stable isotope perspective. Chemical Geology, 114, 365–379.

Madgwick, R., Lewis, J., Grimes, V., Guest, P., 2017. On the hoof: exploring the supply of animals to the Roman legionary fortress at Caerleon using strontium ($^{87}Sr/^{86}Sr$) isotope analysis. Archaeological and Anthropological Sciences.

Major, C.O., 2002. Geochemical tracers of riverine and marine water mixing in the Black Sea. Chapter 4 in: Non-Eustatic Controls on Sea-level Change in Semi-enclosed Basins. PhD thesis, Columbia University, New York, 223 p.

Major, C., Ryan, W., Lericolais, G., 2002a. Constraints on Black Sea outflow to the Sea of Marmara during the last glacial–interglacial transition. Marine Geology, 190, 19–34.

Major, C., Goldstein, S.L., Ryan, W., Piotrowski, A., Lericolais, G., 2002b. Climate change in the Black Sea region through termination I from Sr and O isotopes. Geochimica Et Cosmochimica Acta, 66, A476-A476.

Major, C.O., Goldstein, S.L., Ryan, W.B.F., Lericolais, G., Piotrowski, A.M., Hajdas, I., 2006. The co-evolution of Black Sea level and composition through the last deglaciation and its paleoclimate significance. Quaternary Science Reviews 25, 2031–2047.

Mamaev, V. O. &. Musin O.R., 1997, Black Sea Geographic Information System, CD-ROM, In: Programme, B. S. E. P. - U. N. D. (Ed.): New York, United Nations Publications. Manheim, F.T., Chan, K.M., 1974. Interstitial waters of Black Sea sediments: New data and review. In: Degens, E.T., Ross, D.A. (Eds.), The Black Sea - Geology, Chemistry and BiologyMem. Am. Assoc. Petrol. Geol.Tusla, pp. 155–180.

Marret, F., Mudie, P.J., Aksu, A.E., Hiscott, R.N., 2009. A Holocene dinocyst record of a two-step transformation of the Neoeuxinian brackish water lake into the Black Sea. Quaternary International 197, 72–86.

Matova, M., 2000. Recent geological activity along the northeastern Bulgarian Black Sea coast. Geological Quarterly, 44, 355–361.

Marković, S.B., Stevens, T.S., Kukla, G.J., 22, others, 2015. Danube loess stratigraphy – towards a pan-European loess stratigraphic model. Earth Sci. Rev. 148, 228–258.

McHugh, C.M.G., Gurung, D., Giosan, L., Ryan, W.B.F., Mart, Y., Sancar, U., Burckle, L., Çağatay, M.N., 2008. The last reconnection of the Marmara Sea (Turkey) to the World Ocean: paleoceanographic and paleoclimatic perspective. Marine Geology 255, 64–82.

Mertens, K.N., Bradley, L.R., Takano, Y., Mudie, P.J., Marret, F., Aksu, A.E., Hiscott, R.N., Verleye, T.J., Mousing, E.A., Smyrnova, L.L., Bagheri, S., Mansor, M., Pospelova, V., Matsuoka, K., 2012. Quantitative estimation of Holocene surface salinity variation in the Black Sea using dinoflagellate cyst process length. Quaternary Science Reviews 39, 45–59.

Miall, A.D., 1994. Sequence stratigraphy and chronostratigraphy: problems of definition and precision in correlation, and their implications for global eustasy. Geoscience Canada 21, 1–26.

Mills R., Teagle D., Tivey M., 1998. Fluid mixing and anhydrite precipitation within the TAG mound, in: Herzig, P., Humphris, S., Miller, D., Zierenberg, R. (Eds.), Proceedings of the Ocean Drilling Program, Scientific Results 158. Ocean Drilling Program, College Station, Texas, pp. 119–127.

Mitchum Jr., R.M., Vail, P.R., 1977. Seismic stratigraphy and global changes of sea-level, part 7: stratigraphic interpretation of seismic reflection patterns in depositional sequences. In: Payton, C.E. (Ed.), Seismic Stratigraphy – Applications to Hydrocarbon Exploration. Memoir 26. American Association of Petroleum Geologists, pp. 135–144.

More, K. D., L. Giosan, K. Grice, and M. J. L. Coolen. 2019. "Holocene paleodepositional changes reflected in the sedimentary microbiome of the Black Sea." Geobiology 17 (4): 436-448.

Mudie, P.J., Rochon, A., Aksu, A.E., Gillespie, H., 2002. Dinoflagellate cysts and freshwater algae and fungal spores as salinity indicators in Late Quaternary cores from Marmara and Black Seas. Marine Geology 190, 203–231.

Mudie, P.J., Marret, F., Aksu, A.E., Hiscott, R.N., Gillespie, H., 2007. Palynological evidence for climate change, anthropogenic activity and outflow of Black Sea water during the late Pleistocene and Holocene: centennial- to decadal- scale records from the Black and Marmara Seas. Quaternary International 167–168, 73–90.

Mudie, P.J., Marret, F., Rochon, A., Aksu, A.E., 2010. Non-pollen palynomorphs in the Black Sea corridor. Vegetation History and Archaeobotiology, 19: 531–544.

Mudie, P.J., Yanko-Hombach, V., Kadurin, S., 2014. The Black Sea dating game and Holocene marine transgression. Open J. Mar. Sci. 4, 1–7.

Murray J.W. (1991) The 1988 Black Sea Oceanographic Expedition: introduction and summary. Deep-Sea Research, 38, S655-S661.

Murray J.W. and others (1989) Unexpected changes in the oxic/anoxic interface in the Black Sea. Nature, 337, 411-413.

Murray J.W., Z. Top and E. Ozsoy (1991) Hydrographic properties and ventilation of the Black Sea. Deep-Sea Research, 38, S663-S689.

Murray J.W., L.A. Codispoti and G.E. Friederich. (1995) Oxidation-reduction environments: the suboxic zone in the Black Sea. In: Huang C.P., O'Melia C.R., Morgan J.J. (Eds) Aquatic Chemistry: Interfacial and Interspecies Processes. ACS Advances in Chemistry Series. No. 224. pp. 157-176.

Murray, J.W., Stewart, K., Kassakian, S., Krynytzky, M., DiJulio, D., 2007. Oxic, Suboxic and Anoxic Conditions in the Black Sea. In: V. Yanko-Hombach, A.S. Gilbert, N., Panin N., Dolukhanov P.M. (eds) The Black Sea Flood Question: Changes in Coastline, Climate and Human Settlement. Springer, Dordrecht.

Myers P.G., Wielki, C., Goldstein, S.B., Rohling, E.J., 2003. Hydraulic calculations of postglacial connections between the Mediterranean and the Black Sea. Marine Geology 20, 253–267.

Nazik, A., Meriç, E., Avşar, N., Ünlü, S., Esenli, V., Gökaşan, E., 2011. Possible waterways between the Marmara Sea and the Black Sea in the Late Quaternary: evidence from ostracod and foraminifer assemblages in lakes İznik and Sapanca, Turkey. Geo-Marine Letters 31, 75–86.

Nevesskaya, L. A. (1970). On the classification of enclosed and semienclosed basins based on their fauna characteristics. In D. B. Obruchev, & V. N. Shimanskiy (Eds.), *Modern Problems of the Paleontology* (pp. 258-278). Moscow: Nauka [in Russian].

Ocakoğlu, N., İşcan, Y., Kılıc, F., Ozel, O., 2018. Morphologic and seismic evidence of rapid submergence offshore Cide-Sinop in the southern Black Sea shelf. Geomorphology 311, 76–89.

Oğuz, T., Latun, V.S., Latif, M.A., Vladimirov, V.V., Sur, H.I., Markov, A.A., Ozsoy, E., Kotovshchikov, B.B., Eremeev, V.V., Unluata, U., 1993. Circulation in the surface and intermediate layers of the Black Sea. Deep-Sea Research I 40, 1597–1612.

Oğuz, T., Tuğrul, S., Kideys, E., Ediger, V., Kubilay, N., 2004. Physical and biogeochemical characteristics of the Black Sea. Chapter 33 in: Robinson, A.R., Brink, K.H. (Eds.). The Sea 14, 1331–1369.

Oguz, T., Fach, B. and Salihoglu, B., 2008. Invasion dynamics of the alien ctenophore Mnemiopsis leidyi and its impact on anchovy collapse in the Black Sea. J. Plankton Res., 30, 1385–1397.

Opreanu, G., 2003/2004. Porosity, density and other physical properties of deep-sea sediments from the Black Sea. Geo-Eco-Marina 9–10, Modern and ancient fluvial, deltaic and marine environments and processes, Proceedings of Euro-EcoGeoCentre-Romania.

Orlova, M.I., Therriault, T.W., Antonov, P.I., Shcherbina, G.K., 2005. Invasion ecology of quagga mussels (Dreissena rostriformis bugensis): a review of evolutionary and phylogenetic impacts. Aquatic Ecology 39, 401–418.

Ortiz, J.D., Wheeler, P.A., Mix, A.C., Key, R.M., 2000. Anthropogenic CO_2 invasion into the northeast Pacific based on concurrent $^{13}C_{DIC}$ and nutrient profiles from the California Current. Global Biogeochemical Cycles, 14, 917–929.

Ostlund H.G. and D. Dyrssen (1986) Renewal rates of the Black Sea deep water. In: The chemical and physical oceanography of the Black Sea. Reports of the Chemistry of the Sea XXXIII, University of Goteborg, Goteborg, Sweden.

Ostrovsky, A.B., Izmailov, Y.A., Balabanov, I.P., Skiba, S.I., Skryabina, N.G., Arslanov, S.A., Gey, N.A., Suprunova, N.I., 1977. Novie dannieo palegidrologicheskom rezhime Chernogo moria v verkhnempleistotsene i golotsene [New data on the paleohydrological regimeof the Black Sea in the Upper Pleistocene and Holocene]. In: Kaplin, P.A., Shcherbakov, F.A. (Eds.), Paleogeografiia i OtlozheniiaPleistotsena Iuzhnykh Morei

SSSR [Pleistocene Paleogeographyand Sediments of the Southern Seas of the USSR]. Nauka, Moscow, pp. 131–140 (in Russian).

Özsoy E, Ünlüata Ü, Top Z, 1993. The evolution of Mediterranean water in the Black Sea: interior mixing and material transport by double diffusive intrusions. Progr Oceanogr, 31(3): 275–320.

Özsoy, E., Latif, M.A., Tugflrul, S. & Ünluata, Ü., 1995. Exchanges with the Mediterranean, fluxes and boundary mixing processes in the Black Sea. In: F. BRIAND (Ed.), Mediterranean Tributary Seas. Bulletin de l'Institut Oceanographique, Monaco, Special No. 15, CIESME Science Series 1, p. 1-25.

Özsoy, E., Latif, M.A., Sur, H.I. & Goryachkin, Y., 1996. A review of the exchange flow regimes and mixing in the Bosphorus Strait. In: F. BRIAND (Ed.), Mediterranean Tributary Seas: Bulletin de l'Institut Oceanographique, Monaco, Special No. 17, CIESME Science Series 2, p. 187-204.

Özsoy, E., Ünlüata, Ü., 1997. Oceanography of the Black Sea: a review of some recent results. Earth-Science Reviews 42, 231–272.

Özsoy, E., Latif, M.A., Beşiktepe, Ş., 2002. The current system of the Bosphorus Strait based on recent measurements. 2nd meeting Physical Oceanography of Sea Straits, Villefranche, pp. 177–180 (Abstracts).

Orlova, M.I., Therriault, T.W., Antonov, P.I., Shcherbina, G.K., 2005. Invasion ecology of quagga mussels (Dreissena rostriformis bugensis): a review of evolutionary and phylogenetic impacts. Aquat. Ecol. 39, 401–418.

Palmer, M.R., Edmond, J.M., 1989. The strontium isotope budget of the modern ocean. Earth and Planetary Science Letters 92, 11–26.

Palushka, A. & Degens, E.T., 1979. Climatic and tectonic events controlling the Quaternary in the Black Sea region: Geol. Rundschau 68 (1), p. 284–301.

Panin, N., Jipa, D., 2002. Danube River sediment input and its interaction with the northwestern Black Sea. Estuar. Coast. Shelf Sci. 54, 551–562.

Panin, N., Strechie, C., 2006. Late Quaternary sea-level and environmental changes in the Black Sea: a brief review of published data. Journal of Archaeomythology 2 (1), 3–16.

Pawellek, F., Frauenstein, F., Veizer, J., 2002. Hydrochemistry and isotope geochemistry of the upper Danube River. Geochimica et Cosmochimica Acta 66, 3839–3854.

Pearce, N.J.G. Perkins, W.T. Westgate, J.A., Gorton, M.P., Jackson, S.E., Neal, C.R., Chenery, S.P., 1997. A compilation of new and published major and trace element data for NIST SRM 610 and NIST SRM 612 glass reference materials. The Journal of Geostandards and Geoanalysis, Geostandards Newsletter, 21,115–144.

Perşoiu, A., Onac, B.P., Wynn, J.G., Blaauw, M., Ionita, M., Hansson, M., 2017. Holocene winter climate variability in Central and Eastern Europe. Sci. Rep. 7 (1196), 1–8.

Piper, D.Z., Calvert, S.E., 2011. Holocene and Late Glacial palaeoceanography and palaeolimnology of the Black Sea: changing sediment provenance and basin hydrography over the past 20,000 years. Geochimica et Cosmochimica Acta 75, 5597–5624.

Piper, D.Z., 2016. Geochemistry of the Black Sea during the last 15kyr: a protracted evolution of its hydrography and ecology. Paleoceanography, 31, 1117–1137.

Podoplelov, O.N., Karpov, V.A., Ivanov, V.G., Mokrjak, I.M., Zagorodnij, G.G., 1975. Otchet o geologicheskoi s'emki shelfa severo-zapadnoj chasti Chernogo moria masshtaba 1:50, 000, 1973–1975. In: Report on Geological Survey 1:50,000 within North-western Part of the Black Sea. Krymgeologiia, Odessa, (367 pp., in Russian).

Polonsky, A.B., Bardin, M.Y., Voskresenskaya, E.N., 2007. Statistical characteristics of cyclones and anticyclones in the Black Sea in the second half of the twentieth century. Morskoy Gidrofizicheskiy Zhurnal 6: 47–58 (in Russian).

Popescu, I., Lericolais, G., Panin, N., Wong, H.K., & Droz, L., 2001. Late Quaternary channel avulsion on the Danube deep-sea fan, Black Sea: Marine Geology 179, p. 25-37.

Popescu, I., Panin, N., Jipa, D., Lericolais, G., Ion, G., 2015. Submarine canyons of the Black Sea basin with a focus on the Danube Canyon, pp. 103–121. *In*: F. Briand (ed.), CIESM Monograph 47, Submarine canyon dynamics in the Mediterranean and tributary seas – An integrated geological, oceanographic and biological perspective, 232 pp. CIESM Publisher, Monaco.

Quaresma, L.S., Vitorino, J., Oliveira, A., da Silva, J., 2007. Evidence of sediment resuspension by nonlinear internal waves on the western Portuguese mid-shelf. Mar. Geol. 246, 123–143.

Rangin, C., Demirbag, E., Imren, C., Crusson, A., Normand, A., Le Drezen, E., Le Bot, A., 2001. Marine Atlas of the Sea of Marmara (Turkey). Ifremer, Plouzane, France.

Ravelo, A.C., Hillaire-Marcel, C., 2007. The use of oxygen and carbon isotopes of foraminifera in paleoceanography, in Proxies in Late Cenozoic Paleoceanography. Development in Marine Geology, V.1, C. Hillaire-Marcel and A. de Vernal (Eds), pp. 735–764, Elsevier, Amsterdam, The Netherlands.

Reimer, P.J., Bard, E., Bayliss, A., Beck, J.W., Blackwell, P.G., Bronk Ramsey, C., Grootes, P.M., Guilderson, T.P., Haflidason, H., Hajdas, I., HattŽ, C., Heaton, T.J., Hoffmann, D.L., Hogg, A.G., Hughen, K.A., Kaiser, K.F., Kromer, B., Manning, S.W., Niu, M., Reimer, R.W., Richards, D.A., Scott, E.M., Southon, J.R., Staff, R. A, Turney, C.S.M., van der Plicht, J., 2013. IntCal13 and Marine13 radiocarbon age calibration curves 0–50,000 years cal BP. Radiocarbon 55, 1869–1887.

Reinhardt, E.G., Blenkinsop, J., Patterson, R.T., 1999. Assessment of a Sr isotope vital effect ($^{87}Sr/^{86}Sr$) in marine taxa from Lee Stocking Island, Bahamas. Geo-Marine Letters 18, 241–246.

Ricketts, R.D., Johnson, T.C., Brown, E.T., Rasmussen, K.A., Romanovsky, V.V. 2001. The Holocene paleolimnology of Lake Issyk-Kul, Kyrgyzstan: trace element and stable isotope composition of ostracods. Palaeogeography, Palaeoclimatology, Palaeoecology, 176, 207–227.

Robinson, A., Spandini, G., Cloetingh, S., & Rudat, G., 1995. Stratigraphic evolution of the Black Sea: inferences from basin modelling: Mar. and Petr. Geology, v. 12, no. 8, p. 821-835.

Rögl, F., 1999. Mediterranean and Paratethys: Facts and hypotheses of an Oligocene to Miocene paleogeography (short overview). Geologica Carpathica, 50, 339–349.

Rohling, E.J., Marino, G., Grant, K.M., 2015. Mediterranean climate and oceanography, and the periodic development of anoxic events (sapropels). Earth-Science Reviews 143, 62–97.

Ross, D.A. & Degens, E.T., 1974. Recent sediments of Black Sea. In: E.T. DEGENS & D.A. ROSS (Eds.), The Black Sea-Geology, Chemistry, and Biology, vol. 20: AAPG Mem., p. 183-199.

Rousseau, D.-D., Derbyshire, E., Antoine, P., Hatte, C., 2018. European Loess Records. Reference Module in Earth Systems and Environmental Sciences.

Ruggieri, G., 1967. Due ostracofaune del Miocene allocto dell val Mareccia (Appennino Settentrionale). Rivista Italiana di Paleontologia e Stratigrafia, 73(1), 35 1–384.

Ruiz, F., Abad, M., Bodergat, A.M., Carbonel, P., Rodríguez-Lázaro, J., González-Regalado, M.L., Toscano, A., García, E.X., Prenda, J., 2013. Freshwater ostracods as environmental tracers. International Journal of Environmental Science and Technology, 10, 1115–1128.

Rudoy, A.N., 1998. Mountain ice-dammed lakes of southern Siberia and their influence on the development and regime of the intracontinental runoff systems of north Asia in the

Late Pleistocene. In: Benito, G., Baker, V.R., Gregory, K.J. (Eds.), Palaeohydrology and Environmental Change. Wiley, New York, pp. 215–234.

Rudoy, A.N., Baker, V.R., 1993. Sedimentary effects of cataclysmic late Pleistocene glacial outburst flooding, Altay Mountains, Siberia. Sedimentary Geology, 85, 53–62.

Ryan, W.B.F., Pitman, W.C., III, Major, C.O., Shimkus, K., Maskalenko, V., Jones, G.A., Dimitrov, P., Görür, N., Sakınç, M., Yüce, H., 1997. An abrupt drowning of the Black Sea shelf. Marine Geology 138, 119–126.

Ryan, W.B.F., 2007. Status of the Black Sea flood hypothesis. *In*: Yanko-Hombach, V., Gilbert, A.S., Panin, N., Dolukhanov, P.M. (Eds.), The Black Sea Flood Question: Changes in Coastline, Climate, and Human Settlement. Springer, Dordrecht, The Netherlands, pp. 63–88.

Ryan, W.B.F., Pitman,W.C., Major, C.O., Shimkus, K., Moscalenko, V., Jones, G.A., Dimitrov, D., Görür, P., Sakınç,M., Seyir, H.Y., 1996. An abrupt drowning of the Black Sea shelf at 7.5 kyr BP. Geo-Eco-Marina (Malnas, Romania).

Ryan, W.B.F., Major, C.O., Lericolais, G., Goldstein, S.L., 2003. Catastrophic Flooding of the Black Sea. Annual Review of Earth and Planetary Sciences 31, 525–554.

Ryan, W.B.F., Carbotte, S.M., Coplan, J.O., O'Hara, S., Melkonian, A., Arko, R., Weissel, R.A., Ferrini, V., Goodwillie, A., Nitsche, F., Bonczkowski, J., Zemsky, R., 2009. Global multiresolution topography synthesis. Geochemistry Geophysics Geosystems 10, Q03014.

Ryan, W.B.F., Vachtman, D., McHugh, C., Çağatay, M.N., Mart, Y., 2013. A channeled shelf fan initiated by flooding of the Black Sea. *In*: Gofredo, S., Dubinsky, Z. (Eds.), The Mediterranean Sea: Its History and Present Challenges, pp. 11–27.

Sheriff, R.E., Geldart, L.P., 1995. Exploration Seismology, Cambridge University Press, p. 174, 592 pp.

Schoepfer, S.D., Shen, J., Wei, H., Tyson, R.V., Ingall, E., Algeo, T.J., 2015. Total organic carbon, organic phosphorus, and biogenic barium fluxes as proxies for paleomarine productivity. Earth-Science Reviews, 149, 23–52.

Scholz, F., McManus, J., Sommer, S., 2013. The manganese and iron shuttle in a modern euxinic basin and implications for molybdenum cycling at euxinic ocean margins. Chemical Geology, 355, 56–68.

Schornikov, E.I., 1964. An experiment on the distinction of the Caspian elements of the ostracod fauna in the Azov-Black Sea basin. Zoologicheski Zurnal 43, 1276–1293.

Schornikov, E.I., 1967. Identification key to the fauna of the Black Sea and Azov Sea. Vol. 2: Free living invertebrates, Crustacean. Kiev.

Shurova, N.M., Gomoiu, M.-T., 2006. Present state of mussel population (*Mytilu galloprovincialis*) from the north-west Black Sea. In: Black Sea Ecosystem 2005 and Beyond. Abstract. 1st Biannual Scientific Conference 8–10 May 2006 Istanbul,Turkeypp. 92–93.

Siani, G., Paterne, M., Arnold, M., Bard, E., Métiver, B., Tisnerat, N., Bassinot, F., 2000. Radiocarbon reservoir ages in the Mediterranean Sea and Black Sea. Radiocarbon 42, 271–280.

Sibirchenko, M.G., Karpov, V.A., Ivanov, V.G., Mokrjak, I.M., Zjultsle, V.G., Tatarovskij, V.V., 1983. Otchet po izucheniiu litilogicheskogo sostava donnykh otlozhenii shelfa Chernogo moria s zeliiu sostavleniia geologo-litologicheskoi karty masshtaba 1:200,000 (Report on lithological study of the Black Sea shelf for the preparation of geological-lithological map 1:200,000). Krymgeologia, Odessa, pp. 427 (in Russian).

Sinclair, L., 2018. Sourcing the Origin of Holocene Sediments beneath the Southwestern Black Sea Shelf. Unpublished BSc thesis. Memorial University of Newfoundland (77 pp).

Simonov, A.I., Altman, E.N., 1991. Hydrometeorology and hydrochemistry of seas in the USSR, vol IV. Black Sea. Issue 1. Hydrometeorological conditions. Gidrometeoizdat, Leningrad, 429 pp. (in Russian).

Smalley, I.J., Leach, J.A., 1978. The origin and distribution of the loess in the Danube basin and associated regions of east-central Europe: a review. Sediment. Geol. 21, 1–26.

Soulet, G., Delaygue, G., Vallet-Coulomb, C., Böttcher,M.E., Sonzogni, C., Lericolais, G., Bard, E., 2010. Glacial hydrologic conditions in the Black Sea reconstructed using geochemical pore water profiles. Earth Planet. Sci. Lett. 296:57–66.

Sperling, M., Schmiedl, G., Hemleben, C., Emeis, K.C., Erlenkeuser, H., Grootes, P.M., 2003. Black Sea impact on the formation of eastern Mediterranean sapropel S1? Evidence from the Sea of Marmara. Palaeogeography Palaeoclimatology Palaeoecology 190, 9–21.

Stanev, E.V., He, Y., Staneva, J., Yakushev, E., 2014. Mixing in the Black Sea detected from the temporal and spatial variability of oxygen and sulfide – Argo float observations and numerical modelling. Biogeosciences 11, 5707–5732.

Starostenko, V.I., Rusakov, O.M., Shnyukov, E.F., Kobolev, V.P., Kutas, R.I., 2010. Methane in the northern Black Sea: characterization of its geomorphological and geological environments. In: M., Sosson, N., Kaymakci, R.A., Stephenson, F., Bergerat, V., Starostenko, (Eds.), Sedimentary Basin Tectonics from the Black Sea and Caucasus to the Arabian Platform. Geol. Soc. Lond., Spec. Publ. 340, 57–75.

Stuiver, M., Reimer, P.J., Reimer, R.W., 2019. CALIB 7.1. [WWW program] at. http:// calib.org.

Syvitski, J.P.M., Asprey, K.W., Clattenburg, D.A., Hodge, G.D., 1985. The prodelta environment of a fjord: suspended particle dynamics. Sedimentology 32, 83–107.

Stuiver, M., Braziunas., T.F., 1993. Modelling atmospheric ^{14}C influences and ^{14}C ages of marine samples to 10,000 BC Radiocarbon, 35, pp. 137-189.

Sutherland, B.R., Barrett, K.J., Gingras, M.K., 2015. Clay settling in fresh and salt water. Environ. Fluid Mech. 15, 147–160.

Tankéré, S.P.C., Muller, F.L.L., Burton, J.D., Statham, P.J., Guieu, C., Martin, J.-M., 2001. Trace metal distributions in shelf waters of the northwestern Black Sea. Continental Shelf Research, 21, 1501–1532.

Terakado, Y., Shimizu, H., Masuda, A., 1988. Nd and Sr isotopic variations in acidic rocks formed under a peculiar tectonic environment in Miocene southwest Japan. Contributions to Mineralogy and Petrology 99, 1–10.

Tkachenko, G.G., 1971. Deiaki dani pro uglevodorodni hasy donnikh vidkladiv pivnichno-zakhidnoi chastini Chernogo moria (Some data about hydrocarbon gases of the bottom sediments of north-western part of the Black Sea). In: Mezhvedomstvennii respublikanskii naukovii sbornik "Geologiia uzberezhzhia i dna Chernogo ta Azovs'kogo moriv u mezhakh Ukrainskoi RSR" (Interdepartmental Republican Scientific Miscellanea "Geology of the Coast and Bottom of the Black Sea and Sea of Azov within the Ukrainian SSR"). vol. 5. Vishcha Shkola, Kiev, pp. 80–85 (in Ukrainian).

Thébault, J., Chauvaud, L., L'Helguen, S., Clavier, J., Barats, A., Jacquet, S., Pécheyran, C., Amouroux, D., 2009. Barium and molybdenum records in bivalve shells: Geochemical proxies for phytoplankton dynamics in coastal environments? Limnology and Oceanography, 54, 1002–1014.

Thom, N., 2010. A hydrological model of the Black and Caspian seas in the late Pleistocene and early–middle Holocene. Quaternary Science Reviews 29, 2989–2995.

Traband, P.K., 1984. Applied High-Resolution Geophysical Methods: Offshore Engineering Hazards. Springer Science + Business Media Dordrecht, p. 103, 265 pp.

Tribovillard, N., Algeo, T.J., Lyons, T., Riboulleau, A., 2006. Trace metals as paleoredox and paleoproductivity proxies: an update. Chemical Geology, 232, 12–32.

Tribovillard, N., Algeo, T.J., Baudin, F., Riboulleau, A., 2012. Analysis of marine environmental conditions based on molybdenum-uranium covariation – applications to Mesozoic paleoceanography. Chemical Geology, 324–325, 46–58.

Tolun, L., Çağatay, M.N., Carrigan, W.C., 2002. Organic geochemistry and origin of late Glacial-Holocene sapropelic layers and associated sediments in Marmara Sea. Marine Geology 190, 47–60.

Tolmazin D (1985b) Changing coastal oceanography of the Black Sea, II, Mediterranean effluent. Prog Oceanogr 15: 277–316.

Torres, M.E., Mix, A.C., Kinports, K., Haley, B., Klinkhammer, G.P., McManus, J., de Angelis, M.A., 2003. Is methane venting at the seafloor recorded by δ13C of benthic foraminifera shells? Paleoceanography 18, 1062.

Troitskaya, E., Blinov, V., Ivanov, V., Zhdanov, A., Gnatovsky, R., Sutyrina, E., Shimaraev, M., 2015. Cyclonic circulation and upwelling in Lake Baikal. Aquatic Sciences 77, 171–182.

Tudryn, A., Leroy, S.A.G., Toucanne, S., Gibert-Brunet, E., Tucholka, P., Lavrushin, Y.A., Dufaure, O., Miska, S., Bayon, G., 2016. The Ponto-Caspian basin as a final trap for southeastern Scandinavian ice-sheet meltwater. Quaternary Science Reviews 148, 29–43.

Turney, C.S.M., Brown, H., 2007. Catastrophic early Holocene sea level rise, human migration and the Neolithic transition in Europe. Quaternary Science Reviews 26, 2036–2041.

Tütken, T., Vennemann, T.W., Janz, H., Heimann, E.P.J., 2006. Palaeoenvironment and palaeoclimate of the Middle Miocene lake in the Steinheim basin, SW Germany: a reconstruction from C, O, and Sr isotopes of fossil remains. Palaeogeography Palaeoclimatology Palaeoecology 241, 457–491.

Unesco, 1980. Tenth Report of the Joint Panel on Oceanographic Tables and Standards: Sidney, B.C., Canada 1-5 September 1980 Sponsored by Unesco, ICES, SCOR, IAPSO. Volume 36 of Unesco technical papers in marine science.

Ujvari, G., Kovacs, J., Varga, G., Raucsik, B., Markovic, S.B., 2010. Dust flux estimates for the Last Glacial Period in East Central Europe based on terrestrial records of loess deposits: a review. Quat. Sci. Rev. 29, 3157–3166.

Vasiliev, I., Reichart, G-J., Davies, G.R., Krijgsman, W., Stoica, M., 2010. Strontium isotope ratios of the eastern Paratethys during the Mio-Pliocene transition: implications for interbasinal connectivity. Earth and Planetary Science Letters 292, 123–131.

Valchev, N. N., Trifonova, E. V., & Andreeva, N. K., 2012. Past and recent trends in the western Black Sea storminess. *Natural Hazards and Earth System Sciences*, *12*(4), 961–977.

Van Wagoner, J.C., Posamentier, H.W., Mitchum, R.M., Vail, P.R., Sarg, J.F., Loutit, T.S., and Hardenbol, J., 1988. An overview of sequence stratigraphy and key definitions. In: Wilgus, C.K., Hastings, B.S., Kendall, C.G.St.C., Posamentier, H.W., Ross C.A. and Van Wagoner, J.C. (Eds.) Sea Level Changes – An Integrated Approach. Society of Economic Paleontologists and Mineralogists (SEPM), Special Publication 42, 39-45.

Vespremeanu-Stroe, A., Zăinescu, F., Preoteasa, L., Tătui, F., Rotaru, S., Morhange, C., Stoica, M., Hanganu, J., Timar-Gabor, A., Cardan, I., Piotrowska, N., 2017. Holocene evolution of the Danube delta: an integral reconstruction and a revised chronology. Mar. Geol. 388, 38–61.

Vidal, L., Ménot, G., Joly, C., Bruneton, H., Rostek, F., Çağatay, M.N., Major, C., Bard, E., 2010. Hydrology in the Sea of Marmara during the last 23 ka: implications for timing of Black Sea connections and sapropel deposition. Paleoceanography 25, PA1205.

von Grafenstein, U., 2002. Oxygen-Isotope Studies of Ostracods from Deep Lakes. In: J.A. Holmes, A.R. Chivas (Eds), The Ostracoda: Applications in Quaternary Research,

American Geophysical Union as part of the Geophysical Monograph Series, Volume 131, 249–266.

Walker, M., Johnsen, S., Rasmussen, S.O, Popp, T., Steffensen, J-P., Gibbard, P., Hoek, W., Lowe, J., Andrews, J., Björck, S., Cwynar, L.C., Hughen, K., Kershaw, P., Kromer, B., Litt, T., Lowe, D., Nakagawa, T., Newnham, R., Schwander, J., 2009. Formal definition and dating of the GSSP (Global Stratotype Section and Point) for the base of the Holocene using the Greenland NGRIP ice core, and selected auxilary records. Journal of Quaternary Science, 24, 3–17.

Wall, D. & Dale, B., 1974. Dinoflagellates in the late Quaternary deep-water sediments of the Black Sea. In: DEGENS, E.T., ROSS, D.A. (Eds.), The Black Sea – Geology, Chemistry and Biology: AAPG Memoir 20, Tulsa, OK, p. 364–380.

Wei, G., Liu, Y., Li, X., Chen, M., Wei, W., 2003. High-resolution elemental records from the South China Sea and their paleoproductivity implications. Paleoceanography, 18(2), 1054, doi:10.1029/2002PA000826.

Westerlund, S., 1986. Trace metal concentrations in the Black Sea. In Proceedings of the International Meeting, Chemical and Physical Oceanography of the Black Sea, Goteborg, June, 1986. Report on the Chemistry of Seawater, vol. XXXIII, University of Goteborg, Sweden.

Williams, L.R, Hiscott, R.N., Aksu, A.E., 2011. Holocenepaleoecology of the southwestern Black Sea shelf using ostracodsas proxies.Joannea Geologie & Paläontologie11, 216–219.

Williams, L.R., Hiscott, R.N., Aksu, A.E., Bradley, L.R., Horne, D.J., Stoica, M., 2018. Holocene paleoecology and paleoceanography of the southwestern Black Sea shelf revealed by ostracod assemblages. Marine Micropalaeontology 142, 48–66.

Winguth, C., 1998, Pleistozäne Meeresspiegelschwankungen und Sedimentation im nordwestlichen Schwarzen Meer: Zentrum für Meeres- und Klimaforschung der Universität Hamburg, Institut für Biogeochemie und Meereschemie.

Wong, H.K., Panin, N., Dinu, C., Georgescu, P., & Rahn, C., 1994. Morphology and post-Chaudian (Late Pleistocene) evolution of the submarine Danube fan complex: Terra Nova 6, p. 502-511.

Yamamoto, Y., Takahashi, N., Pinar, A., Kalafat, D., Citak, S., Comoglu, M., Polat, R., Kaneda, Y., 2017. Geometry and segmentation of the North Anatolian Fault beneath the Marmara Sea, Turkey, deduced from long-term ocean bottom seismographic observations. Journal of Geophysical Research: Solid Earth, 122, 2069–2084.

Yanchilina, A.G., Ryan, W.B.F., McManus, J.F., Dimitrov, P., Dimitrov, D., Salvova, K., Filipova-Marinova, M., 2017. Compilation of geophysical, geochronological, and geochemical evidence indicates a rapid Mediterranean-derived submergence of the Black Sea's shelf and subsequent substantial salinification in the early Holocene. Marine Geology 383, 14–34.

Yalçiner, A., Pelinovsky, E., Talipova, T.,Kurkin, A., Kozelkov, A., Zaitcev, A., 2004. "Tsunami in the Black Sea: comparison of the historical, instrumental, and numerical data," *J. Geophys. Res*., 109, C12023.

Yanko, V., 1990, Stratigraphy and paleogeography of marine Pleistocene and Holocene deposits of the southern seas of the USSR: Memorie della Societa Geologica Italiana, 44, 167–187.

Yanko-Hombach, V.V., 2006. Controversy over Noah's Flood in the Black Sea: Geological and foraminiferal evidence from the shelf. *In*: Yanko-Hombach, V., Gilbert, A.S., Panin, N., Dolukhanov, P.M. (Eds.), The Black Sea Flood Question: Changes in Coastline, Climate, and Human Settlement. Springer, Dordrecht, pp. 149–203.

Yanko-Hombach, V., Gilbert, A.S., Panin, N., Dolukhanov, P.M. (Eds.), 2007a. The Black Sea Flood Question: Changes in Coastline, Climate and Human Settlement. Springer, Dordrecht.

Yanko-Hombach , V., Gilbert, A.S., Dolukhanov, P., 2007b. Controversy over the great flood hypotheses in the Black Sea in light of geological, paleontological, and archaeological evidence. Quaternary International 167–168, 91–113.

Yanko-Hombach, V., Mudie, P.J., Kadurin, S., Larchenkov, E., 2014. Holocene marine transgression in the Black Sea: new evidence from the northwestern Black Sea shelf. Quaternary International 345, 100–118.

Yavuz, V., Akcar, N., Schluchter, C., 2007. The frozen Bosphorus and its paleoclimatic implications based on a summary of the historical data. In: Yanko-Hombach, V., Gilbert, A.S., Panin, N., Dolukhanov, P.M. (Eds.), The Black Sea Flood Question: Changes in Coastline, Climate and Human Settlement. Springer, The Netherlands, pp. 633–649.

Zenina, M., Ivanova, E., Bradley, L., Murdmaa, I., Schornikov, E., Marret, F., 2017. Origin, migration pathways, and paleoenvironmental significance of Holocene ostracod records from the northeastern Black Sea shelf. Quaternary Research, 87, 49–65.

Zitek, A., Tchaikovsky, A., Irrgeher, J., Waidbacher, H., Prohaska, T., 2015. The $^{87}Sr/^{86}Sr$ river water isoscape of the Danube catchment. Chapter 33 in: Liska, I., Wagner, F., Sengl, M., Deutsch, K., Slobodnik, J. (Eds.), Joint Danube Survey 3: a Comprehensive Analysis of Danube Water Quality. International Commission for the Protection of the Danube River, Vienna International Centre, Austria and European Commission.